Reliability and Prognostics of Copper-Aluminum Wirebond System Subjected to Extreme Ambient and Operating Conditions

by

Shantanu Deshpande

A dissertation submitted to the Graduate Faculty of
Auburn University
in partial fulfillment of the
requirements for the Degree of
Doctor of Philosophy

Auburn, Alabama
August 4, 2018

Keywords: Copper Wirebonding, Semiconductors, Reliability, Failure Analysis, Life Prediction Modeling

Copyright 2018 by Shantanu Deshpande

Approved by

Pradeep Lall, John and Anne MacFarlane Professor of Mechanical Engineering, Director of NSF-CAVE3 Electronics Research Center
Jeffrey C. Suhling, Quina Distinguished Professor and Chair of Mechanical Engineering
Michael Zabala, Assistant Professor of Mechanical Engineering
Robert Dean, McWane Endowed Professor of Electrical Engineering
Bart Prorok, Professor of Materials Engineering

Abstract

Wire bonding is predominant first level interconnect used in semiconductor packaging industry. Gold (Au) is traditionally used for wirebonding since inception. Recent increase in the cost of Au has forced industry to seek an alternative. Copper (Cu) wire has emerged as the most promising material candidate to replace incumbent Au wires. Along with being very cheap, Copper has better thermal and electric conductivity, better mechanical strength and stiffness than gold. Cu when bonded onto Aluminum (Al) pad form Inter-metallic compounds (IMCs) at the bond-pad interface. IMC growth for Cu-Al system is much slower than Au-Al system even at higher temperatures. This makes Cu wirebonds more reliable than Au wirebonds.

Higher reactivity of Cu is a major issue in the implementation of Cu wirebonding into commercial packaging. Optimal window for wirebonding process is very narrow and small deviations in the process parameters can result into the poor and unreliable bond. These issues have been tacked by past researchers by undertaking various optimization studies and by using inert atmosphere for the bonding process. Cu, being prone to corrosion gets easily affected by the mechanical and chemical properties of surrounding entities. Semiconductor devices are often molded with commercial epoxy mold compounds (EMCs). EMCs contain various levels of ionic contamination introduced in various manufacturing processes. The level of contamination can adversely affect the reliability of Cu wirebond and might result into premature failures. Further, EMCc are hydrophilic in nature. Under high humidity conditions, the moisture can easily penetrate the EMC and can corrode wirebond or pad resulting into open circuit failures. These reliability concerns have stalled the transition from Au to Cu wirebonding in critical automotive, aerospace and down-hole drilling applications.

Past researchers have mainly focused on statistical quantification of the Cu wirebonded parts under various environments. This involves monitoring predetermined number of packages for certain time to check for failures. failed parts are then analyzed using various techniques to identify root cause of failure. This approach does not underline progression of damage as a

function of time; which is critical in understanding response of wirebond junctions to different environments. Cu wire has different failure mode and degradation mechanism than Au wires. Current literature lacks the quantification needed for redefining various accelerated life testing standards for Cu wirebonds.

In this work, various failure modes and mechanisms for Cu wirebonded devices under various environmental conditions is presented in details. Effect of different high temperature and effects of various high humidity levels were separately studied and acceleration factors (AF) were established. Acid based decapsulation technique was developed to dissolve EMC surrounding wirebond without affecting integrity of the wire. Neural Network (ANN) based model was developed to understand the sensitivity of the decapsulation process parameters. Change in electric response of the wirebond was correlated with the change in morphology of bond pad interface and reduction in ball shear strength. Effect of various EMC properties such as ionic contamination, pH value, external bias on time to failure of Cu wirebonded devices was studied and quantified. All reliability test data was then compiled to develop various life prediction models to predict life expectancy of the field extracted part based on current state of electric performance and properties of the EMC. Different techniques such as ANN, Levenberg-Marquardt algorithm (LM), Extended Kalman Filtering (EKF) were used for this purpose. Thermal cycling reliability of the Cu wirebonded parts was studied using FE analysis, performed on the model generated from the computed tomography (CT) database. Finally a brief study is presented which describes different failure modes and time to failure for Gold, Copper, Silver (Ag) and Palladium coated Copper (PCC) wirebonded parts subjected to high temperature and electro-migration test.

Acknowledgments

I would like to sincerely thank my adviser and NSF-CAVE3 center director Dr. Pradeep Lall for his valuable guidance and support during the completion of my PhD degrees at Auburn University. I would like to express my deep gratitude to my sponsors, Texas Instruments and industrial liaison Dr. Luu Nguyen and Masood Murtuza for their support and valuable inputs. Thank you for always fulfilling our wish-list for the project.

I would like to extend my gratitude to Dr. Jeff Suhling, chair person of Mechanical Engineering Department. I have learned a lot in his courses. Special thanks go to Dr. Mike Bozack and Dr. Michael Miller for guiding me through specimen preparation process for SEM imaging! I would like to extend my Thank to other committee members, Dr. Robert Dean and Dr. Michael Zabala and Dr. Bart Prorok for serving as my committee member.

I would like to thank my parents Shashikant and Indrayani Deshpande; my beloved wife Shruti Deshpande for their limitless sacrifices, support, love and encouragement which guided me through some of the toughest times. I want to specially mention my brother and best friend Nakul Kothari, my roommate for three years and lab-mate for 4 years. Thank you for always being there for me!! This work could not have been possible without the help, encouragement and support of my lab seniors, colleagues and well wishers.

Table of Contents

Abstract ii

Acknowledgments iv

1 Introduction 1

1.1 Introduction to Wirebonding 1

1.2 Wirebonding Metallurgy 3

1.3 Accelerated Life Testing 5

1.4 Test Standards 7

1.5 Thesis Layout 11

2 Literature Survey 13

2.1 Wirebonding 13

2.1.1 Reliability of Au Wirebonding 13

2.1.2 Reliability of Cu Wirebonds 15

2.1.3 Decapsulation Techniques for Cu Wirebonded Plastic Encapsulated Microelectronics (PEM) 19

2.1.4 Silver (Ag) and Palladium Coated Copper (PCC) Wirebonding 23

2.1.5 Fatigue Reliability of Wirebonds 26

2.2 Prognostics Health Monitoring (PHM) Systems 28

2.2.1 PHM for Electronics Assemblies 28

3 Microstructural Indicators for Prognostication of Cu-Al Wirebond Reliability under High-Temperature Storage and Temperature Humidity 32

3.1 Overview 32

3.2 Test Vehicle and Test Matrix 33

3.3 Experimental Result and Analysis 35

3.3.1 High Temperature Thermal Aging 35

3.3.2 Accelerated Test for Corrosion Susceptibility of Cu-Al 41

3.3.3 Activation Energy Calculations 48

3.4 Prognostication Approach for HTSL 50

3.4.1 Levenberg Marquardt Algorithm 53

3.4.2 Prognostics Performance Matrix 57

3.5 Summary and Conclusions 62

4 Development of Model for Identification of Process Parameters for Wet Decapsulation of Cu-Al Wirebonds in PEMs 64

4.1 Overview 64

4.2 Test Vehicle and Test Matrix 65

4.3 Decapsulation Process Results 68

4.3.1 BGA337 68

4.3.2 32 Pin CSP 74

4.3.3 FDS6690 and ICS553 79

4.4 Neural Network Modeling 83

4.4.1 NN Framework 83

4.4.2 Model Development 86

4.4.3 Model Validation and Discussion 88

4.5 Summary and Conclusions 94

5 Life Prediction Model for The Interaction of Operating Conditions, EMC Formulation and Applied Bias for Cu Wirebonded Devices 95

5.1 Overview 95

5.2 Test Vehicle 96
5.3 Test Protocol 98
5.4 Test Matrix 100
5.5 Experimental Results for High Temperature Tests 102
5.5.1 Failure at Cu-Al Interface 102
5.5.2 Effect of EMC Formulation on the Cu-Al WB Reliability 111
5.5.2.1 EMC A 111
5.5.2.2 EMC B 113
5.5.2.3 EMC C 114
5.5.2.4 EMC D 116
5.5.2.5 EMC E 118
5.5.2.6 EMC F 120
5.5.3 Compiled Results 122
5.6 Experimental Results for Temperature Humidity Test 124
5.6.1 EMC A 124
5.6.2 EMC F 126
5.6.3 Compiled Results 128
5.7 Predictive Model for High Temperature Condition 129
5.8 Predictive Model for High Temperature High Humidity Condition 133
5.9 Summary and Conclusions 140

6 High Temperature Storage life (HTSL) and Electromigration (EM) Reliability of Copper, Gold, Silver and PCC Wirebonds bonded onto Al pad 142
6.1 Overview 142
6.2 Test Vehicle 143
6.3 Test Matrix and Protocol 144
6.4 Experimental Results 147

6.4.1 High Temperature Test 147
6.4.1.1 Cu Wirebond 147
6.4.1.2 PCC Wirebond 153
6.4.1.3 Ag Wirebond 158
6.4.1.4 Au Wirebond 162
6.4.1.5 Comparison of Wirebonds 167
6.4.2 High Current Test 169
6.4.2.1 Cu Wirebond 169
6.4.2.2 PCC Wirebond 172
6.4.2.3 Ag Wirebond 176
6.4.2.4 Au Wirebond 180
6.4.2.5 Comparison of Wirebonds 183
6.5 Summary and Conclusions 185

7 Effect of Green EMCs on Fatigue Reliability of Molded Wirebond Systems 187
7.1 Overview 187
7.2 Test Vehicle 188
7.3 Mesh Generation 189
7.3.1 Image segmentation 189
7.3.2 Surface Reconstruction 192
7.3.3 Mesh Decimation and Smoothing 193
7.4 FE Analysis 198
7.5 Finite Element Results 200
7.6 Summary and Conclusions 208

8 Summary 210
8.1 Key Highlights 210

8.2 Recommendation for Future Work 212

References 213

Appendices 228

List of Figures

1.1 Schematic of Wirebond 1

1.2 Steps in Ball Bonding Process 2

1.3 Wedge Bonding 3

1.4 Voided Au-Al Interface after 960 Hours of aging at 185°C 4

1.5 Void-free Au-NiPdAl Interface after 4000 Hours of aging at 200°C 4

1.6 Accelerated Life Testing 7

1.7 Ball Shear Test Setup 9

1.8 Wire bond shear failure types 11

2.1 Oxide boundary of Voiding at Au-Al Interface 14

2.2 Decapsulation Process 20

3.1 Optical Images of 32 pin CSP 33

3.2 X-ray Image of 32 Pin CSP 34

3.3 3D Reconstruction of 32 Pin CSP Along with Cu Wirebonds 34

3.4 IMC growth of Cu-Al Junction at 150°C 36

3.5 IMC growth of Cu-Al Junction at 175°C and 200°C 37

3.6 Crack Initiation and Propagation at 175°C 38

3.7 EDX Analysis of the Cu-Al Interface 39

3.8 EDX Analysis at the Corroded Interface 39

3.9 EDX Line Scan Along the Peripheral Crack 40

3.10 Summary of IMC Measurement Technique 40

3.11 IMC Growth During HTSL Test 41

3.12 Cracking at the Cu-Al Interface at (a)110°C (b)120°C and (c)130°C/100%RH . 42
3.13 EDX Point Analysis on Failed CuAl Interface 43
3.14 EDX Line Scan of a Crack in Wirebond 44
3.15 EDX Point Analysis on Failed CuAl Interface 44
3.16 Pourbaix Diagram of (a)Copper, (b)Aluminum 45
3.17 IMC Growth Rate 49
3.18 AE Calculations 49
3.19 Prognostication of thermally aged samples 52
3.20 Normalized IMC vs Square root of aging time 52
3.21 3D Plot of convergence of LM Algorithm at 150°C 55
3.22 3D Plot of convergence of LM Algorithm at 175°C 56
3.23 3D Plot of convergence of LM Algorithm at 200°C 57
3.24 α-λ curve for HTSL test at 150°C 59
3.25 α-λ curve for HTSL test at 175°C 60
3.26 α-λ curve for HTSL test at 200°C 60
4.1 Optical and X-ray Images of 32 pin CSP 65
4.2 Optical and X-ray Images of BGA 337 66
4.3 Optical and X-ray Images of FDS6690A 66
4.4 Optical and X-ray Images of ICS553MILF 67
4.5 Wire Diameter Measurement 68
4.6 Wire Diameter Reduction for BGA 337 at 100°C 69
4.7 Wire Diameter Reduction for BGA 337 at 130°C 69
4.8 Wire Diameter Reduction for BGA 337 at 150°C 70
4.9 Post Decap Cu wire 2:1 Acid Combination at 100°C 70
4.10 Post Decap Cu wire 2:1 Acid Combination at 100°C 71
4.11 Post Decap Al Pad Corrosion at 1:4 acid combination 71

4.12 Post Decap Al Pad Corrosion at 3:1 acid combination 72
4.13 Ball Shear Strength of Post Decap BGA337 Package at 100°C 73
4.14 Ball Shear Strength of Post Decap BGA337 Package at 130°C 73
4.15 Ball Shear Strength of Post Decap BGA337 Package at 150°C 74
4.16 Wire Diameter Reduction for CSP at 100°C 74
4.17 Wire Diameter Reduction for CSP at 130°C 75
4.18 Wire Diameter Reduction for CSP at 150°C 75
4.19 Cu wire for CSP 2:1 Acid Combination 76
4.20 Cu wire - 2:1 Acid Combination at 100°C 76
4.21 Corroded Cu wire - 1:4 Acid Combination at 150°C 77
4.22 Corroded Cu wire due to high nitric acid content 130°C 77
4.23 Ball Shear Strength of Post Decap Wires at 100°C 78
4.24 Ball Shear Strength of Post Decap Wires at 130°C 78
4.25 Ball Shear Strength of Post Decap Wires at 150°C 79
4.26 Percent Wire Diameter Reduction of ICS553 Package at 100°C 80
4.27 Percent Wire Diameter Reduction of ICS553 Package at 130°C 80
4.28 Percent Wire Diameter Reduction of ICS553 Package at 150°C 81
4.29 Post decap sample at 2:1 100°C combination (a) overview (b)(c) closeup 81
4.30 Percent Wire Diameter Reduction of FDS6690 Package at 100°C 82
4.31 Percent Wire Diameter Reduction of FDS6690 Package at 130°C 82
4.32 Post decap sample at 2:1 100°C combination (a) overview (b)(c) closeup 83
4.33 Neural Network architecture 84
4.34 MSE minimization during iterative training. 88
4.35 Error histogram from NN training using Bayesian regularization 88
4.36 Comparison of experimental and predicted reduction in wire diameter 89

4.37 Variation in experimental and predicted wire reduction as a function of change in process temperature . . . 90

4.38 Variation in experimental and predicted wire reduction as a function of change in % nitric acid fraction . . . 90

4.39 MSE minimization during iterative training . . . 91

4.40 Residual plot of ANN . . . 92

4.41 Comparison of experimental and predicted ball shear strength . . . 92

4.42 Variation in experimental and predicted ball shear strength as a function of change in process temperature . . . 93

4.43 Variation in experimental and predicted shear strength as a function of change in % nitric acid fraction . . . 94

5.1 32 Pin QFN . . . 97

5.2 Box Plot of the Time-Zero Resistance of the packages . . . 99

5.3 Distribution of Time-Zero Resistance of the packages . . . 99

5.4 Package heating due to Joule heating . . . 100

5.5 IMC Thickness Measurement . . . 101

5.6 Change in resistance of the package molded with EMC A . . . 102

5.7 Evolution of the morphology of Cu wirebond-Al pad junction with bias . . . 103

5.8 Evolution of the morphology of Cu wirebond-Al pad junction with bias . . . 104

5.9 Evolution of the morphology of Cu wirebond-Al pad junction Without Bias . . 105

5.10 Increase in the IMC thickness for EMC A . . . 105

5.11 EDX Spot Analysis . . . 106

5.12 EDX Spot Analysis . . . 107

5.13 Change in shear strength of WB subjected to unbiased test conditions . . . 108

5.14 Shear failure modes for Cu Wirebonds . . . 109

5.15 Distribution of Shear Failure Modes subjected to unbiased test conditions . . . 109

5.16 Change in shear strength of WB subjected to biased test conditions . . . 110

5.17 Change in shear strength of WB subjected to biased test conditions 110
5.18 Change in resistance of packages molded with EMC A 111
5.19 Change in Shear Strength of packages molded with EMC A 112
5.20 Evolution in Mode II Failure for EMC A 112
5.21 Change in Resistance of packages molded with EMC B 113
5.22 Change in Shear Strength of packages molded with EMC B 113
5.23 Evolution in Mode II Failure for EMC B 114
5.24 Change in Resistance of packages molded with EMC C 115
5.25 Change in Shear Strength of packages molded with EMC C 116
5.26 Evolution in Mode II Failure for EMC C 116
5.27 Change in Resistance of packages molded with EMC D 117
5.28 Change in Shear Strength of packages molded with EMC D 117
5.29 Evolution in Mode II Failure for EMC D 118
5.30 Change in Resistance of packages molded with EMC E 118
5.31 Change in Shear Strength of packages molded with EMC E 119
5.32 Evolution in Mode II Failure for EMC E 119
5.33 Change in Resistance of packages molded with EMC F 120
5.34 Change in Shear Strength of packages molded with EMC F 121
5.35 Evolution in Mode II Failure for EMC F 121
5.36 Time to Failure of the Cu Wirebonded packages 123
5.37 Shear Failure Modes (a) Mode I (b) Mode II (c) Mode III 124
5.38 Change in Resistance for EMC A 125
5.39 Change in Shear Strength for EMC A 125
5.40 Shear Failure Mode Distribution for EMC A 126
5.41 Change in Resistance for EMC F 126
5.42 Change in Shear Strength for EMC F 127

5.43 Shear Failure Mode Distribution for EMC F 127
5.44 Compiled Change in Resistance of Cu Wirebonds Molded with Different EMCs 128
5.45 Neural Network Topology 129
5.46 Minimization of MSE during NN training Process 130
5.47 Residual plot of NN Fitting 130
5.48 Comparison of experimental and predicted time to failure 131
5.49 Variation in the experimental and predicted time to failure due to change in aging temperature 132
5.50 Variation in the experimental and predicted time to failure due to change in ionic contamination 132
5.51 3D Predictive plot for interaction of pH and ionic contamination 133
5.52 EKF Performance and RUL Prediction 138
6.1 Optical and X-ray Images of the Package 144
6.2 Optical Image of Fabricated Package 145
6.3 Temperature Change in The Package Due to Joule Heating 146
6.4 IMC Measurement Technique 147
6.5 Increase in the resistance of Cu wirebonds at 200°C aging temperature 148
6.6 Growth of Cu-Al IMC at bond-pad interface 148
6.7 log-log plot of IMC thickness vs aging duration 149
6.8 log-log plot of IMC thickness vs aging duration 149
6.9 Evolution of different IMC phases due to high temperature exposure 150
6.10 Crack initialization and propagation in Cu-Al wirebond system 150
6.11 Change in shear strength of bond-pad interface as a function of time 151
6.12 Shear failure modes (A) Mode I (B) Mode II 152
6.13 Evolution of shear failure modes 153
6.14 Increase in Resistance of PCC wirebonds 153
6.15 Growth of PCC-Al IMC at bond-pad interface 154

6.16 log-log plot of IMC thickness vs aging duration 154

6.17 Phases in PCC-Al wirebond system due to exposure to high temperature 155

6.18 Evolution of different IMC phases due to high temperature exposure 156

6.19 Crack initialization and propagation in PCC-Al wirebond system 156

6.20 Change in shear strength of bond-pad interface as a function of time 157

6.21 Evolution of shear failure modes 158

6.22 - Increase in Resistance of Ag wirebonds 159

6.23 Growth of Ag-Al IMC at bond-pad interface 159

6.24 log-log plot of IMC thickness vs aging duration 160

6.25 Phases in Ag-Al wirebond system due to exposure to high temperature 160

6.26 Evolution of different IMC phases due to high temperature exposure 161

6.27 Crack initialization and propagation in Ag-Al wirebond system 161

6.28 Increase in Resistance of Au wirebonds 162

6.29 Growth of Au-Al IMC at bond-pad interface 163

6.30 log-log plot of IMC thickness vs aging duration 163

6.31 Phases in Au-Al wirebond system due to exposure 164

6.32 Voiding in Au-Al wirebonds 165

6.33 Change in shear strength of bond-pad interface as a function of time 165

6.34 Change in shear strength of bond-pad interface as a function of time 166

6.35 Change in shear strength of bond-pad interface as a function of time 166

6.36 Change in resistance of wirebonds due to high temperature exposure 167

6.37 Change in resistance of the packages vs IMC growth 167

6.38 Change in resistance of the packages vs IMC growth 168

6.39 Increase in The Resistance of Cu-Al Wirebond 169

6.40 IMC Growth of Cu-Al Interconnect 170

6.41 Interfacial Cracking in Cu Wirebonds 171

6.42 Evolution of Cu-Al IMCs 171

6.43 Effect of Current Direction on Cu-Al IMC Growth 172

6.44 Increase in Resistance of PCC-Al Wirebond 173

6.45 IMC Growth of PCC-Al Interconnect 173

6.46 Evolution of PCC-Al IMCs 174

6.47 Effect of Current Direction on PCC-Al IMC Growth 174

6.48 Interfacial Cracking Observed Upon Failure 175

6.49 Increase in Resistance of Ag-Al Wirebond 176

6.50 IMC Growth of Ag-Al Interconnect 177

6.51 Interfacial Cracking Observed Upon Failure 178

6.52 Evolution of Ag-Al IMCs 178

6.53 Effect of Current Direction on Ag-Al IMC Growth 179

6.54 Increase in Resistance of Ag-Al Wirebond 180

6.55 IMC Growth of Au-Al Interconnect 181

6.56 Interfacial Voiding Observed Upon Failure 181

6.57 Evolution of Au-Al IMCs 182

6.58 Effect of Current Direction on Au-Al IMC Growth 182

6.59 Compiled Resistance Data of All Wirebond Candidates 183

6.60 Compiled IMC Growth Data of All Wirebond Candidates 184

6.61 Compiled IMC Growth Data of All Wirebond Candidates 185

7.1 32 Pin QFN 188

7.2 CT Reconstruction of 32 Pin QFN Package 189

7.3 Image Segmentation using Otsu Method (a)X-ray projection, (b)Boundary identification (c)Area selection for conversion. 192

7.4 Lead from lead-frame package (a) pre-surface reconstruction (b) post surface reconstruction 193

7.5 Lead from lead-frame package (a) post-surface reconstruction (b) after quadratic decimation and smoothing 196

7.6 Dimension of single lead after CT to mesh conversion 197

7.7 Dimension of single lead after CT to mesh conversion 198

7.8 Dimension of single lead after CT to mesh conversion 199

7.9 Stress-strain curve for 1mil Cu wire 200

7.10 Thermal cycling profile 201

7.11 Von Mises stresses during cooling step on Si Chip for (a) EMC A (b) EMC F . 201

7.12 Von Mises stresses during cooling step on lead frame for (a) EMC A (b) EMC F 202

7.13 Von Mises stresses during cooling step on EMC for (a) EMC A (b) EMC F . . . 203

7.14 Von Mises stresses during cooling step on the Wirebond for (a) EMC A (b) EMC F 204

7.15 Plastic equivalent strain in the wedge bond at the end of one cycle for (a) EMC A (b) EMC C (c) EMC F 204

7.16 Plastic equivalent strain in Wedge bond after 1 cycle 205

7.17 Wirebonds molded with EMC A after 1 cycle (a) Plastic Strain (b) Von Mises Stresses 205

7.18 Plastic Strain in Wedge bond after 1 cycle 206

7.19 Plastic strain in the ball bond at the end of one cycle for (a) EMC A (b) EMC C (c) EMC F 206

7.20 Maximum and Average Plastic Strain in Ball bond for various EMCs 207

7.21 Comparison of plastic strain in wedge bond and ball bond after 1 cycle 207

7.22 Fatigue crack in wedge bond after thermal cycling test 208

List of Tables

1.1 Material Properties of Au, Cu and Ag 5
1.2 Comparison of Typical Application Conditions of Electronics 6
1.3 Part Operating Temperature Grades 8
1.4 Accelerated Stress Test Standards for Grade-0 Packages 9
3.1 Dinemsions of Test Vehicle 33
3.2 Percent Atomic Weight of Elements 43
3.3 Comparison of Activation Energies for Cu-Al 50
3.4 Comparison of IMc Growth Rates 50
3.5 Comparison of experimental and prognosticated Results at 150°C 56
3.6 Comparison of experimental and prognosticated Results at 175°C 57
3.7 Comparison of experimental and prognosticated Results at 200°C 57
3.8 Comparison for Prognostics Metrics for Three Aging Conditions 62
4.1 Dimensions of 32 pin CSP 65
4.2 Dimensions of BGA 337 65
4.3 Dimensions of FDS6690 and ICS553 66
4.4 Details of the Packages 67
4.5 Inputs for Wire Diameter Reduction Model 87
4.6 Inputs for Shear Strength Model 87
5.1 Package Dimensions 97
5.2 Properties of Molding Compound 97
5.3 EMCs and Respective Test Conditions 100

5.4 EDX Analysis Result at point A, B and C 106
5.5 EDX Analysis Result at Crack Tip 107
5.6 Time to Failure of the Cu Wirebonded packages 122
5.7 Average absolute error in prediction of RUL (Remaining Useful Life) 139
6.1 32 Pin QFN Dimensions 144
6.2 EDX analysis of IMC phases at point A, B and C 149
6.3 EDX analysis of IMC phases at point A, B, and C 155
6.4 EDX analysis of IMC phases at point A, B 160
6.5 EDX analysis of IMC phases at point A, B 164
6.6 EDX Analysis at The Crack Front 175
7.1 Package Dimensions 188
7.2 Sample Dimension Comparison 196
7.3 Dimensional Consistency 197
7.4 Table of material Properties 199
7.5 Table of EMC Properties 199

Chapter 1

Introduction

1.1 Introduction to Wirebonding

Wirebonding is primary interconnect between Silicon (Si) chip and the substrate of the package or PCB, as shown in, Figure 1.1 by Suhling[1]. It is the most dominant first level interconnect used in the packaging industry. According to Kulicke and Soffa [2] by 2021, 25 trillion wirebonds will be bonded onto the Si chip; 50 percent higher than 2016. The wire used for bonding is typically in the range of 0.8mil-5mil diameter. 1mil thick wire is most commonly used for wirebonding purpose.

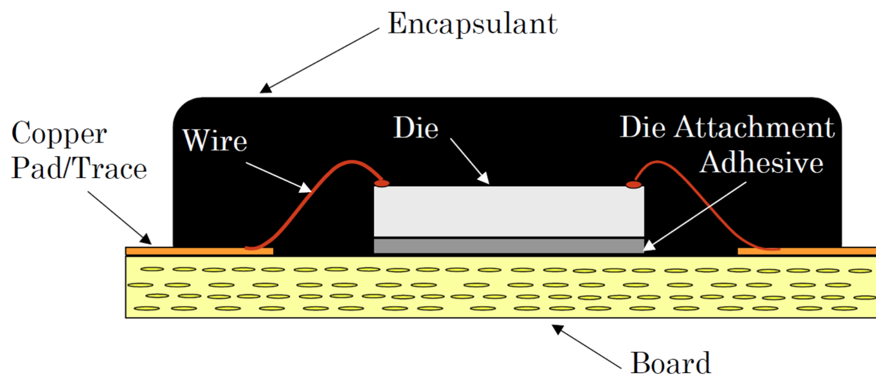

Figure 1.1: Schematic of Wirebond

Wirebonds can be categorized into two different types; ball bonding and wedge bonding. In the ball bonding process, metal wire is welded to the chip metallization (usually Al pad) by thermosonic or thermocompression method. A typical bonding process is shown in Figure1.2[3]. Wire overhanging from the capillary is melted locally using electrical flame off

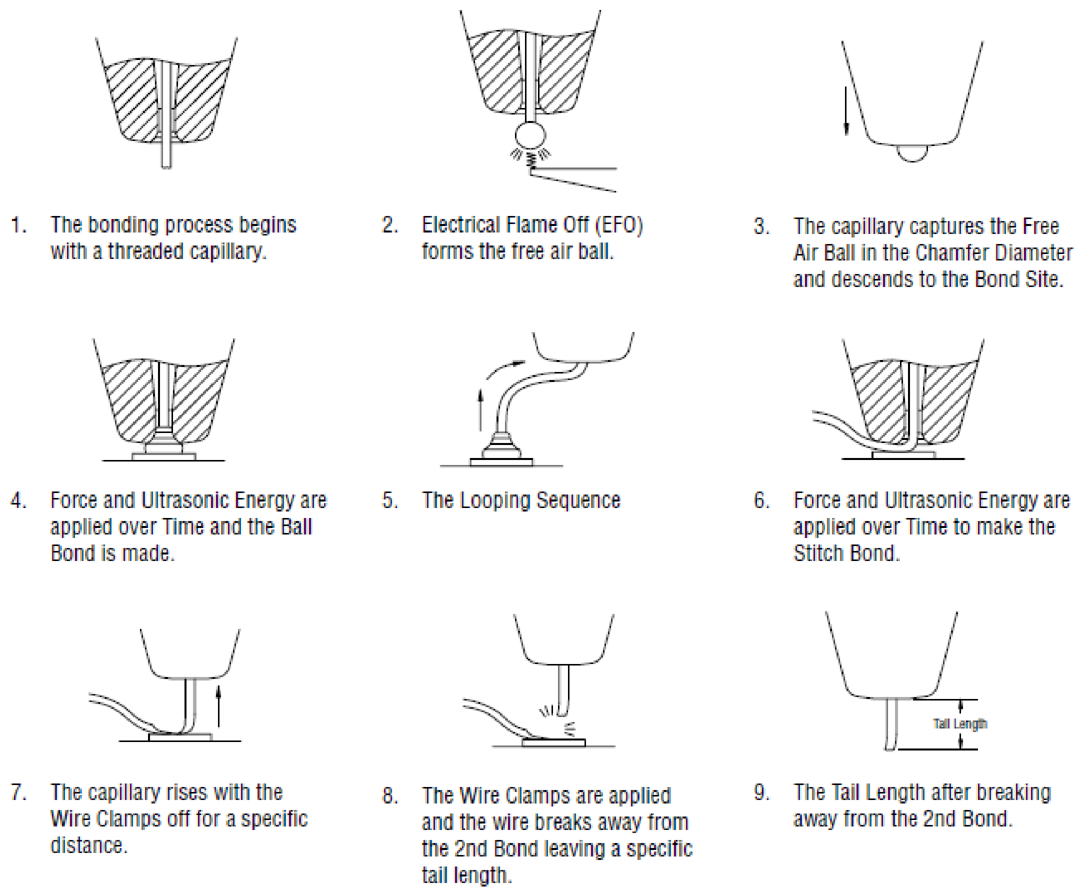

Figure 1.2: Steps in Ball Bonding Process

(EFO). In this process very large voltage is applied for very short time to fuse the wire. Capillary catches the melted part and forms free air ball (FAB). This ball is then bonded onto the pad using combination of high temperature, ultrasonic energy and mechanical force. This causes formation of the IMCs at bond pad interface, ensuring strong bond; Chauhan [4]. Wire is then released from capillary to form the loop. Second bond or stitch bond is bonded onto the substrate using mechanical force and ultrasonic energy. Wire is then broken off from the stitch joint by clamping the wire in capillary. The overhanging tails is then used to form FAB for next wire. The wirebonding process is very fast, self cleaning, high yield, low cost and flexible process.

Wedge bonding does not involve FAB formation. Both welds are formed using special wedge shape capillary fixture and by applying mechanical and ultrasonic energy. Summary of wedge bonding process is shown in Figure1.3 [5]. This type of bonding is majorly used in applications where very small wire loop height, deep access is desired. Wedge bonding is

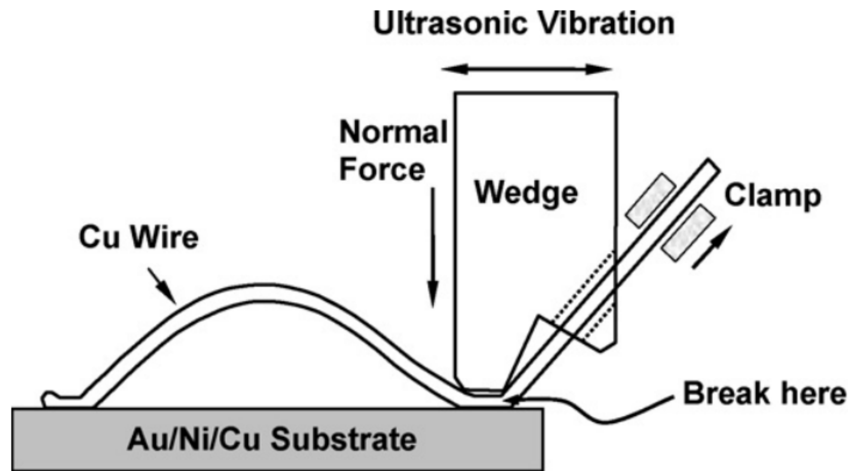

Figure 1.3: Wedge Bonding

preferred for very thick wires (>75 µm). Ball bonding is much faster than wedge bonding and is less susceptible to pad corrosion based defect. Hence ball bonding is more common in the industry and will be studied in this work.

1.2 Wirebonding Metallurgy

Traditionally gold wire has been used for wirebonding purpose. Aluminum pad is most widely used chip metallization for wirebond to land. Au and Al diffuse easily into each other to form different IMC phases which provided wirebond necessary strength. At elevated temperatures the IMC grows rapidly and causes large amount of voiding at the bond pad interface. This voiding not only degrades mechanical strength of the bond, but also increases resistance of the electron flow path, causing electric failures. Figure1.4 shows severe voiding at WB interface only after aging part for 960 hours at 185°C. The detailed mechanism of the void formation, growth and its effect on the reliability of wirebond is discussed in further chapters. Coating Al pad by Nickel-Palladium(NiPd) and bonding Au on this barrier layer is the only way to avoid this phenomenon. Even at elevated temperatures, the barrier layer restricts the IMC layer growth and void formation. Figure1.5 shows the void-free interface observed for Au wirebond bonded onto NiPd coated Al pad after 4000 hours of aging at 200°C. However, implementation of NiPd coated pads is limited due to very high material and process cost.

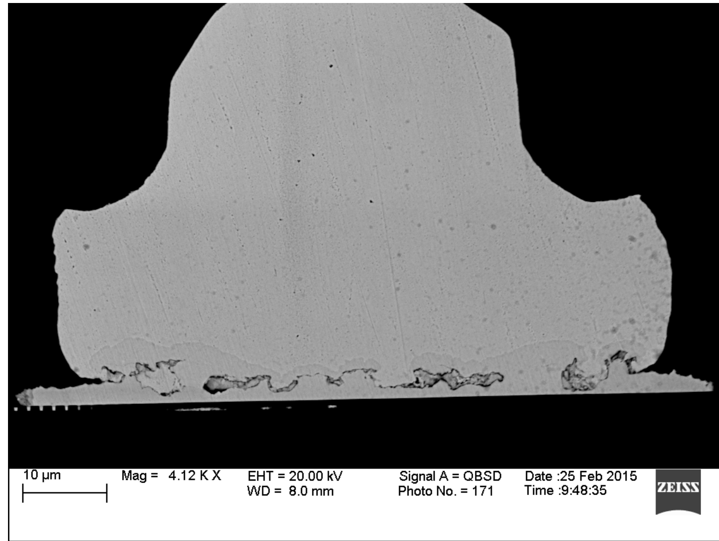

Figure 1.4: Voided Au-Al Interface after 960 Hours of aging at 185°C

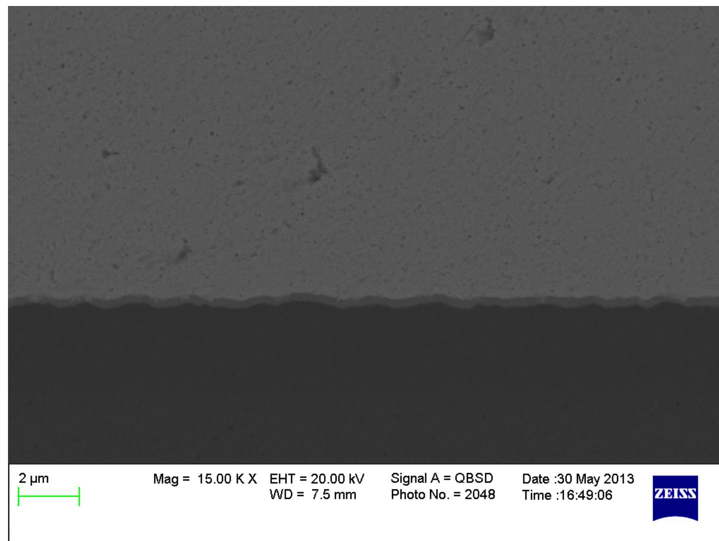

Figure 1.5: Void-free Au-NiPdAl Interface after 4000 Hours of aging at 200°C

In the recent years very rapid growth of Au wire has forced semiconductor industry to seek alternatives; in-order to keep the packaging cost down. Cu and Ag are the two most likely candidates to replace Au wire. Comparison of material properties of all three materials is shown in 1.1 [6].

Cu and Ag have higher thermal conductivity and lower electrical resistivity than Au. This enables implementation of finer wire than Au to carry the same current without any overheating issues. Better thermal conductivity of Ag and Cu ensures better heat dissipation in case of small form factor-high current density electronics applications. Heat generated during FAB travels

Table 1.1: Material Properties of Au, Cu and Ag

Property	Unit	Cu	Au	Ag
Thermal Conductivity	W/mK	400	320	430
Electrical Resistivity	m	1.72	2.2	1.63
Youngs Modulus	GPa	130	60	82.5
Poisson Ratio		0.34	0.44	0.364
Yield Stress	MPa	200	32.7	45.5
CTE	ppm/C	16.5	14.4	18.9
Vickers Hardness	MPa	369	216	251

in transverse direction in the wire and causes elongation of grains. This local phenomenon is called heat affected zone (HAZ). HAZ weakens the wire neck section and restricts short looping of wires. Better thermal conductivity of material ensures rapid dissipation of extra heat and shortens HAZ [7]. Copper has much higher strength than gold which minimizes wire sweep phenomenon during molding process. Higher hardness of copper and its tendency to easily oxidizing makes process window of wirebonding much narrower. Numerous studies have been published relating to optimization of process parameters and consistently forming reliable Cu bonds. Tang[8] showed that PCC coating significantly improves adhesion of second bond (stitch bond) and controls copper oxide formed during FAB. However, coating very thin layer of Pd on the Cu wire significantly increases cost of the wire. Silver wires have highest thermal conductivity and lowest electric resistivity among all candidates, which makes it more suitable for power electronics applications. Youngs modulus and hardness of silver is higher than gold, but lower than copper which makes Ag wires easier to bond on the pad. Even though bonding Ag on Al pad has wider process window, it is still significantly costlier than Cu and PCC wire bonding

1.3 Accelerated Life Testing

The most important milestone in the development of an electronic equipment or changing the bill of material (BOM) is to verify that the customer requirements are completely fulfilled.

These requirements often include life expectancy of the part under standard predefined operating conditions Pascoe[9]. Table1.2 by Canumalla[10] Shows the comparison of typical application conditions for various electronic parts. Consumer office electronics such as desktops see little variation in the environment. Parts used in such applications are easy to test and quantify. Automotive under the hood electronics have more wider temperature range. This include engine control unit (ECUs), different safety sensors, autonomous driving electronics etc. These are much critical for proper functioning of the vehicle.

Table 1.2: Comparison of Typical Application Conditions of Electronics

	Product Life (Years)	Power Cycles /day	Power On Hours	%RH	Environmental Temperature Range (C)	Operational Temperature Range (C)	Voltage (V)
Desktop	5	1 to 17	13,000	10 to 80	10 to 30	20 to 30	12
Mobile Terminals	5	20	43,800	10 to 100	-40 to 40	32 to 70	1.8-3.3
Automotive Under the Hood	15	5	8200	0 to 100	-40 to 125	-40 to 125	12

Manufacturer or supplier has to ensure that the new parts with changed material will function as intended during their deployment. This requires physical intensive testing of the parts to foresee the reliability problems. However due to it is practically impossible to test the assemblies for years to gather the data. Instead different stress testing methods are utilized which simulates the normal wear and degradation of the assemblies that would normally be experienced over the usable life in a shorter time period.

According to Pascoe[9], these stresses include elevated temperature and humidity, higher current and voltage bias, contaminated environment and solar radiation. Mechanical stresses can be simulated using vibration or drop testing. Time to failure data obtained from such accelerated tests can then be projected on operational stress conditions. Fig1.6 shows simplified process of accelerated life test.

Successful projection of time to failure (TTF) is performed by modelling acceleration factor (AF). AF is defined as the ration of the expected time-to-failure under normal operating

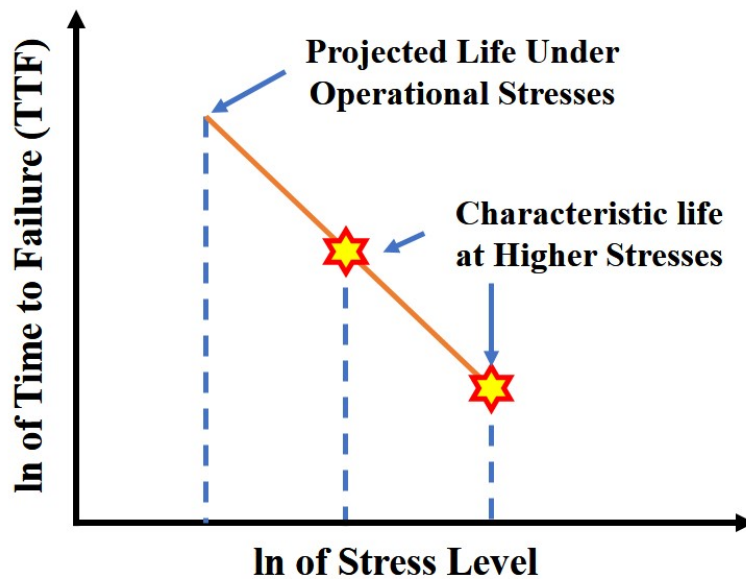

Figure 1.6: Accelerated Life Testing

conditions to the time-to-failure under some set of accelerated stress conditions. Simplified equation of AF calculation is shown in Equation 1.1.

$$AF = \frac{TTF_{Operation}}{TTF_{Stress}} \tag{1.1}$$

Acceleration factor is a unique factor which only depend on the physics of failure kinetics and is independent of process dependent coefficient and device to device variation; Mcpherson[11]. Change in the underlined physics of failure of the devices during accelerated life test is indication of excessive stresses. High levels of stresses can introduce new failure modes which might never occur in the normal operating conditions. TTF data for such experiments should not be part of AF model.

1.4 Test Standards

Reliability tests are performed at known condition. They need to be reproducible, hence a standard set of testing is used across industry. These conditions are different for different applications based on the environment in which the electronics is deployed. There are different test standards established for testing of semiconductor products covering broad spectrum

of applications. These different standards include U.S Military Standards (MIL-STD-810F), Japan Electronics and Information Technology Industries (JEITA), International Electrochemical Commission (IEC), Joint Electronic Device Engineering Council Solid State Technology Association (JEDEC), Automotive Electronics Council (AEC) etc. All standards describe the application field, types of tests required, environmental conditions and test time, test statistics, desirable failure modes in details. Since the current work is focused towards reliability of Cu wirebonded parts under extreme conditions, only AEC test standards will be briefly described. AEC-Q100-Rev-H is published on 11 Sept. 2014 is the most updated document used for failure mechanism based stress test quantification for integrated circuits (IC) [12]. Test methods described in AEC standards refers to different JEDEC standards with minor modifications. In

Table 1.3: Part Operating Temperature Grades

Grade	**Ambient Operating Temperature Range**
0	$-40°$C to $150°$C
1	$-40°$C to $125°$
2	$-40°$C to $105°$
3	$-40°$C to $85°$

AEC standards, there are different grades of packages from reliability perceptive. Grade 0 packages are used in critical applications hence have to undergo much severe reliability tests. On the other end, Grade 3 packages are not used in critical applications and does not see harsh environmental conditions. Hence test conditions for grade 3 quantification are comparatively simple. Part operating temperature grades are shown in Table 1.3.

According to AEC-Q100-Rev-H [12] grade 0 packages have to survive ambient temperature of $175°$C for 1000 hours or ambient temperature of $150°$C for 2000 hours under High Temperature Storage Life Testing (HTSL). Temperature Cycling (TC) test requires parts to survive 2000 thermal cycles from $-55°$C to $150°$C. Table 1.4 shows different accelerated stress test standards for grade-0 packages. TC, Highly Accelerated Stress Test (HAST) and high temperature operating life (HTOL) conditions requires 3 lots of 77 samples each for testing with 0 failures.

HTSL and Power Temperature Cycling (PTC) requires testing only one lot of 45 samples. AEC-Q006-Rev-A [13] is the new set of standards published for quantification of components

Table 1.4: Accelerated Stress Test Standards for Grade-0 Packages

Test	Conditions
HTSL	175°C for 1000 Hours or 150°C for 2000 Hours
PTC	−40°C to 150°C, 1000 Cycles
TC	−55°C to 150°C, 2000 Cycles
HTOL	150°C for 1000 Hours
bHAST	85°C/85%RH for 1000 Hours or 130°C/85%RH for 96 Hours
HAST	121°C/15psig for 96 Hours or 130°C/85%RH for 96 Hours

using Cu wirebond as a interconnect. Test standards are similar to the standard test conditions but requires larger sample sizes across all tests. Standard also recommends carrying frequent cross-sectioning to analyze integrity of ball bond and wedge bond. It also encourages conducting ball shear test to quantify strength of the ball bond. In this step, first EMC surrounding package is stripped away or dissolved using either acids or using LASER/Plasma techniques. Then ball shear test is performed, in which ball bond is sheared off using specialized load cell and force required to shear the ball is captured. Schematic of bond shear setup is shown in Figure 1.7[14].

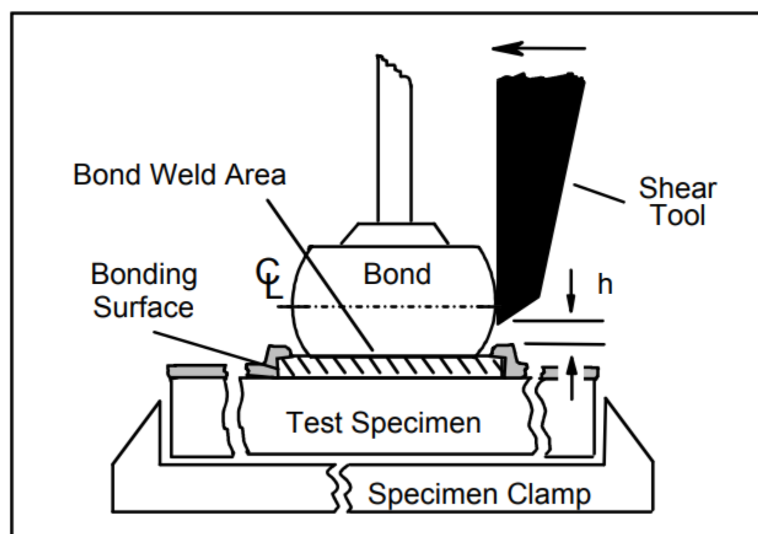

Figure 1.7: Ball Shear Test Setup

Sheared surface is then studied under microscope to identify the location of the failure and classify it into different modes of failure. AEC-Q101-REV-A [14] has documented different failure modes of ball shear test failures for Au wirebonds. Six types of failure modes are described in the standard as shown in Figure 1.8[14]. When the bond between wire and pad is weak, wirebond separates from the bonding surface with very little or no residue of IMC on the sheared surface. This is called as bond lift and is first type of failure. In second type, wire gets sheared but keeps major chunk of IMC intact; which indicates strong weld between bond-pad. If the bonding force used during wirebonding are high, they can cause fracture of Si underneath pad; also known as cratering. In this type of failures fractured Si gets chipped away with sheared wire. Type 4 and 6 are related to the adhesion of pad to the Si chip. If this type of failure is observed, Ci chip and Al pad should be checked for contamination. The failure modes described in the standard are for Au wires only. Cu wires have different bond strength than Au wires. They also have different IMC formation rate and IMC phases. This significantly affects the type of failure modes one could expect during test. Hence AEC-Q101-REV-A cannot be used for classifying shear failure modes in Cu wirebonded parts.

As seen earlier, current reliability standards are only valid for an applications with ambient temperatures of 150°C. With increasing electrification of the vehicles and introduction of autonomous driving features, electronics in automobiles is facing new challenges. In all the sensors based feedback systems it's important for different sensors to be as close as possible to the critical components such as engine, power transmission, differential. This significantly increases stresses onto the censor circuitry and temperatures can sore as high as 200°C. Current AEQ standards does not cover such extreme conditions. Quantification of the parts is often difficult and required extensive testing. In this thesis, a framework is presented which will address this issue. Degradation of daisy chained packages bonded with Cu wirebond was studied under various high temperature [150°C-225°C], humidity [130°C/100%RH, 120°C/100%RH, 110°C/100%RH], external voltage bias [0V, 2.5V] conditions. The test were performed on samples molded with eight different EMCs to cover material aspect of the reliability issues. Failure modes, mechanisms and damage accumulation was developed for each case separately

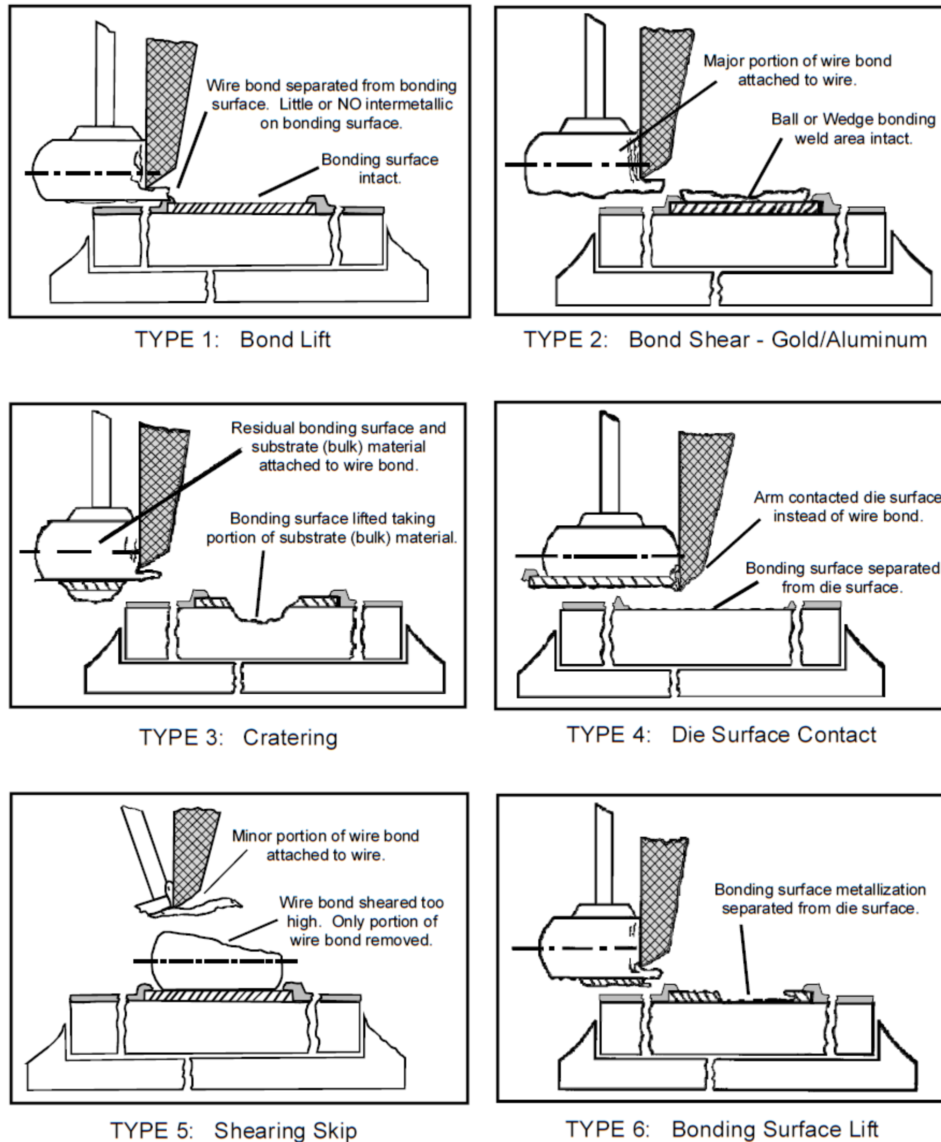

Figure 1.8: Wire bond shear failure types

using technique such as resistance measurement, cross-sectioning, ball shear testing etc. Acceleration factors were calculated and life prediction models were developed using different techniques such as EKF, ANN, PCR etc.

1.5 Thesis Layout

Chapter 1 covers introduction section. In this section basics of wirebonding process, metallurgy are described. This section also briefly discusses fundamentals of accelerated life testing and current reliability test standards implemented in various industries.

Chapter 2 encompasses literature survey on Cu wirebonding technology. Current state of knowledge for the reliability of Cu wirebonded parts is discussed in details. This HAST failures of Cu wirebonds. Prognostics framework is also reviewed in this chapter along with literature available on CT to mech conversion.

Chapter 3 presents failure mode and mechanisms for Cu wirebonded devices subjected to HAST and HTSL conditions. IMC thickness was used as a leading indicator of failure and Levenberg-Marquardt (LM) algorithm was used to predict RUL based on damage proxy. Electric response of wirebonds to the stress test was not recorder.

Chapter 4 consists of development of optimized acid chemistry based decapsulation technique for Cu wirebonded PEMs without damaging wires. ANN based model was developed to study effect of different process and geometric parameters on the quality of decapsulation, and was validated with experimental data set.

Chapter 5 is a continuation of chapter 3. In this chapter combined effect of environmental temperature, humidity, external bias and different EMCs was studied. Different predictive models were developed based on EKF, ANN and PCR to predict remaining useful life of field extracted part. This chapter also establishes correlation between change in electric response of wirebonds with change in the bond pad morphology and change in shear strength of the ball bond.

Chapter 6 focuses on thermal cycling reliability aspect of the Cu wirebonded parts. In this chapter FE model was developed based of STereoLithography files extracted from X-ray CT scanner. Chapter briefly focuses on the conversion work-flow followed by FE based analysis. Effect of green EMCs on the cyclic reliability of QFN devices is presented.

In Chapter 7, failure modes for Cu, Au, Ag and PCC wires under HTSL test are discussed in details. Another set of parts with these four wire candidates was subjected to high current test to study electromigration (EM) phenomenon. Failure modes for EM study are discussed in this chapter.

Chapter 8 includes the conclusion of the presented work and briefly discusses the scope for future work.

Chapter 2

Literature Survey

2.1 Wirebonding

In this section reliability related issues available in open literature will be briefly discussed.

2.1.1 Reliability of Au Wirebonding

Gold wirebonding has been vastly studied by researchers. Since gold has been used since inception of wirebonds, the bonding process itself is very robust. Philofsky[15] studied IMC formation in Au-Al wirebond system. Butt-welded diffusion couples were aged at very high temperatures (200°C to 460°C) to accelerate IMC formation process. Au_5Al_2 was the predominant phase identified at the initial stages. In the later stages three more phases were present in the IMC and were identified as AuAl, Au_2Al and Au_4Al. After aging the joint for extended timing, voiding was observed at the interface.

Murali[16] studied effect of different wire diameter on void formation and growth. Study reported that thinner wires tends to for much severe voiding as compared with their thicker counterparts. Thicker wirebonds had thicker IMC compared to thin wires. Zhang[17] aged gold wirebonded QFN devices at 175°C for 168hours. Study concluded that wirebonds with uniform IMC formation at the interface had longer HTS life compared to wirebonds with non-uniform IMCs. Later ones were more prone to voiding. An FE analysis was performed to analyze the stresses at the wirebond interface and it was concluded that axial forces acting within the ball bonds with non uniform IMC could cause rapid void formation. Volumetric shrinkage of different IMC phases was contributed to the axial force.

Xu[18] studied mechanism of phase transformation in Au-Al wirebonds subjected to elevated ambient temperatures. Two IMC phases, Au_4Al and $AuAl_2$ were found in "as bonded" state. In the early stage of annealing Au_8Al_3 phase was observed in between the prior two phases. As the aging continued, Al pad was completely consumed and $AuAl_2$ phase was transformed into Au_8Al_3. Even though Al pad is completely consumed, Au still continues to diffuse from the bond side to pad side. The continuous supply of Au atoms converts Au_8Al_3 to Au_4Al phase. Au_4Al was the terminal phase.

Xu[19] proposed new mechanism behind the void formation and growth. Authors proposed that combination of three mechanisms drives this phenomenon. These mechanisms were volumetric shrinkage, oxidation of IMC and Kirkindall voiding. Volumetric shrinkage was associated with IMC formation and growth. Oxidation of the IMC causes formation of oxide boundary along the void. TEM image of such corroded void is shown in Figure 2.1 . These results were consistent with some of the earlier work published by Noolu[20].

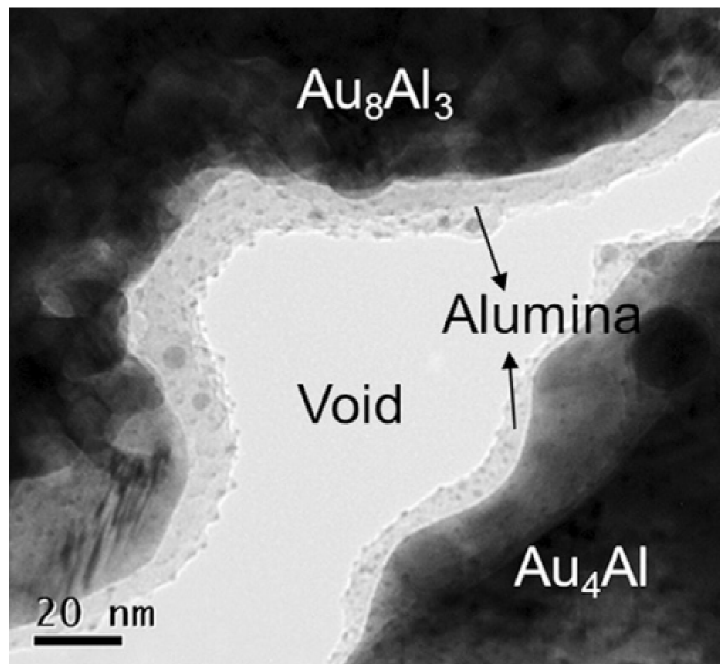

Figure 2.1: Oxide boundary of Voiding at Au-Al Interface

Zin[21] studied electromigration phenomenon in Au wirebonds. Very high current density ($5*10^5$A/cm^2) was passed via wirebonds. Authors concluded that EM does happen in the Au wirebonds and can lead to premature failures. When EM force was directed towards bond pad,

void formation and growth was aggressive when compared with EM forces working in opposite directions. Similar dependence of IMC and void growth on current direction was reported by Krabbenborg[22].

Even though there is wide variety of literature available on Au wirebonding, correlation between change in electric response of wirebond with change in shear strength and evolution of bond pad morphology is not yet well established. In mission critical application, failure of part is defined in terms of change in electric response. Electric properties of wirebond can change significantly before complete cracking is observed and result in false time to failure data. In this work, detailed analysis on the relation between electric failures in wirebonds with the physical change is presented. Data obtained from Au wires was used as benchmark and compared with Cu, PCC and Ag wirebonding.

2.1.2 Reliability of Cu Wirebonds

Lee[23] studied IMC formation and growth in details for friction welded Cu-Al bimetallic joint subjected to very high temperatures. Two IMC phases, CuAl and $CuAl_2$ were identified during annealing process. Activation energy for the diffusion based growth of IMc was found to be 110.22KJ/mol. It was also concluded that thicker IMC was susceptible to tensile failure and was significantly weaker than initial weld.

Xu[24] examined Cu-Al wirebond in as bonded state and used different techniques such as SEM, TEM, XRD to identify the phase formed at the Interface. Only one phase was present in this state. This phase was characterized to be $CuAl_2$.

Hang[25] studied the behavior of formation and growth of IMCs of Cu/Al wirebond system under HTSL. As the aging duration increased, decres in IMC growth rate was reported. Three phases were reported during the study. They were Cu_9Al_4, $CuAl_2$ and CuAl respectively. Prior two were major phases, while the later one was present in small amount. Cavity like defect originated at the periphery of the ball bond and propagated towards the center of the ball bond. Once it reached center, ball bond lift was observed. Similar studied were undertaken by Kim[26] and Gan[27]. Kim[26] also studied change in shear strength of Cu wirebond due to thermal aging. Upon aging, distribution of shear strength of the wirebond became wider.

Spread towards higher shear strength was contributed to thicker and stronger IMCs and lower shear values were contributed to peripheral cracking which made bond weaker.

Kouters[28] measured various mechanical and electric properties of different IMc phases. All IMC phases had different properties than pure Cu and Al. They were significantly harder and stronger and had higher resistivity. Xu[29] studied IMC growth mechanism and voiding in Cu-Al system. $CuAl_2$ was the only initial phase observed. Cu_9Al_4 phase was observed only after annealing had started. Both phases grew simultaneously. However, at the later stages Cu_9Al_4 became dominant phase and started to consume $CuAl_2$ phase. Activation energies for both phases were 75.61KJ/mol and 60.66KJ/mol respectively. A discontinued alumina layer present between two phases was contributed for voiding phenomenon. This voiding was negligible compared to voiding observed in Au wirebonds was was observed only at extremely high temperatures(200°C).

Ratchev[30] performed reliability tests (HTSL at 150°C) on Cu and Au wirebonds bonded on different pad metallization. Growth rate of Cu-Al IMCs was much slower than Au-Al system. Cu wire also had overall higher shear strength than Au wires which was contributed to stiffer Cu wire. Kirkindall voiding was not observed for Cu wirebonds. Similar results were reported by Gan[31].

Breach[32] studied shear failure modes of Cu and Au wirebonds in as bonded state. Au being softer wire had lower strength and upper part of the wire was removed, keeping lower part bonded to pad. In Cu bonding, shear strength was mainly a function of IMC distribution. More uniform IMC results into higher shear strength in which Al pad was peeled away.

Cu is more reactive than Au which can make it susceptible to external contamination. Su[33] studied effect of different properties of EMCs on reliability of Cu wirebonds molded on lead-frame based package. Packages molded with different EMCs were subjected to HTSL and HAST type testing. Cu wires molded with low pH and higher ionic contamination containing EMCs had faster degradation. This effect was more dominant in presence of humidity. Seki[34] carried out similar study on Cu and Au wirebonds under HAST testing and concluded that EMCs with low ionic contamination significantly enhanced reliability. Green EMCs showed good and consistent HAST performance.

Mathew[35] confirmed dependence of Cl ions and pH value on time to failure of Cu wire-bonded packages. Study future underlined that formate, acetate, phosphate and nitrate ions could inhibit corrosive impact of Cl ions. Rongen[36] studied effect of different EMCs on high temperature and temperature humidity reliability of Cu wirebonded packages. Planar analysis technique was used to study crack front propagation. In this technique by O'halloran[37], Cu wires are dissolved using fuming nitric acid and residual IMC is then studied under SEM. Author showed that crack propagation rate for wirebonds was highly dependent on temperature and EMC used. At higher temperature, crack propagation was faster. EMCs with higher Cl concentration also had faster crack growth leading to early failures.

Gan[38]studied degradation mechanism of CuAl wirebond system subjected to HAST test. Author reported presence of Cu_9Al_4, $CuAl_2$ phases at the interface. Under HASt conditions, ionic contamination (Cl ions) from EMC and presence of moisture attack the IMC's. Oxygen penetrates from the edge of the ball and induces oxidation in CuAl IMCs. Kim[39] performed HAST test on Au and Cu wires with 4N purity and 20 μm wire diameter. During initial period of aging, Cu wire had higher pull strength. However, as the aging period increased, pull strength of Cu wires reduced drastically; which was attributed to corrosion based crack initiation and propagation at CuAl interface. The interfacial degradation was contributed to aluminum oxide layer found at interface. In CuAl system, Cu acts as a oxidizing agent for Al. Although Au is stronger oxidizing agent, is does not react with water to form free ions.

Tan[40] studied corrosion of CuAl wirebonds under pressure cooker test (PTC) at 120°C/100%RH. Extent of corrosion in Cu wirebond was studied at predetermined time interval. As the test duration increased, copper oxidation was identified at the wire region and spread into the interracial region. Initial cracking was observed at the interface after aging duration of 384 hours and complete cracking was observed after 576 hours of aging. After the initial cracking was observed, drop in shear strength was observed.

Similar studies were performed using different FA techniques such as XRD, TEM by Osenbach[41], Boettcher[42] and concluded that amorphous matrix containing aluminum oxide dispersed just below Cu wirebond caused ball bond lift type of failure. Aluminum was not observed on the ball side but Cu and Al were both found on the pad side of the leftover surface.

Corrosion was prone to happen in Cu rich phase Cu_9Al_4 while the Al rich phase ($CuAl_2$) was much more stable and did not undergo corrosion easily. Gan[31] studied reliability and Cu and Au wire under different aging conditions. Au was found to be much more reliable and stable than Cu under HAST conditions. Under HTSL conditions, Cu was more reliable than Au.

Tian[43] studied failures in CuAl wirebond in different environmental conditions. Under thermal cycling conditions, even after 1500 cycles of aging IMC growth was not significant. This was contributed to rapidly changing temperatures and lower time spent by devices at elevated temperatures. HTOL test was carried at $150°C$ ambient temperature and parts did not failed after 600 hours of aging. When the ambient temperatures were raised to $200°C$, thicker IMc was observed. Cracking in IMC was also reported after 100 hours of aging. Cracking continued to grow till 500 hours followed by ball lift failure.

Rongen[44] studied degradation of Cu wirebonded contacts under high current (1.0A) and high temperature condition ($200°C$) using in-situ resistance monitoring. Even though external current was present, failure mechanism in wirebonds was interfacial corrosion. Degradation of IMC was independent of the current direction. Interfaces with higher contact temperatures were associated with rapid degradation of the bond. Yang[45]studied damaged induced by Joule heating phenomenon on wedge bonds. Study was conducted on 0.8mil stitch bonded wire. Joule heating was induced using very high current densities passing via wire. Abnormal cracking and rapid IMC growth was observed irrespective of the current direction. Rapid IMC formation and growth resulted into cracking at the wedge bond interface and resulted into failure. There is a sparsity of literature available on effect of high current densities in reliability and time to failure of Cu ball bonds.

Arjmand[46] performed thermal cycling reliability study on Cu wirebonds. Stitch wirebonds with $381\,\mu m$ diameter were subjected to thermal cycling from -$55°C$ to $125°C$. Crack initiation and propagation was studied using 3D X-ray computed tomography system. After 2900 cycles cracking was observed at the substrate and wire interface.

Mazloum[47] performed FEM based analysis on Cu wirebonded molded quad flat package with 176I/O. Thermal cycling temperatures were from -$55°C$ to $150°C$. Heat affected zone

(HAZ) was chosen to be life limiting factor. Van[48] studied delamination induced stitch cracking in copper wires. 3D plane stress model was formulated and molded with generic (high coefficient of thermal expansion (CTE) and low modulus (E)) and green EMCs. Green EMCs are contamination free epoxies with higher filler content; hence lower CTE and higher E. It was concluded that delamination in the EMC is a prerequisite for stitch bond failures. Green low CTE EMCs imposed significantly higher stresses at the wedge bond due to CTE mismatch than traditional EMCs. Study was performed in the temperature range of -65°C to 180°C.

Studying interaction of different parameters on reliability of Cu wirebond and their quantification is critical step in transition of Cu wirebonds into automotive realm. In this work, effect of ionic contamination, pH value on time to failures, acceleration factors is quantified. This will provide a statistics based framework for understanding reliability of Cu wirebonded devices under different environmental and operating conditions.

2.1.3 Decapsulation Techniques for Cu Wirebonded Plastic Encapsulated Microelectronics (PEM)

PEMs are preferred over hermetically sealed packages because they are cheaper, reliable, small and weight when compared to their predecessor. These devices are molded with the epoxy compounds. Pecht[49] reported that a commercial EMC is a combination of epoxy resin, accelerators, inert filler material, flame retardants, curing agent, stress relief agents, adhesion agent, mold release agents, carbon black etc. Depending on the operating conditions, these additives are added with specific ratio. EMCs serve as a protection for semiconductor devices from external contamination, moisture, shock etc.

Decapsulation is a failure analysis technique often used to exposes the die and first level interconnects such as wirebonds by dissolving the surrounding epoxy molding compound (EMC). Decapsulation can be used for investigation of different defects related to interconnect; different modes of failure such as short-circuits, electric overheating, ion-migration etc. Schematic representation of before and after decapsulated package is shown in Figure 2.2 by Tang[50]. Ideally, the decapsulation process should not compromise the mechanical, electrical, or chemical properties of the semiconductor device and just dissolve the surrounding EMC. According

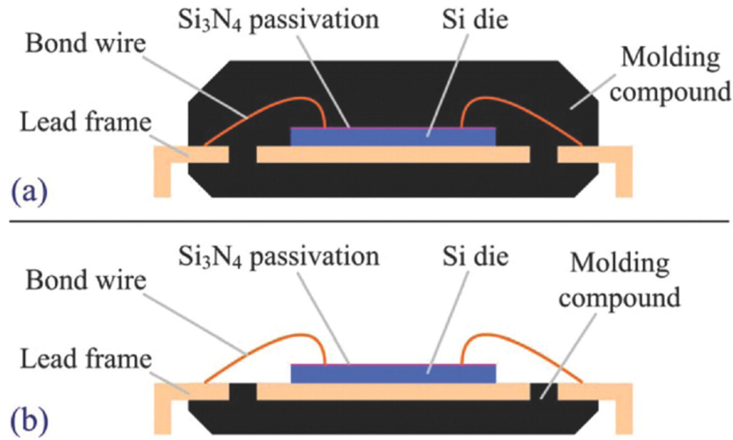

Figure 2.2: Decapsulation Process

to Murali[51] in PEMs Aluminum (Al), Cu and Au are the three main interconnect materials accompanied by Silver (Ag), Palladium (Pd), Tin (Sn) etc. are used for different purpose.Decapsulation technique should carefully designed such that all elements of the PEM stay intact and he process does not yield into addition device degradation.

Ma[52] classified decapsulation process into two groups, dry methods and wet methods. Wet method involves use of combination of highly concentrated and aggressive acids to dissolve EMCs, while the dry method uses high energy lasers and microwave plasma pulses.

Lefevre[53] used combination fo cold nitric acid and laser pulses for decapsulation. Short laser pulses were used for localized heating and vaporization of the material. This process is continued till the EMC is completely evaporated. A laser pre-cavity was made on the bulk EMC side and stitch joint side. It was followed by removal of EMC using cold nitric acid. Laser based system was again used to expose the Cu ball bond and stitch bond, followed by complete removal of EMCs.

Different types of plasma systems (microwave plasma, pressure plasma) were used by Tang[54], [50], Tan[55]. Laser ablation was used to remove top layer of EMC. Plasma's with combination of O_2 and CF_4 were used to etch molding compound. High etching sensitivity of the plasma ensured the integrity of Cu wires. Different plasma gas combinations and process temperatures were tested to check decapsulation quality and find the optimum combination. Plasma based decapsulation technique was tried on multi-tired wirebonded applications with limited success. Tan[55] studied degradation of Cu wire during decapsulation technique by

performing ball shear and ball pull tests. Authors used combination of plasma etching and methane sulfonic acid cleaning process. Lower pull strength and shear strength was observed for degraded wirebonds. This was contributed to highly localized corrosion which made bond very weak.

De La Cruz[56] and Ma[52] performed comparison of different copper wire decapsulation techniques for failure analysis. In laser based decapsulation process, high powered laser pulses could cause localized heating and damage the die passivation layer. Etching rate in this process depends on energy absorption capacity of material. Absorption capacity of filler and resin material were different. This causes an in-homogeneous etch. In such cases, removal of molding compound from hard to reach areas, such as molding compound below bond wire loop became time consuming, and required frequent orientation changes. Even though plasma etching offered high selectivity of the process parameters, and restricted overheating of the die, internal metallization of the package could easily be oxidized due to the existence of oxygen during plasma etching process. High pressure air used to blow out byproduct of the process, could damage the wire-bond. In dry decapsulation techniques, one need to find optimum settings for different package type and metallization system. Furthermore, these parameters need to be updated for different geometries of packages.

The wet decapsulation technique is a fast, cheap yet effective decapsulation technique; uses a combination of concentrated or fuming acids. Red fuming nitric acid is the most widely used acid for wet decapsulation since it reacts very well with the EMC. The fuming nitric acid does not react with Au or Si, and when in contact with Al forms strong passivation layer to prevent further corrosion. However, it does severely corrode the Cu as shown in Equation 2.1[57].

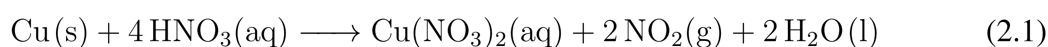

$$\mathrm{Cu\,(s) + 4\,HNO_3(aq) \longrightarrow Cu(NO_3)_2(aq) + 2\,NO_2(g) + 2\,H_2O\,(l)} \tag{2.1}$$

Cu is highly reactive than Au which makes the development of acid based decapsulation process challenging. Concentrated sulfuric acid can be used for decapsulation process only at very high temperatures (More than $150°$C), which can damage the package architecture.

Ohalloran[37] reported that Sulfuric acid does not react with copper but it aggressively reacts and digests the Al pad. Previously researchers have studied the effect of different mixing ratios of nitric and sulfuric acids, at different process temperatures and acid flow rates on decapsulation of Cu-Al wirebond system.

When fuming nitric acid and sulfuric acid are mixed, Nitronium ion, Hydronium ion and hydrogen sulfate ions are formed as shown in equation 2.2. This reaction were provided by Left Coast Instruments[58].

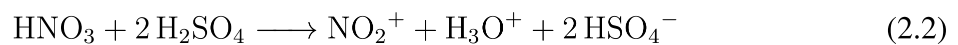

$$HNO_3 + 2\,H_2SO_4 \longrightarrow {NO_2}^+ + H_3O^+ + 2\,{HSO_4}^- \quad (2.2)$$

Copper reacts with the hydrogen sulfate ions to form copper sulfate. Copper sulfate is a passivation layer which does not get affected by acids thus restricts further corrosion of Cu wire; Ng[59].

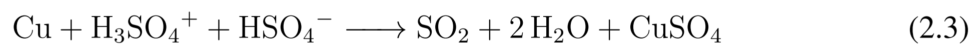

$$Cu + {H_3SO_4}^+ + {HSO_4}^- \longrightarrow SO_2 + 2\,H_2O + CuSO_4 \quad (2.3)$$

If water or moisture is present during this reaction, it causes dissolution of Copper. This can be avoided by using very concentrated Sulfuric acid, which reacts with water and produces more bisulfate ions. Since bisulfate ions are highly unstable, fresh acid solution is required for each iteration of experiment. By mixing two acids together, ill effects of both acids were minimized.

Murali[51] studied effect of different acid combinations on post decap wire quality for Cu wirebonds. Quality of decapsulation was quantified based on reduction in wire diameter during the decapsulation process. Optimum process temperature and acid ratio was established. Authors reported that acid concentration and process temperature had inverse relation between them. Highly concentrated acids at lower temperatures produced optimum results at the cost of higher decapping time.

Ng[59] introduced dual stage decapsulation process. The health of the post decapped device was verified by comparing electric characteristics of the decapped and un-decapped devices. In the dual stage decapsulation, a small cavity was created by using fuming nitric acid,

and then desired acid combination is poured in the cavity to make decaping process faster. It was shown by the authors that even wire reduction as high as 10% does not significantly affect the electrical characteristic of the device. Even though efforts have been taken in past to address decapsulation issue, comprehensive study which correlates different decapsulation process parameters to the quality of decap is not yet clearly established. Articles available in open literature do not comment or provide exact information about the optimum acid ratio and process temperatures.

2.1.4 Silver (Ag) and Palladium Coated Copper (PCC) Wirebonding

Ag has lower Young's modulus and hardness compared to Cu. It also has lower resistivity than Au and Cu. Ag wire could be bonded onto Al pad at lower bonding force than Cu, which translates into more reliable bonds. Some of these process advantages of Ag over Cu has made silver one of the competitors to Cu wirebonding.

Jang[60] performed long term reliability study on 0.7mil thick Ag wires bonded onto $1.3\,\mu m$ thick Al pad. HTSL test was carried out for 2000 hours at 150°C and 200°C. IMC growth for AgAl system was faster than CuAl system but slower than AuAl system. Two phases of IMCs (Ag_3Al and Ag_2Al) were found during the test. IMC growth was only function of environmental temperate and was independent of EMC used for molding. Under HTSL micro-cracking was observed at the AgAl interface which was contributed to Cl related corrosion of the IMCs.

Kai[61] studied reliability of 0.8mil Ag wires bonded on Al pad. IMc coverage was studied by performing chemical etching on Ag wirebonds. No failures were observed even after 1000 cycles of thermal cycling (-65°C to 150°C), 1000 hours at 150°C condition. Parts also passed 196 hours of HAST and PTC testing. IMC growth was observed under HTSL conditions and (Ag_3Al and Ag_2Al) phases were reported. Study was repeated on Au and Pd doped Ag wire, but results were the same.

Cheng[62], Xi[63] and Tsai[64] performed similar studies on Ag and Ag alloy wires. All studied found only two IMC phases under HTSL condition which were consistent with prior

literature. Ag wires also passed all the standard reliability tests required for quantification without any premature failures.

Fu[65] studied effect of highly contaminated EMCs and temperature humidity on Ag wirebonding. The corrosion rate of Ag3Al was twice of that of Ag2Al, meaning that Ag2Al is more resistant to corrosion. In the corroded regions, Ag3Al and Ag2Al compounds disintegrate into aluminum oxide pieces and dispersed Ag precipitates with voids and cracks. The chlorine detected near voids and cracks suggest formation of aluminum chloride as an intermediate product that is hydrolyzed into aluminum oxide.

Electromigration phenomenon is another critical issue with Ag wirebonding. Hsu[66] studied effect of high current densities and elevated temperatures on Au wirebonds. Ag wire with $25.4\,\mu m$ wire diameter was subjected to $175°$C and current density of 8*$10^4 A/cm^2$. After 112 hours of aging, abnormal protrusions were reported at the cathode side of the sample. Variation in IMC thickness at cathode and anode was reported by authors.

Hsueh[67] studied change in mechanical properties of Ag wires due to joule heating and electromigration phenomenon. Compared to Pd-coated Cu wires, the tested Ag-based wires had lower tensile strength and elongation in the current stressing test because Cu features superior electromigration resistance than Ag. Massive electromigration induces many voids and cracks at the grain boundaries in Ag-based wires, both of which later propagate to form intergranular fractures. Hence, although Ag-based wires are applied in the microelectronic packaging industry, the working current must be lower than that in Cu-based wires to prevent failure. Wang[68] studied electromigration in un-molded Au and Ag wires at $250°$C and 5mA/$microns^2$. No abnormal surface defects were found in Au wires after the test; however for Ag wires, morphology was significantly change. This phenomenon was observed on the surface and within the wire too. Large amount of voiding and cracks in and on the wire confirmed tendency of Ag atoms for electromigration.

As discussed earlier, AgAl interface is prone to cracking and susceptible to electromigration. Even though Ag prices are lower than Au, they are significantly higher than Cu. Palladium is usually added into pure Ag to improve reliability performance which increases resistivity of

the wire[4]. Due to such limitations, implementation of Ag into into high performance critical electronic systems is yet restricted.

PCC wirebonding was introduced to get over the poor bond ability of Cu wires at second bond. Surface oxidation was the contributing factor in this phenomenon. Coating Cu wire with Pd is accepted as viable alternative to control the defect[4].

Kaimori[69] studied development of the wirebonding process by applying oxidation resistant coating. Cu wire with $25\,\mu m$ diameter was coated with $0.8\,\mu m$ thick Pd layer. This was then bonded onto $(80\,\mu m*80\,\mu m)$ Al pad and Ag plated QFP lead frame. Bond strength was studied used wire pull tests. Pd plated wirebonds showed excellent second bond strength along with excellent bond-ability and reliability.

Tang[8] studied effect of Pd coating on formation of FAB. FAB is the key factor which directly affects quality of ball bond. Different FAB were formed by varying process parameters and the distribution of Pd on the surface was analyzed. Irrespective of the FAB parameter, thicker Pd coating was observed at the neck portion. Continuous reduction in thickness was observed towards the FAB. The Pd diffuses into Cu and disperses during FAB process. This causes random distribution of Pd coating on FAB.

Lim[70] studied effect of different bonding parameters on Pd distribution and the reliability of PCC wires. Pd distribution was function of type of EFO gas used, EFO duration and power. Wider and more uniform distribution of Pd was concluded to be important from reliability standpoint.

Abe[71] compared reliability of Cu and PCC wires subjected to HAST testing. Better reliability of PCC wires was reported by extensive testing. Chemical reaction simulation were performed to understand corrosion kinetics. Simulations concluded that distribution of Pd at the ball bond worked as Cl ion trapper and resisted corrosion of Cu rich IMC for significant duration.

Uno[72] evaluated performance of PCC wirebond under biased HAST. At $175°C100\%$RH, PCC wires survived for 800 hours, while Cu wires failed after 250 hours due to continuous cracking. Augar electron microscopy showed that presence of Pd can form Pd-Cu barrier restricted crack propagation under high temperature-humidity conditions.

Krinke[73] studied reliability of PCC wires under high temperature storage life. Test was performed at 150°C, 175°C, 200°C and 250°C. Intrinsic degradation of pcc-wires at HTSL conditions above 150°C was observed. The mechanism was driven only by temperature. A crack of the Pd coating was necessary to start the degradation. Ball pull test values were satisfied even after extensive aging at 150°C, while at 175°C, values were well below standard.

Lee[74] studied void formation mechanism in PCC wires under HTSL. These Cu voids observed in the bulk ball bond could only occur at PdCu ball bond and were not observed at bare Cu ball bonds. Cu voids at PdCu ball bond was result of galvanized corrosion formed by coupling of Pd and Cu due to small area of Cu exposed to the mold compound. Thus, Cu voids were always located at the capillary chamfer side wall. These voiding did not affect the reliability of PCC wires.

2.1.5 Fatigue Reliability of Wirebonds

Along with high temperature and high humidity reliability, fatigue aspect of the wirebonds is also very important. Frequent on-off cycles and storage conditions causes wide variation at the junction temperature. The difference in the mismatch of coefficient of thermal expansions (CTE) and cyclic nature of loading can exert on the ball bond and wedge bond.

Reliability of 1mil Al wire was studied by Ravi[75] under on-off package condition. Fatigue crack growth was observed at the heel section of the bond. Al wire with 1% Mg was found to be more reliable than Al wire with 1% Cu additive.

Ramminger[76] studied reliability models doe Al bonds subjected to heel crack failures. Analysis was performed on 500 µm thick Al wires capable of carrying up to 75A current. Finite element based crack propagation model was developed for cracking at Al0Si interface due to cyclic loading.

Deyhim[77] studied reliability of bond wires in different types of cavity type packages. Wire fatigue testing machine was developed for test purpose. Aluminum wires and different gold alloy wires were subjected to mechanical fatigue loading at different ambient temperatures. Leong[78] undertook comparative Au, PdCu and Pd doped Cu wires. 80 samples were subjected to thermal cycling test with the range of -40°C to 150°C. Pd doped Cu wires was

found to be most reliable one, whereas Au wires were the least reliable wires. Cycles to failure data is very subjective and changes when the EMCs are changed.

Medjahed[79] studied thermal cycling reliability of bonded wires used in IGBT modules under AC and DC current conditions. Numerical and FE based model was developed to analyze the critical parts of the wirebonds subjected to power cycling. Maximal stress distribution was produced by using the Von-Mises yield criterion. It was noted that the maximal mechanical stress is obtained at the heel of the bond wire which is exactly where the main bond wire failure modes occur.

In recent years "green EMCs" are introduced which are known for their lower ionic contamination, and very high thermal stability. This makes them ideal for extreme environment applications. Green molding compounds often have higher filler content as compared traditional EMCs. Filler material is usually glass fibers which are very stiff and has low CTE. This addition does not only reduces CTE of overall mold compound matrix (7ppm-11ppm), but also makes it stiffer compared with traditional EMCs (16ppm-24ppm). . Vandevelde[80] studied effect of green EMCs on the fatigue failures observed in Cu wirebonded parts. 3D slice of QFN package was modeled in FE platform and the thermal cycling simulation was performed in the range of -40°C to 150°C. Maximum plastic strain was found to be at wire loop region. The simulation based findings were then validated with experimental results. It was also shown that reduction of CTE of EMCs from 12ppm to 6ppm increased the PEEQ in the wirebonds by 400%.

Czerny[81] studied mechanical fatigue response in Cu wirebonded LQFP packages using finite element technique. The testing setup was especially designed to mimic the thermo-mechanical loading conditions of the encapsulated package by inducing specified multi-axial stresses to the non-encapsulated wire bond loops. The accumulated plastic strain in the wires was calculated with extended FEA and customized material parameters. A Coffin Mason type lifetime model was established and verified based on the FEA calculations and experimental fatigue results providing a reliability margin for fine wire bond loops in the tested package. Failure location predicted by FE software was in the wire neck region, and this was confirmed using experimental testing.

2.2 Prognostics Health Monitoring (PHM) Systems

Maintenance of electronic assemblies is of utmost importance in order to ensure smooth functioning of the system. At the beginning of industrialization, maintenance was only performed in corrective way. This approach is not only extremely dangerous in mission critical applications, but also results into excessive down times of the system. A new time based preventive maintenance was then introduced, in which system maintain was performed at the predetermined time intervals. Kothamasu[82] pointed out that even the time based maintenance system can result into significant downtime, hence cause loss of revenue in sectors such as aviation, power, automotive etc. Prognostics approach is modeled towards minimizing repair and maintenance costs and associated operational disruptions, while also minimizing the risk of unscheduled downtime. This is achieved by performing ongoing assessment of machine health and prediction of future failures based on the history data obtained by various sensors. Various critical parameters are usually monitored with the help of array of sensors and the data is stored for prediction purpose. Combination of various algorithms such as regression, maximum likelihood, expectation maximization, particle filtering etc. are then used for parameter estimation in future vector space. Currently PHM systems are successfully implemented in different industries. Applications include but not limited to aircraft structure integrity, power plants, mega-structures such as skyscrapers and dams, ships and submarines, space applications and in mission critical electronics assemblies.

2.2.1 PHM for Electronics Assemblies

Implementation of PHM systems in electronics applications is still at testing phase and is not widely used in industry. First attempt of diagnostics monitoring of electronics involved use of built in test (BIT). These include series of on board hardware-software tool that can locate and isolate the damage, can detect errors and self rectify them [83]. BIT can be implemented in circuit, module or system level electronics. Despite the apparent sophistication of BIT, it was implemented only in very limited applications. BIT is prone to false alarms which can result into unnecessary maintenance scheduling, part quantification, loss of system availability.

Vichare[84] showed that classification of the fault log into errors and imminent real danger is very tedious process.

Mishra[85] introduced circuit cell approach to detect the degradation of the parts and predict failures in automobile engine control units (ECU). The circuit cells are the part of actual circuit that is being monitored. These prognostics monitors were then used along with different algorithms to calculate accumulated damage and the remaining life.

Anderson[86] used canary component on the same board to track the degradation. Canary devices are sacrificial devices which are more sensitive to the surrounding environment that the real active components. Researchers were successfully track the solder fatigue failure and corrosion related failure using this approach. Impedance characteristics of the circuit were tracked over time to isolate the failure mechanism. However, this approach is difficult to use in legacy parts. Maintenance guidelines, canary circuit replacement directions and their effect on the active circuitry is not yet standardized.

Kanniche[87] used mathematical algorithms based on wavelet transforms and fuzzy logic to monitor pulse width modulation of voltage inverts. The algorithm was able to track the abnormalities and intermittent misfiring by analyzing current wave-forms using wavelet transforms. Upon detection of fault, fuzzy logic based algorith was used to pinpoint the fault location.

Saxena[88] outlined prognostics system used in space exploration application. In such critical applications reliability of the spacecraft is extremely important as they are under service for extended period of time without undergoing any maintenance. Effective prognostics system could not only be able to predict the level detecting problems before they become serious but also help schedule their efficient maintenance.

Previously Lall[89][90] presented a new methodology for prognostics of leaded and lead free solder interconnect. Proxies for leading indicator of failure were identified and correlated with the damage progression in thermo-mechanical loading for 63Sn37Pb and SnAgCu solder alloys used in BGA format. Similar approach of using IMC growth and phase evolution in Sn3Ag0.5Cu as leading indicator of failure was presented by Lall[91]. Analysis was performed on BGA packages subjected to sequential loading conditions of first HTSL followed

by thermal cycling. Error of predictive model was quantified using different prognostics metrics. Kwon[92] proposed a novel approach of using RF impedance of solder ball as a leading indicator of failure under thermo-mechanical loading. The impedance of solder interconnect increased when the interconnects were getting damaged. This pre-failure data in conjunction with Gaussian process regression was successfully able to predict remaining useful life of the interconnect.

Shock and vibration loading of electronics application is know to be very random in nature and hard for predictive models when compared to thermo-mechanical loading. Lall[93] proposed a method for failure mode classification using a combination of Karhunen Loeve transform with parity-based step-wise supervised training of a perceptrons. Classified failure modes and failure regions belonging to each particular failure mode in the feature space were validated by simulation of the designed neural network used for parity of feature space. Lall[94] presented a novel resistance spectroscopy based approach to monitor pre-failure space in the electronic assemblies subjected to vibration loading. Future state of the system was estimated based on a second-order Kalman Filter model and a Bayesian Framework. The measured state variable was then related to the underlying interconnect damage in the form of inelastic strain energy density. Lall[95] also studied and developed the predictive model framework to track the degradation in electric connectors subjected to random vibrations.

Increase in electrification of the automotive, oil drilling applications have pushed electronics industry in unexplored territory for which environmental conditions data is not clearly defined. The parts in such applications can either be used for long term deployment or they can be subjected to multiple deployments in which they are usually subjected to sequential thermal stresses. PHM implementation in such systems is needed to ensure predictable operation when needed and avoid any catastrophic damage during the service life. Change in materials such as introduction of new EMCs, Au to Cu or PCC wirebond transition makes this process further complicated. Identification of leading indicator of failures in such system and statistics based predictive model for prediction of remaining useful life of the field deployed parts. In this thesis, PHM models have been developed and implemented for the assessment of prior accrued damage without the time history data of the part. Different leading indicators of failure were

developed for this purpose and used for remaining useful life(RUL) prediction. Sophisticated prognostics matrices were used to evaluate the performance of the developed algorithm in terms of accuracy of predictions.

Chapter 3

Microstructural Indicators for Prognostication of Cu-Al Wirebond Reliability under High-Temperature Storage and Temperature Humidity

3.1 Overview

Gold wire bonding has been widely used as first-level interconnect in semiconductor packaging. The increase in the gold price has motivated the industry search for an alternative to the gold wire used in wire bonding and the transition to copper wire bonding technology. Potential advantages of transition to Cu-Al wire bond system includes low cost of copper wire, lower thermal resistivity, lower electrical resistivity, higher deformation strength, damage during ultrasonic squeeze, and stability compared to gold wire. However, the transition to the copper wire brings along some trade-offs including poor corrosion resistance, narrow process window, higher hardness, and potential for Al pad cratering. Formation of excessive Cu-Al IMC may increase the electrical resistance at the junction and reduce the mechanical bonding strength. Current state-of-art for studying the Cu-Al system focuses on accumulation of statistically significant number of failures under accelerated testing. In this section, a new approach has been developed to identify the occurrence of impending apparently-random defect fall-outs and premature failures observed in the Cu-Al wirebond system. The use of IMC thickness, composition and corrosion as a leading indicator of failure for assessment of the remaining useful life for Cu-al wirebond interconnects has been studied under exposure to high temperature. Damage in the wire bonds has been studied using an x-ray Micro-CT system. Microstructure evolution was studied under HTSL aging conditions of $150°C$, $175°C$, and $200°C$ till failure. Activation energy was calculated using growth rate of IMCs at different temperatures. Effect of temperature and humidity on Cu-Al wirebond system was studied using Parr Bomb technique

at different elevated temperature and humidity conditions (110°C/100%RH, 120°C/100%RH, 130°C/100%RH) and failure mechanism was developed. The present methodology uses evolution of the IMC thickness, composition in conjunction with the Levenberg-Marquardt algorithm to identify accrued damage in wire bond subjected to thermal aging. The proposed method can be used for quick assessment of Cu-Al parts to ensure manufactured part consistency through sampling.

3.2 Test Vehicle and Test Matrix

The test vehicle used for the study is a 32-pin chip scale package. The package is 4.5mm in length, 5.5mm in width, 0.7mm in height. Each pin has a length of 0.45mm and width of 0.3mm. The package interconnects have an I/O pitch of 0.5mm. All packages have $25.4\,\mu m$ diameter copper wires and aluminum pads. The packages used for the study were not daisy chained. Package dimensions are listed in Table 3.1.

Table 3.1: Dinemsions of Test Vehicle

Parameter	Dimensions (mm)
Width of Package	4.50
Height of Package	0.70
Length of Package	5.50
Length of Pin	0.45
Width of Pin	0.30
Pitch	0.50

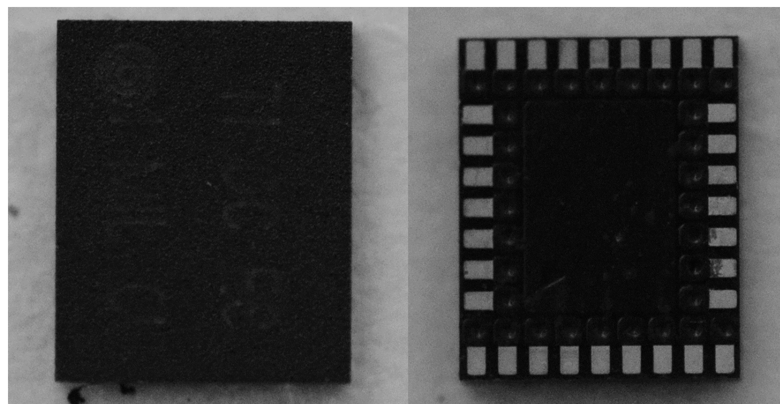

Figure 3.1: Optical Images of 32 pin CSP

Figure 3.1 shows the optical microscopic images of the package. Figure 3.2 shows X-ray images of the package taken using the YXLON Cougar CT System. Figure 3.3 shows the 3D -CT reconstruction showing details captured on the package and first level interconnect level. The chip and the electronic mold compound have been deselected for better visibility of the copper-aluminum interconnects.

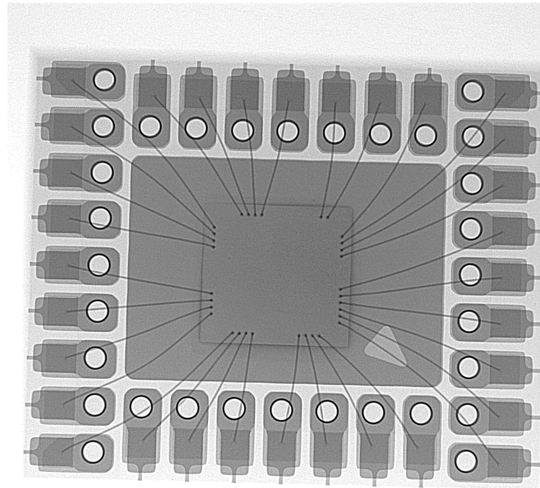

Figure 3.2: X-ray Image of 32 Pin CSP

Figure 3.3: 3D Reconstruction of 32 Pin CSP Along with Cu Wirebonds

Test packages were subjected to HTSL test at 150°C (25 samples), 175°C (10 samples), and 200°C (10 samples). For aging at 150°C and 175°C, IMC growth was monitored at the interval of 168 hours. For aging temperature of 200C, reading interval was 48 hours. To study the effect of temperature-humidity bias, set of packages were subjected to three different conditions, 130°C/100%RH, 120°C/100%RH, 110°C/100%RH. Reading interval for these tests was

24 hours. Packages were potted into resin, polished, and then the polished surface was sputter coated with gold, at 25μA, for 45 seconds. Cross-sectioning was performed to expose the center of the ball bond. This was selected because this view covers maximum cross-sectional area of wirebond. IMC growth was observed using scanning electron microscopy (Accuracy of $0.01\,\mu\text{m}$). IMC thickness at multiple locations was recorded in each image, and mean value of readings was considered as final IMC thickness. This ensured accuracy in measurement. Different modes of EDS scans (e.g. line scan, point scans) were performed for material characterization.

3.3 Experimental Result and Analysis

In this section, results of the HTSL and Parr bomb test will be discussed along with material characterization of the IMC phases.

3.3.1 High Temperature Thermal Aging

Figure 3.4 shows development of IMC layer when packages were subjected to $150°$C HTSL condition. IMC growth over period of temperature can be observed. Similarly, images of IMC growth have been captured at the thermal aging conditions of $175°$CC and $200°$C, and are shown in Figure 3.5. Bright square dots that appear in the images were tungsten (W) vias located below Al pad.

At $150°$C, even after aging for 3360 hour, IMC corrosion or cracking was not found. IMC growth was very slow but consistent throughout the test. Initially only Al-rich phase of IMC was visible. However, after aging for 840 hours, Cu-rich phase was distinctly visible in the Cu-Al IMC. In case of thermal aging at $175°$C, the Cu-rich phase was detected after aging after only 336 hours of thermal aging, much sooner than the 840 hours required at $150°$C. Initial cracking of wirebond was observed after 1008 hours of aging at $175°$C. Initial cracks were observed at edges of ball bond, in copper rich interface, and then they propagated towards center, resulting into complete cracking in most of the wirebonds after 1176 hours of aging. Similar trend was observed in third thermal aging condition at $200°$C. IMC growth at $200°$C was the fastest of the three aging conditions measured in this study. Crack initiation and propagation was

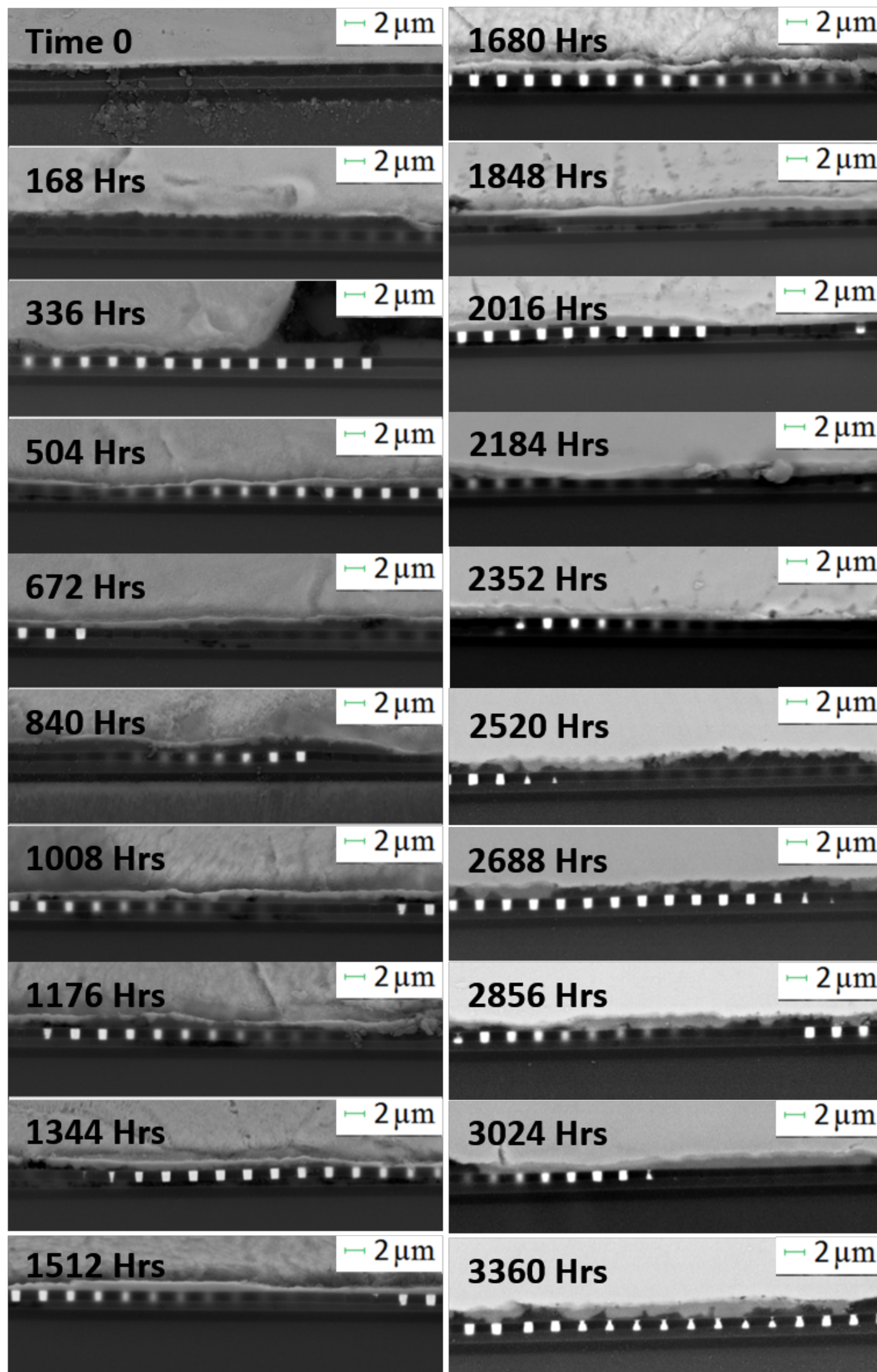

Figure 3.4: IMC growth of Cu-Al Junction at 150°C

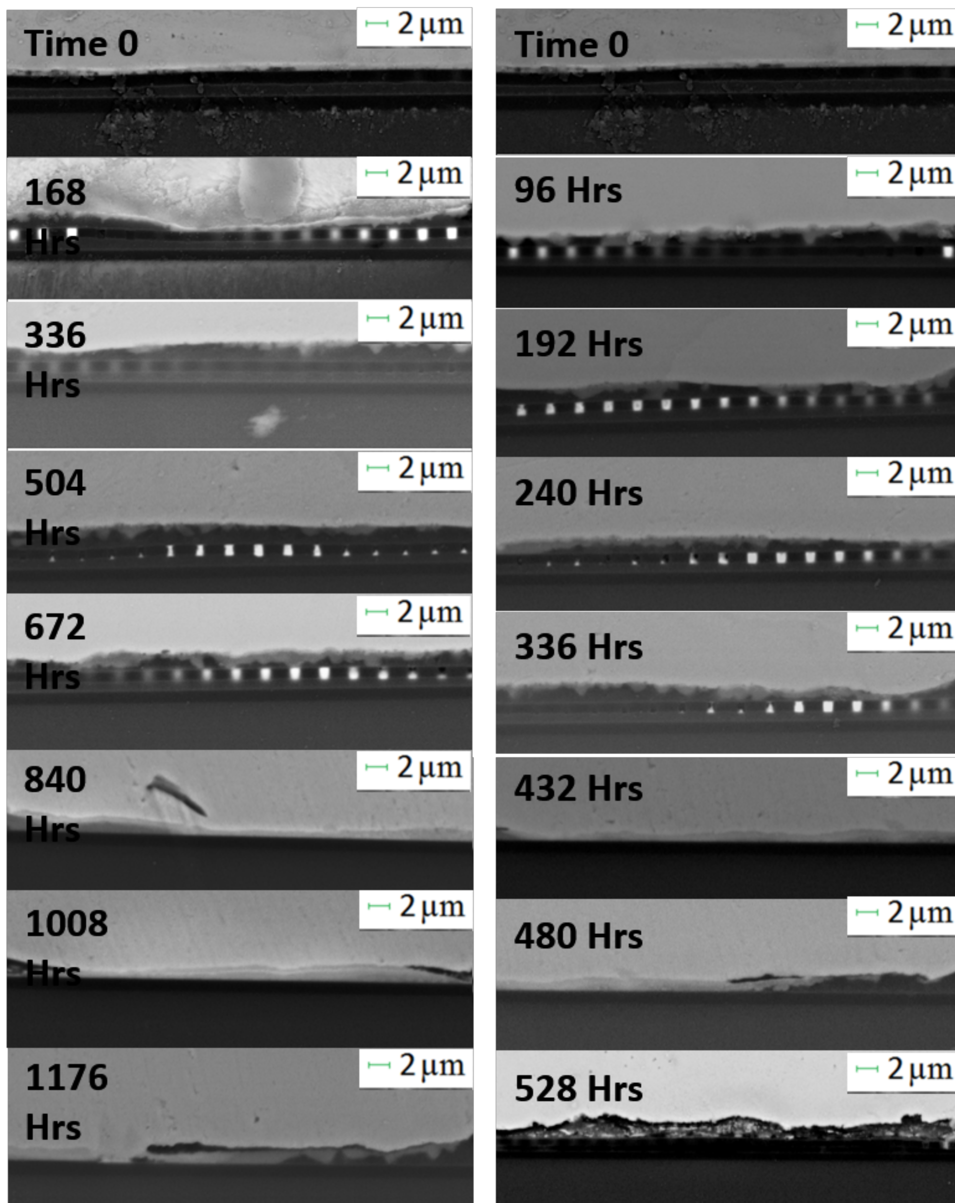

Figure 3.5: IMC growth of Cu-Al Junction at 175°C and 200°C

faster at higher ambient temperature with the crack initiation observed after 432 hours and near complete cracking in majority of the wirebonds after 528 hours of 200°C aging.

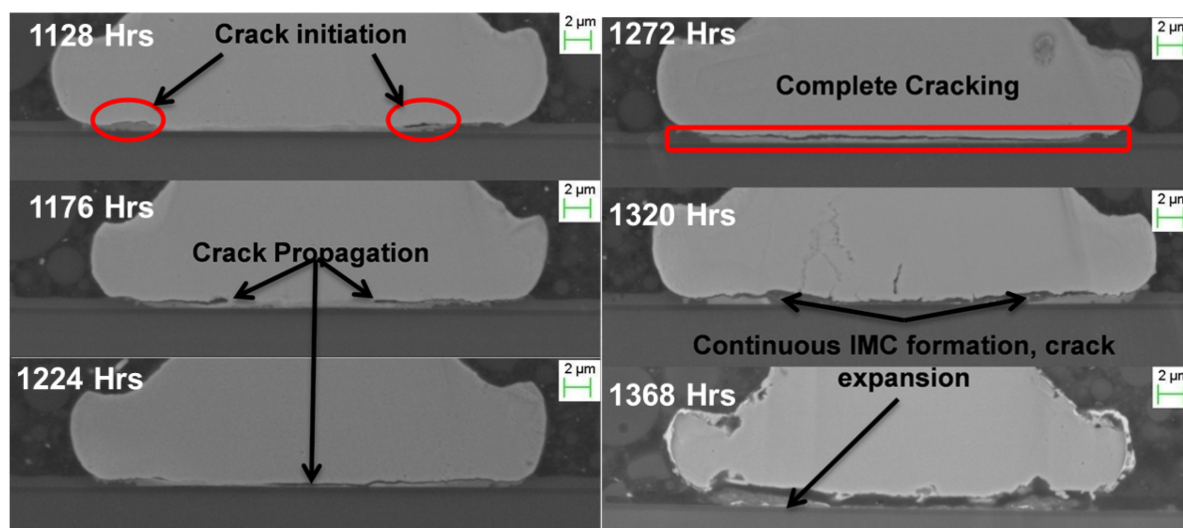

Figure 3.6: Crack Initiation and Propagation at 175°C

Sequential crack initiation and propagation observed at ambient temperature of 175°C is shown in Figure 3.6. Irrespective of temperature condition, initial cracking was observed at the periphery of the ball bond, followed by propagation towards the center. Even after complete cracking it was observed that the IMC growth continued resulting in formation of singular IMC phase below the crack. The aluminum from the Al-pad continued to diffuse into the IMC, but diffusion of copper from ball bond got restricted due to crack. IMC growth after crack formation resulted in the development of a continuous layer of aluminum rich phase below the crack.

Point scans and line scanning techniques were used to analyze IMC phases, as well as region of cracking, using EDX. EDX analysis on IMC phases to determine its composition is shown in Figure 3.7.

Two difference phases were found at the Cu-Al interface. The phase near bulk Cu was Cu rich phase and phase near pad region was Al rich phase. Cu rich phase was characterized as Cu_9Al_4 and Al rich phase was $CuAl_2$, as shown in spectrum 3 and 4 of Figure 3.7. These results are consistent with some of the previously published work by Laik[96], Lee[23], Tian[5]. EDX spot scan was also performed at the cracked interface as shown in Figure 3.8. Spectrum 4 confirmed that cracking phenomenon took place only in Cu rich interface. Further, to confirm

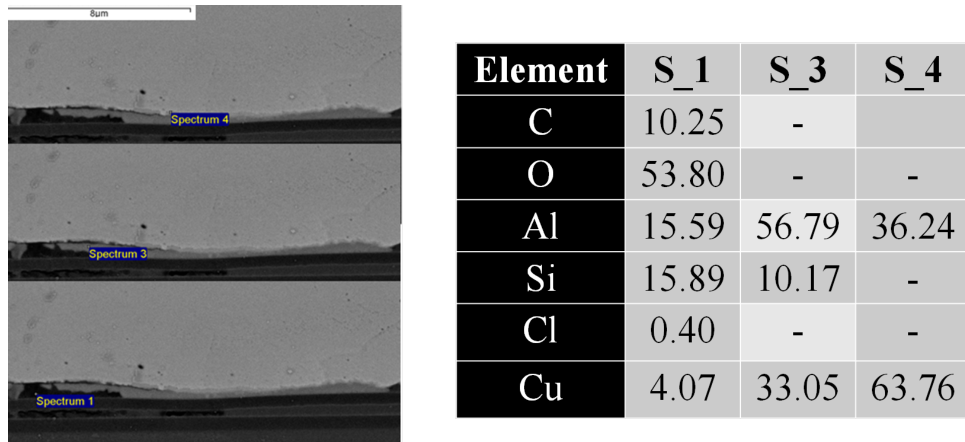

Element	S_1	S_3	S_4
C	10.25	-	
O	53.80	-	-
Al	15.59	56.79	36.24
Si	15.89	10.17	-
Cl	0.40	-	-
Cu	4.07	33.05	63.76

Figure 3.7: EDX Analysis of the Cu-Al Interface

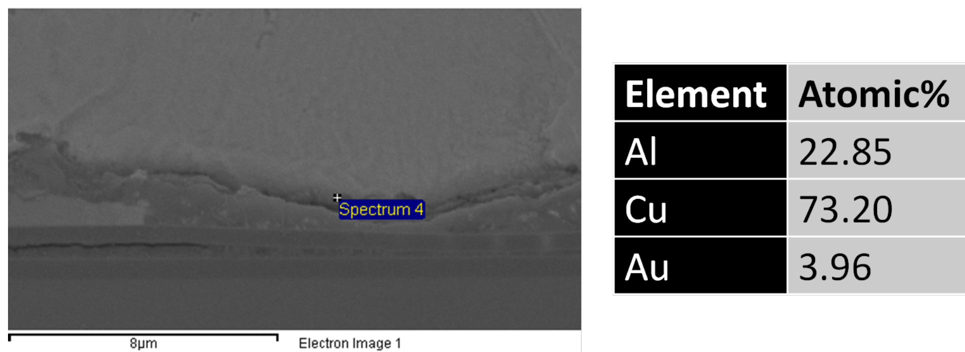

Element	Atomic%
Al	22.85
Cu	73.20
Au	3.96

Figure 3.8: EDX Analysis at the Corroded Interface

the claim, elemental line scan was performed at the peripheral crack at very high magnification as shown in Figure 3.9. Line scan provides the elemental composition change along the line of interest. The area of crack and IMC was marked by black box, projected as circle in scan result. Image analysis showed that Cu rich zone had undergone oxidation induced cracking. Source of this oxygen was hypothesized to be outgassing from the molding compound under thermal aging. It was shown by Lall [97] that extensive aging of mold compounds at elevated temperatures can cause breakdown of long polymeric chains and result into outgassing of the reaction byproducts. The same mechanism also results into oxidation of EMC and hence increased free oxygen content in the EMCs. Ionic contamination from the EMCs aids and accelerates the corrosion process.

To measure IMC thickness, first, number of pixels in the IMC area were calculated with the help of image processing software. First region with IMC coverage (marked red in Figure 3.10) was selected and the area was calculated. Dividing the area by length of the IMC provided

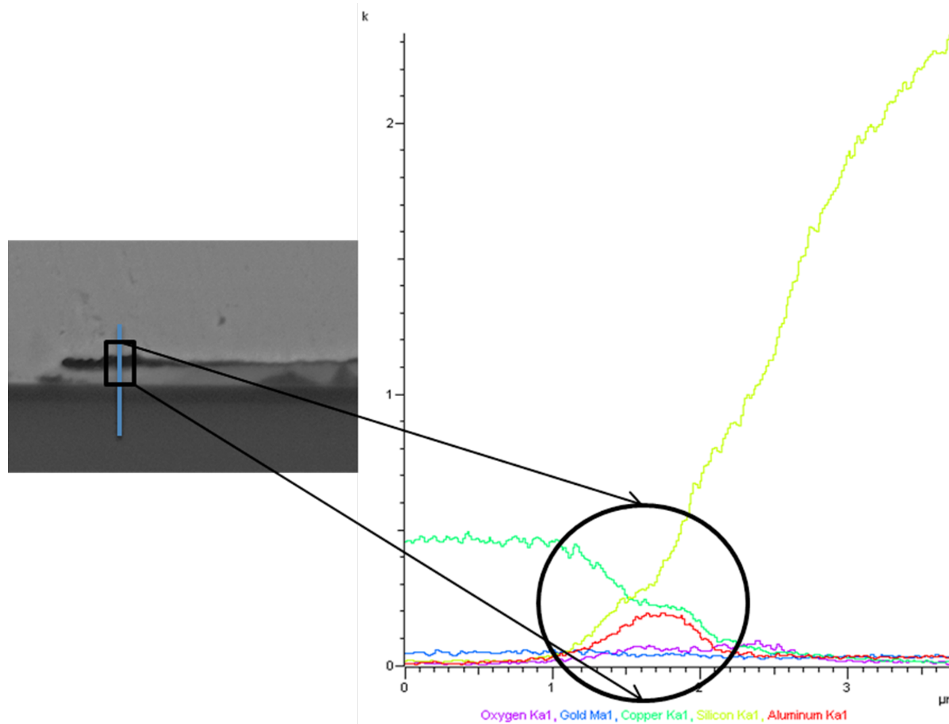

Figure 3.9: EDX Line Scan Along the Peripheral Crack

single thickness value of the IMC. Summary of IMC measurement process is shown in Figure 3.10.

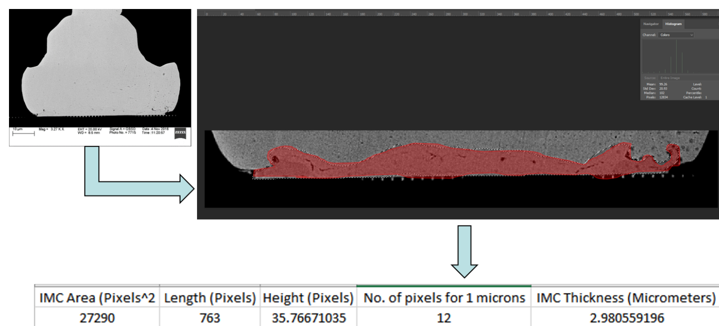

IMC Area (Pixels^2	Length (Pixels)	Height (Pixels)	No. of pixels for 1 microns	IMC Thickness (Micrometers)
27290	763	35.76671035	12	2.980559196

Figure 3.10: Summary of IMC Measurement Technique

Figure 3.11 shows plot of log of normalized IMC vs log of aging duration. IMC was normalized by first subtracting and then dividing IMC thickness measurement by IMC thickness of time 0. Plot shows that IMC grows much faster at higher temperatures. Slopes of all three lines representing three different temperature conditions were approximately same, making them parallel lines. This shows that the growth mechanism was constant irrespective of ambient temperature condition. This makes IMC thickness growth an excellent leading indicator of

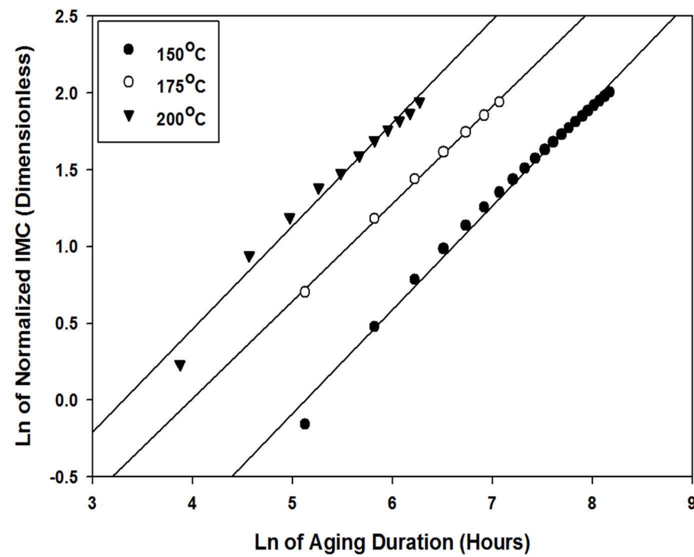

Figure 3.11: IMC Growth During HTSL Test

failure for prognostics purposes. This IMC growth data will be later used for development of prognostics matrix.

3.3.2 Accelerated Test for Corrosion Susceptibility of Cu-Al

In this test, three sets of 10-packages each were subjected to three different conditions of 130°C/100%RH, 120°C/100%RH, 110°C/100%RH.To achieve these test conditions, a Parr bomb test apparatus was used. Parr bomb test apparatus shown in Figure is a closed high pressure vessel in which 100%RH can be maintained at high ambient temperatures. PTFE cup inside the Parr bomb was filled with water, and packages were placed in cup such that they will not be immersed into water but rather only in contact with the water vapors. Special teflon fixture was developed for this purpose.

Microstructure analysis using scanning electron microscope was performed on parts subjected to the highly-accelerated stress test. Figure 3.12 shows cross-section images of the wirebond. In all cases, no significant growth of IMC was found. Test temperatures and duration were not high enough to observe significant IMC growth. Only other explanation for failure is potential corrosion of either very thin layer of IMC or Al due to combination of high temperature and humidity. In 3.12 (a), micro crack initiation was found after aging duration of 96 hours, at 110°C/100%RH. Cracks are highlighted with red box. Bigger cracks were

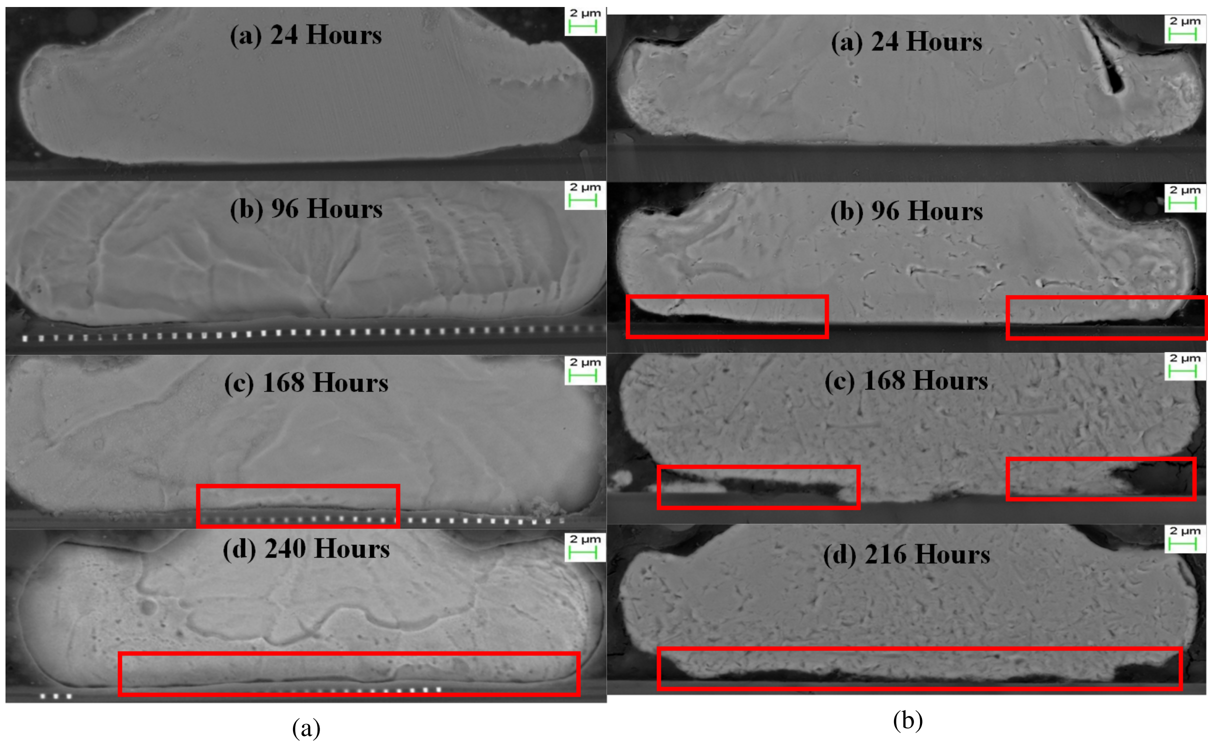

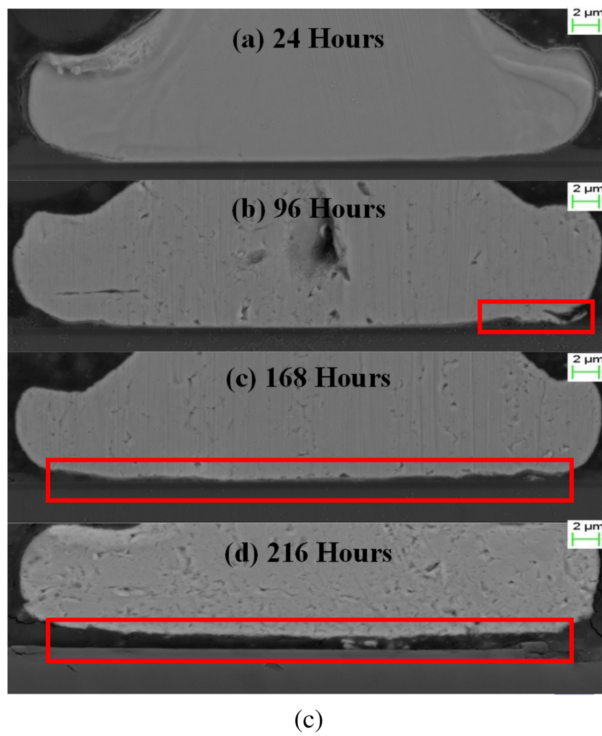

Figure 3.12: Cracking at the Cu-Al Interface at (a)110°C (b)120°C and (c)130°C/100%RH

found after 240 hours of aging, but complete interfacial cracking was not observed. However, at 120°C/100%RH condition, instead of crack, complete corrosion of IMC and Al pad was observed, as shown in 3.12 (b). Completely corroded interface was seen after 216 hours of testing. For 130°C/100%RH testing condition, ball bond lift was observed after 168 hours of aging. Thick layer of corroded interface can be seen in Figure 3.12 (c). EDS line scans, point scans and area scanning techniques were used to confirm the mechanism of cracking and ensure that the cracks observed were not a polishing artifact.

Figure 3.13 shows the point scan analysis at the Cu-Al wirebond interface. Three points, two at the end and one at the center were selected from the same wirebond. Results (percent atomic weight) of all three point scans are tabulated into Table 3.2. Analysis indicates that oxygen was present at the Cu-Al interface. Percentage atomic weight of oxygen was higher at edges, showing that initial corrosion took place at edges, and then it propagated towards center. For all three cases, oxidation was predominantly found in the Cu-rich phase. Chlorine contamination was aldo found at the corroded interface.

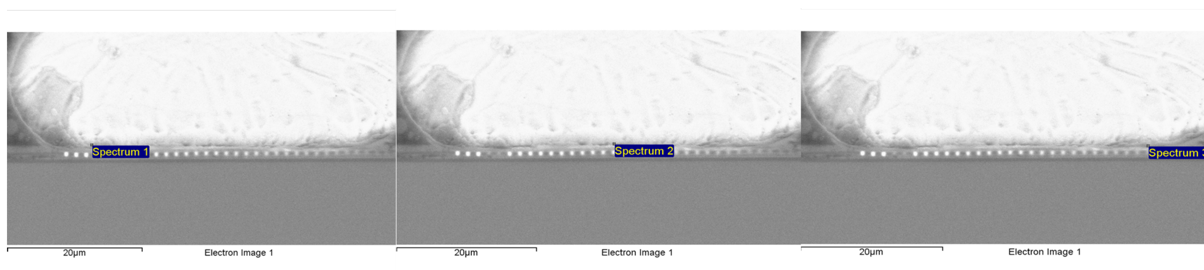

Figure 3.13: EDX Point Analysis on Failed CuAl Interface

Table 3.2: Percent Atomic Weight of Elements

Elements	Spectrum 1	Spectrum 2	Spectrum 3
O	33.36	12.37	21.56
Al	3.08	2.74	2.63
Si	13.00	5.25	7.80
Cl	0.19	0.03	0.03
Cu	50.37	74.61	67.98

Figure 3.14 shows EDS line scan from Cu ball bond through Al pad to the Si-Chip. Analysis results indicate that cracking of wirebond took place in Cu-rich zone, and the Al-rich zone was still intact. Higher amount of Cu than Al could be seen in the line scan result at cracked

interface. In order to ascertain that the cracking is due to corrosion; but a visual polishing artifact, area mapping was done. Figure 3.15 shows area mapping performed to find oxygen content of selected area. Intensity of red dots indicates concentration of oxygen at the location of the red dot. Figure 3.15 shows that dark red spots were spotted in the region of cracking, and area near it. Density of the oxygen rich region indicated by the red-dots shows that the root cause of the cracking was oxidation.

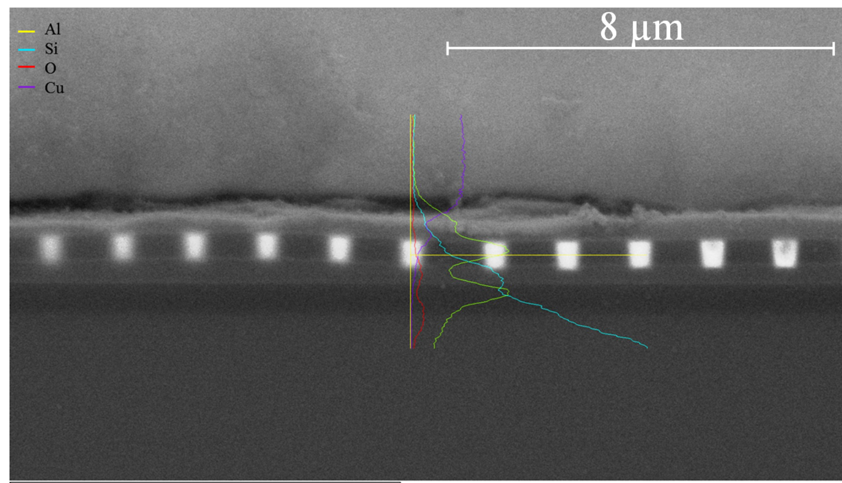

Figure 3.14: EDX Line Scan of a Crack in Wirebond

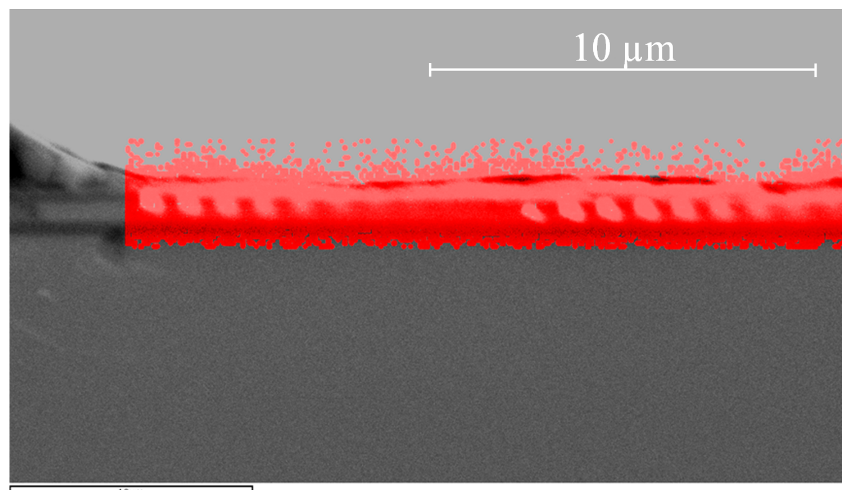

Figure 3.15: EDX Point Analysis on Failed CuAl Interface

The corrosion mechanism has been analyzed using the Pourbaix Diagram or the potential/pH diagram which maps out the potential stable phases of the aqueous electro-chemical

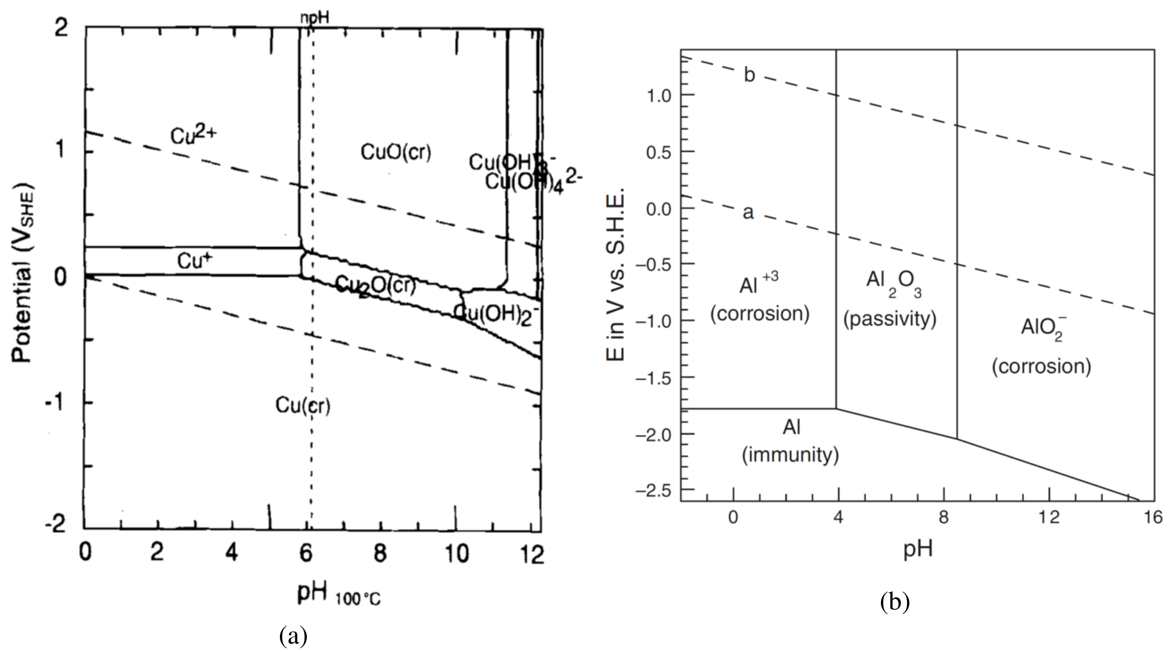

Figure 3.16: Pourbaix Diagram of (a)Copper, (b)Aluminum

system. The vertical axis is labeled for the voltage potential with respect to a standard hydrogen electrode (SHE) as calculated by the Nernst Equation. The lines in the Pourbaix diagram show the equilibrium condition where the activities for each of the species are equal on either side of the line.

Pourbaix diagrams for Copper and Aluminum are shown in Figure 3.16 [98][99]. On either side of the line one of the ionic species is said to be predominant. The Pourbaix Diagram has been used to identify the regions of immunity, corrosion, and passivity for both copper and aluminum. The vertical lines indicate the species that are in acid-alkali equilibrium. The non-vertical lines separate the species at redox equilibrium. Specifically, the horizontal lines separate redox equilibrium species not involving hydrogen or hydroxide ions. The diagonal lines separate redox equilibrium species involving hydrogen or hydroxide ions. The dashed lines enclose the practical region of stability of the aqueous solvent to oxidation or reduction and thus the region of interest in aqueous systems. Outside the dashed region, water breaks down and not the metal. In general, the metal is not attacked and forms stable un-reacted metal species in the region of immunity, metal forms a stable oxide or stable hydroxide in the region of passivity, and metal is susceptible to corrosion in the region labeled as corrosion. Low E (or

pE) values represent a reducing environment. High E values represent an oxidizing environment. Electrochemical potential represents the driving force for oxidation or reduction. The electrochemical potential is generally cited as standard reduction potential and quantifies the tendency of the chemical species to be reduced. More positive values of reduction potential indicate higher ease with which that the chemical species will be reduced. Corrosion of metal usually occurs at the anode. Standard electrochemical potential of pure Cu is +0.34V. Electrochemical potential of aluminum is -1.67V. Thus in the copper-aluminum system, copper is easier to reduce and aluminum is easier to oxidize. Exact value of electrochemical potential of IMC components, i.e. Cu_9Al_4 and $CuAl_2$ is unknown and it reported that it should be in between potential values of pure Cu and Al [100]. So theoretically based on electrochemical potential values, being most active metal in the system, Al would act as sacrificial anode, and undergo reaction 3.1,

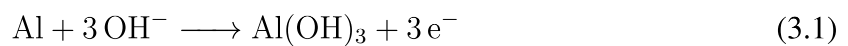

$$\mathrm{Al} + 3\,\mathrm{OH^-} \longrightarrow \mathrm{Al(OH)_3} + 3\,\mathrm{e^-} \quad (3.1)$$

Pourbaix diagram shows that corrosion prone are in Cu is much less than that of Al. In regions where Al+++ is stable, corrosion is possible. In the region where aluminum oxide is stable, resistance or passivity to corrosion is possible. If the pH is between 4 and 8.3, Al_2O_3 is stable and thus protects the aluminum. Aluminum hydroxide forms stable passivation layer around bare Al pad. The pH values of most of the commercial electronic molding compounds falls in this range of 4 to 8.3. Passivation layer stability window might get narrow in the presence of ionic contamination, such as halide ions. With the industry migration to green molding compound, which are halide ion free or having very less halide concentration; the possibility of narrowing of the stability window and the possibility corrosion of Al pad are lower.

During testing of samples in the current study, corrosion of wirebond was found during highly accelerated stress test in the Parr Bomb apparatus. Two main phases found in the IMC development study were Cu_9Al_4 and $CuAl_2$. Cu_9Al_4 is on copper ball side, while $CuAl_2$ was found on Al pad side of IMC. Previous study by Osenbach[41] and Birbilis[101] have shown that the higher fraction of Aluminum in Al rich IMC phase forms strong passivation layer which

stops further reaction, even at low pH values. On the other hand, Cu_9Al_4 which is Cu rich IMC layer has lower Al fraction which means it will have weaker passivation layer than $CuAl_2$ and Al pad. This layer can be easily attacked by moisture and even small concentration of ionic contamination can trigger the corrosion reaction, making it corrosion prone. Detailed microstructure analysis of the aged samples revealed that IMC formed during bonding process was corroded. IMC layer formed near copper ball region (Cu rich interface) found to be corrosion prone than other IMC layer. Line scans and point scans showed in Figure 3.14 and Figure 3.15 confirmed presence higher oxygen content i.e. corrosion followed by cracking was found in Cu-rich interface. There are different possibilities in which reaction may occur as shown in reaction 3.2,3.3,3.4.

$$\mathrm{Cu_9Al_4 + Cl_2 \longrightarrow 4\,AlCl_3 + 9\,Cu} \tag{3.2}$$

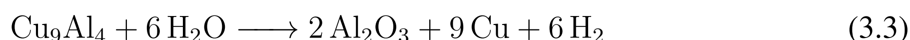

$$\mathrm{Cu_9Al_4 + 6\,H_2O \longrightarrow 2\,Al_2O_3 + 9\,Cu + 6\,H_2} \tag{3.3}$$

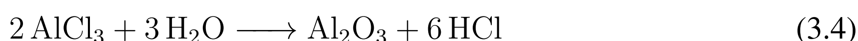

$$\mathrm{2\,AlCl_3 + 3\,H_2O \longrightarrow Al_2O_3 + 6\,HCl} \tag{3.4}$$

Main byproducts of reaction are Aluminum oxide and Hydrochloric acid. Aluminum oxide is brittle oxide and is an insulator. Presence of aluminum oxides can not only cause extensive cracking, but also reduce the area available for electron flow. Hydrochloric acid further gets dissolved into moisture and breaks into chlorine ions. These chlorine ions again attack Cu_9Al_4 and continue corrosion process. The continuation of process can eat away Cu-rich IMC phase, making it mechanically and electrically unstable, causing excessive stresses, and mostly results into crack formation, and propagation. The observations noted in this experiment are in good agreement with previous literature by Boettcher[42], Breach[32] , Su[33] and Liu[102].

Prior studies were limited to maximum 120 hours of aging. However, for 120°C and 130°C Parr bomb testing after 168+ hours of aging, it was found that along with Cu rich IMC, Al rich IMC and Al pad were also oxidized. This might be due to prolonged exposure to extreme atmospheric conditions. It could have caused degradation of molding compound, releasing some byproduct which can make reaction more aggressive. Initially Al will react with moisture to produce passivation layer of aluminum hydroxide. This can be attacked by chlorine ions and

broken down as shown in 3.5,3.6,3.7.

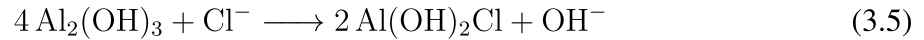

$$4\,Al_2(OH)_3 + Cl^- \longrightarrow 2\,Al(OH)_2Cl + OH^- \tag{3.5}$$

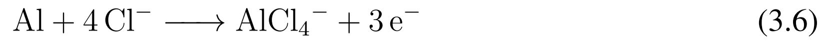

$$Al + 4\,Cl^- \longrightarrow AlCl_4{}^- + 3\,e^- \tag{3.6}$$

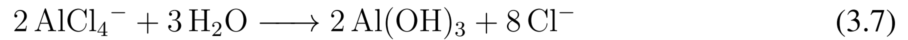

$$2\,AlCl_4{}^- + 3\,H_2O \longrightarrow 2\,Al(OH)_3 + 8\,Cl^- \tag{3.7}$$

One of the products of reaction is chlorine ion. So once the reaction initiates, it will keep on going and Al pad will undergo pitting corrosion. Typical corrosion reaction of CuAl2 can be described as following reaction 3.8. [41]

$$CuAl_2 + 6\,Cl^- \longrightarrow 2\,AlCl_3 + Cu \tag{3.8}$$

3.3.3 Activation Energy Calculations

In this section, calculations of activation energy for Cu-Al IMC growth are presented. IMC growth data for all three temperature conditions was fitted into following equation 3.9

$$X^2 = Kt + C \tag{3.9}$$

Where, X is the IMC thickness μm, t is the aging time (s), K is the reaction rate of IMC formation (μm^2/s), C is the constant related to initial IMC thickness (μm^2). The reaction rate is represented as function of temperature as

$$K = K_0 * e^{\frac{-\Delta Q}{R*T}} \tag{3.10}$$

Where, K_0 is the multiplication Factor (μm^2/s), R is the Gas constant (1.99 cal/molK), T is the Aging Temperature (K), ΔQ is activation energy(Kcal/mol). Equation 3.9 IMC growth data was fitted, and the plot is shown in Figure 3.17

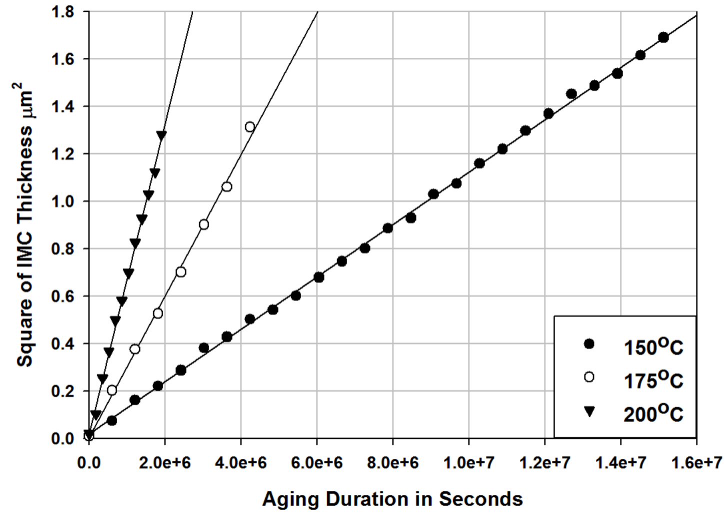

Figure 3.17: IMC Growth Rate

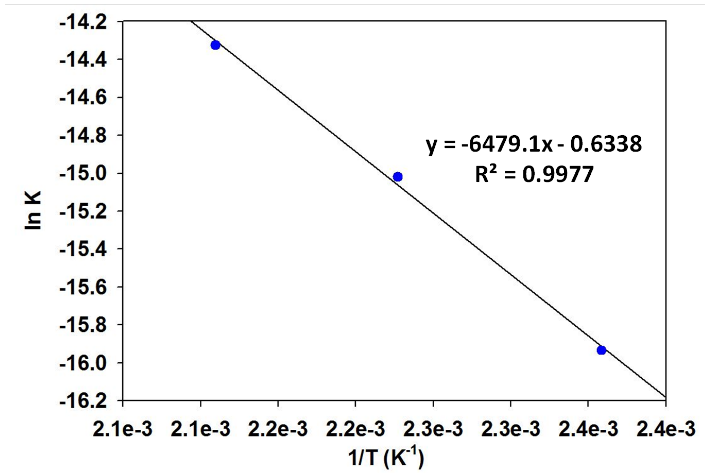

Figure 3.18: AE Calculations

Three values of growth rate i.e. k were obtained, and plotted against 1/T as shown in Figure 3.18. Activation energy calculated from the plot is 12.893 Kcal/mol, i.e. 0.559eV. Table 3.3 and Table 3.4 show comparison of energy of activation and IMC growth rate with data previously published in literature. Activation energy obtained in current experiment is in good agreement with the activation energy reported by Na[103] and Goh[104] . In both the papers, growth rate of IMC because of the temperature bias is in the range of 10^{-6} $\mu m^2/s$ to 10^{-8} $\mu m^2/s$, which is also in good agreement with current study (10^{-7} $\mu m^2/s$).

Table 3.3: Comparison of Activation Energies for Cu-Al

WB type	Reference	Test Temperatures (C)	AE (Kcal/mol)
Copper	[104]	175, 200, 225	6.1
	[26]	150, 250, 300	26
	[103]	150, 200, 250	10.71
	Current Study	150, 175, 200	12.89

Table 3.4: Comparison of IMc Growth Rates

WB type	Temperature (C)	Reference	Growth Rate $\mu m^2/s$
Copper	150	[26]	$1.88 * 10^{-8}$
		[103]	$2.15 * 10^{-8}$
		Current Study	1.21*10{-7}
	175	[104]	$3.57 * 10^{-7}$
		Current Study	$3.25 * 10^{-7}$
	200	[103]	$2.56 * 10^{-8}$
		[104]	$6.26 * 10^{-7}$
		Current Study	$7.02 * 10^{-7}$

3.4 Prognostication Approach for HTSL

In order to assess the accrued damage in the Cu-Al package, IMC growth was used as a leading indicator of failure for interrogation of state of system and remaining useful life calculations. Measurements of IMC thickness growth have been fit into equation 3.11

$$\frac{y_1 - y_0}{y_0} = kt_1^n \tag{3.11}$$

Prior damage in each case has been prognosticated based on the IMC evolution. Prognostication involves withdrawal of three samples at three periodic intervals. The samples were then cross-sectioned, potted and polished to measure intermetallic thickness. Prior damage accrued was prognosticated. IMC growth parameter was used to compute life consumed due to exposure to thermal aging were,

$$\frac{y_1 - y_0}{y_0} = kt_1^n \tag{3.12}$$

$$\frac{y_2 - y_0}{y_0} = k(t_1 + \Delta t)^n \tag{3.13}$$

$$\frac{y_3 - y_0}{y_0} = k(t_1 + 2\Delta t)^n \tag{3.14}$$

Where y_1 is IMC thickness at time t_1, Δt is the time interval for future IMC thickness measurements, k is coefficient standing for square root of aging duration. The parameter y_0 is IMC thickness before initiation of thermal aging. The solution requires three equation and three unknowns. Levenberg- Marquardt (LM) algorithm was used to solve these three nonlinear equations 3.12, 3.13 and 3.14 and optimization of three unknowns. Figure 3.19 gives an overview of the methodology used for prognostication of Cu-Al wire bond for prior accrued damage using IMC layer as leading indicator of failure. Consider a field deployed electronic package, which has been used for certain time, say t_1, which is unknown. For prognostication, samples will be taken from field at uniform-interval of Δt. IMC thickness of all packages can be measured and then using equations 3.12, 3.13 and 3.14 unknown y_1, y_2 and y_3.

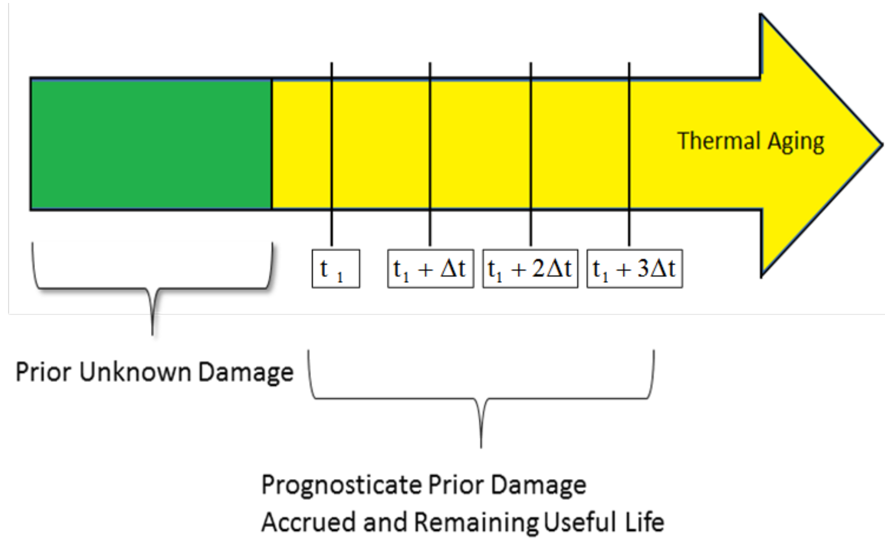

Figure 3.19: Prognostication of thermally aged samples

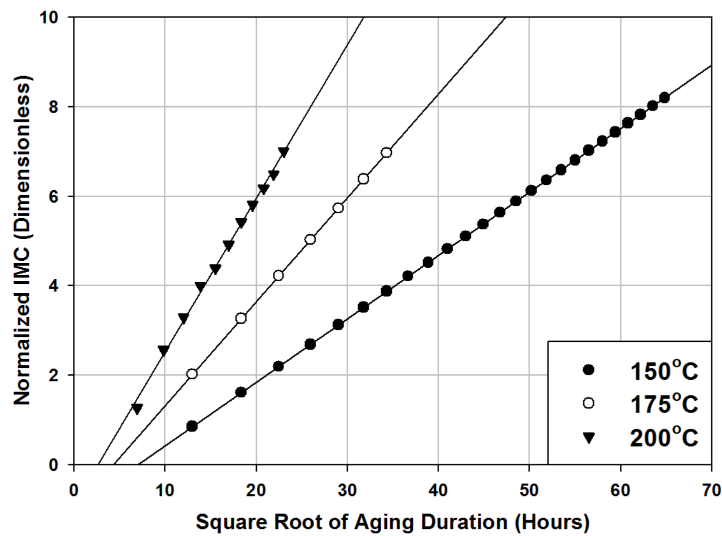

Figure 3.20: Normalized IMC vs Square root of aging time

In case of isothermal aging, in which IMC development is primarily driven by diffusion value of n is theoretically known to be 0.5, which is matching with the experimental data. Updated equations can be written as,

$$\frac{y_1 - y_0}{y_0} = kt_1^{0.5} \tag{3.15}$$

$$\frac{y_2 - y_0}{y_0} = k(t_1 + 168)^{0.5} \tag{3.16}$$

$$\frac{y_3 - y_0}{y_0} = k(t_1 + 336)^{0.5} \tag{3.17}$$

Equation 3.11 was used to plot graph of normalized IMC against square root of aging time, for all three cases, shown in 3.20. Linear plot implies that value of n is approximately 0.5.

3.4.1 Levenberg Marquardt Algorithm

The relationship between the IMC growth parameter and time is nonlinear. Inverse solution for interrogation of system-state is challenging for damage evolution in such systems. Levenberg-Marquardt (LM) algorithm n iterative technique that computes the minimum of a non-linear function in multidimensional variable space has been used for identifying the solution in the prognostication neighborhood. Let f be an assumed functional relation between a measurement vector referred to as prior damage and the damage parameter vector, p, referred to as predictor variables. The measurement vector is the current value of the leading-indicator of failure and the parameter vector includes the prior system state, and accumulated damage and the damage evolution parameters. An initial parameter estimate p0 and a measured vector x are provided and it is desired to find the parameter vector p, that best satisfies the functional relation f i.e. minimizes the squared distance. the minimize parameter vector p, given by

$$F(p) = \frac{1}{2}\sum_{i=1}^{m}(g_i(p)^2) = \frac{1}{2}g(p)^T g(p) \tag{3.18}$$

$$F'(p) = J(p)^T g(p) \tag{3.19}$$

$$F''(p) = J(p)^T J(p) + \sum_{i=1}^{m} g_i(x) g_i{}''(x) \tag{3.20}$$

Where, F(p) represents the objective function for the squared error term, J(p) is the Jacobian, F'(p) is the gradient, F"(p) is Hessian. The variation of an F-value starting at p and with direction h is expressed as a Taylor expansion, as follows

$$F(p + \alpha h) = F(p) + \alpha h^T F'(p) + o\alpha^2 \tag{3.21}$$

Where α is the step length from point "p" in the descent direction "h". Mathematically "h" is the descent direction of F(p) if h^TF'(p)¡0. If no such "h" exists, then F'(p)=0, showing that in this case the function is stationary. Since the condition for the stationary value of the objective function is that the gradient is zero, i.e.

$$F(p+h) = L'(h) = 0 \tag{3.22}$$

The descent direction can be computed from the equation,

$$(J^T J + \mu I)h = -J^T g \tag{3.23}$$

Where, μ is called as the damping parameter, μ¿0 ensures that coefficient matrix is positive definite, and this ensures descent direction. When the value of μ is very small, then the step size for LM and Gauss-Newton are identical. Algorithm has been modified to take the equations of inter-metallic growth under isothermal aging to calculate the unknowns. Levenberg-Marquardt algorithm was developed based on equations 3.15, 3.16 and 3.17 for prediction of remaining useful life, when packages were subjected to HTSL condition. Equation 3.24, 3.25 and 3.26 represents damage accrual relationships, where K_n is IMC thickness at any time t. The equations were derived from experimental data. Exponent of time t in all three cases is in the vicinity of 0.5. It shows that IMC growth in Cu-Al wire bond system is driven by Fickian diffusion. In the Fickian diffusion, kinetic exponent (exponent of time) is 0.5. It means that rate of diffusion follows linear trend as a function of square root of aging duration.

$$K_n = 0.023(t)^{0.482} \tag{3.24}$$

$$K_n = 0.427(t)^{0.498} \tag{3.25}$$

$$K_n = 0.045(t)^{0.513} \tag{3.26}$$

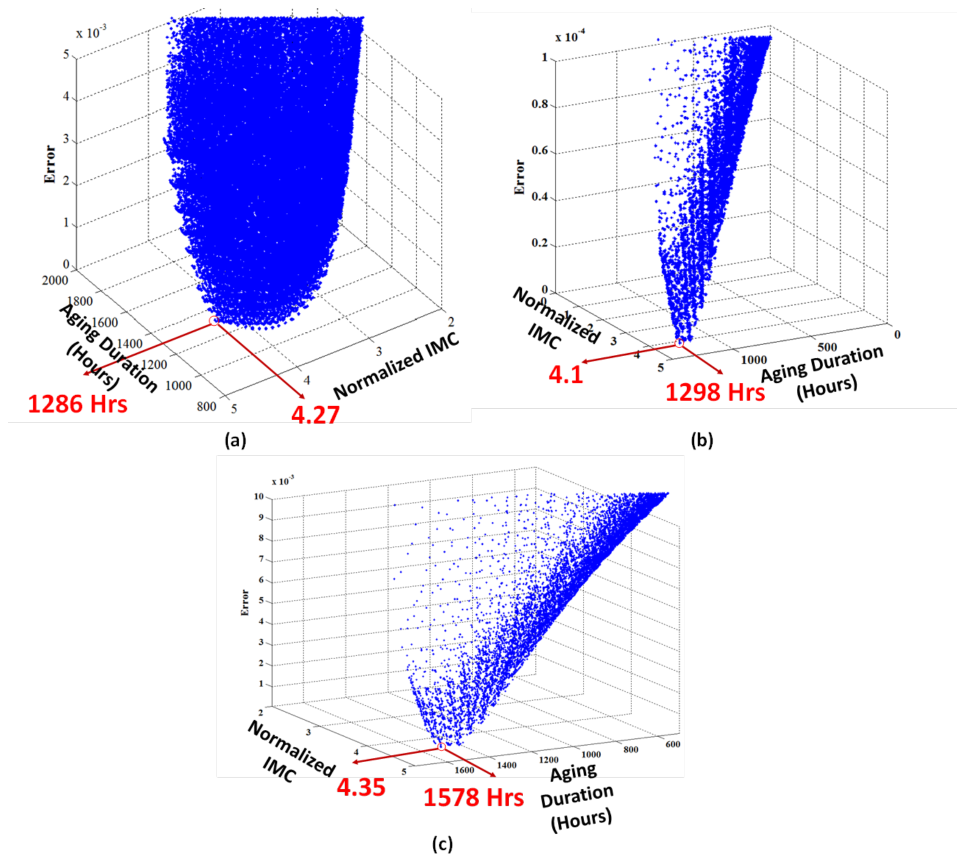

Figure 3.21: 3D Plot of convergence of LM Algorithm at 150°C

Since it governs IMC formation rate, careful evaluation of exponent is required. This exponent was used in prognostics model to capture prior accrued damage. For ambient temperature of 150°C, prognostication was done at 1176, 1344, 1512 hours of thermal aging Results of the prognostication are shown in Table 3.5. 3D plots of algorithm output are shown in Figure 3.21. Z-axis shows error term. LM algorithm iterative tries to find such values of aging duration and normalized IMC so that model will have minimum error. The aim is to find a single point which will have minimum global error i.e. point of convergence. This point represents solution i.e. prior accrued damage. Solution points are marked in red circle, and their X and Y coordinate values shows predicted prior accrued damage and normalized IMC thickness. Percentage error in between experimental aging duration and prognosticated aging duration was calculated. The error bound was in the range of 3.5% to 8.5%. The solution in Figure 3.21 corresponds to the point at minimum error. The minimum error point represents prognosticated aging duration. Similar approach was used to prognosticate prior accrued damage when packages were sub-

Table 3.5: Comparison of experimental and prognosticated Results at 150°C

Time	Experimental (Hours)	Prognosticated (Hours)	% Error
t_1	1176	1286	8.50%
t_2	1344	1298	3.50%
t_3	1512	1578	4.10%

jected to thermal aging of 175°C. Results are tabulated in Table 3.6 and 3D plot of output are shown in Figure 3.22. Percentage error bound for this model was in between 2.5% to 6.5%. The approach was extended to packages subjected to thermal aging at 200C. Results are shown in Table 3.6 and 3D plots are shown in Figure 3.23. Percentage error in models prediction was in between 2.8% to 8.7%.

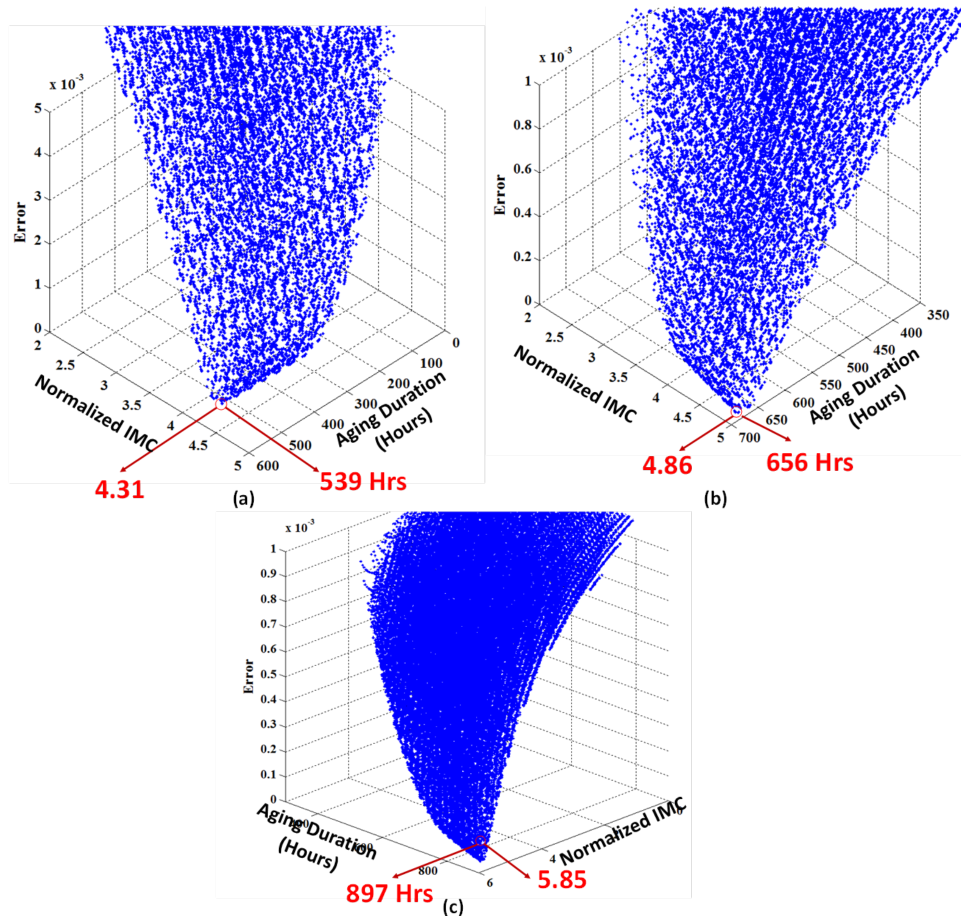

Figure 3.22: 3D Plot of convergence of LM Algorithm at 175°C

Table 3.6: Comparison of experimental and prognosticated Results at 175°C

Time	Experimental (Hours)	Prognosticated (Hours)	% Error
t_1	504	539	6.50%
t_2	672	656	2.50%
t_3	840	897	6.30%

Table 3.7: Comparison of experimental and prognosticated Results at 200°C

Time	Experimental (Hours)	Prognosticated (Hours)	% Error
t_1	288	265	8.70%
t_2	336	361	7.0%
t_3	384	395	2.80%

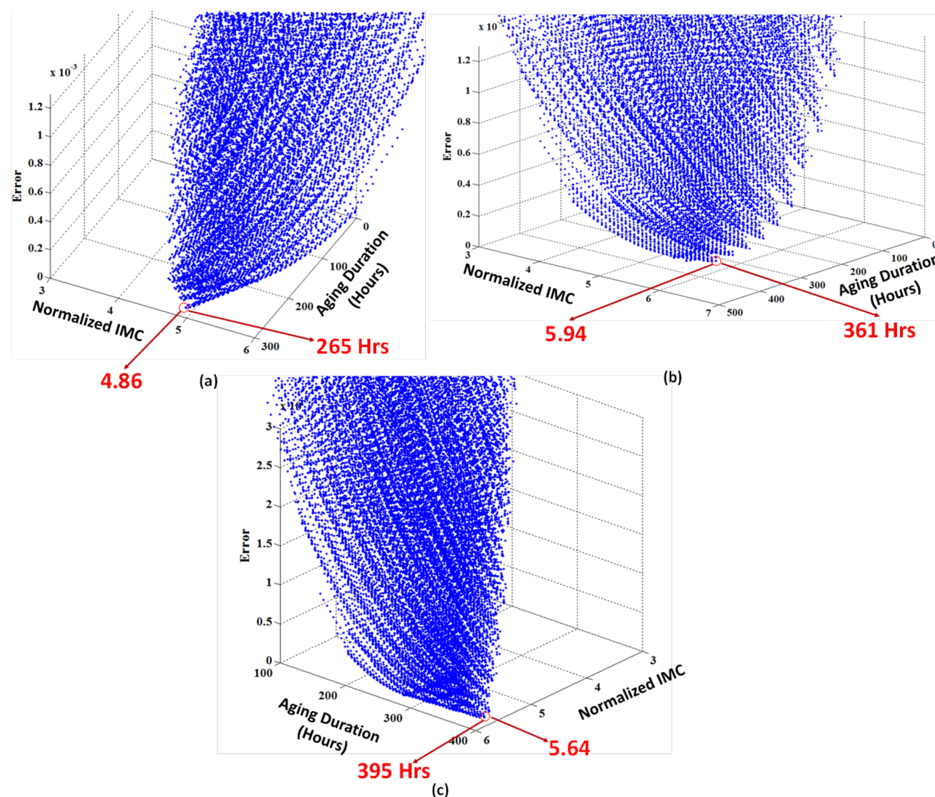

Figure 3.23: 3D Plot of convergence of LM Algorithm at 200°C

3.4.2 Prognostics Performance Matrix

In this paper we will use different performance metrics to evaluate performance of model developed based on LM algorithm and IMC growth as a leading indicator of failure, when Cu-Al incorporated parts are subjected to sustained operation at elevated temperatures. The model will be evaluated based on average bias, precision, Mean Squared Error (MSE), Mean

Absolute Percentage Error (MAPE), α-λ performance, Relative Accuracy (RA), Cumulative Relative Accuracy (CRA). These parameters were used to compare performance of different prognostics metrics by past researchers Saxena[105]. [88].

A. Average Bias

This method averages prediction errors made at all subsequent time steps after l^{th} unit under test (UUT). This method is then extended to establish overall bias over all UUT. In this form variability in prediction and presence of outliers is neglected. Average bias B_1 can be calculated by

$$B_1 = \frac{1}{l} * \sum_{i=P}^{EOP} \Delta'(i) \tag{3.27}$$

Where, l=EOP-P+1. Where, l is cardinality of the set of all time indices at which predictions are made, EOP is End of Prediction is earliest time index, i, after prediction crosses failure threshold, and P is time index at which first prognostic model made prediction. $\Delta'(i)$ is the error between predicted and true remaining useful life (RUL) at time index i for UUT l. LM algorithm predicts prior accrued damage i.e. prior aging duration. If we know total life expectancy of the part, subtraction of life expectancy from prior aging duration will yield predicted RUL.

B. Sample Standard Deviation (SSD)

Precision in predictions is as important as accuracy. SSD calculates variability in prediction by measured spread of error with respect to sample mean of the error. This metric is restricted to assumption of normal distribution of errors

$$SSD(i) = \sqrt{\frac{\sum_{l=1}^{n}[\Delta'(i) - M]^2}{n-1}} \tag{3.28}$$

C. Mean Squared Error (MSE)

In simple average bias calculation, over prediction and under prediction cancel out each other so it might not reflect actual accuracy and precision of model. To avoid this, average of the square of prediction error for multiple UTT is calculated, which is known as MSE. Derivative

of MSE is root mean square error (RMSE)

$$MSE = \frac{1}{l}\sum_{i=1}^{l}[\Delta'(i)]^2 \tag{3.29}$$

D. Mean Absolute Percent Error (MAPE)

MAPE is unit free accuracy measure only for ratio scaled data. MAPE weights errors with RUL and averages the absolute percentage error in the multiple predictions

$$MAPE(i)) = \frac{1}{l}\sum_{i=1}^{l}\frac{[100\Delta'(i)]}{r^1(i)} \tag{3.30}$$

Where $r^l(i)$ is true RUL at time t_1 given that data is available up to l^{th} UTT.

E. α-λ Accuracy

It is essential to know whether the model predictions are within the specified limit of error bound at given time. Time instances are defined as percentage of remaining useful life after first prediction was made.

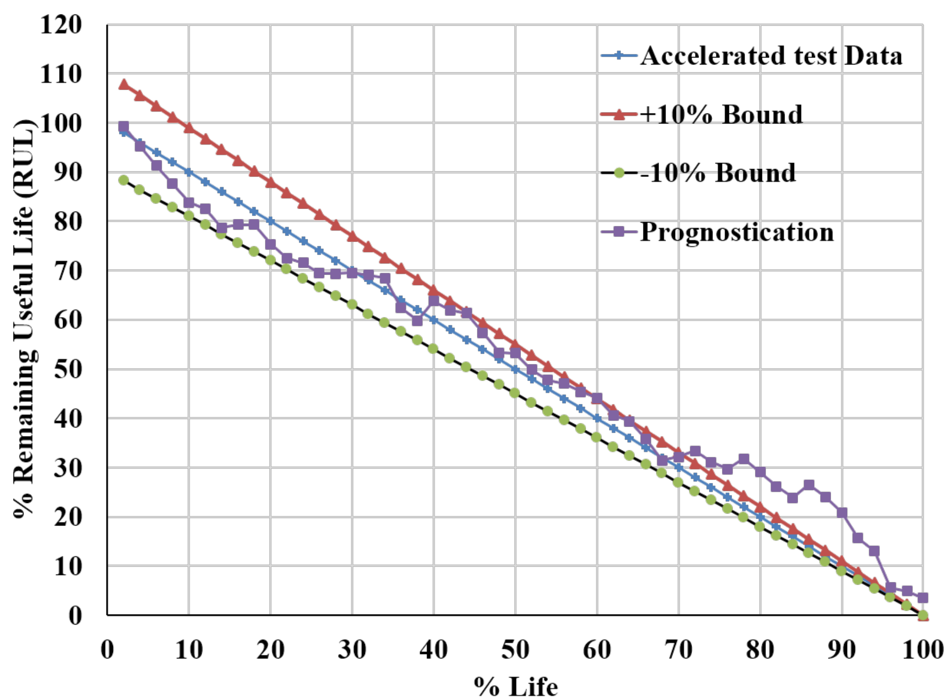

Figure 3.24: α-λ curve for HTSL test at 150°C

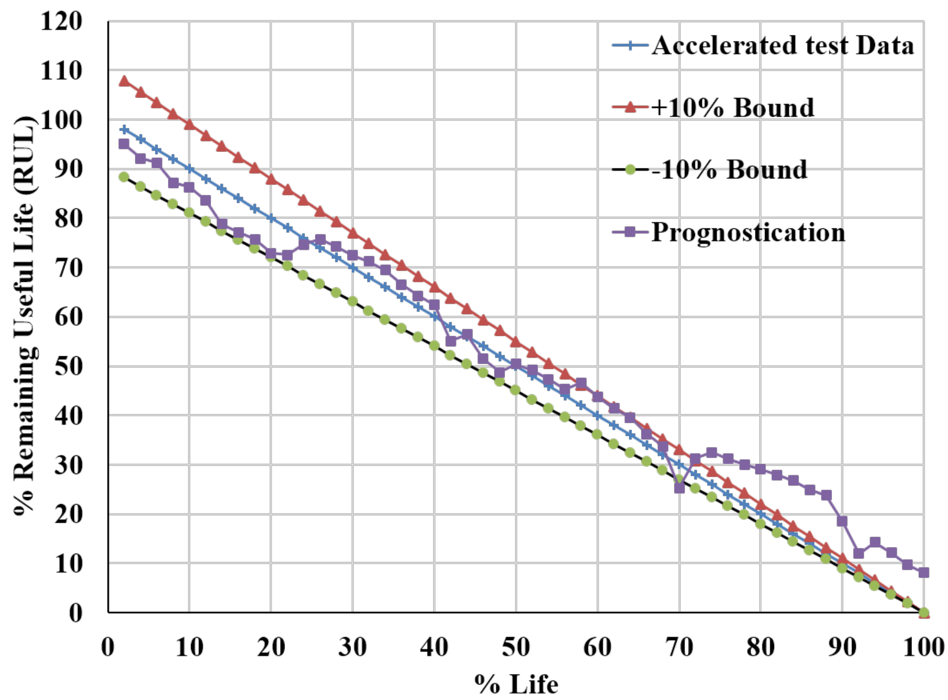

Figure 3.25: α-λ curve for HTSL test at 175°C

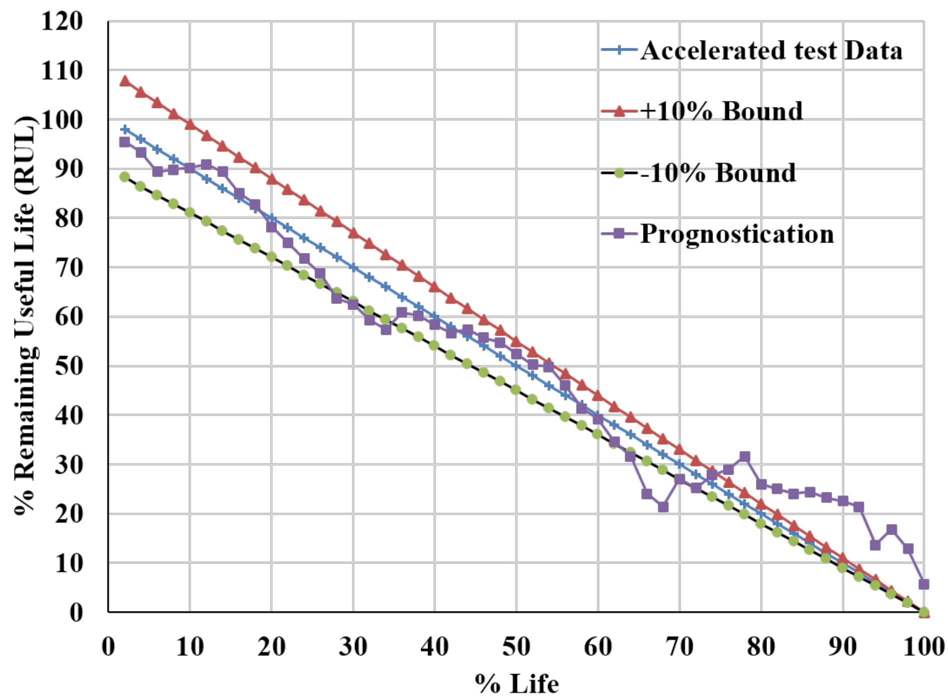

Figure 3.26: α-λ curve for HTSL test at 200°C

α-λ curves are plotted for all three thermal aging conditions in Figure 3.24, Figure 3.25 and Figure 3.26. It is plot of percentage RUL vs percentage life. In this case failure was defined as complete cracking of wirebond interface. Each prognosticated point in the plot represents algorithm prediction of prior accrued damage and RUL. It is plotted against actual accrued damage and RUL which was obtained from accelerated test data. This provides comparison between actual RUL and predicted RUL over complete life of the package. The plot shows whether predicted RUL stays in error bound of 10%. Errors bounds are application specific. Critical applications have narrow error bounds while for some other applications it can go up to 20%. Prognostics prediction for 200°C thermal aging are well within error bound for about 73% of total life and then it bounces beyond +10%. For 175°C, prediction maintains error bound for around 70% of total life, and for 200°C it dropped down to 64%. Predictions of developed model and acceptable for major part of life of Cu-Al incorporated device, when subjected to high temperature sustained operations.

F. Relative Accuracy (RA)

Relative accuracy for prediction is similar to α-λ curve, but here we measure accuracy level. The time instant is described as a fraction of actual remaining useful life from the first prediction point.

$$RA_\lambda = 1 - \frac{r_*(t_\lambda) - r^1(t_\lambda)}{r_*(t_\lambda)} \tag{3.31}$$

G. Cumulative Relative Accuracy (CRA)

CRA aggregates the accuracy levels calculated at multiple time intervals. CRA is normalized weighted sum of relative prediction accuracy's at specific instances

$$CRA = \frac{1}{l} * \sum_{i=1}^{l} w(r^1) RA_\lambda \tag{3.32}$$

Where, w is a weight factor as a function of RUL at all the time indices. In most cases it is desirable to weight the relative accuracy's higher when closer to end of life.

Table 3.8 shows comparison of prognostics models based upon parameters discussed earlier. Equations 3.27, 3.28, 3.29, 3.30, 3.31 and 3.32 were uses to calculate the parameters shown in the table. Algorithm maintains higher relative accuracy at λ (i.e. after consuming 50% life)

Table 3.8: Comparison for Prognostics Metrics for Three Aging Conditions

Prognostic Parameter	150C	175C	200C
Average Bias	-1.02356	-1.10249	-0.45483
SSD	209.621	63.5503	32.6862
MSE	49649.57	4374.163	1080.598
MAPE	0.78975	0.073164	0.03171
RA (λ=0.5)	0.9352	0.9916	0.09507
CRA	0.009164	0.0299	0.05812

for all three temperature ranges. Higher RA is always desirable. SSD and MSE drops down as we increase the aging temperature. Testing at 150°C goes on for 4200 hours, while for 175°C and 200C it finished in about 1200 hours and 528 hours respectively. Since at high temperatures, test finishes in very short time, with less error bound SSD and MSD remain restricted. Overall developed model delivers satisfactory performance at all three aging conditions.

3.5 Summary and Conclusions

Microstructure evolution of Cu-Al intermetallics when subjected to thermal aging has been studied in this paper. Two distinct phases were found, namely Cu-rich interface (Cu_9Al_4) and Al rich interface ($CuAl_2$). Complete cracking of wirebond was found after prolonged thermal aging at 175°C and 200°C. Crack initiates from edges of ball bond, and propagates towards center. Cu-rich IMCs were found to be corrosion at the Cu-Al interface. A method has been developed for prognostication of accrued prior damage and remaining useful life after exposure to thermal aging. The presented approach uses the Levenberg-Marquardt Algorithm in conjunction with development of damage based leading indicator for estimating prior accrued damage. Specific damage proxies examined is the intermetallic thickness in Cu-Al wire bond. Viability of this approach has been demonstrated with 32 pin chip-scale package without any prior knowledge of aging duration, subjected to thermal aging at 150°C, 175°C, and 200°C. The prognosticated values have been validated versus experimental data. Correlation between the prognosticated damage and the actual accrued damage demonstrates that the proposed approach can be used to assess prior damage accrued because of aging. Performance of prognostication model was evaluated for all three temperature conditions. Concept of CRA, RA, MAPE, SSD, α-λ accuracy

were used for evaluation purpose. It was found that model developed based on LM algorithm and IMC thickness growth as a leading indicator of failure for Cu-Al wire-bonded devices when subjected to HTSL conditions delivers acceptable performance and predicts remaining useful life and prior accrued damage with high confidence.

Chapter 4

Development of Model for Identification of Process Parameters for Wet Decapsulation of Cu-Al Wirebonds in PEMs

4.1 Overview

Decapsulation is a failure analysis technique often used to exposes the die and first level interconnects such as wirebonds by dissolving the surrounding epoxy molding compound (EMC). The wet decapsulation technique, which uses fuming acids works very well for traditional Gold (Au) wirebonds. On the other hand, its latest alternative, Copper (Cu) wirebond reacts with the nitric acid vigorously and undergoes severe corrosion. It is important to develop an acid chemistry that can be used to perform decapsulation of Cu-Al incorporated plastic encapsulated microelectronics (PEMs) without damaging the Cu wires. This chapter presents the wet decapsulation technique based on different ratios of the red fuming nitric acid and concentrated sulfuric acid. Quality of post decap part was examined using reduction in the wire diameter and changes in ball shear strength. Reduction in wire diameter was monitored with the scanning electron microscopy (SEM) and shear strength was measured using a DAGE2400 shear tester. These tests were performed on the PEMs molded with different EMC, wire diameters, pad thickness to cover process as well as geometric variability. Artificial neural network (ANN) based regression model has been developed correlating the decapsulation process parameters with the post decap wire diameter reduction. PCR was used to identify variables which significantly affects the decap process. These influential variables were then used to develop predictive model for prediction of the percent reduction in wire diameter and change in shear strength separately. Models were then validated with the test data set.

Table 4.1: Dimensions of 32 pin CSP

Parameter	Dimensions (mm)
Width of Package	4.5
Length of Package	5.5
Height of Package	0.7
Length of Pin	0.45
Pitch	0.5

Table 4.2: Dimensions of BGA 337

Parameter	Dimensions (mm)
Width of Package	16.10
Length of Package	16.10
Height of Package	1.40
I/O Count	337
Pitch	0.8

4.2 Test Vehicle and Test Matrix

Four types of packages from different manufacturers were used in this study. 32 pin chip scale package (CSP), BGA 337 were daisy chained test dies. FDA6690A and ICS553MILF were commercially available devices. All packages were bonded with bare Cu wire and Al pad. Package dimensions of 32 pin CSP and BGA 337 are listed in Table 4.1 and Table 4.2. They had 1 mil and 0.8 mil Cu wire respectively. Figure 4.1 and 4.2 shows optical and X-ray images of 32 pin CSP and BGA 337. X-ray images were taken using YXLON Cougar CT system.

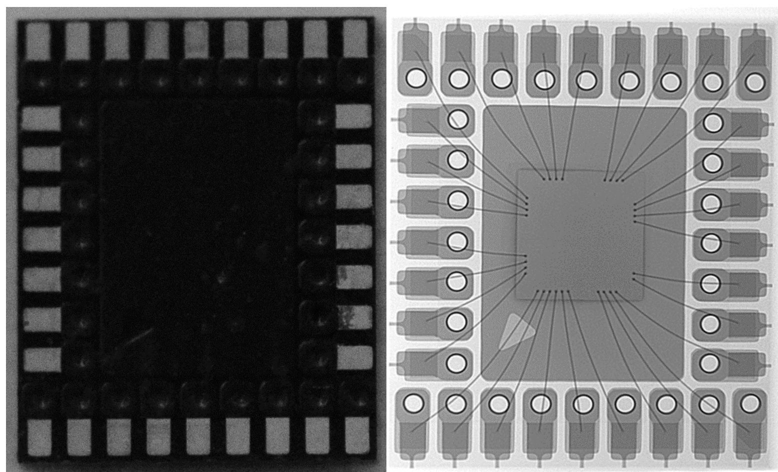

Figure 4.1: Optical and X-ray Images of 32 pin CSP

FDA 6690A is 8 lead small outline N-channel logic MOSFET from Fairchild semiconductor.

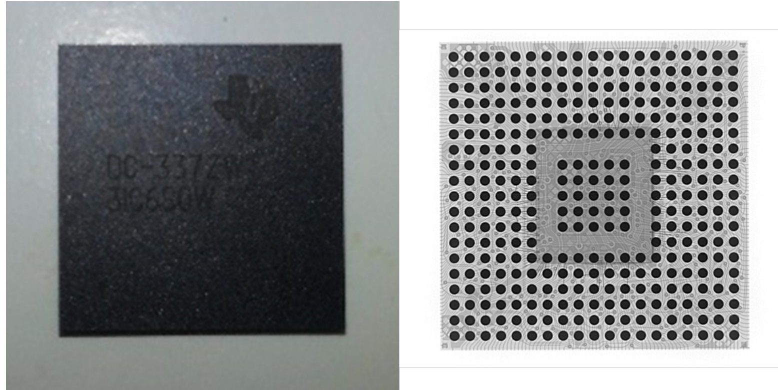

Figure 4.2: Optical and X-ray Images of BGA 337

It had 2 mils thick copper wire and 6m thick Al pad. ICS553MILF is 8 lead SOIC clock buffer device. It has 1 mil Cu wire with 2.3 µm thick Al pad. Package dimensions are provided in Table 4.3. Optical and X-ray images of FDS6690A and ICS553MILF are shown in 4.3 and Figure 4.4.

Table 4.3: Dimensions of FDS6690 and ICS553

Parameter	**FDS6690A**	**ICS553MILF**
Width of Package	4.93	4.97
Length of Package	5.96	5.92
Height of Package	1.74	1.52
Pitch	1.26	1.52

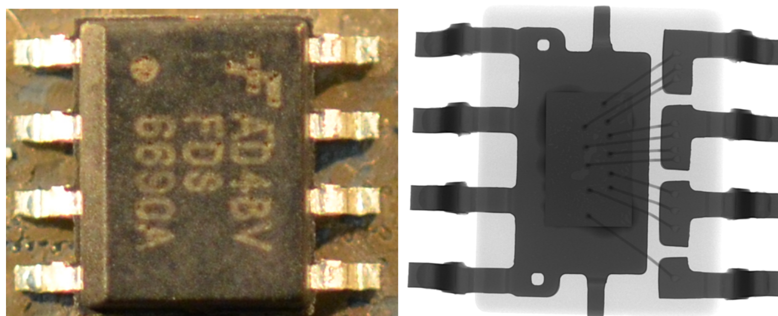

Figure 4.3: Optical and X-ray Images of FDS6690A

Table 4.4 Shows details about the package architecture. Details include percent filler content of EMC, chip dimensions, Cu wire diameter, Al pad thickness, and wire ball diameter. All

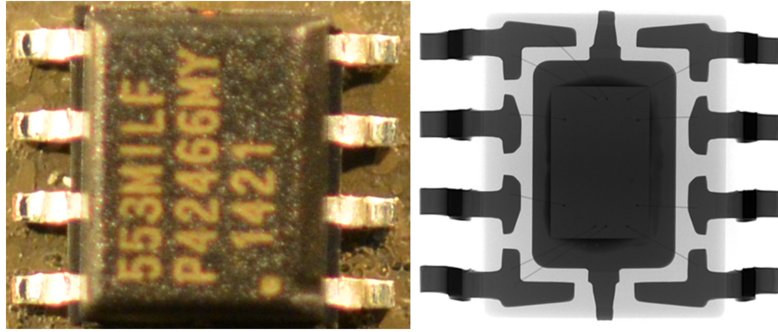

Figure 4.4: Optical and X-ray Images of ICS553MILF

Table 4.4: Details of the Packages

Parameter	**CSP**	**BGA**	**FDS6690**	**ICS553**
Die Size (mm*mm)	1.6*1.5	7*6	2.4*1.5	2.0*1.3
Wire Dia. (m)	20.32	25.4	50.8	25.4
Al Pad Thickness	1	1	5.9	2.3
WB Ball Dia. (m)	68.52	36.83	64.26	126.49
Percent Filler Content	88%	86%	84%	85%
Wire loop Height (m)	254	375	302	290

packages had bare copper wire bonded on Al pad. These variables were used in the development of the model.

The packages were post mold cured at 150°C for 4 hours to allow cross-linking of polymers in the EMC. Combinations of 98 percent concentrated red fuming nitric acid and 95 percent concentrated sulfuric acid were used. Different acid ratios by volume of (Nitric to Sulfuric acid) 1:1, 6:5, 3:2, 2:1, 3:1, 4:1, 1:4 were tested. Initial decapsulation process was carried at elevated temperatures in the range of 100°C to 130°C. For the acid combinations with promising results, decap process was carried out from 80°C to 150°C, at the interval of 10°C. Prior to the actual decap process, packages were heated on a hot plate at 120°C for 5-6 hours to get rid of the residual moisture. Dual stage decapsulation technique was used in this study. Initial cavity was formed using nitric acid at 80°C. Micro-pipettes were used for this process, so that acid will not flow all over package. After this, hot plate was set at desired process temperature and the parts were decapped using freshly prepared acid mixtures, which were at the room temperature. Decapped parts were cleaned with the spray of acetone, and then soaked into methanol for about 5 minutes. SEM was used for inspection of the post decapped Cu wires. Image processing software Image-J was used for dimension measurements. DAGE 2400 ball shear tester

was used to monitor changes in the shear strength of the wirebond interface. Shear tool height was set to be 2 µm above the Al pad. Shear tool speed was 150 µm/s. Industry standard of minimum shear force value of 5.5gf/mil^2 was set as passing criterion. At least 30 wirebonds were sheared for each device and each condition.

SEM images were used to measure the wire diameter. Backscatter detection was used to ensure that wires were properly cleaned, and the wirebond surface was properly exposed. Inadequate cleaning can cause false readings and affect the dataset. Images of the clean wirebond were captured from all sides of the devices. For each wire, thickness was measured for at least 10 times, and the process was repeated for 7 wirebonds from same package. The mean value of thickness was considered as wire diameter for respective decap condition. Figure 4.5 shows 10 different locations of diameter measurement for one wirebond.

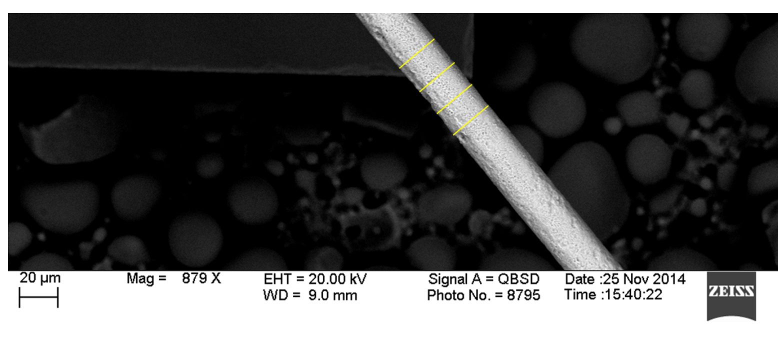

Figure 4.5: Wire Diameter Measurement

4.3 Decapsulation Process Results

4.3.1 BGA337

Percentage reduction in the wire diameter for BGA-337 devices for the process temperatures of 100°C, 130°C and 150°C is shown in Figure 4.6, Figure 4.7, and Figure 4.8 respectively. Each box-plot is made-up of at least 70 readings as discussed earlier. Minimum wire diameter reduction of 1.35% was obtained for acid combination of 2:1 (Nitric to Sulfuric) at 100°C. SEM images of post decapped Cu wire with minimum damage is shown in Figure 4.9. Wire had very few spots of localized corrosion, and no Aluminum pad corrosion was found. It was

observed that higher decap temperature tends to corrode the copper wire more severely, which results in higher reduction in the wire diameter.

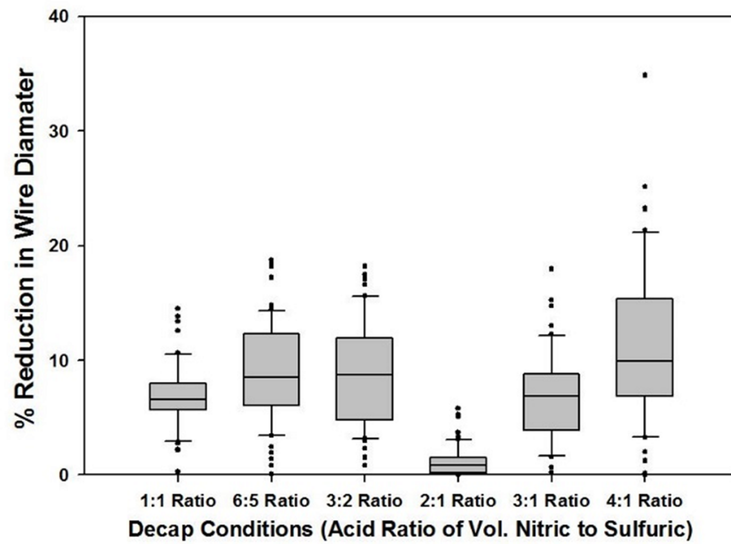

Figure 4.6: Wire Diameter Reduction for BGA 337 at 100°C

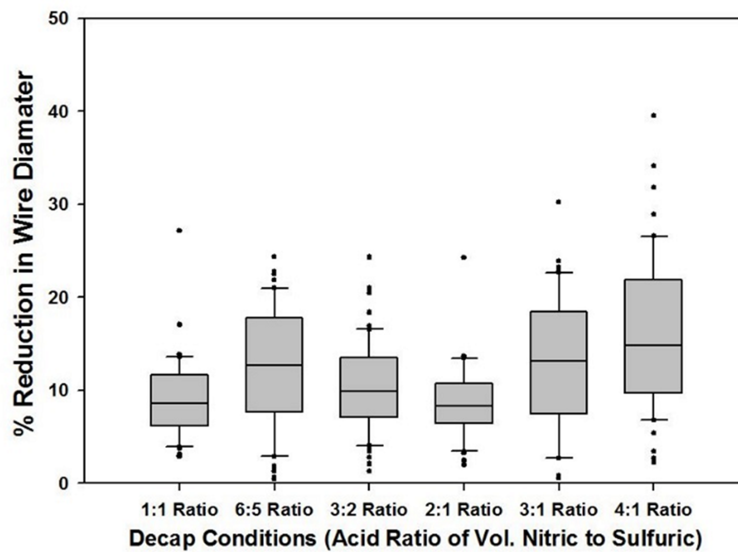

Figure 4.7: Wire Diameter Reduction for BGA 337 at 130°C

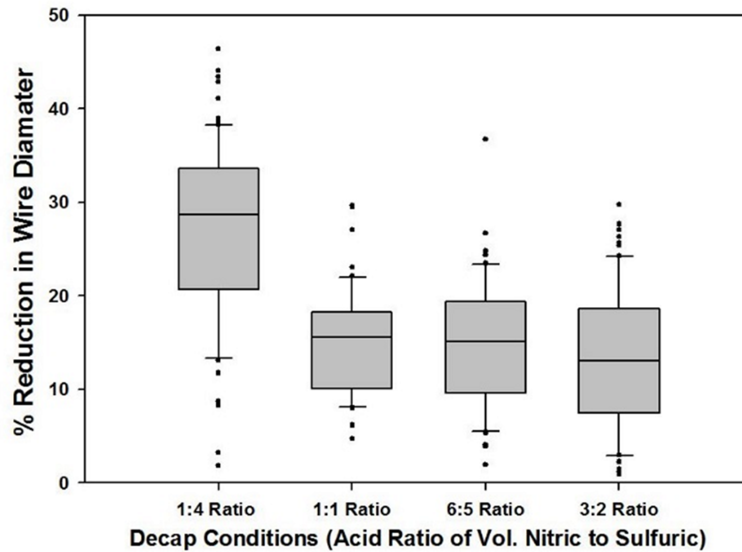

Figure 4.8: Wire Diameter Reduction for BGA 337 at 150°C

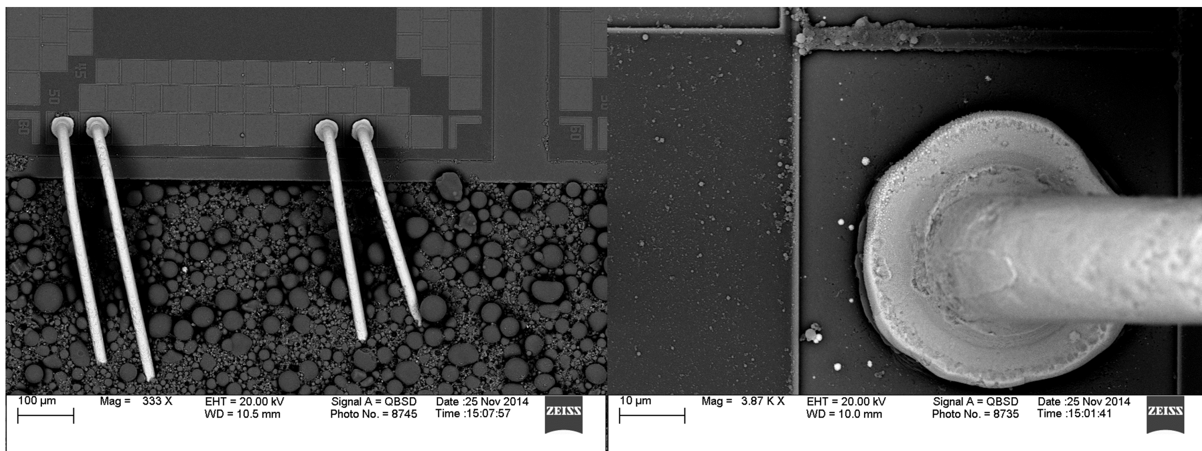

Figure 4.9: Post Decap Cu wire 2:1 Acid Combination at 100°C

It was found that 2:1 acid combination produced minimum reduction in wire diameter. Effect of different process temperatures for 2:1 combination is shown in Figure 4.10. Nitric acid is typically highly reactive in the range of 90°C to 130°C, while sulfuric acid is very effective at temperatures above 150°C. For this reason, high nitric content ratios were selected for lower temperatures, and higher sulfuric acid ratios were selected for process at around 150°C.

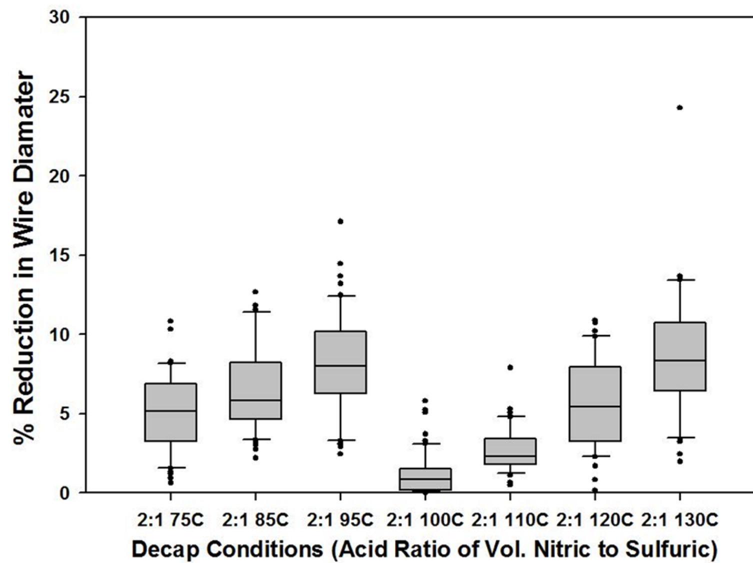

Figure 4.10: Post Decap Cu wire 2:1 Acid Combination at 100°C

For 1:4 ratio at 150°C and 160°C condition, Cu wires and the Al pad were severely corroded. Figure 4.11 shows the corroded Al pad for 1:4 acid ratio. Figure 4.12 shows corroded copper wire at 3:1 and 4:1 acid combination. Process temperature was 130°C for both cases. Wire reduction obtained was 12.96% and 16.23% respectively.

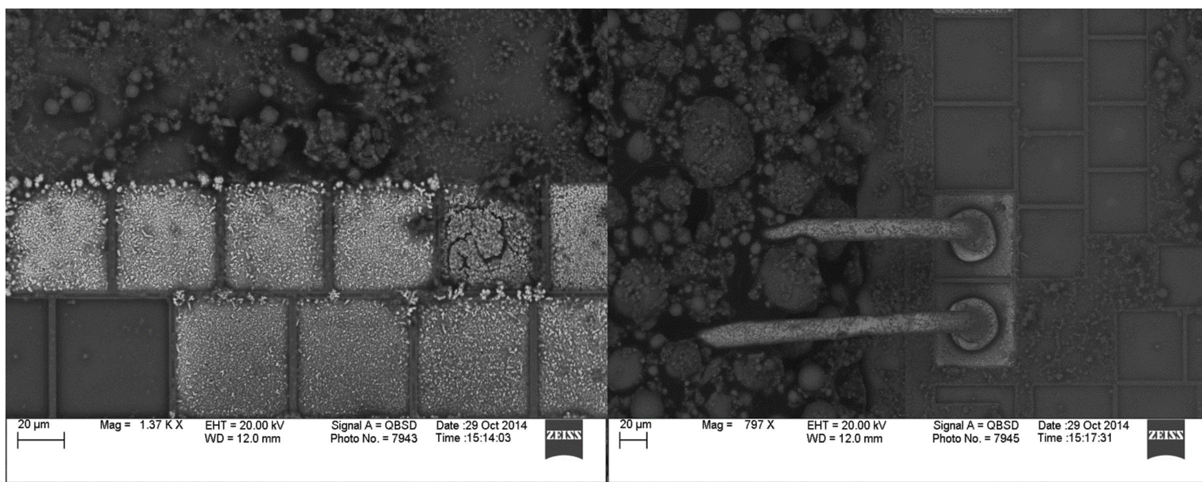

Figure 4.11: Post Decap Al Pad Corrosion at 1:4 acid combination

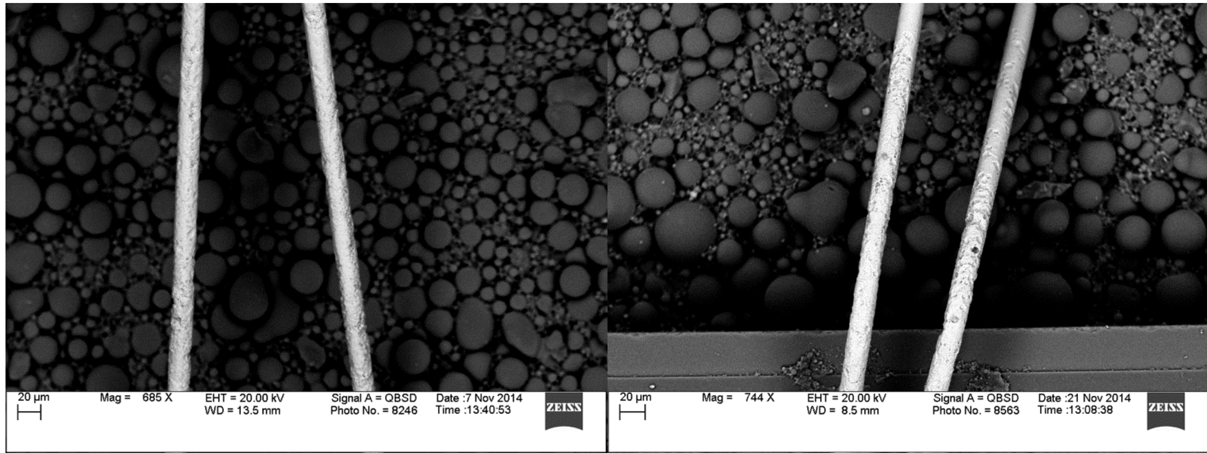

Figure 4.12: Post Decap Al Pad Corrosion at 3:1 acid combination

In general, for higher nitric acid content (more than 2 parts), higher reduction in Cu wire was observed. For these conditions, sulfuric acid content was not enough to form a passivation layer around the wirebond. This causes direct contact of nitric acid with copper and corrodes it.

On a few of the samples, ball shear test was performed to check for the degradation at the wirebond interface. Figure 4.13, Figure 4.14, and Figure 4.15 shows change of shear strength of wirebonds from post decap parts for process temperature of 100°C, 130°C and 150°C respectively.

Lower shear strength correlates to the severely corroded Cu wire or Al pad. For 1:4 acid combination, shear strength was abnormally low. The Al pad was found to be completely corroded and very little contact was left. Corroded Al pad is shown in Figure 4.11. IS in the graph stands for the industrial standard passing criterion as discussed earlier. Any shear value above 9.12 grams was desirable in this case. For the cases where ball shear strength was less than standard value, very high diameter reduction in the Cu wire or the Al pad corrosion was observed.

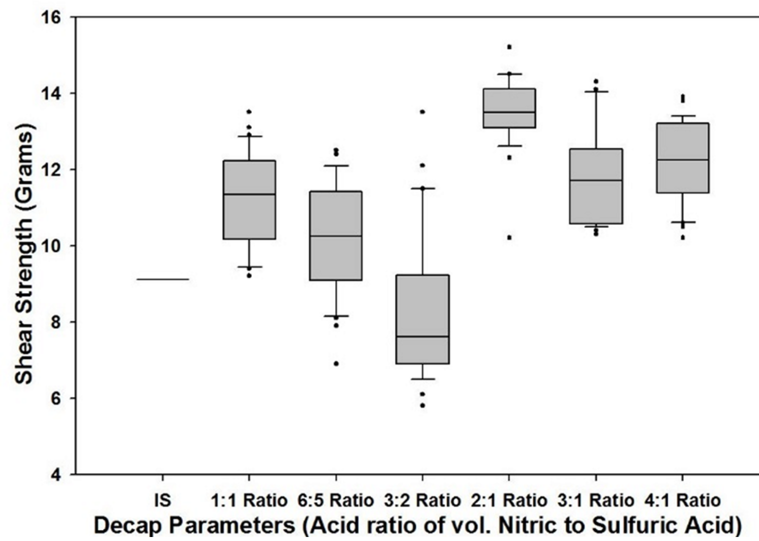

Figure 4.13: Ball Shear Strength of Post Decap BGA337 Package at 100°C

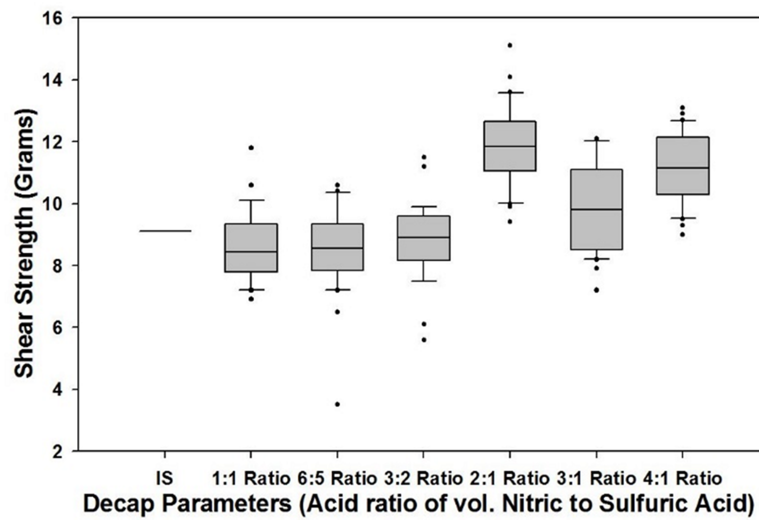

Figure 4.14: Ball Shear Strength of Post Decap BGA337 Package at 130°C

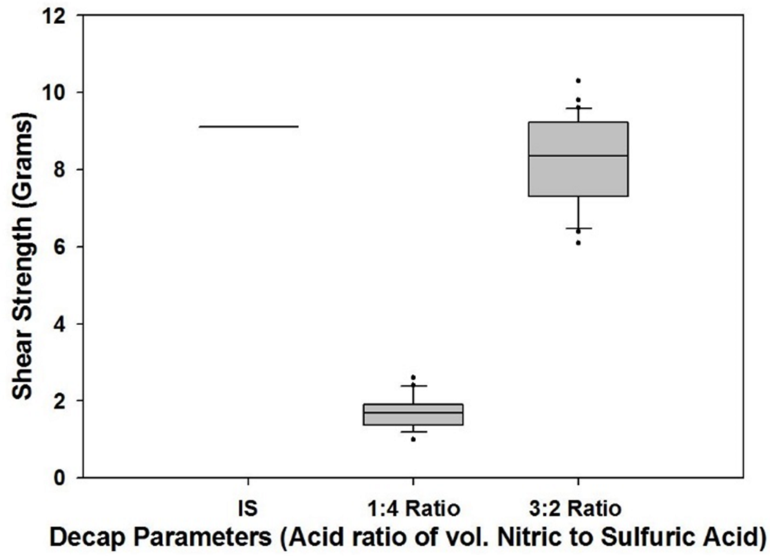

Figure 4.15: Ball Shear Strength of Post Decap BGA337 Package at 150°C

4.3.2 32 Pin CSP

Wire diameter reduction for 32 pin CSP at 100°C, 130°C, and 150°C is shown in Figure 4.16, Figure 4.17 and Figure 4.18.

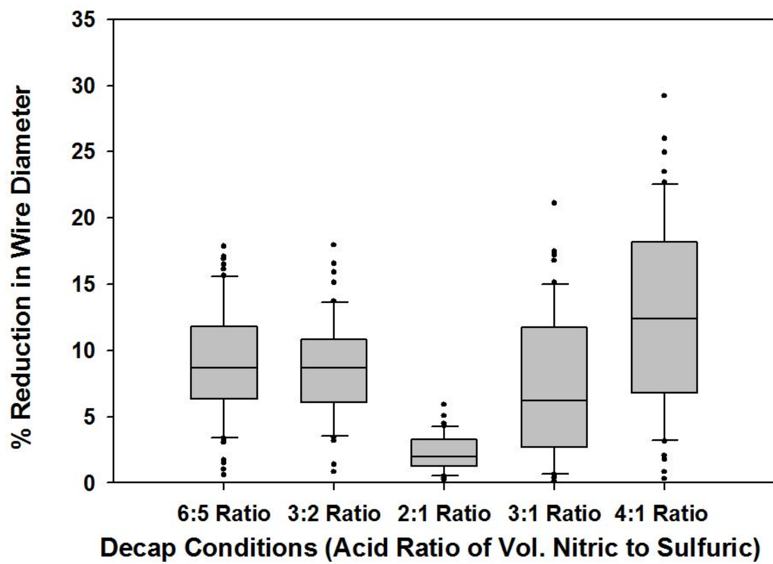

Figure 4.16: Wire Diameter Reduction for CSP at 100°C

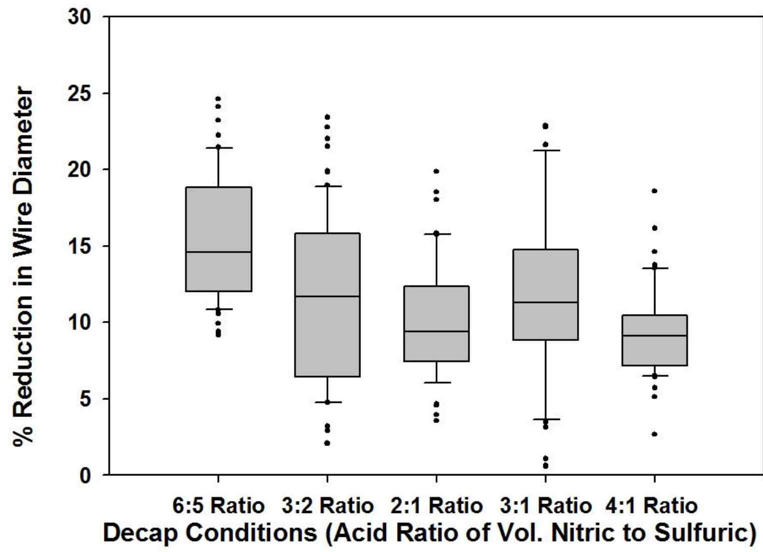

Figure 4.17: Wire Diameter Reduction for CSP at 130°C

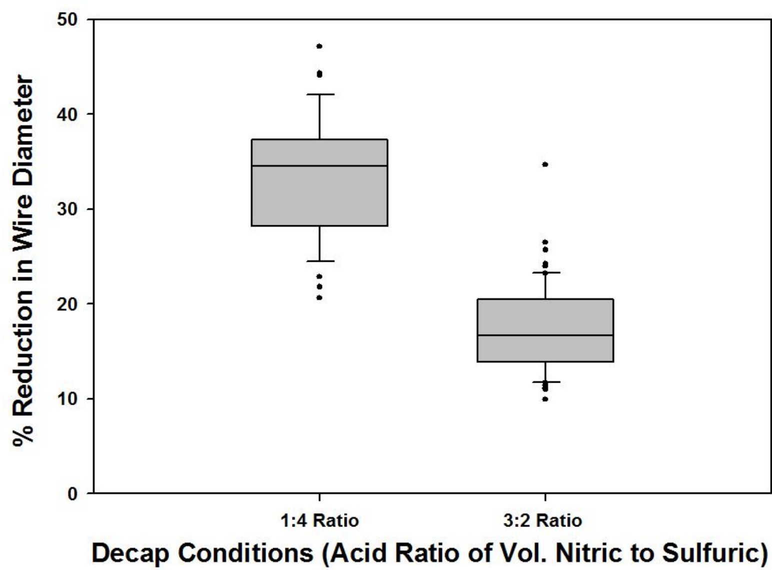

Figure 4.18: Wire Diameter Reduction for CSP at 150°C

The best decapsulation result i.e. minimum reduction in the wire diameter was observed for 2:1 acid combination at 100°C.

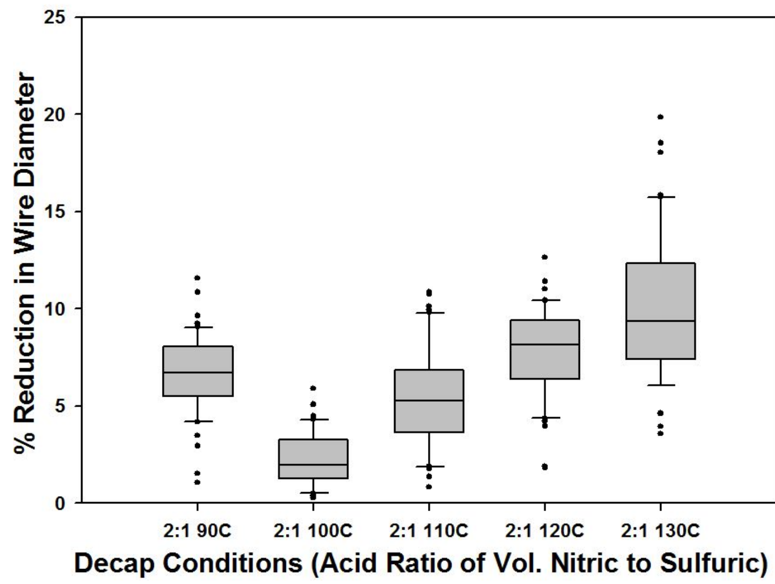

Figure 4.19: Cu wire for CSP 2:1 Acid Combination

Figure 4.19 shows effect of temperature on the wire diameter reduction when acid combination was 2:1.

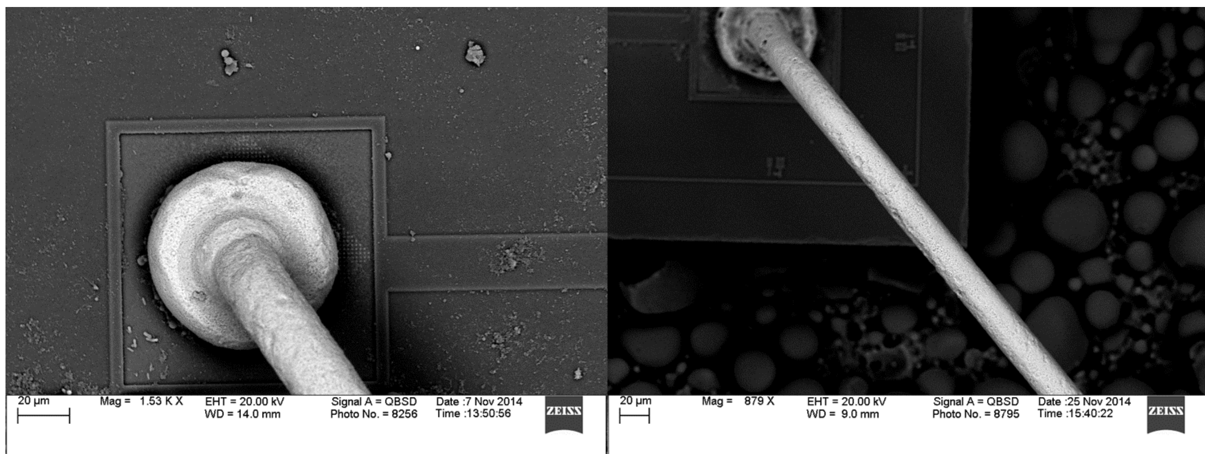

Figure 4.20: Cu wire - 2:1 Acid Combination at 100°C

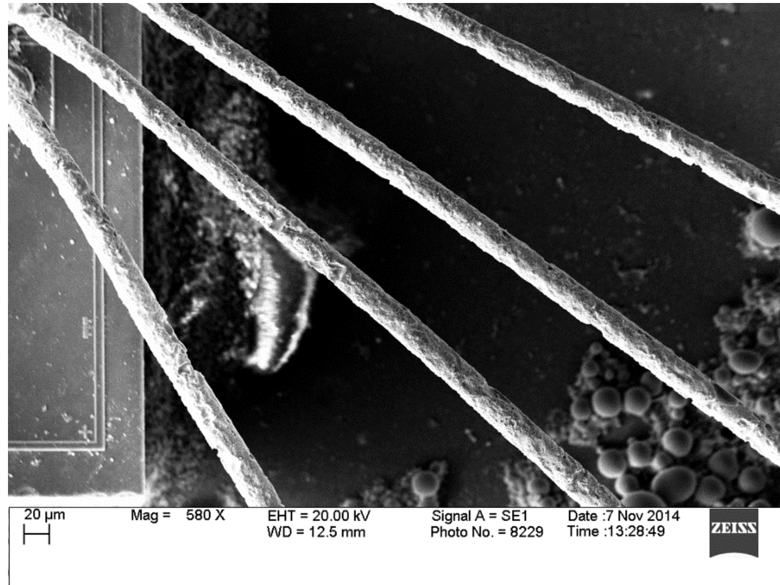

Figure 4.21: Corroded Cu wire - 1:4 Acid Combination at 150°C

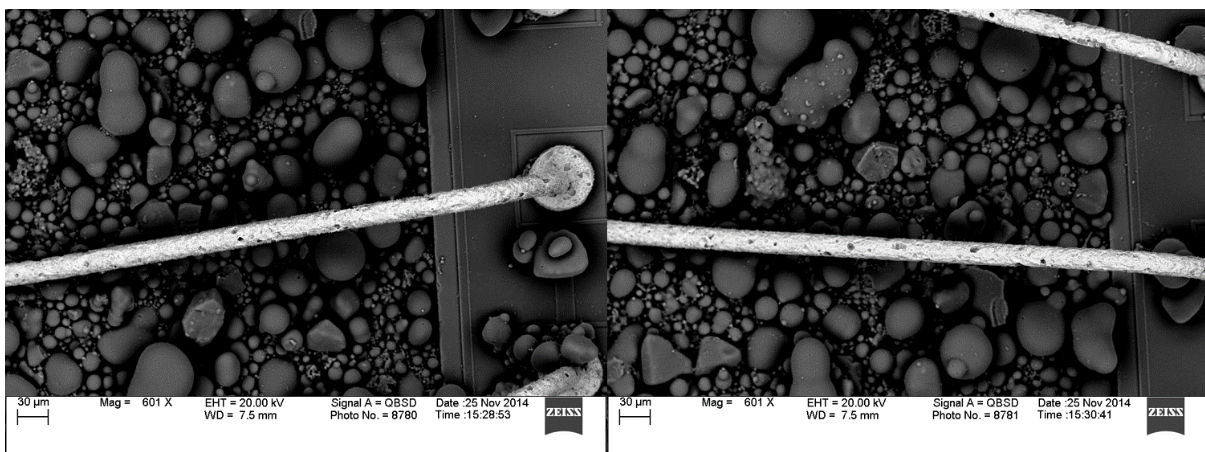

Figure 4.22: Corroded Cu wire due to high nitric acid content 130°C

If the temperature goes past 100°C, severe corrosion of the Cu wires was observed. This might be due to elevated acid reactivity. Cu wire corrosion was predominant at the lower temperatures(¡ 100°C). Lower temperature reduces reaction speed; Thus, making decap process slower. It results into increasing contact time of acids with the wire, which eventually causes degradation of Cu wire. Figure 4.20 shows post decap ball bond and wire, with minimum damage. Figure 4.21 shows severe corrosion of the Cu wires for 1:4 acid combination. Since the wire diameter reduction was more than 10%, shear tests were not performed for this condition. Figure 4.22 shows corroded Cu wirebond for 3:1 and 4:1 acid combinations, both at 130°C. Percentage wire diameter reduction was 7.28% and 12.83% respectively for these cases.

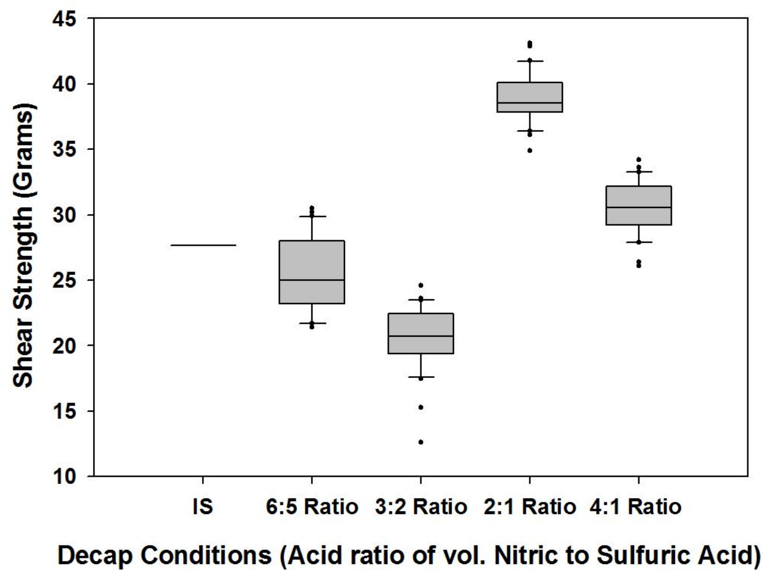

Figure 4.23: Ball Shear Strength of Post Decap Wires at 100°C

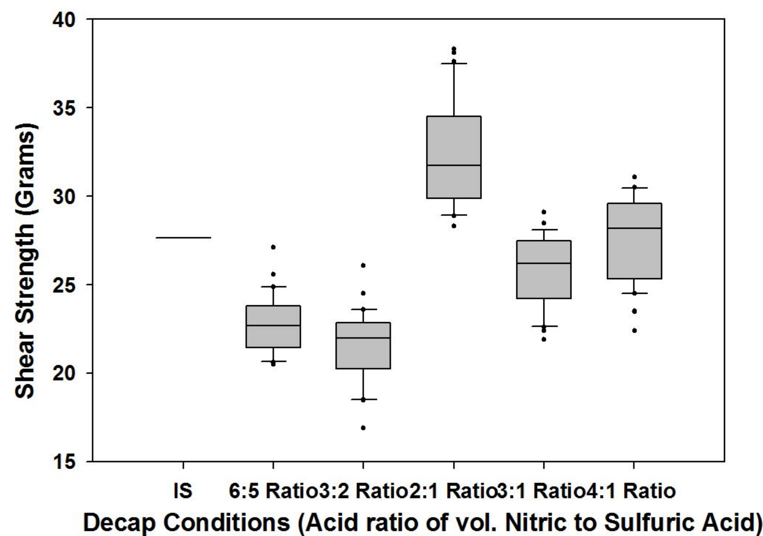

Figure 4.24: Ball Shear Strength of Post Decap Wires at 130°C

Comparison of shear strength of post decap parts with minimum industry standard(IS) shear strength for process temperature of 100°C, 130°C and 150°C are shown in Figure 4.23, Figure 4.24, and Figure 4.25. Drastic changes in the shear strength were observed for 3:2 acid combination at 100°C, and for 2:1 combination at 130°C. Average shear strength for those combinations were 23.10 grams and 32.79 grams respectively. Excessive Al pad corrosion due to high sulfuric acid content caused this large variation. Excessive acid reacts and oxidizes Al pad and cause degradation of the diffusion joint, which leads to the lower shear strength.

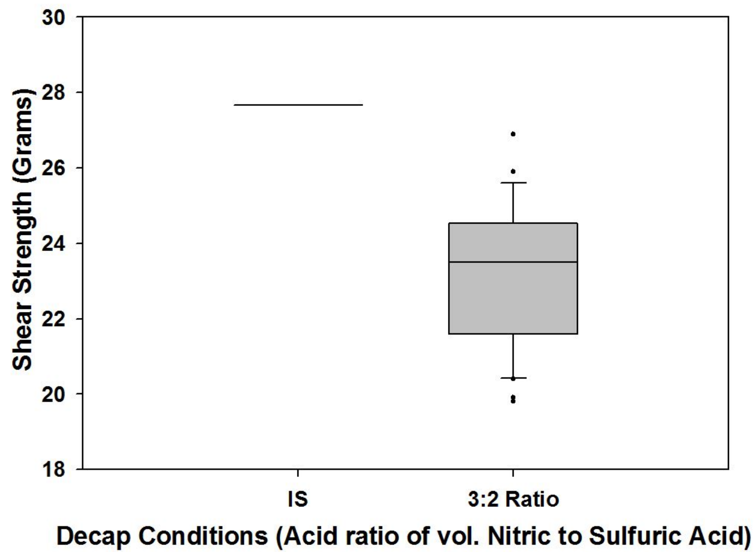

Figure 4.25: Ball Shear Strength of Post Decap Wires at 150°C

4.3.3 FDS6690 and ICS553

Figure 4.26, Figure 4.27, and Figure 4.28 show reduction in the wire diameter for process temperatures 100°C, 130°C and 150°C respectively for ICS553 devices. Minimum 5.66% wire diameter reduction was obtained for 2:1 acid combination at 100°C. Figure 4.29 (a) shows an overview of the package, while (b) and (c) shows post decap Cu wire with the minimum corrosion. ICS553MILF took a long time for EMC etching as compared to other devices. Longer etching period causes acid to be in contact with Cu wires for longer time, which increases the chances of corrosion of Cu wire. For the same combination of 2:1, 100°C, FDS6690 had 1.06% reduction. Post decap wire diameter reduction results at 100°C and 130°C are shown in Figure 4.30, and Figure 4.31. Figure 4.32 (a) shows overview of package while (b) and (c) shows post decap Cu wire and ball bond for 2:1 acid combination at 100C. Wedge bond can be seen in some parts when the part was over etched. No visible damage or pitting corrosion spots were observed for this combination.

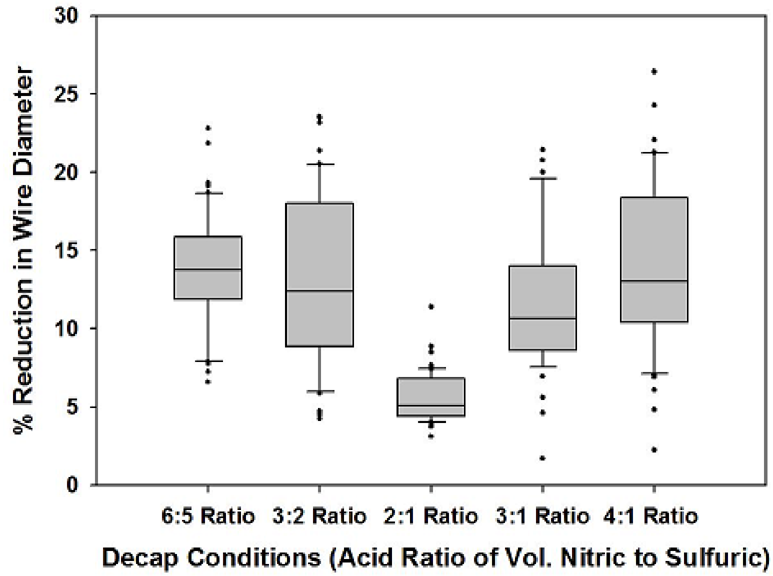

Figure 4.26: Percent Wire Diameter Reduction of ICS553 Package at 100°C

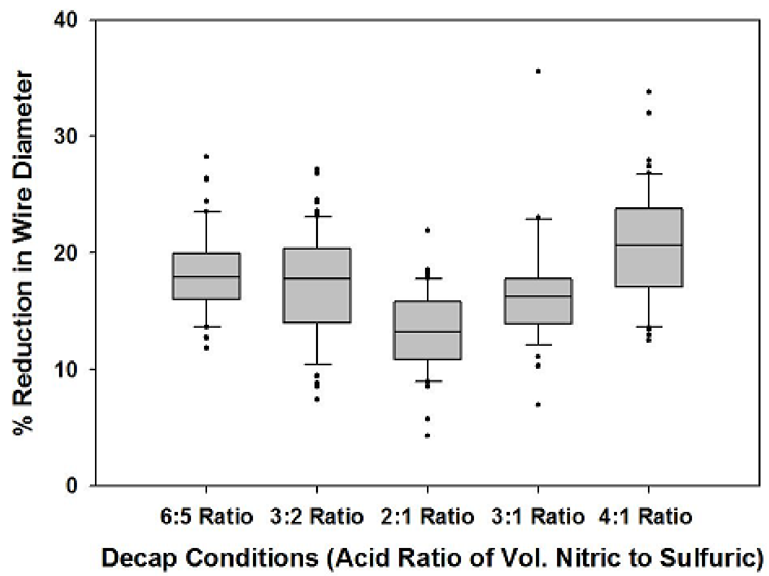

Figure 4.27: Percent Wire Diameter Reduction of ICS553 Package at 130°C

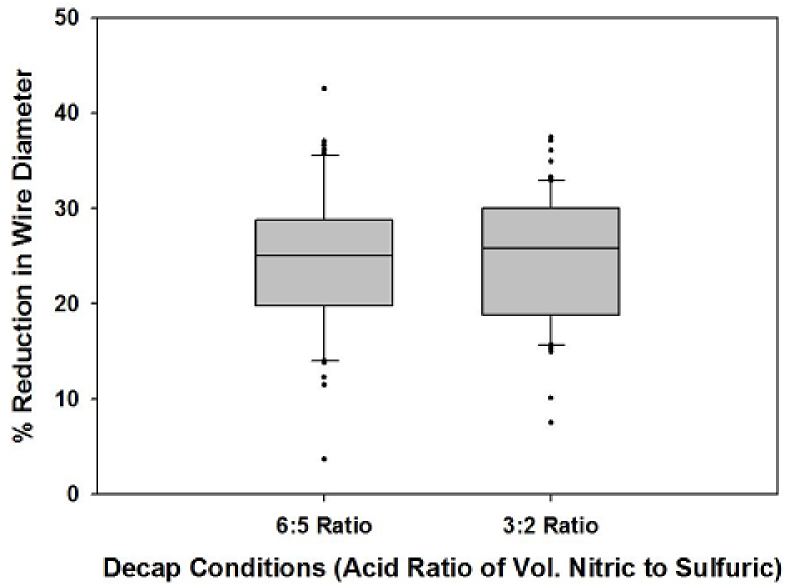

Figure 4.28: Percent Wire Diameter Reduction of ICS553 Package at 150°C

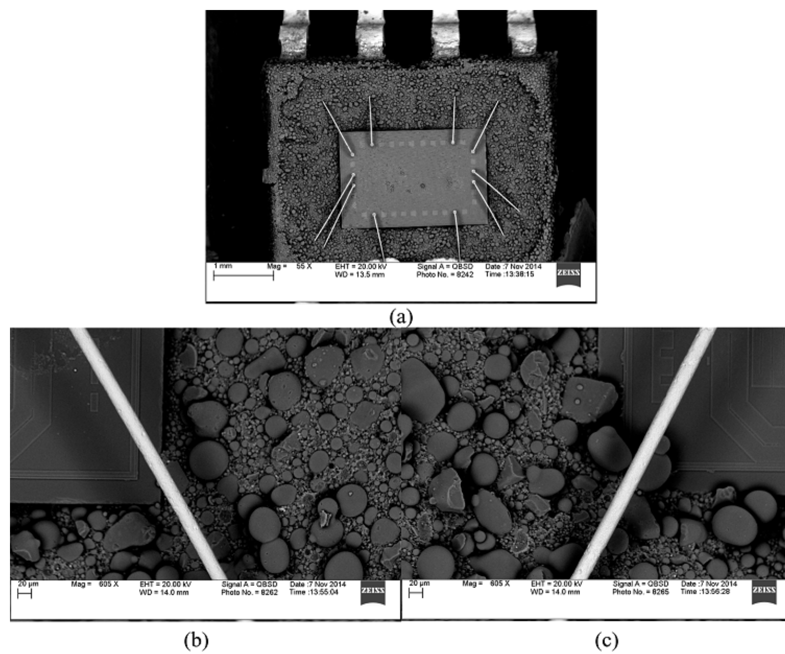

Figure 4.29: Post decap sample at 2:1 100°C combination (a) overview (b)(c) closeup

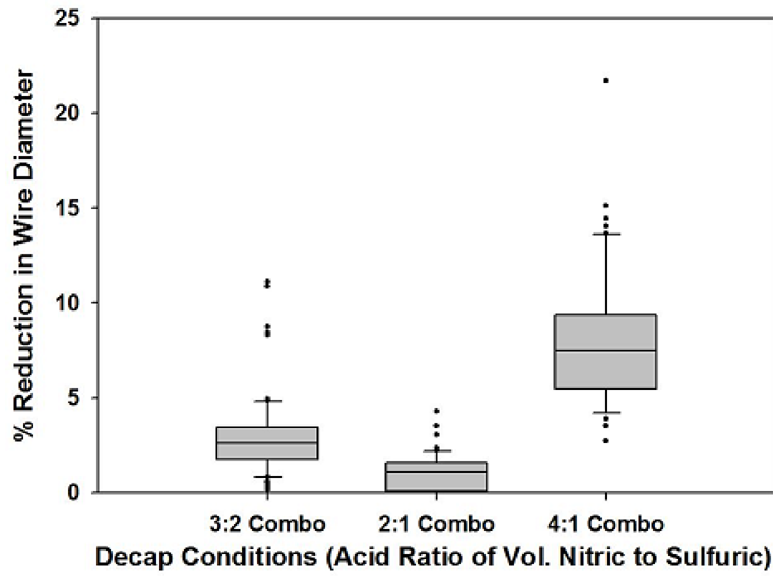

Figure 4.30: Percent Wire Diameter Reduction of FDS6690 Package at 100°C

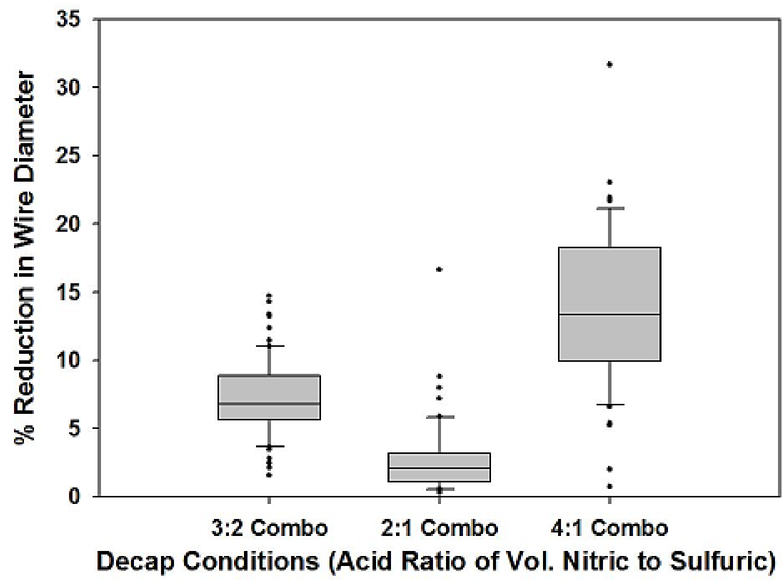

Figure 4.31: Percent Wire Diameter Reduction of FDS6690 Package at 130°C

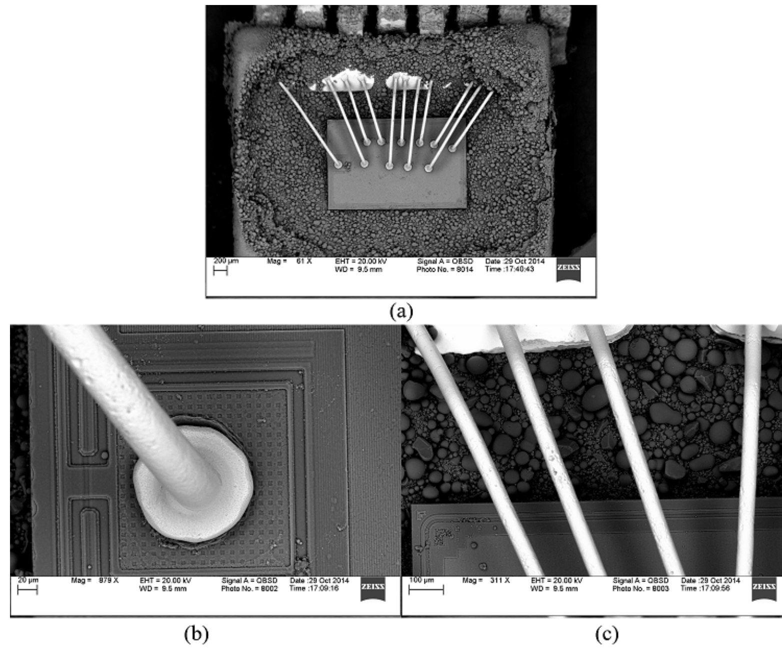

Figure 4.32: Post decap sample at 2:1 100°C combination (a) overview (b)(c) closeup

4.4 Neural Network Modeling

4.4.1 NN Framework

In this model, a feed-forward, two-layered network with 16 neurons (15 hidden, 1 output) has been used as shown in Figure 4.33. The decaping process parameters and package parameters are the inputs of the NN model.

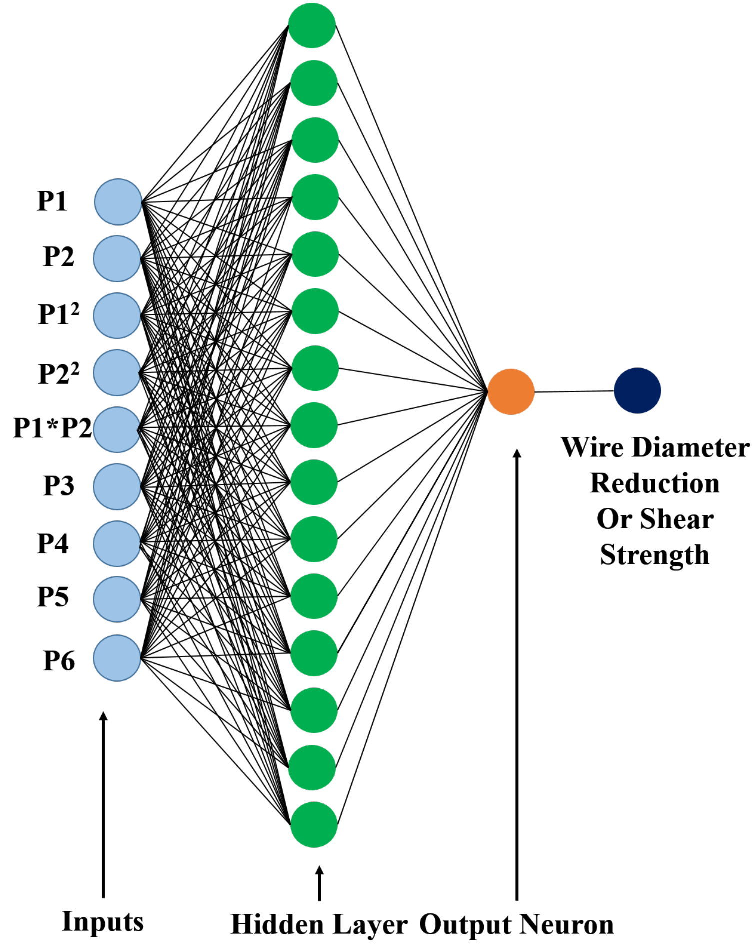

Figure 4.33: Neural Network architecture

Two models have been developed using this approach. In the first model, the output variable is the reduction in wire diameter in response to different environmental, test, and package related variables. In the second model, the output variable is shear strength of the wirebond versus environmental, test, and package related variables. In the conventional NN training process, a common performance function that depends on the distance between the real and predicted data is used for assessment of convergence of weights [106], [107], [108].

$$F = E_D(D \mid w, M) = \frac{1}{N}\sum_{i=1}^{n}(\widehat{t_i} - t_i)^2 \tag{4.1}$$

Where, E_D is the mean sum of the squares error of the network output, D is the training set of inputoutput pairs, M is the NN architecture including the number of inputs, number of layers, and the choice of activation function, and t_i is the real data. Since the information content of the

training set is ordinarily not sufficient by itself to uniquely reconstruct the inputoutput mapping and may result in over fitting of the data, the method of regularization is used to restrict the solution of the hyper surface reconstruction problem through minimization of an augmented cost function. The regularized cost function involves the addition of a second term in order to obtain a smoother mapping between the inputs and the outputs [107], [108].

$$F = \beta E_D(D \mid w, M) + \alpha E_w(w \mid, M) \tag{4.2}$$

Where,

$$E_w(w \mid, M) = \sum_{i=1}^{n}(w_i^2) \tag{4.3}$$

Where E_w is the sum of the squares of network weights. α, also called the weight decay rate, and β are hyper-parameters that have yet to be estimated. In the case that α¡¡β, the training algorithm will make the errors smaller. However, if α¿¿β, training will result in weight size reduction at the expense of network errors, resulting in a smoother surface. Once the data are taken with the Gaussian additive noise assumed in the target values, the posterior distribution of the ANN weights can be updated according to Bayes rule,

$$P(w \mid D, \alpha, \beta, M) = \frac{P(D \mid \ w, \beta, M).P(w \mid \alpha, M)}{P(D \mid \alpha, \beta, M)} \tag{4.4}$$

where the prior distribution of weights are defined as

$$P(w \mid \alpha, M) = (\frac{\alpha}{2\pi})^{\frac{m}{2}} e^{-(\frac{\alpha}{2})w'w} \tag{4.5}$$

where w is the vector of network weights, M is the ANN, and α is the weight decay rate. The optimal weights should maximize the posterior probability $P(D \mid \alpha, \beta, M)$ and thus minimize the regularized objective function, F given by 4.2 [109]. Furthermore, 4.4 can be represented as follows

$$P(D \mid \alpha, \beta, M) = \frac{P(D \mid \ w, \beta, M).P(w \mid \alpha, M)}{P(w \mid D, \alpha, \beta, M)} \tag{4.6}$$

$$P(D \mid \alpha, \beta, M) = \frac{Z_F(\alpha, \beta)}{(\frac{\pi}{\beta})^{\frac{n}{2}} . (\frac{\pi}{\alpha})^{\frac{m}{2}}} \tag{4.7}$$

where n is the number of observations, and m is the total number of network parameters. Furthermore, the parameter, $Z_F(\alpha, \beta)$ depends on the Hessian of the objective function,

$$Z_F(\alpha, \beta) \propto \frac{e^{-F(w_{map})}}{\sqrt{|H_{map}|}} \tag{4.8}$$

where the subscript map indicates maximum a posteriori. The Hessian matrix (H) is calculated from the Jacobian (J)

$$H = J^T J \tag{4.9}$$

where the Jacobian Matrix contains the first derivatives of the network errors with respect to the synaptic weights and is matrix of dimension N n, where N is the number of network errors, and n is the number of synaptic weights. In the LevenbergMarquardt algorithm, the synaptic weights are updated as follows:

$$w^{k+1} = w^k - [J^T J + \mu I]^{-1} J^T e \tag{4.10}$$

where k is the iteration number and μ is the damping parameter.

4.4.2 Model Development

Input variables in the model were geometric parameters and process parameters. Six variables were considered influential for the model development. Process variables were process temperature (P1 in K) and percent fraction of nitric acid content (P2 in %). Geometric variables were initial wire diameter (P3 in µm), die area (P4 in mm*mm), wire loop height (P5 in micrometers), and percentage filler content of the EMC (P6 in %). It was observed that the wire diameter reduction is minimum for 2:1 (52.38% nitric acid by vol.) acid combination at 100°C for all packages. Tables 4.5 and 4.6 show the inputs for the wire-reduction model and the shear strength model, respectively.

Table 4.5: Inputs for Wire Diameter Reduction Model

	Model Input	**Unit**
P1	Process Temperature	K
P2	Nitric Acid Content	Percent
$P1^2$	Square of Temp	K^2
$P2^2$	Square of Acid Content	$Percent^2$
P1*P2	Acid-Temp Interaction	
P3	Initial Wire Diameter	Micrometers
P4	Die Area	$micrometer^2$
P5	Wire Loop Height	microns
P6	Filler Content	Percent

Table 4.6: Inputs for Shear Strength Model

	Model Input	**Unit**
P1	Process Temperature	K
P2	Nitric Acid Content	Percent
$P1^2$	Square of Temp	K^2
$P2^2$	Square of Acid Content	$Percent^2$
P1*P2	Acid-Temp Interaction	
P3	Initial Wire Diameter	Micrometers
P4	Diameter of Ball Bond	Micrometers
P5	Wire Loop Height	microns
P6	Filler Content	Percent

When the acid chemistry deviates from this ratio on either side, the wire reduction increases and shows a parabolic pattern as observed in Figures 4.6, 4.7, and 4.23. Similar observation was made for the process temperature as shown in Figs. 10 and 19. To account for this trend, second-degree polynomial terms were introduced. They were square of % nitric acid fraction ($P1^2$), temperature ($P2^2$), and product of acid content and temperature ($P1 * P2$).

Framework of the network was the same for both models. In the case of the shear strength prediction model, the die area was replaced with the thickness of the ball bond. The die area did significantly affect the wire diameter reduction. However, in the case of shear strength change, size of the ball bond directly affects the shear strength of the CuAl interface.

4.4.3 Model Validation and Discussion

Figure 4.34 shows change in MSE between experimental and predicted reduction in wire diameter. MSE was minimum after 119 iterations and was stable for the calculated weights. Figure 4.35 shows a histogram of the residues from the ANN analysis. The nature of the histogram resembles a bell curve at the center, i.e., higher instances with less error.

Figure 4.34: MSE minimization during iterative training.

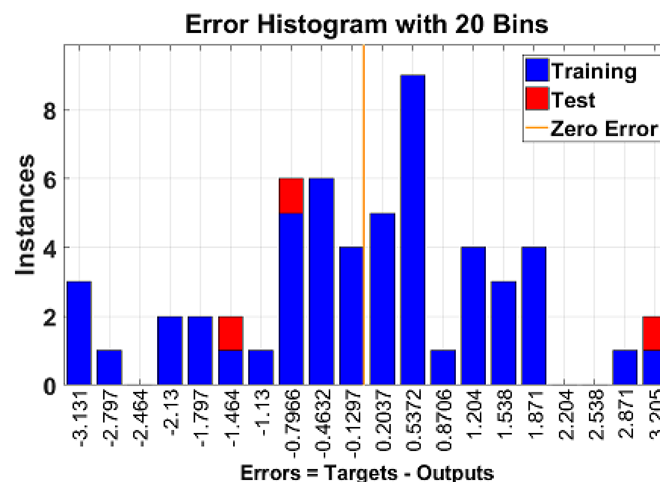

Figure 4.35: Error histogram from NN training using Bayesian regularization

Output of the predicted was then plotted against experimental percent reduction in wire diameter in Figure 4.36. Resulting data points were regressed using a linear line with r^2 value of 0.87, and predicted data are equally distributed along the diagonal fitted line. Average mean absolute error in the experimental and predicted values was 17.26%. MSE value was 1071.19. The fitted line makes an approximate diagonal line with either axis, proving that the model predictions are consistent with the experimental values.

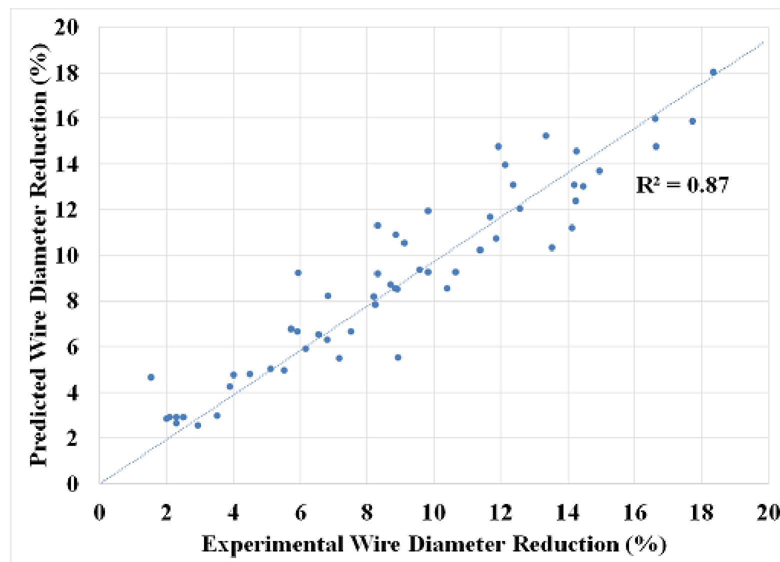

Figure 4.36: Comparison of experimental and predicted reduction in wire diameter

The nature of the experiments and variables involved in the model makes the decapsulation process highly nonlinear. Predictive model of percent wire reduction uses experimental wire reduction data from the wire loop part of the bond wire. This area has highest susceptibility to the combination of chemicals used and the temperature of the process. Temperatures selected in the decapsulation process affect the reaction rate and activity level of the acids. At higher temperatures, aggressive nature of the reaction damages the wirebond and results in higher wire reduction. At low temperatures (less than 100°C), acid activities are so slow that the decap process takes a long time and adversely affect the quality of the wirebond. Figure 4.37 shows experimental and predicted reduction in wire diameter for BGA packages decapped at different process temperatures using 2:1 acid combination. The plot shows that the predictive model was successfully able to follow the trend and have the minimum value of prediction at

373°C. Acid mixing ratio affects stability of the passivation layer around Cu wirebond and has great impact on the decap quality as discussed earlier.

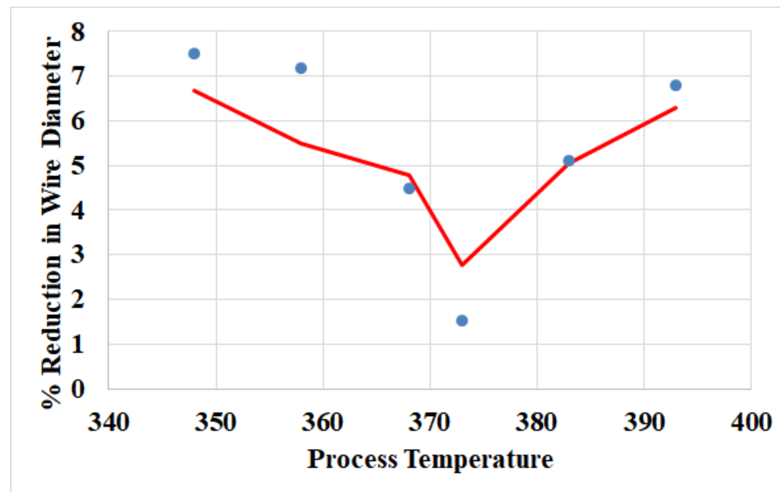

Figure 4.37: Variation in experimental and predicted wire reduction as a function of change in process temperature

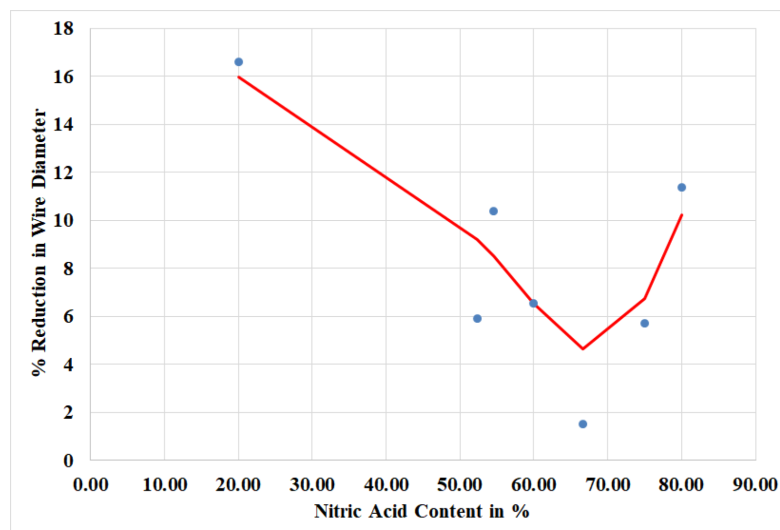

Figure 4.38: Variation in experimental and predicted wire reduction as a function of change in % nitric acid fraction

Lower nitric acid content yields more Cu sulfate ions, which act as a passivation layer, but also makes decap process very slow. Cu sulfate ions are very unstable and break down easily in a short amount of time. This causes delayed attack of nitric acid on Cu wires and corrodes them. Fraction does not form a complete layer of passivation, which makes wirebond corrosion-prone. If the nitric acid content in the mixture is very high (4:1), high concentration

and volume of nitrate ions can break down the passivation layer and cause corrosion. Figure 4.38 shows experimental and predicted reduction in wire diameter for BGA packages when process temperature was 373°K, and acid ratio was varied from 20% nitric acid to 80% nitric acid. The predicted values closely followed the experimental data, which is consistent with the discussion presented earlier. The model was successfully able to predict the optimum point at which the wire reduction is minimum. Figure 4.37 and Figure 4.38 prove the robustness of the predictive model and its ability to track the different trends observed in the experimental data.

Figure 4.39 shows MSE minimization plot during the training of predictive model for shear strength. Minimum MSE during the training phase was observed after 219 iterations and was stable for all next iterations. Figure 4.40 shows the residual plot of predicted and the experimental data. Residue frequency was centered very near to zero. There were only two points with large residue that were categorized as outliers. Fig. 41 shows a plot of experimental shear strength against shear strength predicted by the model. Most of the data are concentrated along the diagonal lines, except for a few outliers. r^2 value of the fit was 0.984. Average mean absolute error in the experimental and predicted values was 1.90%. MSE value was 32.72. The fitted line makes an approximate diagonal line with either axis, proving that the model predictions are consistent with the experimental values.

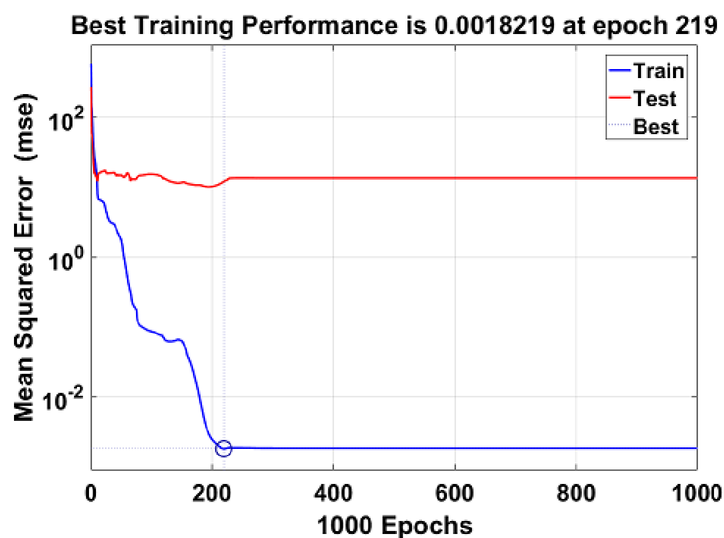

Figure 4.39: MSE minimization during iterative training

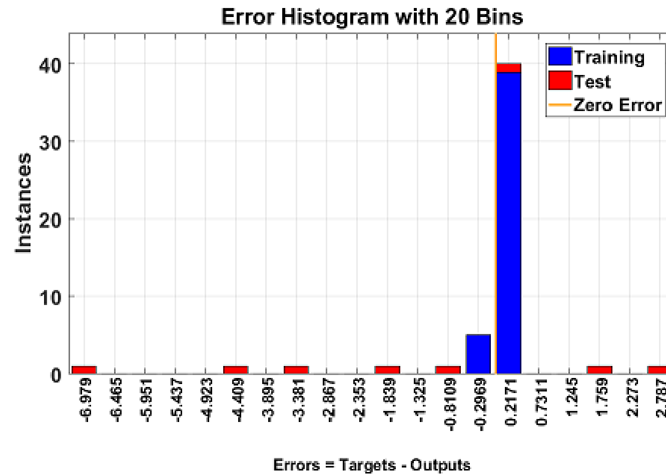

Figure 4.40: Residual plot of ANN

Different acid combinations and temperatures can corrode the interfacial Cu or Al, resulting in weaker bond. At higher process temperatures, sulfuric acid becomes highly reactive and can break the diffusion layer of aluminum oxide from the surface of the aluminum pad. Hence at higher temperature, corroded Al pads were found in this paper, as reported earlier. Depending on the severity of corrosion, the Al pad beneath the pad can be completely consumed 150°C or partially corroded. Partially corroded bonds will have lower shear strength because of lack of mechanical integrity. At very low temperatures, Cu wire gets highly corroded. As the acid stays in contact with the wire for a long time, it starts to consume the Cu from the junction point, weakening the ball bond.

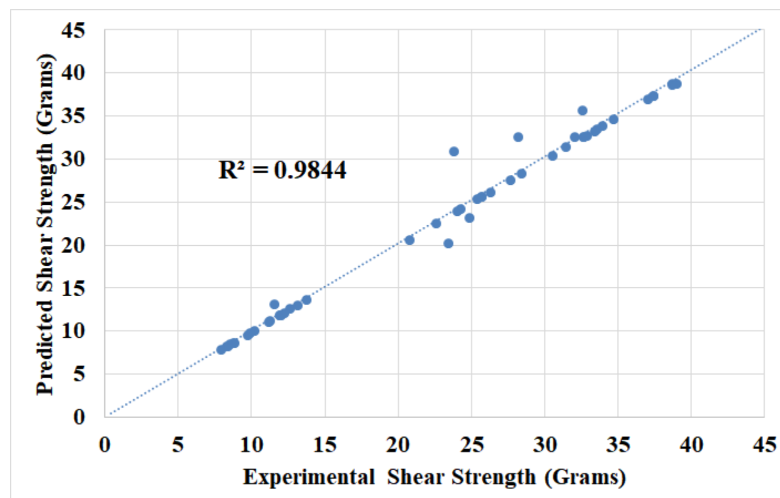

Figure 4.41: Comparison of experimental and predicted ball shear strength

Figure 4.42 shows the experimental and predicted shear strength for BGA packages. All packages were decapped with 2:1 acid combination, at various process temperatures. The model prediction was successfully able to follow the trend observed in the experimental data with accurate prediction of the maximum value of shear strength at 373°K. When the nitric content in the acid mixture reduces, or sulfuric acid content increases, higher pad corrosion is observed. Higher sulfuric content increases chances of passivation layer of Al pad being attacked and broken down by sulfuric acid, hence reducing the shear strength. How- ever, if there is too much nitric acid in the solution, it can corrode the Cu wire and adversely affect the shear strength. This behavior was observed when the 32-pin CSP was decapped at 373°K, using various acid combinations as shown in Figure 4.43. The ANN-based model could accurately predict the maximum value of shear strength along with the trend observed on either sides of the 2:1 acid combination. ANN-based models for prediction of reduction in wire diameter and change in shear strength predicted the experimental data with high r^2 value. The ability of both models to follow the trends observed in the data set for process parameters ensures robustness of the model.

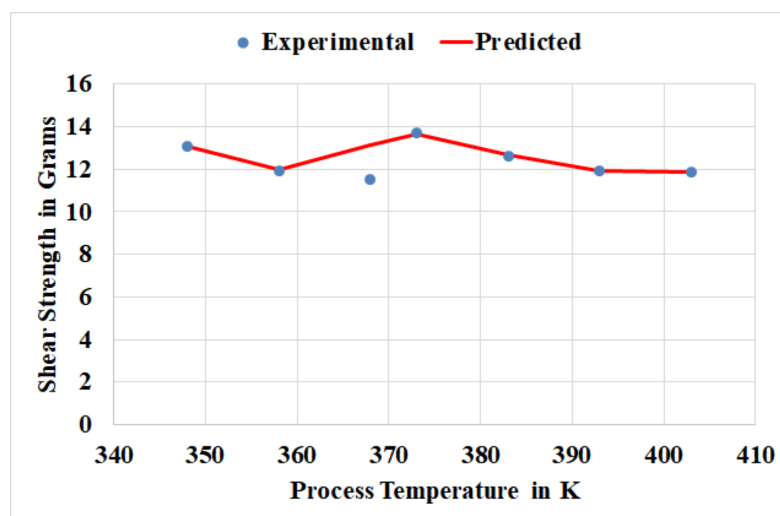

Figure 4.42: Variation in experimental and predicted ball shear strength as a function of change in process temperature

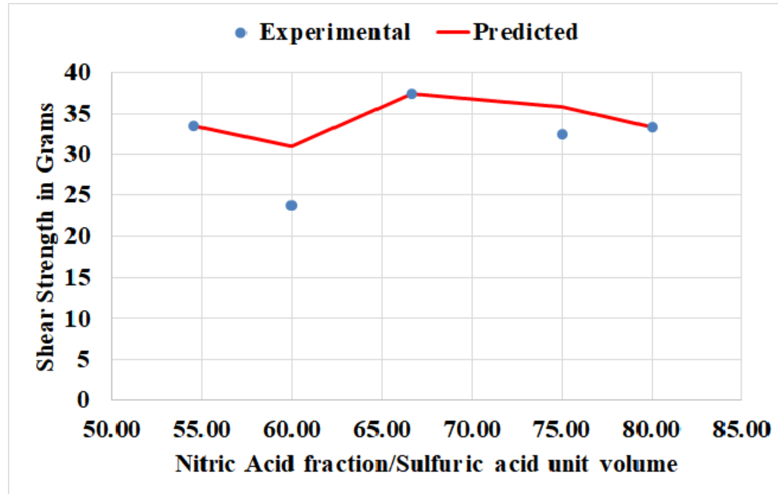

Figure 4.43: Variation in experimental and predicted shear strength as a function of change in % nitric acid fraction

4.5 Summary and Conclusions

This section shows successful implementation of the ANN- based regression analysis approach for evaluation of effect of decap parameters such as acid ratio, process temperature, and package variables such as wirebond diameter, die size, percent filler content of EMC, and wirebond loop height on wire diameter reduction and shear strength change. The model was validated experimentally for packages with different EMCs. Different acid combinations at different temperatures were tested on two test dies, and then on two active devices having bare CuAl interconnect, molded with different EMCs. Ball shear strength of post-decapped parts was measured and compared to the industrial standard of 5.5 gf/mil^2. Ball shear tests were used as a measure of degradation of CuAl bond and corrosion of Al pad. It was found that 2:1 ratio of nitric- to-sulfuric acid at 100°C performed the best and had highest shear strength. Typically for less corroded wires, higher shear strength was observed. The models were validated with an average absolute error of 17.26% and 1.90%, respectively. ANN with Bayesian regularization models were not only able to predict the experimental data over a wider range, but were also able to follow the parabolic nature of the dependence of the process variables on the post-decap quality of the Cu wirebonds.

Chapter 5

Life Prediction Model for The Interaction of Operating Conditions, EMC Formulation and Applied Bias for Cu Wirebonded Devices

5.1 Overview

The migration of high-reliability applications requiring sustained operation in harsh environments needs a better understanding of the acceleration factors under the stresses of operation. Prolonged exposure of the copper wire to elevated temperatures results in growth of excessive intermetallics and degradation of the interface. Behavior of Copper wirebond under high current-temperature conditions is not yet fully understood. Exposure to high current may induce Joule heating and electromigration, and thus significantly increase the degradation rate in comparison with low current operating conditions. Further, the accelerated test results of unbiased conditions cannot be used for life prediction of such high powered parts. EMCs used for encapsulation of the chip and the interconnects may vary widely in their formulation including pH, porosity, diffusion rates, levels and composition of the contaminants. Selection of different materials, such as EMC used in the molding process plays key role in defining lifetime for wirebond system. There is need for predictive models which can account for the exposure to environmental conditions, operating conditions and the EMC formulation in order to be realistically representative of the expected reliability. In this chapter, a set of parts, molded with different EMCs were subjected to high temperature-current environment (temperature range of $150°$C-$200°$C, 0.2A-1A). An artificial neural network (ANN) driven predictive model for estimation of the beta-sensitivities of the input variables has been developed for computation of the acceleration factor for the Cu-Al WB under high voltage and high temperature. Prognostics model for Cu WB subjected to high temperature-humidity environment is also presented.

A set of parts were subjected to high temperature- high humidity environment. Resistance, change in shear strength and shear failure modes were monitored during this study. Resistance spectroscopy was used for accurate measurement of resistance. Ball shear tester was used to calculate change in shear strength. This data was used to identify leading indicator of failure and prognostics matrix was developed for prediction of remaining useful life based on extended kalman filtering (EKF) technique.

5.2 Test Vehicle

In this study, 32 pin QFN devices molded with different molding compounds have been used for the study of Cu-Al WB reliability. All packages had 1-mil Cu wire bonded on $0.9\,\mu m$ thick Al pad.Optical and X-ray image of the package is shown in 5.1. There are 32 wirebonds in each package. The daisy-chained pattern includes two wirebonds are connected to each other on the silicon-chip, forming a connected wirebond pair. Detailed dimensions of package are listed in Table 5.1. Packages were molded with six different molding compounds. Molding compounds were from different suppliers, and have different mechanical and chemical properties. Properties of EMCs including filler content, pH, glass-transition temperature, and the Cl-concentration are listed in Table 5.1. EMC-A has excellent moldability and is suitable for high temperature applications. EMC-B is intended for fine-pitch applications, has low warpage, and exhibits excellent crack resistance. EMC-C has high thermal conductivity and humidity resistance. EMC-D is upgraded version of B, with excellent flammability, moldability and crack resistance. EMC-E is high temperature high stability molding compound with low ionic contamination. EMC-F is silicone based molding compound, suitable for high voltage applications. It has high thermal and mechanical stability. All packages were post mold cured at $175°C$ for four-hours.

Table 5.1: Package Dimensions

Parameter	Dimensions (mm)
Width	5.02
Length	5.02
Height	1.52
Pitch	0.5
Wire Diameter	25.4 μ
Pad Thickness	0.9 μ

Table 5.2: Properties of Molding Compound

EMC	Filler Content (Percent)	Cl Conc (ppm)	pH	Tg (C)
A	86	10	6	180
B	82	7	6	120
C	89	5	6.2	150
D	87	5	6.5	220
E	80	3	7.4	213
F	74	1	7.6	250

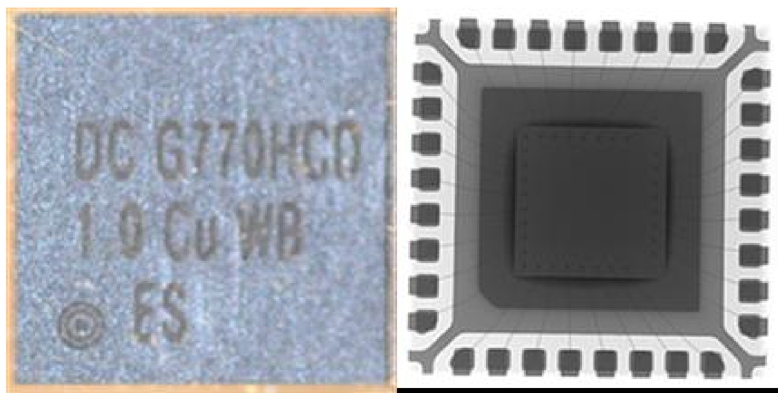

Figure 5.1: 32 Pin QFN

A two-layer, high Tg, FR4 PCB was designed so that all wirebonds are connected in series on each side of the package. Parts were mounted using SAC 305 solder paste. Fabricated assembly is shown in Figure 2. Daisy-chained channels A, B, C, and D were then connected so that all 32-wirebonds were in series. Five such packages were connected to 30V, 5A DC power supply with constant voltage setting to avoid current surge in case of abnormal failure.

5.3 Test Protocol

To ensure the repeatability of the fabrication process, resistance of the fabricated daisy chained devices was measured before the aging started. Figure 4 5.2 show the time- zero box-plot for all the Mean values of the initial observed resistance and Figure 5.3 shows normal distribution of the data set. Black lines in the figure shows 95% CI. Mean resistance of the packages was 4.48Ω with standard deviation of 0.26Ω. Due to the daisy chained pattern of the packages, a current of 0.19A flows through the package in presence of 2.5V bias. Current amplitude caused an increase in temperature of the package. This increase in temperature was quantified using thermocouples placed exactly on top of the packages. Figure 5.4 shows change in the temperature of the package when power is turned on with the packages exhibiting an increase of 13°C to 16°C depending on the configuration. In the powered-off state, the temperature of the package is same as temperature set on thermal chamber. Once the part is powered up, temperature of the package increased by 13°C when ambient temperature was 150°C. The package exhibited a higher increase of 16°C when ambient temperature was at a higher ambient value of 175°C. A higher temperature increase at a higher ambient temperature is expected as the resistance increases with the increase in temperature, resulting in a higher joule heating under identical current conditions. Duty cycle of 0.5 was used. During the testing, packages were powered on for 1 hours, and powered off for 1 hour. This cycle was repeated till the end of the testing. In the result section, ambient temperature of the package is used to describe test condition.

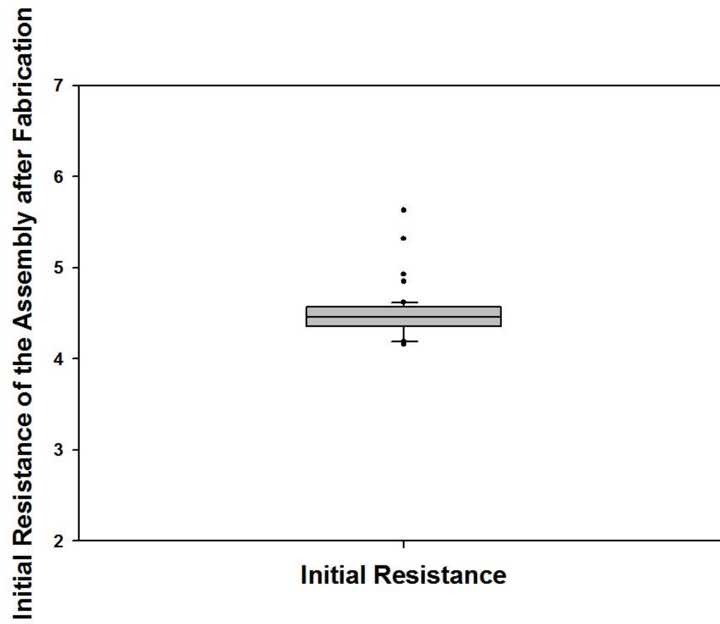

Figure 5.2: Box Plot of the Time-Zero Resistance of the packages

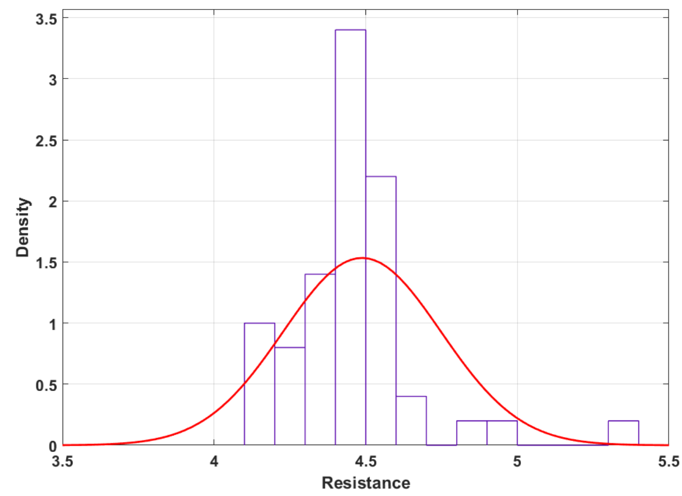

Figure 5.3: Distribution of Time-Zero Resistance of the packages

Table 5.3: EMCs and Respective Test Conditions

	Voltage Bias		No Bias			
EMC	150C	175C	150C	175C	180C	200C
A	Y	Y	Y		Y	Y
B	Y	Y	Y	Y		Y
C	Y	Y	Y	Y		Y
D	Y	Y	Y		Y	Y
E	Y	Y	Y		Y	Y
F	Y	Y	Y		Y	Y

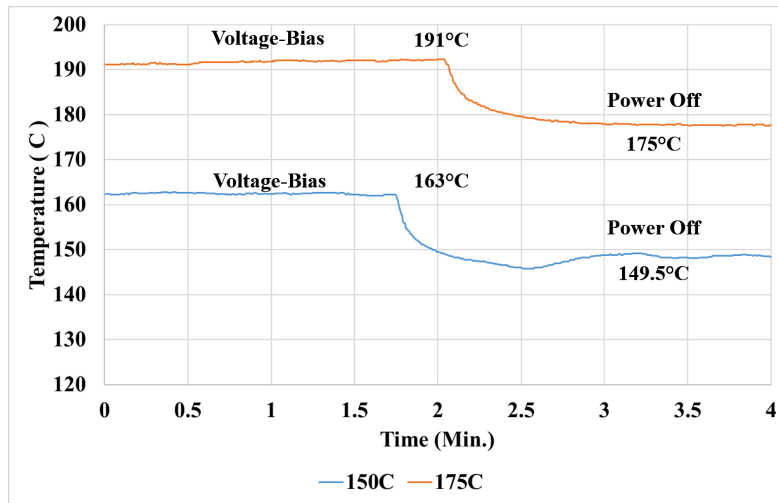

Figure 5.4: Package heating due to Joule heating

5.4 Test Matrix

Samples were exposed to high temperature in the automotive operating range of 150°C to 200°C both with bias and without bias. The test temperatures for the experiment are well below the maximum rated temperatures for EMCs to avoid over-stress failures that are not representative of normal operation. Applied voltage was 2.5V for all packages at different temperature conditions. Table 5.3 provided below shows temperature and bias conditions for all the EMCs.

Packages were taken out at periodic time intervals. Resistance was recorded with resistance spectroscopy technique. Parts were then decapsulated using acid chemistry described in earlier chapter. DAGE 2400 ball shear tester was used to perform ball shear test. Shear tool

height was set to be 2.5 µm above aluminum pad. Shear tool speed was 150 µm/s. 32 wirebonds were sheared for each reading interval. Sheared surface was then analyzed using SEM. Failure threshold for the part was decided as 20-percent change in resistance. Once the part failed, SEM and EDX techniques were used to analyze morphology at the bond-pad interface. To measure IMC thickness, the number of pixels in the IMC area were calculated with the help of image processing software. Dividing the area by length of the IMC bond interface was used to calculate the average thickness of the IMC. Summarized process is shown in Figure 5.5. Change in electric response of the package was then correlated with change in morphology of bond wire interface.

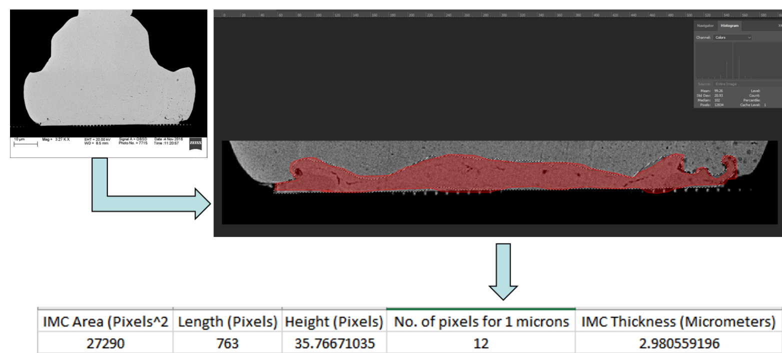

IMC Area (Pixels^2	Length (Pixels)	Height (Pixels)	No. of pixels for 1 microns	IMC Thickness (Micrometers)
27290	763	35.76671035	12	2.980559196

Figure 5.5: IMC Thickness Measurement

To study effect of high temperature and humidity condition, accelerated testing methods were chosen. Instead of traditional highly accelerated stress test (HAST) testing (130°C/85% RH) Parr bomb test, which is harsher than the prior one was chosen. Parr bomb apparatus is a closed pressure vessel, in which 100% relative humidity could be achieved even at higher temperatures. PTFE cup was half way filled with de-ionized water and packages were placed in the fixture in such a way that they are not immersed in water, but will come in contact with the steam that is generated due to higher temperatures. Packages were subjected to harsh environments of 130°C/100% RH. Packages were taken out at periodic time intervals and resistance of the wirebond pairs was measured using highly sensitive resistance spectroscopy technique. Ball shear test were performed along with cross-section after failure.

5.5 Experimental Results for High Temperature Tests

5.5.1 Failure at Cu-Al Interface

Resistance data, shear strength data and C/S analysis is explained in detail below for EMC A subjected to 2.5V bias at 175°C, and 185°C unbiased condition. Figure 5.6 shows increase in the resistance of the package in presence of bias. Significant resistance increase was observed only after aging for 144 hours. This trend continued and package failed (more than 20% increase in resistance was observed) after 620 hours of aging. Ambient temperature for the unbiased test (185°C) was higher than that of biased test (175°C).

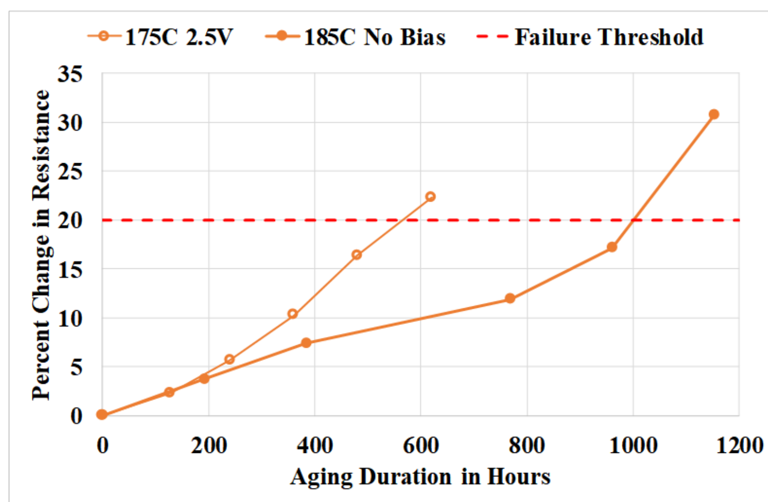

Figure 5.6: Change in resistance of the package molded with EMC A

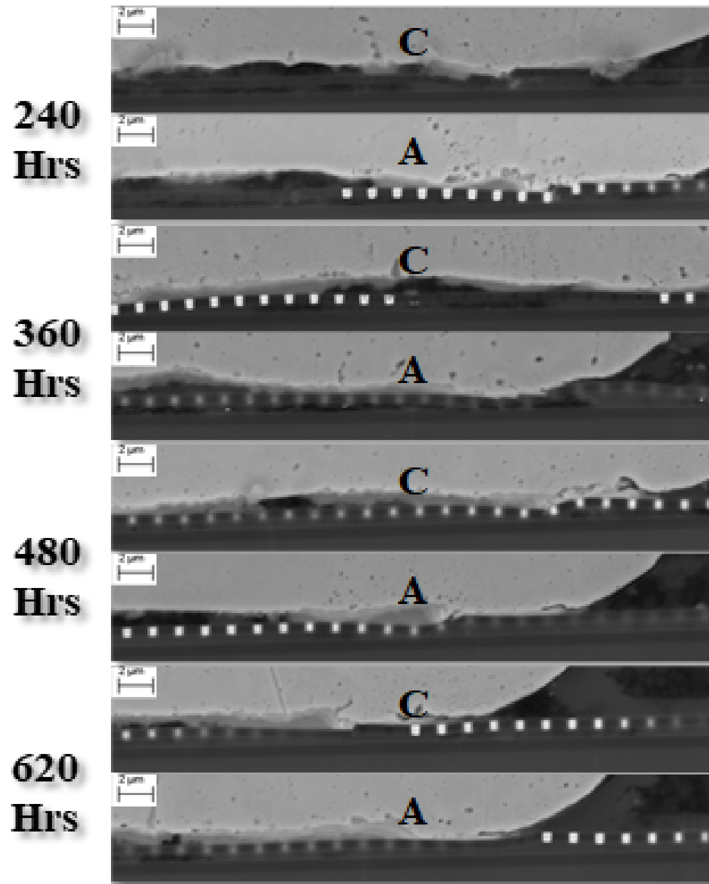

Figure 5.7: Evolution of the morphology of Cu wirebond-Al pad junction with bias

However, parts sustained nearly 1200 hours of aging before failure was observed. Rate of increase in resistance was slow for unbiased test form the beginning. Rapid degradation of the wirebond at lower ambient temperature can be solely contributed to presence of applied bias. Parts subjected to both tests were cross-sectioned at each time interval. Figure 5.8 shows the change in morphology of the bond pad with bias. Figure 5.9 shows change in morphology of the bond-pad interface without bias. In each micrograph, C denotes cathode and A denotes anode. One pair of each reading interval is shown in the picture. Since there is not anode or cathode in unbiased test, only one micrograph per data point is shown. As the aging duration increases, IMC thickness also increased. IMC thickness of the parts was measured by analyzing number of pixels present in the area, as explained earlier. Figure 5.10 shows the change in the thickness of the IMC due to the combined effects of high temperature and current flow as a function of duration of operation. Thickness of the IMC was in the neighborhood of $0.8\,\mu m$ at failure. thickness was calculated separately for wirebonds functioning as a cathode as well as anode.

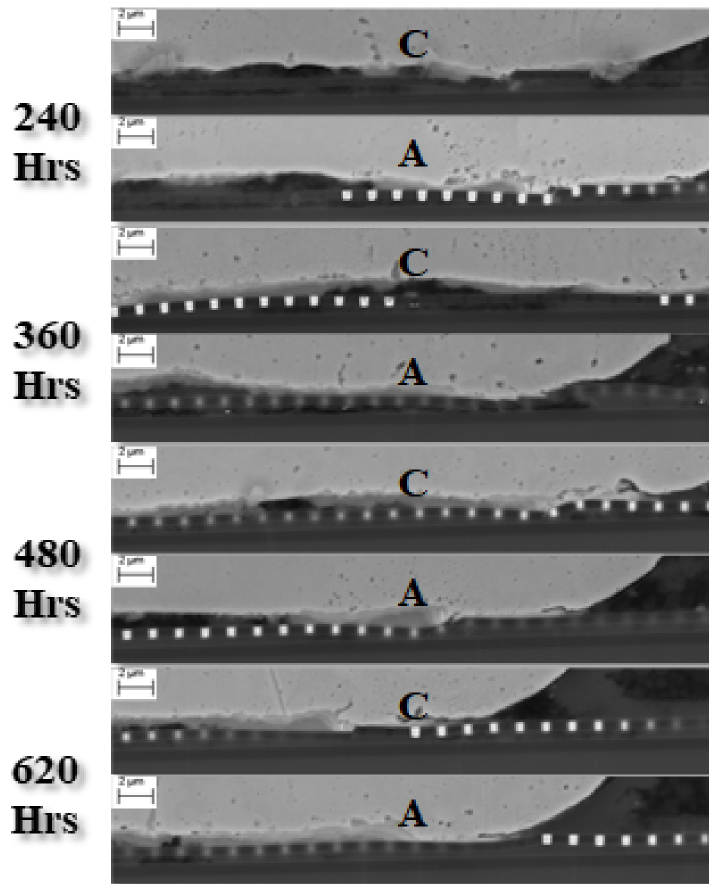

Figure 5.8: Evolution of the morphology of Cu wirebond-Al pad junction with bias

After 620 hours of operation at high temperature under bias, the average difference between thickness of the anode and cathode was $0.02\,\mu m$, i.e., about 3-percent of the thickness of the IMC observed for that data point. The difference was much smaller for the prior data points. At time zero condition, no such phenomenon was observed. For unbiased testing, not much IMC thickness variation was observed. At the time of failure, much thicker IMC ($1.05\,\mu m$) was observed. Absence of bias in this case, did not accelerated the degradation process, hence sustained IMC growth was observed for much longer time when compared with biased tests.

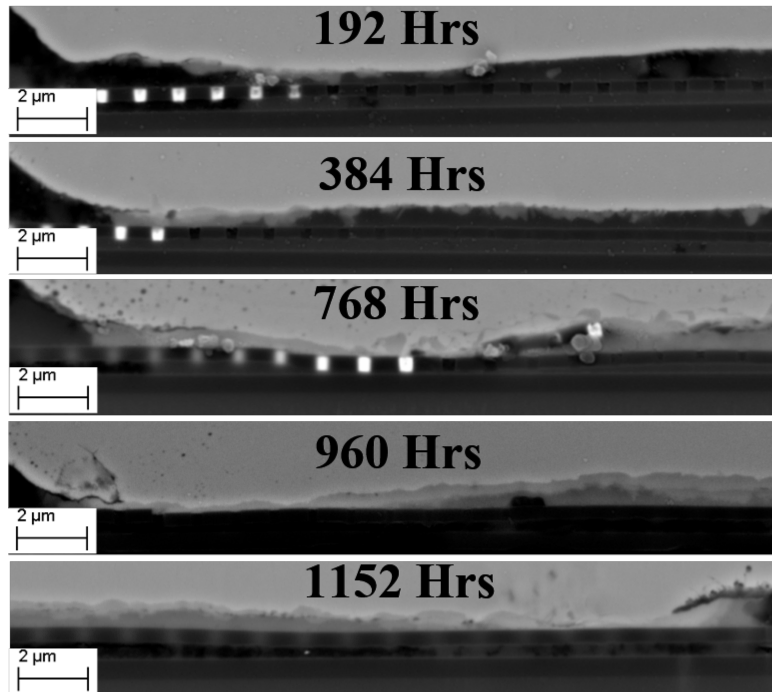

Figure 5.9: Evolution of the morphology of Cu wirebond-Al pad junction Without Bias

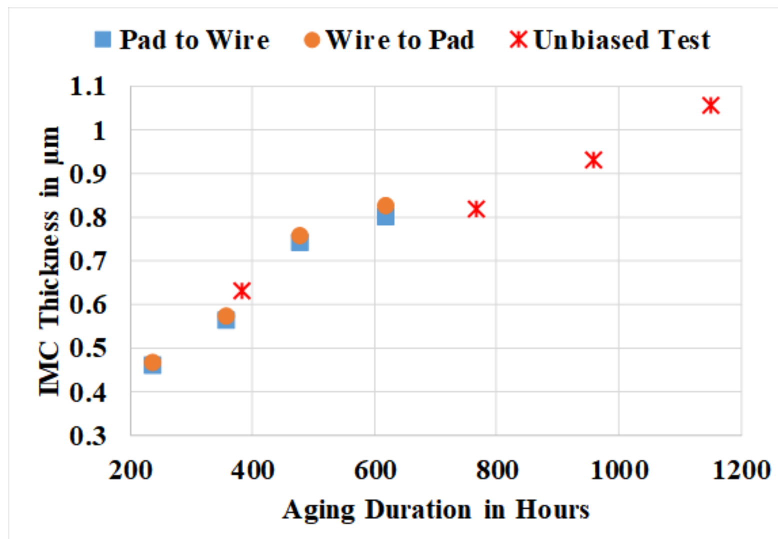

Figure 5.10: Increase in the IMC thickness for EMC A

The difference in the direction of current flow produces a change in the thickness of the anode and the cathode. In anodes, the electrons flow from wirebond to the bond pad. Even though the current density of 5.2x10^3A/cm^2 is not very high, the momentum of the electron wind aids diffusion and accelerates the formation of IMC at the anode. On the contrary, at the cathode, the electrons flow from pad to wirebond, which opposes the diffusion of the heavier

Table 5.4: EDX Analysis Result at point A, B and C

Elements	Atomic Content		
	A	B	C
Al	30.96	48.64	50.63
Cu	65.48	47.91	27.18
Si	-	-	18.40
Au	3.56	3.45	3.79

atoms into the lighter atoms. The opposing direction of current flow with respect to the direction of diffusion, results in a slower growth of IMC at the interface. Similar behavior has been noted earlier [22], [21].

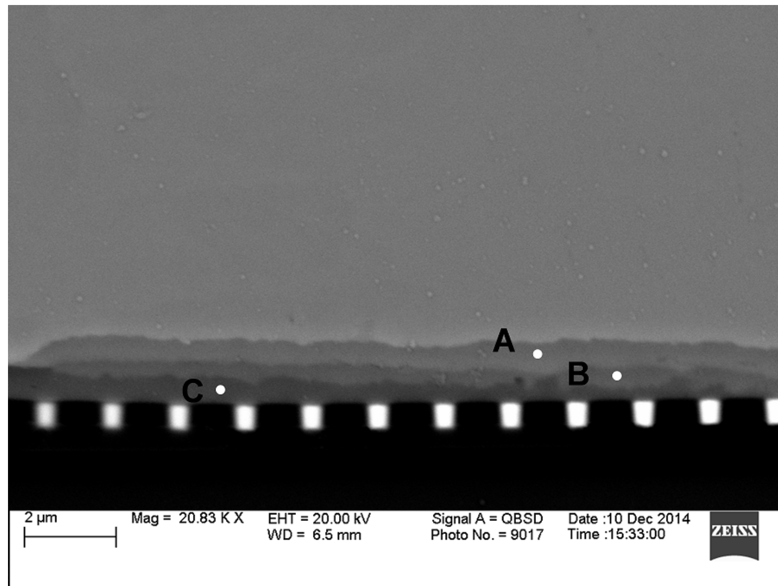

Figure 5.11: EDX Spot Analysis

During analysis, three distinct phases of IMC were found. EDX analysis was performed to analyze the phases and understand their composition. Figure 5.11 shows sample cross-section at 240 hours of thermal aging. Three white points, A, B and C are the points on which EDX analysis was performed. Results of percent atomic content at each point are tabulated in Table 5.4. Analysis shows that point A, which is near Cu ball is copper rich phase with composition Cu_9Al_4, point C, which is near Al pad, is aluminum rich phase with composition $CuAl_2$. Phase in between those two, point B is CuAl phase. These results are consistent with previously published literature.

Table 5.5: EDX Analysis Result at Crack Tip

Elements	Atomic Content			
	A	B	C	D
Cu	9.31	20.85	68.64	66.27
Al	54.34	40.18	31.36	14.99
Cl	-	-	-	0.30
Si	13.19	16.69	-	3.89
O	21.96	22.27	-	14.55
W	1.20	-	-	-

Formation of peripheral cracks precedes the failure of the wirebond interconnect, as shown in Figure 5.9 for cathode. The cracking initiates at the periphery of the ball bond, and propagates towards the center with the time in operation at temperature under bias. The location of the crack is between the bulk Cu wire and the topmost IMC phase as shown in 5.12. EDX analysis was performed to find the IMC formulation. Table 5.5 shows the results of the EDX analysis. Two distinct IMC phases were found. Composition of the Al rich phase (Point B) was found to be $CuAl_2$ and that of Cu rich phase was Cu_9Al_4 (Point C). EDX analysis as crack front (Point D) confirmed the presence of the Cl and oxygen. This implies that the peripheral cracking is accompanied with corrosion. Cl- ions released due to degradation of the EMC attracts towards positively charged cathode. In presence of Cl- ions, corrosion initiates at the periphery of the ball bond and then propagates via Cu_9Al_4 IMC layer. These findings are consistent with the published literature [4], [36], [44], [97].

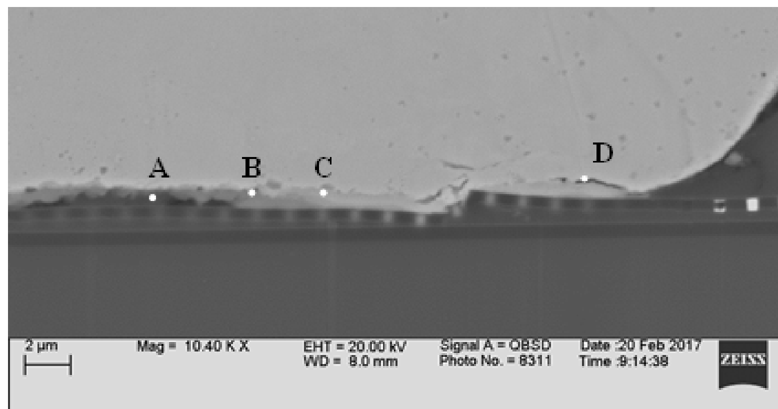

Figure 5.12: EDX Spot Analysis

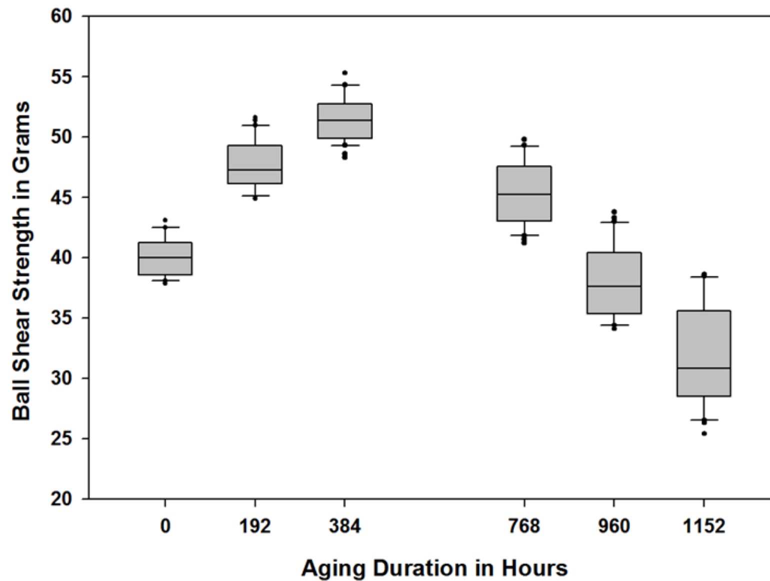

Figure 5.13: Change in shear strength of WB subjected to unbiased test conditions

Figure 5.13 shows evolution of shear strength for package subjected to unbiased aging. Shear strength at the start was around 40grams, and it went up till around 53 grams after 348 hours of thermal aging. After it started dropping drown rapidly, and after failure it was in the vicinity of 30 gram force. The highest peak in the plot is at 5% change in resistance. Sheared surface were analyzed using SEM to identify shear failure modes. Two modes were observed during the study as shown in Figure 5.14. Mode I showed very small or no residue of Cu or IMC on sheared surface. Al pad was peeled off during shear test, ensuring strong mechanical bond between Cu and IMC. Mode 2 on the other hand showed residues of Cu or Cu-Al IMC on sheared surface. The residues were concentrated along periphery of the ball bond. This means that link between IMC and Cu ball bond was the weak one, and was sight of failure. After excessive aging, a clean cut (no sign of peeling) was observed at the center of the ball bond. This is because of localized detachment. This is consistent with the peripheral cracking, and detachment that we found during cross-sectioning, as discussed earlier. The modes were then classified, and their plot is shown in Figure 5.15. Mode I was dominating initially, till 240 hours of aging. After that point, Mode II started to become dominating. This time frames resembles drop in shear strength and rapid increase in resistance. Initial increase in shear strength is caused by lateral growth of IMC. This growth makes bond stronger. However, due to excessive

growth and extended aging, interface starts degrading. During this phase, excessive cracking can be seen. This causes drop in shear strength with dominant mode II failure mode.

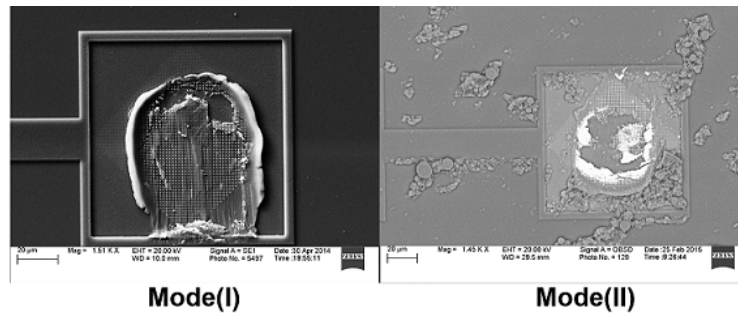

Figure 5.14: Shear failure modes for Cu Wirebonds

Figure 5.16 shows results of the shear test for the packages subjected to biased test conditions. Initial average shear strength of the device was 39.59 grams. during the initial stages of the aging, average shear strength increased up to 49.71 grams (240 hours of aging). The change in resistance was in the neighborhood of 5-percent and observed IMC thickness was 0.39 µm. The distribution of the shear failure modes and their evolution over time was then plotted and shown in Figure 5.17.

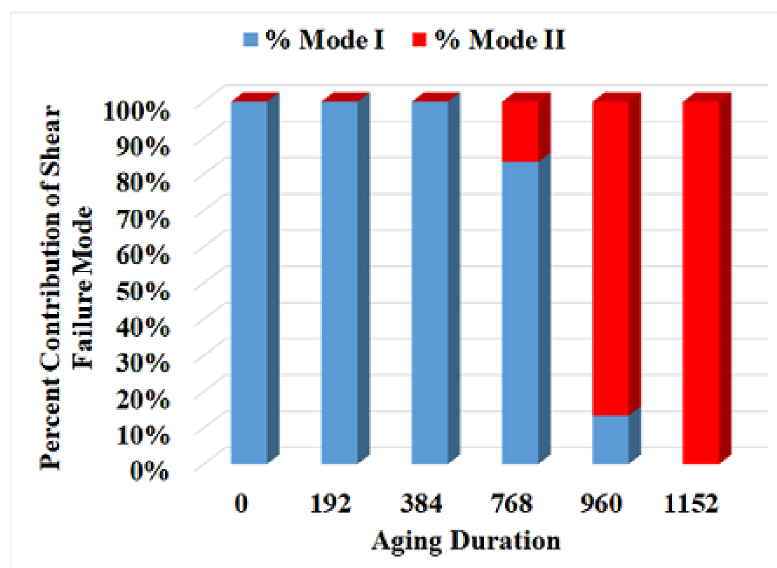

Figure 5.15: Distribution of Shear Failure Modes subjected to unbiased test conditions

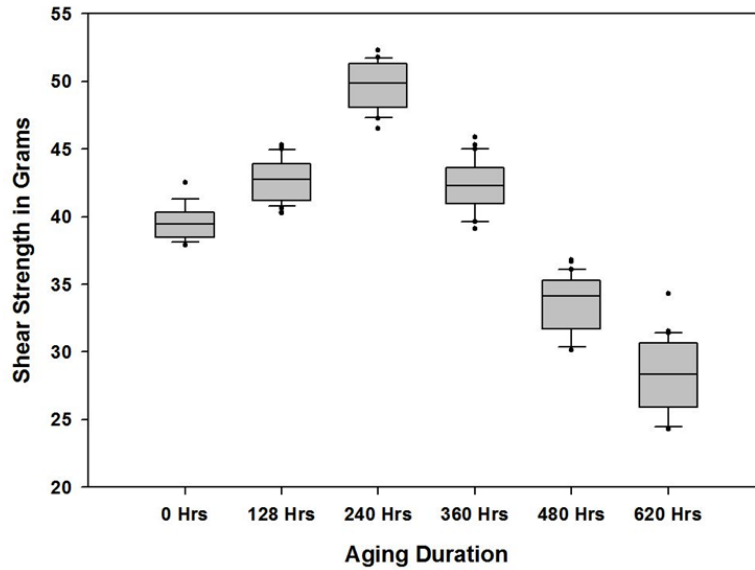

Figure 5.16: Change in shear strength of WB subjected to biased test conditions

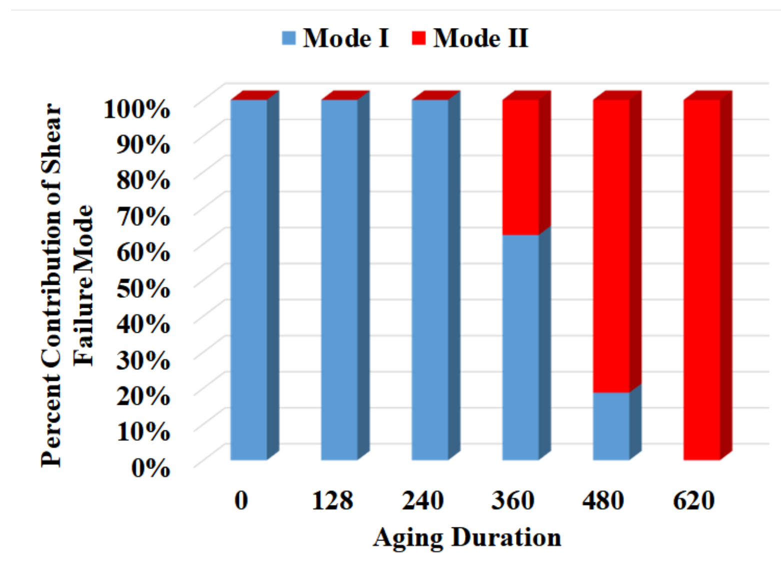

Figure 5.17: Change in shear strength of WB subjected to biased test conditions

Only mode I type shear failure mode was observed during the initial aging stage. The initial growth in the shear strength is due to growth of IMC with exposure to temperature which enhances diffusion at the Cu-Al interface and strengthens the bond. A drop in the shear strength was observed after 240 hours of aging. The drop is associated with high increase in resistance and peripheral cracking found during the cross-sectioning. The drop in the shear-strength is accompanied with predominance of mode II type failure. Peripheral residues observed on the shear surface confirms the presence of peripheral cracking. Clean lift in the center indicates a

completely corroded Al pad. The last-stage of failure exhibited an average shear strength of 28.22 grams, with predominantly Mode-II type shear failure mode.

5.5.2 Effect of EMC Formulation on the Cu-Al WB Reliability

The measurements of resistance and shear strength in accelerated tests of for all EMCs in the experimental matrix are presented in this section. Ambient temperature for biased test were 150°C and 175°C, whereas for the unbiased testing, they were 150°C, 185°C and 200°C.

5.5.2.1 EMC A

Figure 5.18 shows change in resistance of the packages molded with EMC-A subjected to accelerated tests. In the 150°C unbiased condition, packages failed after 4200 hours of aging. When the operating temperature was raised higher to 185°C without bias, the Cu-Al WBs failed in a shorter period after 1152 hours. When the operating temperature was raised even higher to 200°C without bias, the Cu-Al WBs failed in a shorter period after 600 hours. In contrast, with the presence of bias at 150°C (i.e., 163°C package temperature, when powered on), Cu-Al WBs failed after 1210 hours, almost 3x faster than the unbiased condition.

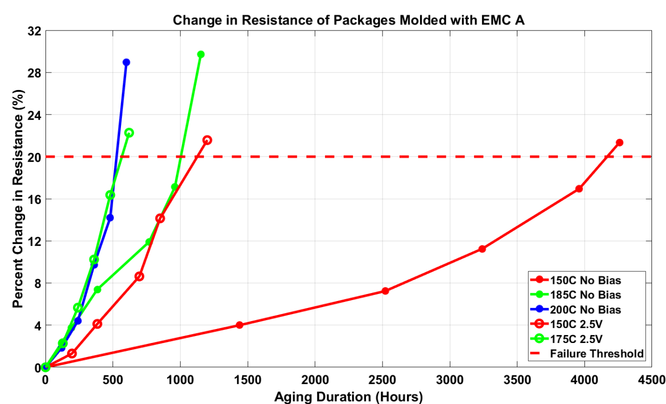

Figure 5.18: Change in resistance of packages molded with EMC A

A comparison of the failure times indicates that the failure time of the 185C without bias are comparable with the failure time of the 150°C with bias conditions. It is important to note that even when powered on, the 163°C maximum temperature of the package in the 150°C with bias condition, was 22°C lower than 185°C. Yet, both tests showed very small difference in

time to failure. This comparison of the failure times demonstrates the importance of bias in acceleration of the degradation processes in the Cu-Al WB system and the incidence of early failures. Similar pattern of failure progression was observed during biased testing at 175°C (peak temperature of package was 191°C when powered on). The Cu-Al Al WB failed after 620 hours of aging which was comparable with the result of 200°C unbiased test results. This underline importance of considering applied voltage bias very important factor when designing high reliability systems.

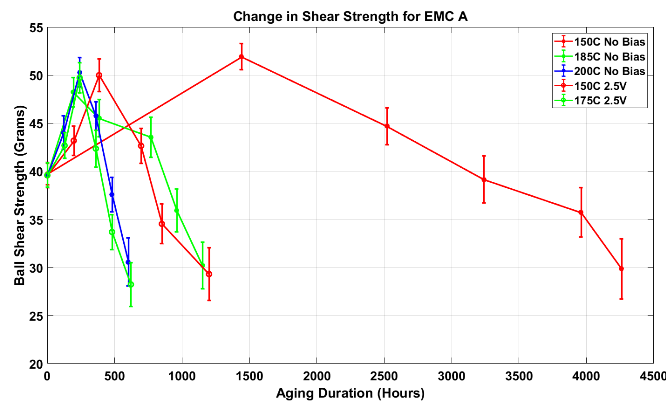

Figure 5.19: Change in Shear Strength of packages molded with EMC A

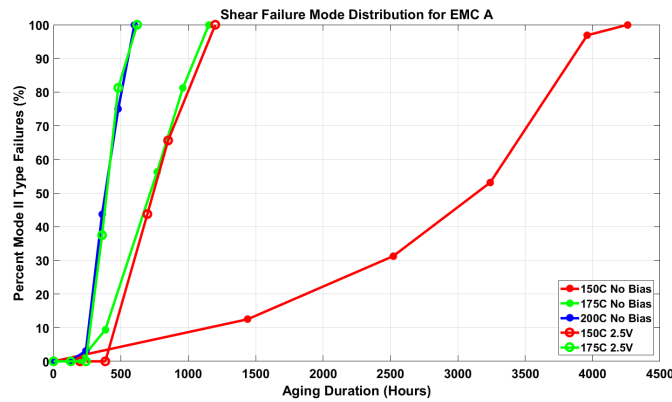

Figure 5.20: Evolution in Mode II Failure for EMC A

Figure 5.19 and Figure 5.20 shows change in shear strength and evolution of mode II type failure observed on to sheared surface. As discussed earlier, mode II type of failure is contributed to degraded wirebond and is dominant towards the end of the test. Increase in this type of failure mode was result of the reduction in ball shear strength. The trend was the same for biased as well as unbiased test conditions. At lower temperatures, IMC growth takes place

at much slower rate; hence it takes longer time for shear strength to reach the peak. For elevated temperatures, faster shear strength growth followed by rapid drop was observed.

5.5.2.2 EMC B

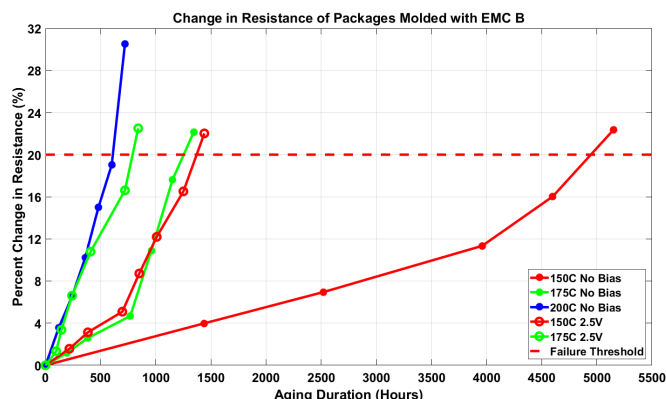

Figure 5.21: Change in Resistance of packages molded with EMC B

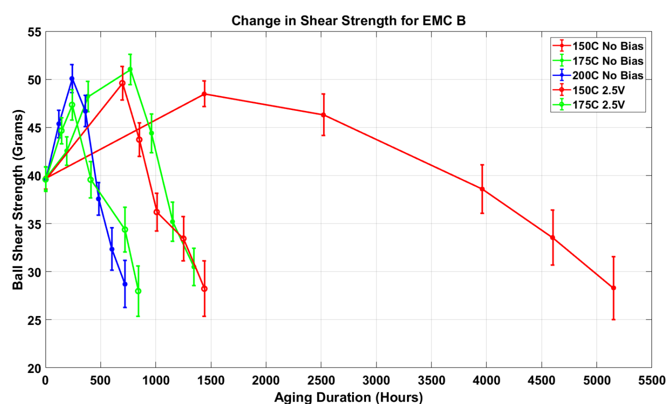

Figure 5.22: Change in Shear Strength of packages molded with EMC B

Figure 5.21 shows change in resistance of packages molded with EMC-B. The packages subjected to 150°C ambient temperature, unbiased condition, package failed after 5150 hours of aging. When the operating temperature was raised higher to 175°C without bias, the Cu-Al WBs failed in a shorter period after 1344 hours. When the operating temperature was raised even higher to 200°C without bias, the Cu-Al WBs failed shortly after 720 hours. In contrast, with the presence of bias at 150°C (i.e., 163°C package temperature, when powered on), Cu-Al WBs failed after 1210 hours, almost 4x faster than the unbiased condition. Figure 5.22

shows change in shear strength of the package under different temperature and bias conditions. Irrespective of the condition, shear strength initially increases due to lateral growth of IMC, followed by reduction in the shear strength. Depending on the environmental conditions, slope of increase and decrease were different.

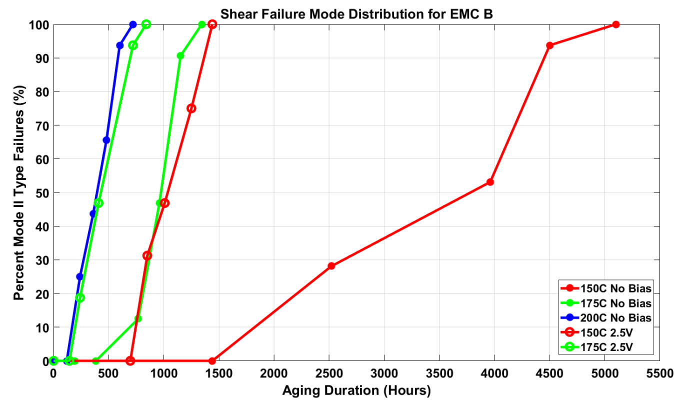

Figure 5.23: Evolution in Mode II Failure for EMC B

A comparison of the failure times indicates that the failure time of the 175°C without bias are comparable with the failure time of the 150°C with bias conditions. It is important to note that even when powered on, the 163°C maximum temperature of the package in the 150°C with bias condition, was 12°C lower than 185°C. Similarly, the failure times for the 175°C biased condition are comparable with the 200°C unbiased test condition. This trend was similar with the EMC-A as discussed earlier. However, samples with EMC-B did not fail as fast as EMC-A. The longer failure times in EMC-B can be attributed to lower ionic contamination and higher pH value of EMC-B. When parts were aged at 150°C ambient temperature, rate of change of resistance was steady for first 10% change, and it increased rapidly as the aging duration increased. Figure 5.23 shows distribution of shear failure modes over time. Similar to earlier observations, only mode II type failure was observed at the time of failure.

5.5.2.3 EMC C

EMC-C was high temperature molding compound with high thermal conductivity and humidity resistance. Change in resistance for the packages molded with EMC-C is shown in Figure 5.24. For the 150°C ambient temperature, without bias, the Cu-Al WB system packages

molded with EMC-C failed after 5600 hours. Rate of increase of resistance was relatively slower till 4000 hours of operation at 150°C, where only 7 percent increase in resistance was observed.

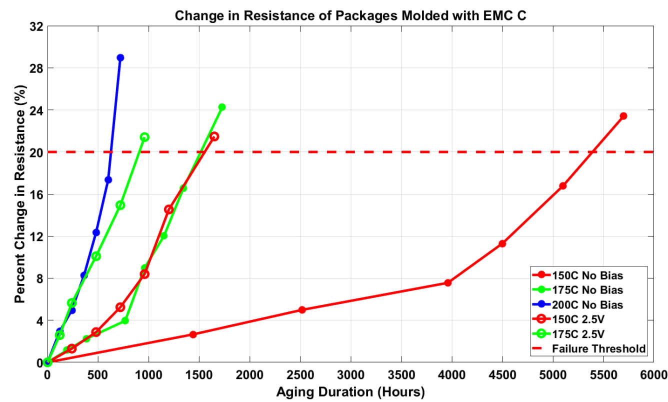

Figure 5.24: Change in Resistance of packages molded with EMC C

Under biased condition, for the same ambient temperature of 150°C, the Cu-Al WB system failed 3x faster, after 1650 hours of operation. Presence of applied bias significantly affected reliability of the packages. The fastest degradation rate was observed for the test condition of 200°C without bias with the Cu-Al WB system exhibiting failure within 780 hours. Packages failed after 1728 hours for ambient temperature of 175°C under unbiased condition. For biased case with same ambient temperature of 175°C, failure was observed after 960 hours of aging. For all temperature and bias conditions, rate of increase of resistance in the unbiased condition was slower when compared with the bias conditions for the same ambient temperature.

Figure 5.25 and Figure 5.26 shows change in ball shear strength and evolution of shear failure modes for packages molded with EMC C. Initial increase in ball shear strength was observed irrespective of the ambient temperature conditions. For lower temperatures, the rate of increase was much slower than other higher temperatures. As discussed in earlier sections, rate of IMC growth is very slow at lower temperatures. Initial shear strength growth is associated with increase in IMC thickness, hence at aging temperature of 150°C, max shear strength was observed only after 2500 hours of aging. During this phase, only mode I type of failure was observed. Mode II was observed as the shear strength started to drop down. At failure, only mode II was observed.

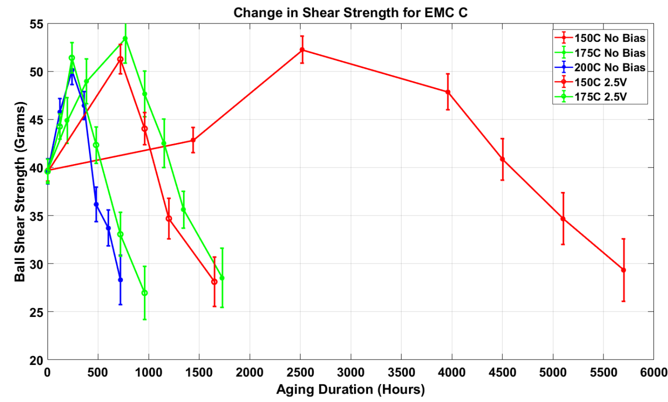

Figure 5.25: Change in Shear Strength of packages molded with EMC C

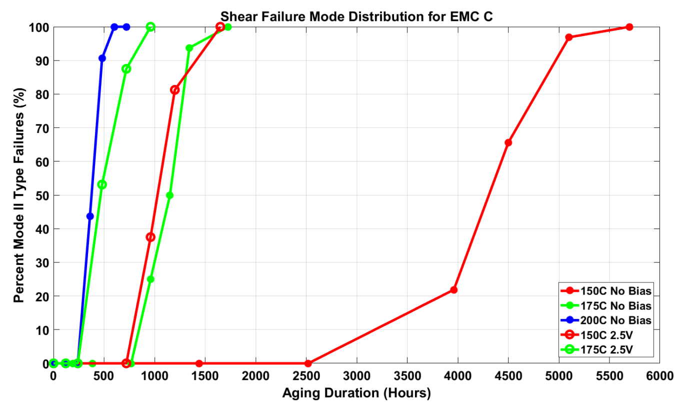

Figure 5.26: Evolution in Mode II Failure for EMC C

5.5.2.4 EMC D

Figure 5.27 shows change in resistance of packages molded with EMC-D subjected to different test conditions. The Cu-Al WB system failed after 1536 hours and 960 hours when exposed to ambient temperatures of 185°C and 200°C without bias respectively. The Cu-Al WB parts survived for 6250 hours under unbiased test at ambient temperature of 150°C. In comparison with EMC-A and EMC-B, the EMC-C had lower rate of change of resistance in response to the high-temperature environment. During biased test, at 175°C ambient temperature, the packages failed after 1030 hours of aging. The degradation rate for the 175°C biased test condition was faster than the rate observed for 185°C unbiased test. The influence of voltage on the reliability of Cu-Al WB can also be seen for ambient temperature of 150°C (biased test), where the package failed after 1760 hours of aging. For test conditions of 150°C (biased as

well as unbiased), and 185°C unbiased condition, the rate of increase of resistance was slower initially, exhibiting a 5-percent to 7-percent change. Even though EMC-C and EMC- D had very similar properties, the EMC-D exhibited a slightly better reliability performance under all tests in comparison with EMC-C owing to it near neutral pH value.

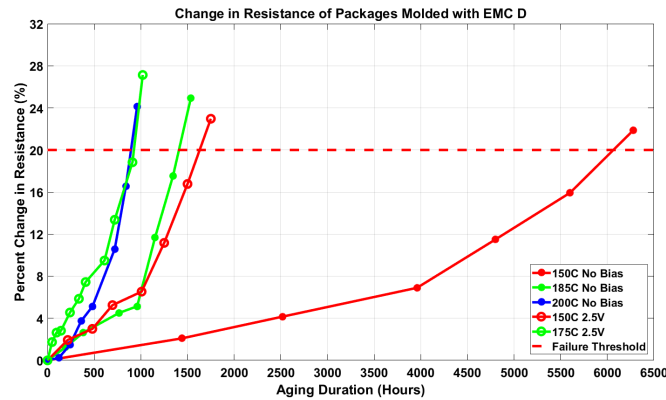

Figure 5.27: Change in Resistance of packages molded with EMC D

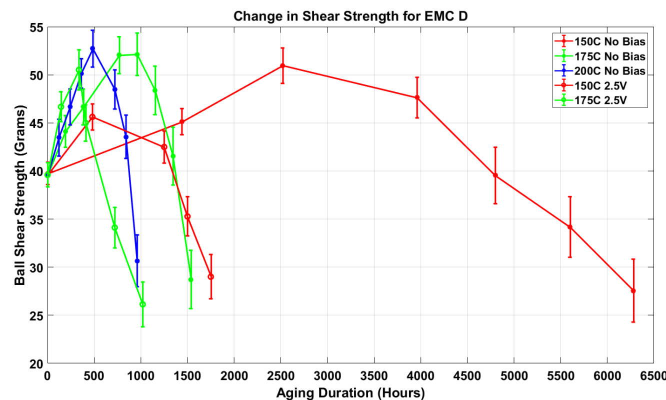

Figure 5.28: Change in Shear Strength of packages molded with EMC D

Figure 5.28 and Figure 5.29 shows change in ball shear strength and evolution of shear failure modes for packages molded with EMC D. Trends observed in the increase and decrease of shear strength along with increasing fraction of Mode II type shear failure were same as discussed for previous EMCs.

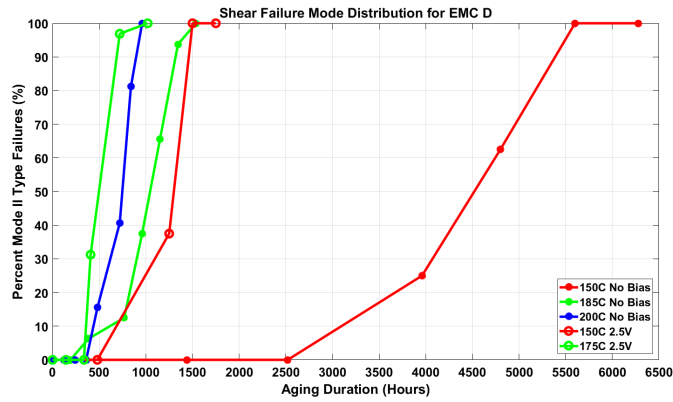

Figure 5.29: Evolution in Mode II Failure for EMC D

5.5.2.5 EMC E

Figure 5.30 shows change in resistance of Cu-Al WB system in packages molded with EMC-D subjected to different aging conditions. Figure 5.31 and Figure 5.32 shows change in ball shear strength and evolution of shear failure modes for packages molded with EMC E. After 7900 hours of aging, more than 20-percent change in resistance was observed at 150°C.

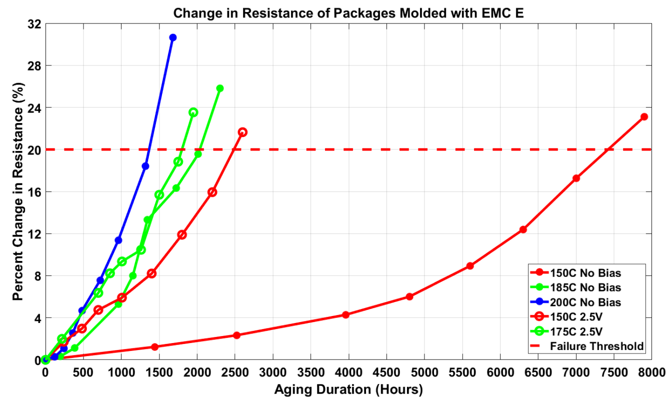

Figure 5.30: Change in Resistance of packages molded with EMC E

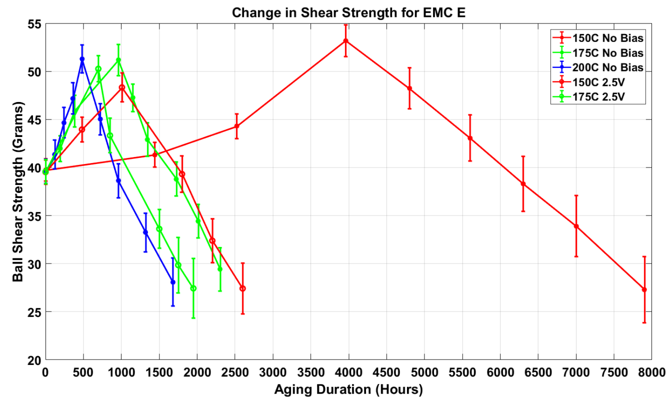

Figure 5.31: Change in Shear Strength of packages molded with EMC E

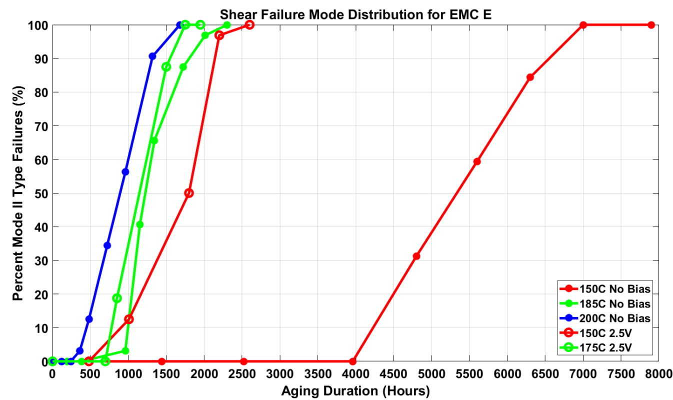

Figure 5.32: Evolution in Mode II Failure for EMC E

EMC-E had very low ionic contamination and near neutral pH value. Packages failed after 2304 and 1630 hours of exposure to unbiased 185°C and 200°C test conditions respectively. For biased tests, package failed after 2600 and 1944 hours of aging when ambient temperatures were 150°C and 175°C, with 2.5V bias applied across package. Even though applied bias accelerated the degradation rate, it was not as high as other EMCs studied in the experimental matrix. In the presence of bias, ions from EMC migrate towards cathode resulting in the increase of concentration of ionic contaminants at junction points. Thus, faster degradation rates are observed for EMCs with higher ionic concentrations, with the Cl- ions migrating and accumulating at Cu-Al interface resulting in corrosion. The low levels of ionic contamination allowed EMC-D to surpass the other EMCs A-D in the experimental matrix with the Cu- Al WBs exhibiting longer time-to-failure.

5.5.2.6 EMC F

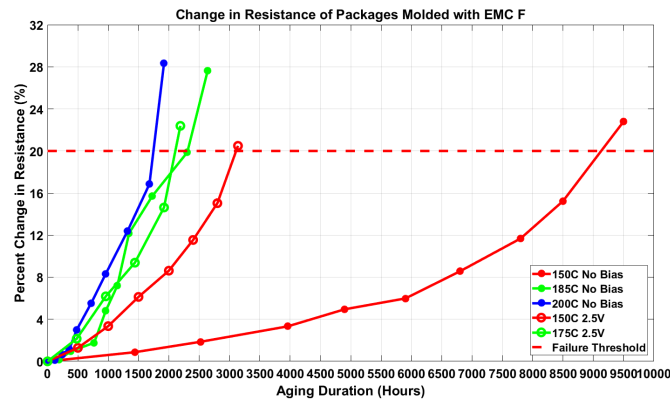

Figure 5.33: Change in Resistance of packages molded with EMC F

Figure 5.30 shows increase in resistance of the packages molded with EMC F, subjected to different aging conditions. EMC-F was silicone based molding compound with very low ionic contamination, and suitable for harsh environmental applications. In comparison with EMC A-E, the EMC-F was found to be most reliable molding compound. When exposed to ambient temperature of 150°C in the unbiased condition, the Cu-Al WB system exhibited a time-to-failure of nearly 9500 hours. Only 5-percent increase in resistance was observed after 5000 hours of exposure to 150°C ambient temperature in the unbiased condition. For the same ambient temperature, under biased testing package failed after 3190 hours of aging. When the ambient temperature was raised to 175°C with bias, the degradation rate of the wirebond was much faster in comparison with the unbiased test even with a higher ambient temperature of 185°C. Similar to the rest of the EMCs A-E, the Cu-Al WB packages molded with EMC-F failed fastest when aging temperature was increased to 200°C.

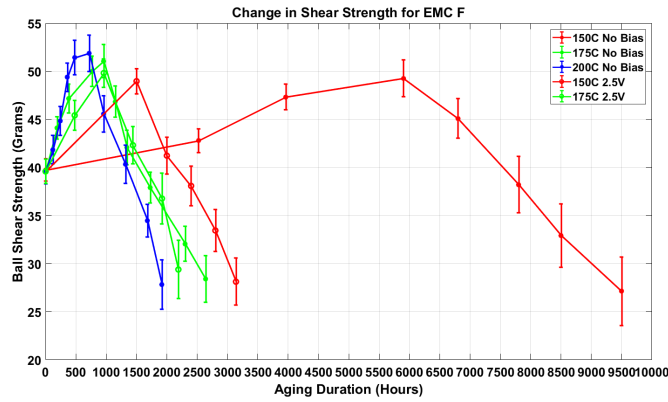

Figure 5.34: Change in Shear Strength of packages molded with EMC F

Figure 5.34 and Figure 5.35 shows change in ball shear strength and evolution of shear failure modes for packages molded with EMC F. for unbiased testing at 150°C, maximum shear strength of 49 grams was observed after 5500 hours of aging. At this point, mode I type failure was still dominant. As the aging duration increased, shear strength reduced to 27 grams at the time of failure. Wider variation in shear strength was observed at lower temperatures. This was contributed to higher bond to bond variation. For ambient temperature of 200°C, maximum shear strength observed was 53 grams, after 650 hours of aging. Time to failure data was consistent for both resistance and shear strength change. Similar to other EMCs, only mode II type failure was observed at the end of testing.

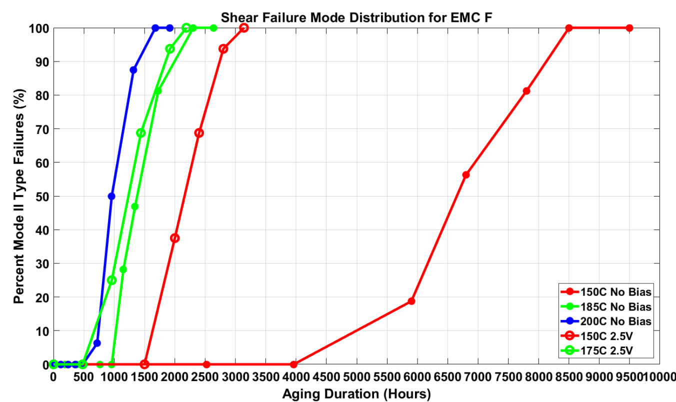

Figure 5.35: Evolution in Mode II Failure for EMC F

5.5.3 Compiled Results

In this section, compiled results of all EMCs are presented to establish dependency of environmental and physical properties of EMC on Cu-Al wirebond reliability.

Table 5.6: Time to Failure of the Cu Wirebonded packages

EMC	Unbiased (Hours)				Biased (Hours)	
	150C	175C	185C	200C	150C	175C
A	4260		1152	600	1210	620
B	5150	1344		720	1440	840
C	5700	1728		740	1650	960
D	6280		1536	960	1750	1020
E	7900		2304	1680	2600	1950
F	9500		2640	1920	3140	2190

Table 5.6 shows summary of the time to failure for the Cu wirebonded packages molded with different EMCs subjected to accelerated life tests. Wide variation in time to failure was observed for different EMCs. At lower temperature of 150°C, the time-to-failure varied from 4260 hours to 9500 hours for EMC A-F; whereas at higher test temperature of 200°C, the time-to-failure varied from 600 hours to 2040 hours . The trend in the failure times highlights the importance of selection of the proper EMC for Cu wirebonded applications. In general, for all the EMCs A-F, an increase in the ambient temperature was accompanied with a decrease in failure time. At elevated temperatures, IMc growth is faster. Due to prolonged sustained higher ambient temperatures, EMC can break down and release ionic contamination's initially bound to long polymeric chains. The ionic contamination then work as a catalyst and accelerates corrosion mechanisms which results into initiation of peripheral cracking, later into failure.

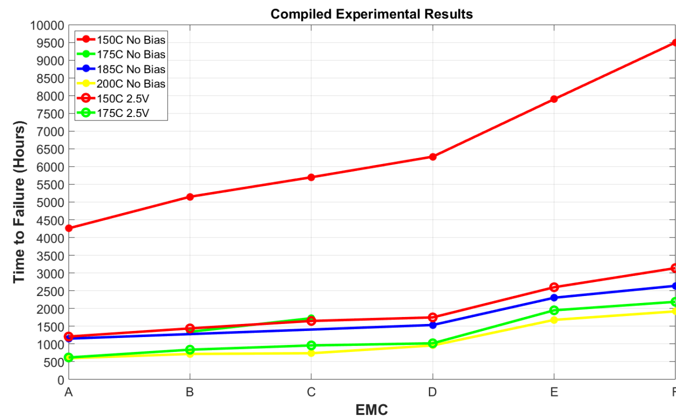

Figure 5.36: Time to Failure of the Cu Wirebonded packages

Figure 5.36 shows graphical representation of summary of all experimental data. Presence of bias had a noticeable effect on the reliability of the Cu-Al WB interconnects. Under biased test condition, at 150°C ambient temperature, the degradation rate was approximately 3x higher than the unbiased 150°C test condition. In the presence of bias at an ambient temperature of 150°C, when current flows through the package, the temperature of the package increases by 13°C to 163°C. The 150°C biased test condition and the 175°C unbiased test conditions exhibit similar failure times. The similarity of the failure times is undoubtedly achieved because of the presence of bias in spite of the lower ambient temperature. It would thus be expected that the Cu-Al WB would exhibit a lower time-to-failure in the presence of higher-bias. Similar observation was made when results of 175°C biased test (Package temperature - 191°C) were compared with 200°C unbiased tests. The reliability of Cu-Al WB was also affected by the level of ionic contamination in the EMC used for molding. EMCs with lower ionic contamination-levels show better reliability performance even at higher temperatures. At 200°C unbiased condition, EMC-F failed after aging for 2040 hours, while packages molded with EMC-A failed after only 600 hours of aging. Similar trend was observed for the biased testing as well. There were two EMCs (C and D) with 5ppm Cl concentration. However, they had different pH values EMC-D which had near neutral pH value had longer time to failure than the EMC C, which was slightly on the acidic side of the scale.

5.6 Experimental Results for Temperature Humidity Test

Parts were subjected to high temperature-humidity condition, and resistance measurements along with ball shear test were performed on parts which were periodically taken out.It is shown that IMC growth is very slow for Cu-Al WB system for temperatures lower than 150°C. It is also shown that the IMC growth cannot be used as leading indicator of failure for parts subjected to highly humid environment. Keeping this in mind, IMC was not considered as a potential parameter for this study.

Wirebond shear test showed three distinct failure modes. In mode I, minimal or no trace of copper was found on sheared surface. In most of the cases Al pad was peeled away. This indicates good bonding between Cu and Al. Mode II showed significant amount of Cu or IMC residue on sheared surface. This indicates presence of micro cracks in between Cu and IMC layers. In Mode III even though good wirebond contact was present, significant pad cratering was found. Pad cratering is contributed to variation in wirebonding process parameters. Sample images of Mode I, mode II and mode III are shown in 5.37. Detailed results of EMC A and EMC F are presented in this section followed by compiled results for all other EMCs.

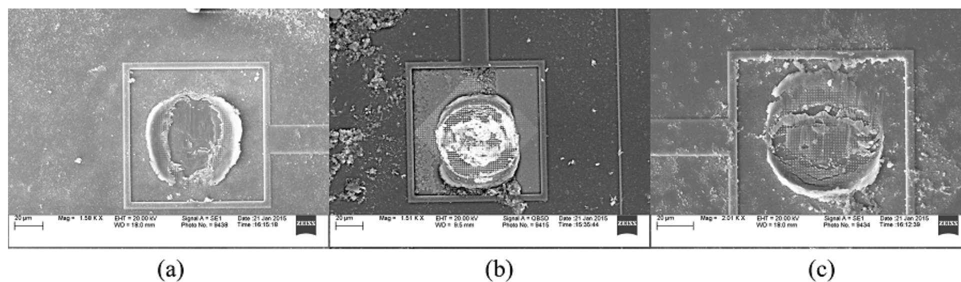

Figure 5.37: Shear Failure Modes (a) Mode I (b) Mode II (c) Mode III

5.6.1 EMC A

EMC A as shown in 1.1 had 10 ppm Cl concentration. Parts molded with this EMC, failed after 648 hours, as shown in Figure 5.38. Figure 5.39 shows change of Shear strength of wirebond as a function of aging duration. Graph shows that shear strength started degrading rapidly after 192 hours of aging, which translates to around 7% change in resistance in Figure 5.38. Shear failure mode distribution shown in Figure 5.40 confirms the same. Mode II failure,

became dominant after 192 hours of aging, Mode II failures are caused by formation of micro-cracks in between Cu and IMC layer. This causes failure along the cracks during shear test, and part of IMC is left on the sheared surface. At the time of failure, shear strength was 30 grams force. Mode II failure mode was observed in more than 95% of the cases at the event of failure.

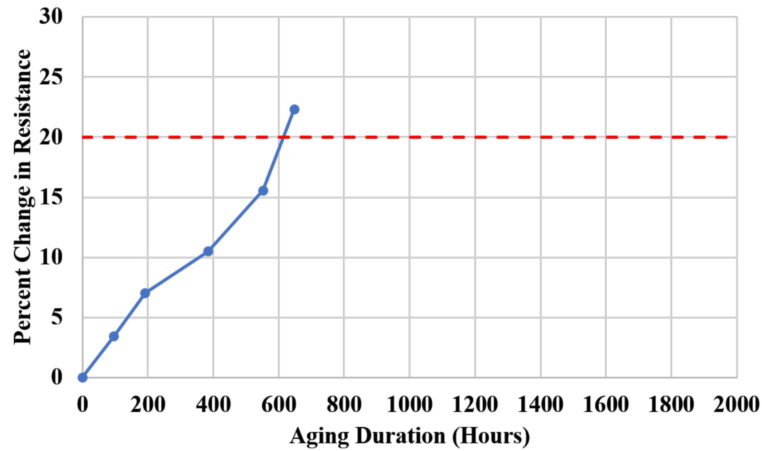

Figure 5.38: Change in Resistance for EMC A

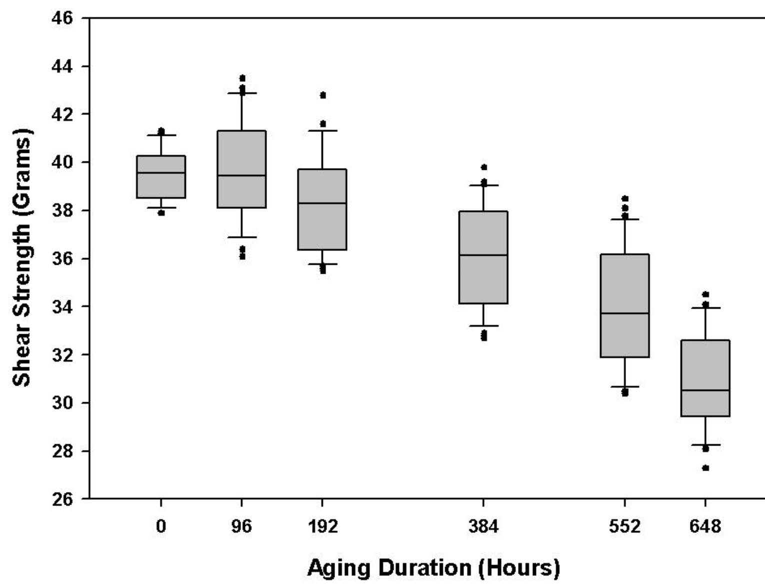

Figure 5.39: Change in Shear Strength for EMC A

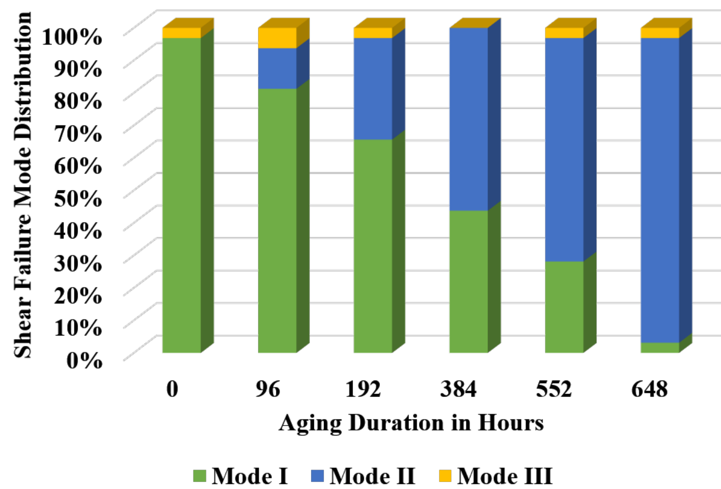

Figure 5.40: Shear Failure Mode Distribution for EMC A

5.6.2 EMC F

EMC F had 1 ppm chlorine concentration, which is least among all of the EMC candidates. Parts molded with EMC G sustained for more than 1800 hours of aging, which is highest among all EMC candidates. Resistance threshold of 20% change was crossed after 1848 hours of aging. Change in resistance versus of time is plotted in Figure 5.41.

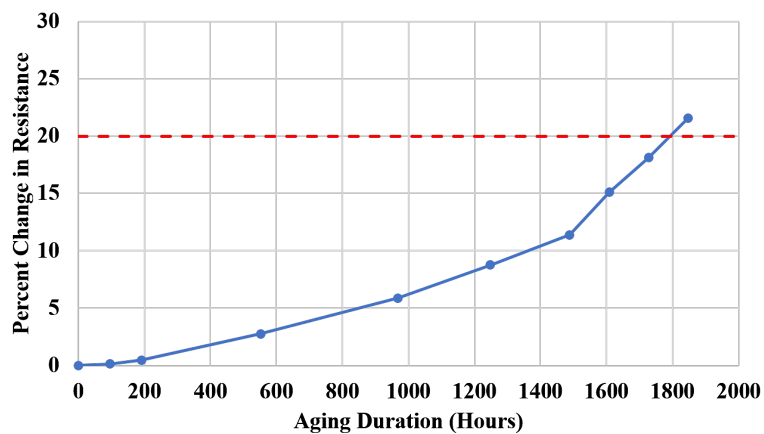

Figure 5.41: Change in Resistance for EMC F

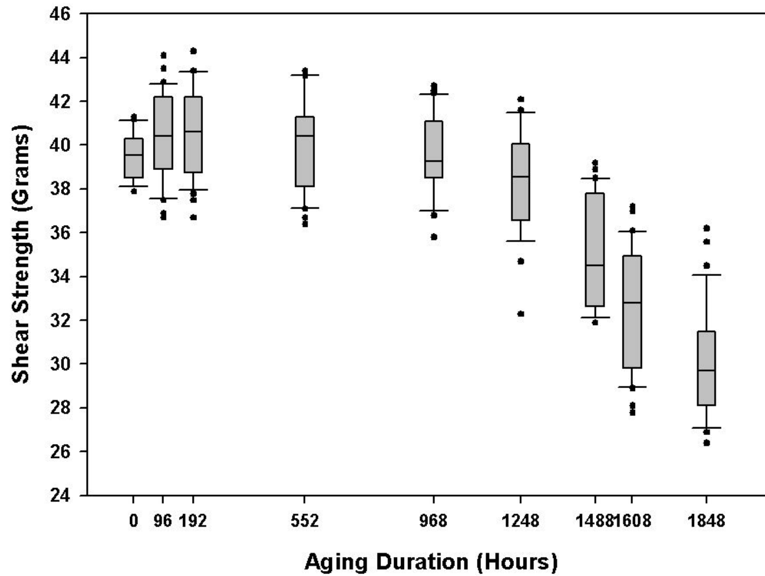

Figure 5.42: Change in Shear Strength for EMC F

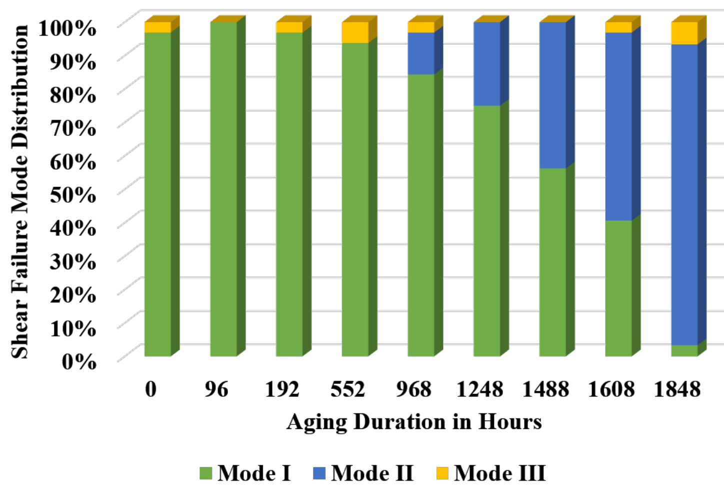

Figure 5.43: Shear Failure Mode Distribution for EMC F

Shear strength of wirebonds did not change significantly till 968 hours of aging, as shown in Figure 5.42. At 968 hours of data point; resistance change was approximately 5%. After that, shear strength dropped rapidly, with increase in resistance of WB pair. Figure 5.43 shows shear failure mode distribution. The point after which the shear strength started dropping, mode II started to become dominant. At the end of the test, shear strength dropped to approximately 29-gram force, with 90% mode II type failure in ball shear test. Since the test was not carried till the pair shows open circuit, we did not see near zero value of shear strength.

5.6.3 Compiled Results

Earlier sections describes time to failure related data of the packages molded with EMC A and F. In this section compiled data for all other EMCs is presented. For comparison purpose, Figure 5.44 shows change in resistance for all packages tested in this study. Time to failure is significantly different for each of the EMC.

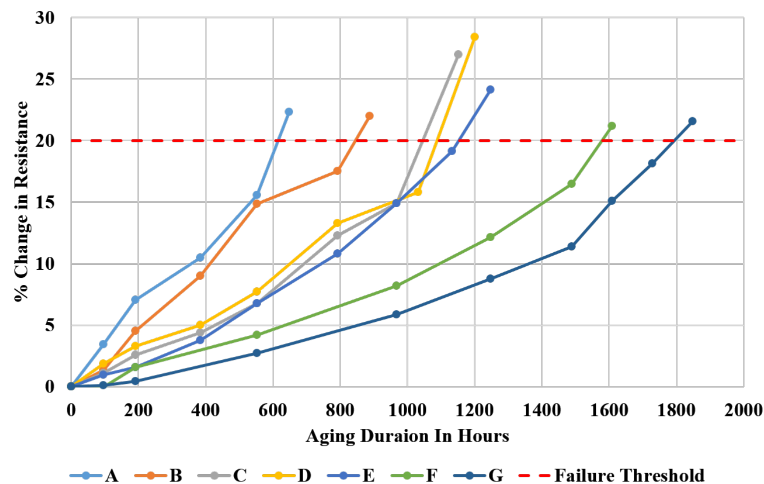

Figure 5.44: Compiled Change in Resistance of Cu Wirebonds Molded with Different EMCs

EMC A which had highest ionic contamination failed after 648 hours of aging. As discussed in earlier chapters, failure under temperature humidity condition is driven by corrosion of the IMC. EMC B had slightly less ionic concentration hence survived 888 hours of aging. Drop in the rate of increase of resistance was observed. EMC C and D same ionic contamination but different pH value. EMC D had near neutral pH value, hence survived for 1200 hours compared to EMC C which failed after 1150 hours. EMC E and F had very low cl concentration and failed after 1608 and 1848 hours of testing respectively. Rate of degradation of wirebond depend on the properties of EMC such as pH value, Cl ion concentration etc. The results reported here are consistent with the results published by [35], [33]. Irrespective of chemical properties, all packages tend to show same trend in shear strength change. This proves that degradation mechanism is the same in irrespective of the EMC used to mold packages.

5.7 Predictive Model for High Temperature Condition

Model to predict remaining useful life of Cu wirebonded devices under different operational and ambient environment was developed using artificial neural network as discussed in Chapter 4. In this model, a feed-forward, two layered network with 11 neurons (10 hidden, 1 output) has been used. Dependent variables for the model development include operational and chemical parameters of the corrosion process in the CuAl WB system. The dependent operational parameters analyzed include, applied bias (V), change in resistance (percent) and ambient temperature (K). The dependent chemical parameters included, ionic contamination in the EMC (ppm), pH value, Tg (K) and filler content (percent) of the molding compound. Figure 5.45 shows topology of neural network model.

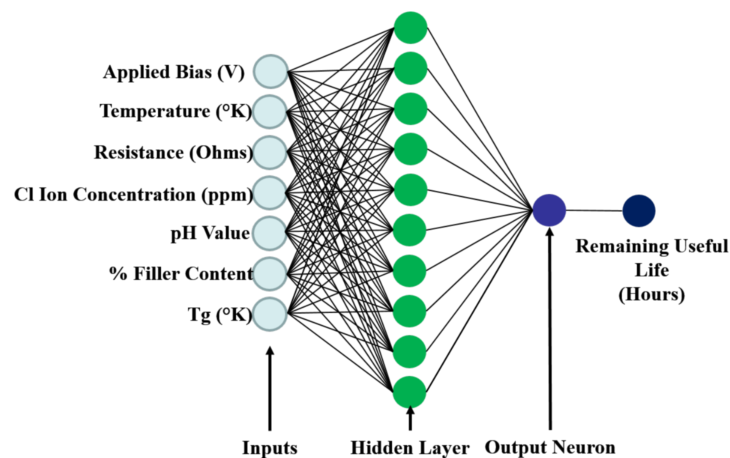

Figure 5.45: Neural Network Topology

Single hidden layer consisting of 10 neurons was used. Feed forward network with Bayesian regularization was used for the fitting purpose. NN fitting equation can be written as,

$$TF = purlin[b_2 + LW * tansig(b_1 + IW * X)] \tag{5.1}$$

Where Where purlin is linear activation function, and tansig is tan- sigmoid activation function as discussed earlier. X is input vector of all dependent variables and TF is time to failure. IW is [10x7] matrix of initial weights, LW is [1x10] matrix of linear weights. b_1 is an initial bias parameter vector [10x1], and b_2 [1x1] is an output bias parameter. Figure 5.46 shows change in

mean squared error between experimental and predicted time-to-failure of the Cu- wirebonded package. MSE was minimum after 153 iterations and was stable for the calculated weights of the neurons. Figure 5.47 shows histogram of the residues from the NN fitting. The nature of the histogram resembles a bell curve with highest instances near zero error, i.e. low instance of model deviation from the experimentally observed values of time-to-failure.

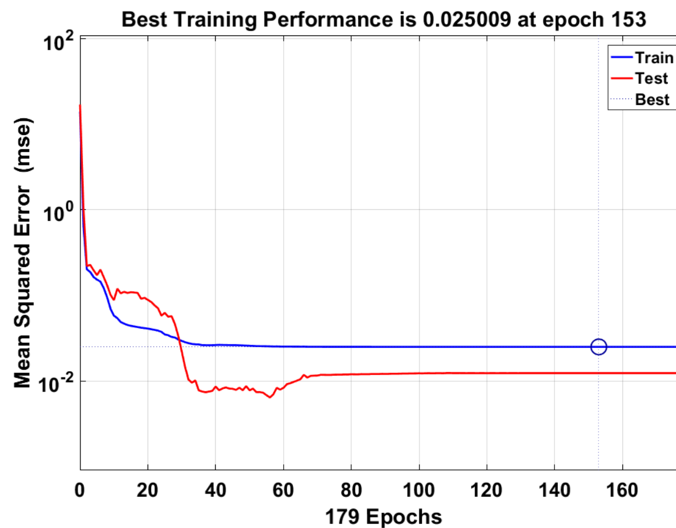

Figure 5.46: Minimization of MSE during NN training Process

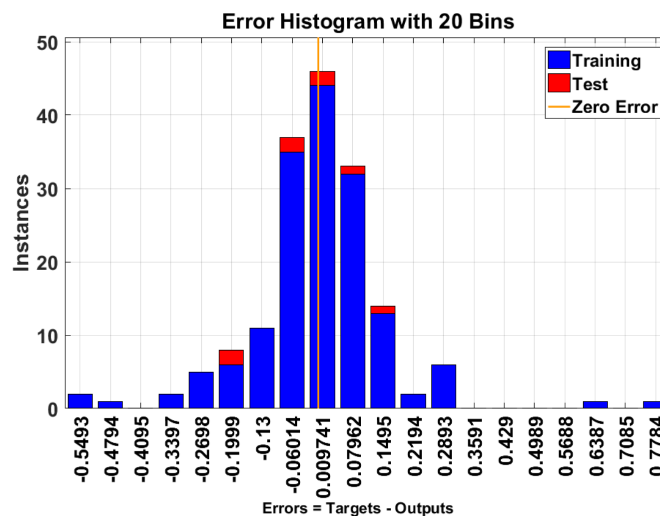

Figure 5.47: Residual plot of NN Fitting

Experimental measurements of time-to-failure were compared with NN predicted time-to-failure data. Figure 5.48 shows the plot of comparison with 20% error bound lines represented by solid lines and the blue dots represent the actual data point. Comparison indicates that

majority of the predictions were in the 20-percent error bound. Assessment of the variance in the experimental data explained by the model indicates that R2 value of the fit was 96.05%. The average absolute error of the prediction was 10.19% with standard deviation of 12.54%. Fitted line makes approximately $45°$ line with either axis, proving that the model predictions are consistent with the experimental values.

Experimental measurements discussed earlier in the paper indicate that operation at higher temperatures correspond to shorter time-to-failure. To assess the capability of the model to capture the influence of the EMC such as Cl concentration and pH value on the time-to-failure, the model predictions were compared with the experimental data over the complete range of variation of the input parameters. Figure 5.49 shows experimental and predicted time to failure of the package molded with EMC-A for the temperature range of $423°$K to $473°$K indicating a trend of shorter lifetimes with higher operating temperature.

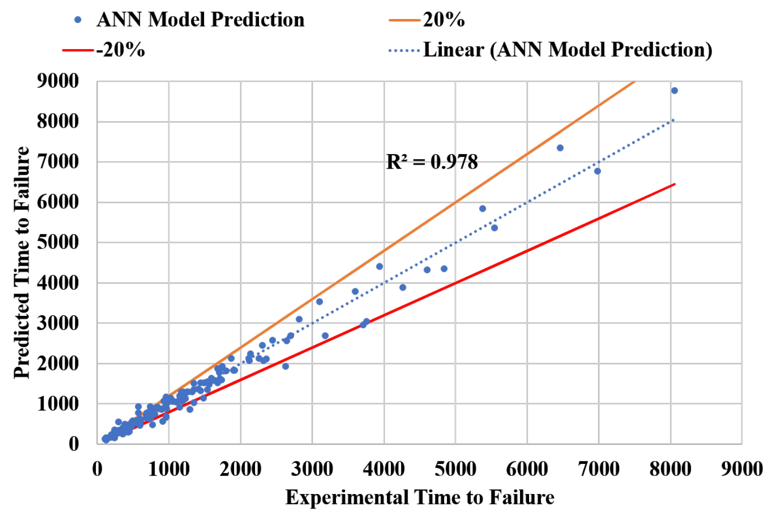

Figure 5.48: Comparison of experimental and predicted time to failure

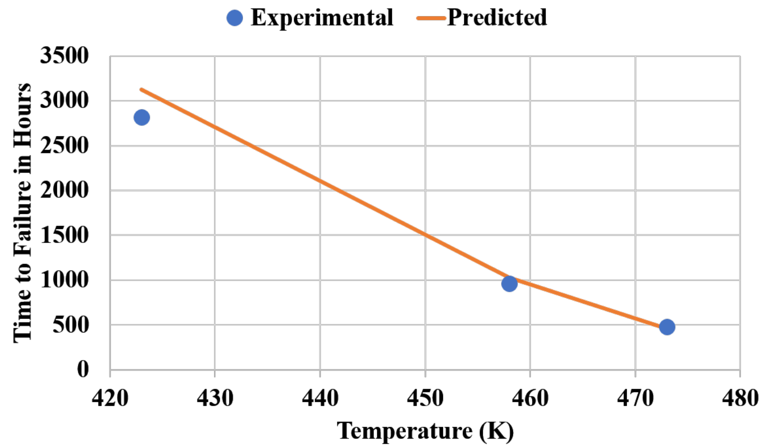

Figure 5.49: Variation in the experimental and predicted time to failure due to change in aging temperature

Figure 5.50 shows experimental and predicted time to failure of the package molded different EMCs at temperature of 473°K. As the ionic contamination in the EMC reduces, time oF failure increases. The model was able to capture this trend and predict remaining useful life of the package successfully across wide range of EMC formulations.

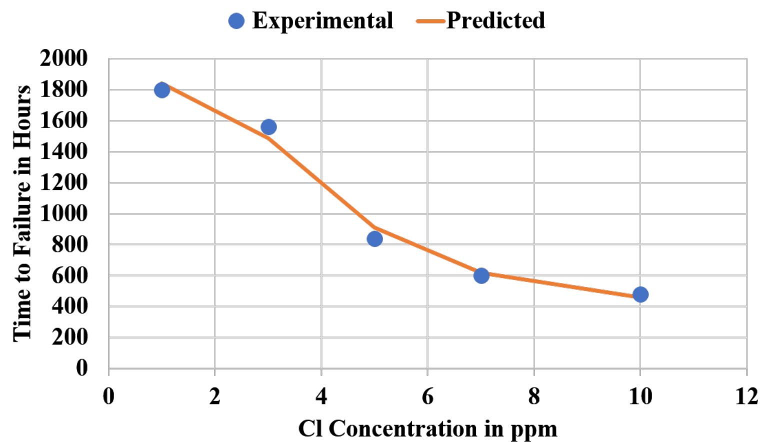

Figure 5.50: Variation in the experimental and predicted time to failure due to change in ionic contamination

Figure 5.51 shows comparison of experimental and predicted time to failure of the Cu wirebonded package molded with EMCs A-F, at 448°K. In this case, only the formulation of the EMC has been varied to assess the effect of change in the EMC composition on the time-to-failure. The model predictions correlate well with experimental data as the EMCs A-F are arranged in the order of decreasing Cl concentration. Further, the EMCs E-F are both near

neutral in their pH value. In both cases, trend follows the expected variation of the lifetime with Cl concentration and pH value with the lower Cl concentration and neutral pH values corresponding to longer lifetimes. Time to failure was higher for EMCs with higher ionic contamination. Furthermore, acidic pH value of the EMC adversely affects the reliability of the Cu wirebonds and can cause early failures.

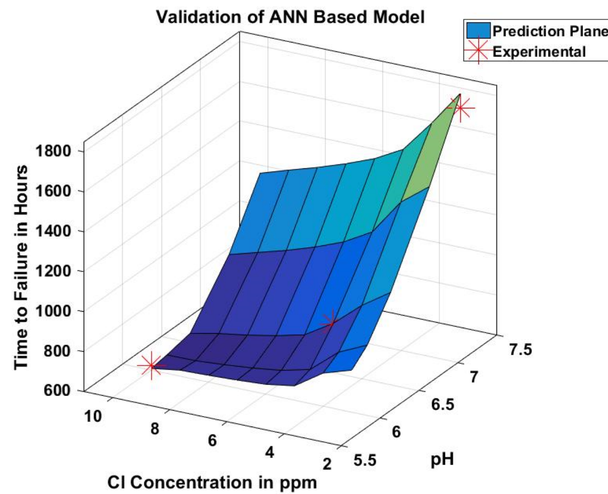

Figure 5.51: 3D Predictive plot for interaction of pH and ionic contamination

5.8 Predictive Model for High Temperature High Humidity Condition

Extended kalman filtering was used to predict remaining useful life subjected to temperature humidity condition. Resistance increase as discussed earlier was used as a leading indicator of failure. Kalman filtering is a recursive algorithm which estimates true state of system based on the noisy measurements [110], [111]. Noise could be process noise or measurement noise or both. This technique is extensively used in guiding and tracking applications. Nonlinear version of Kalman filtering is known as extended kalman filter (EKF). Here, system state that is resistance of wirebond pair is described in state space by using measurement of feature vector (change in resistance), its velocity and acceleration. System state at each time interval is computed based on evolution history of system state, system dynamic matrix, control matrix, measurement matrix, and process and measurement noise. First order nonlinear differential equations for extended kalman filtering is given in Equation 5.2,

$$\dot{x} = f(x) + w \tag{5.2}$$

Where, x is a system state vector, f(x) is non-linear function of vector state and w is random zero mean process. In this paper, we are assuming linear relationship between system states (x) and measurements (z). Measurement vector z can be given by,

$$z = h(x) + v \tag{5.3}$$

Here, v is a zero-mean random process described by measurement noise matrix R, and H is measurement matrix. R is defined as,

$$R = E(vv^T) \tag{5.4}$$

Since system dynamic matrix and measurement equations are non-linear, first order approximation is used in the continuous Riccati equations for the system dynamic matrix (F) and measurement matrix (H). Matrix are related to the non-linear system and measurement equations according to

$$F = \frac{\partial f(x)}{\partial x} \mid_{x=\widehat{x}} \tag{5.5}$$

$$H = \frac{\partial h(x)}{\partial x} \mid_{x=\widehat{x}} \tag{5.6}$$

The fundamental matrix required for discrete Riccati equation can be approximated by Taylor-series expansion and is given by

$$\Phi_k = I + FT_s + \frac{F^2T^2}{2!} + \frac{F^3T^3}{3!} + ... \tag{5.7}$$

T_s is the sampling period and I is the identity matrix. Since the fundamental matrix will not be used in propagation of state vector, we can ignore higher order terms from Equation 5.7. The series can be approximated to

$$M_k = \Phi_k P_{k-1} \Phi_k^T + Q_k \tag{5.8}$$

$$K_k = M_k H^T (H M_k H^T + R_k)^{-1} \tag{5.9}$$

$$P_k = (I - K_k H) M_k \tag{5.10}$$

Where P_k and M_k are covariance matrices representing errors in state estimates after an update and before the updates respectively, K_k is kalman gain. Φ_k is discrete fundamental matrix. Discrete process noise matrix Q_k can be calculated by

$$Q_k = \int_0^{t_s} \Phi(t) Q \Phi^T(t) dt \tag{5.11}$$

$$Q = \Phi_s \begin{bmatrix} 0 & 0 & 0 \\ 0 & 0 & 0 \\ 0 & 0 & 1 \end{bmatrix} \tag{5.12}$$

The resistance of the package was measured using direct experimental technique. First and second order derivatives were used to extrapolate feature vector. Simple numerical derivatives calculated from raw feature vectors are usually very noisy and of very little help. EKF provides very powerful tool for smoothing and estimating state of all variables. General form of the resistance data is assumed to be,

$$x = ae^{bt} \tag{5.13}$$

Where, X is resistance measurement in Ohms, e is Eulers constant, a and b are the constants and t is aging duration in hours. First derivative of resistance with time and parameter b are used in state vector. Parameter b will evolve for each time step and provide us more robust estimates. The state vector is,

$$X_k = \begin{bmatrix} x & \dot{x} & b \end{bmatrix}^T \tag{5.14}$$

Derivative of equation 5.13 can be given by,

$$\dot{x} = bx \tag{5.15}$$

$$\ddot{x} = b\dot{x} \tag{5.16}$$

$$\dot{b} = w \tag{5.17}$$

w is white process noise that had been added to the acceleration equation for future projection. Now equation 5.2 can be written as

$$\begin{bmatrix} \Delta\dot{x} \\ \Delta\ddot{x} \\ \Delta\dot{b} \end{bmatrix} = \begin{bmatrix} \frac{\partial\dot{x}}{\partial x} & \frac{\partial\dot{x}}{\partial\dot{x}} & \frac{\partial\dot{x}}{\partial\, b} \\ \frac{\partial\ddot{x}}{\partial x} & \frac{\partial\ddot{x}}{\partial\dot{x}} & \frac{\partial\ddot{x}}{\partial b} \\ \frac{\partial\dot{b}}{\partial x} & \frac{\partial\dot{b}}{\partial\dot{x}} & \frac{\partial\dot{b}}{\partial b} \end{bmatrix} \begin{pmatrix} \Delta x \\ \Delta\dot{x} \\ \Delta b \end{pmatrix} + \begin{bmatrix} 0 \\ 0 \\ w \end{bmatrix} \tag{5.18}$$

Based on the equation 5.18, system dynamic matrix is calculated as follows

$$F = \begin{bmatrix} b & 1 & x \\ b^2 & b & 2bx \\ 0 & 0 & 0 \end{bmatrix} \tag{5.19}$$

Discrete fundamental matrix can be calculated from equation 5.7 as,

$$\Phi(t) = \begin{bmatrix} 1+bt & t & xt \\ b^2t & bt+1 & 2btx \\ 0 & 0 & 1 \end{bmatrix} \tag{5.20}$$

Discrete process noise Q_k is calculated from Equation 5.11, 5.12 and 5.20 as, 5.7 as,

$$Q_k = \begin{bmatrix} x^2t & 2bx^2t_s^2 & 0 \\ 2bx^2t_s^2 & (2bx)^2t_s^2 & 0 \\ xt_s & 2bxt_s & 0 \end{bmatrix} \tag{5.21}$$

Posterior error covariance was used calculate uncertainty of each prediction. The extrapolation of the estimated state into the future to determine RUL was accomplished by using the state evolution equation to iterative solve the intersection with critical resistance threshold. The matrix required for solving Riccati equations are defined in equation 5.9, 5.10 and 5.11. Next step in the algorithm is to propagate the extended state from the present state sampling time to the next sampling time using one step Euler numerical integration of the nonlinear differential

equations as,

$$\bar{\dot{x}} = \hat{x_{k-1}} + T_s \ddot{x_{k-1}} \tag{5.22}$$

$$\bar{x} = \hat{x_{k-1}} + T_s \dot{x_{k-1}} \tag{5.23}$$

Now the kalman filtering equations can be written as,

$$\hat{x_k} = \bar{x_k} + K_{1k}(\tilde{x_k} - \bar{x_k}) \tag{5.24}$$

$$\hat{x_k} = \hat{x_k} + K_{2k}(\tilde{x_k} - \bar{x_k}) \tag{5.25}$$

$$\hat{b_k} = b_{k-1} + K_{3k}(\tilde{x_k} - \bar{x_k}) \tag{5.26}$$

$$\bar{\ddot{x_k}} = \hat{b_k}\hat{\dot{x_k}} \tag{5.27}$$

Where, $\hat{x_k}$, $\hat{x_{k-1}}$ and $\bar{x_k}$ denotes all projections of the state from preceding estimate to current time. $\tilde{x_k}$ Denotes present measurement. Summary of filtering and projection is provided below,

1.Initialize variables at time step t=0.

2.Project state at the next time step.

3.Calculate error covariance from equation 5.8

4.Calculate Kalman gain from equation 5.9

5.Take measurement from equation 5.3

6.Update estimate with measurement

7.Calculate error covariance from equation 5.10

8.Extrapolate feature vector to threshold value and report predicted RUL

9.Iterate to step 2 for next measurement.

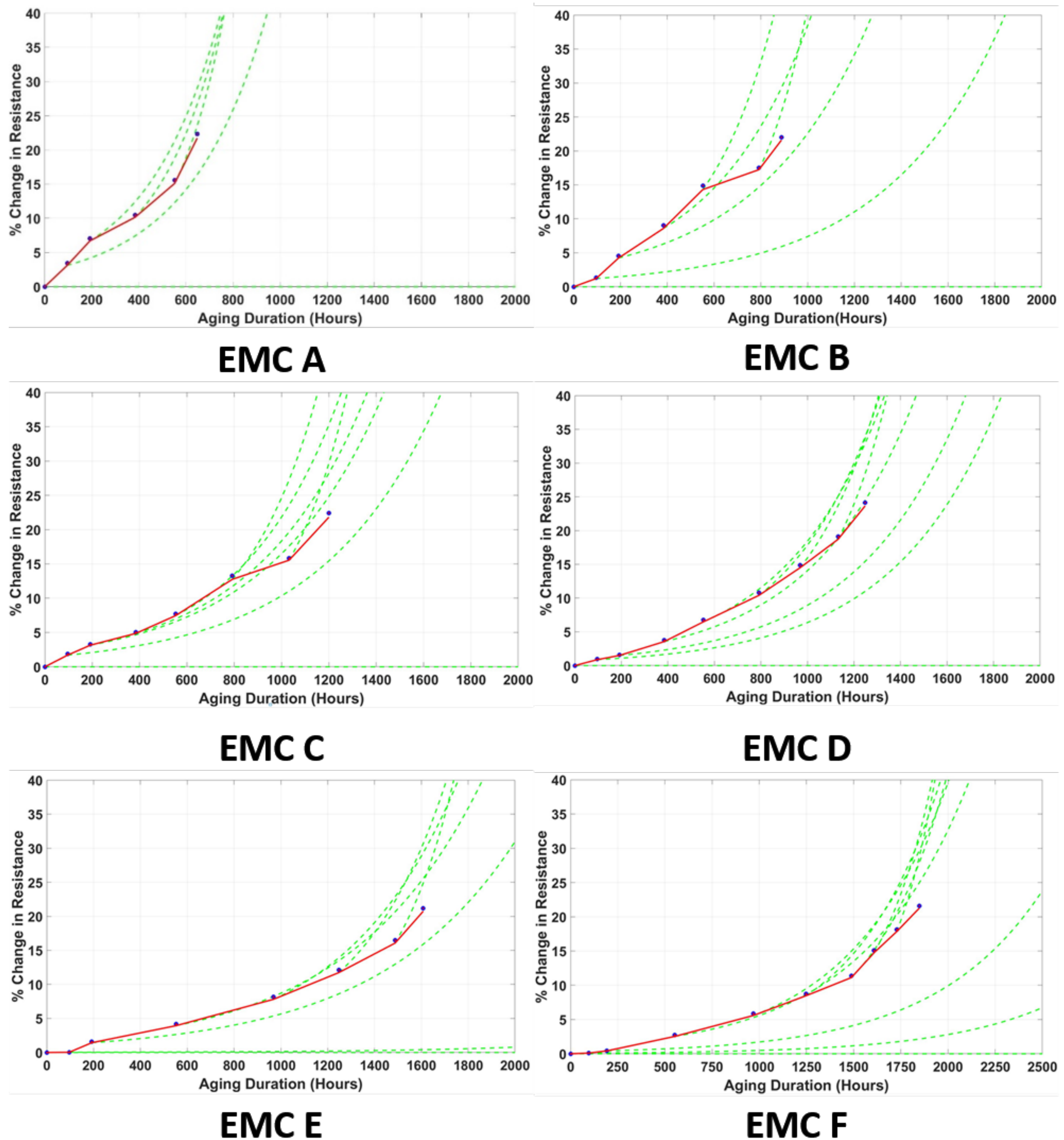

Figure 5.52: EKF Performance and RUL Prediction

Extended kalman filter, based on exponential model was developed as described in earlier section. Resistance of the package was selected as leading indicator of failure.Figure 5.52 shows EKF results for packages molded with EMC A to EMC F respectively. Blue data points represent actual experimental resistance measurement. Red line shows EKF predictions. Green dashed line indicates extrapolation from each prediction point into future space. The extrapolation is achieved with the help of state vector, which includes first derivative of resistance and

Table 5.7: Average absolute error in prediction of RUL (Remaining Useful Life)

EMC	Average Absolute Error (%)
A	15.56
B	19.89
C	19.23
D	15.46
E	20.05
F	27.95
Average Error	**19.69**

exponent b. Exponent b evolves for each time step. The evolution of b defines future projection from each observation.

Sampling time T_s was set as 0.01 for all the cases. Spectral density of white noise source was kept constant irrespective of the dataset. Each molding compound has different time to failure, and different rate of degradation. To capture this correctly, only initial exponent guess, which is required for initialization of algorithm was changed for each molding compound. For all the EMCs, extrapolation from time 0 reading and 1st reading after it can be ignored. At that time steps, algorithm does not have enough knowledge about behavior of state vector. As we pass more data from the filter, it converges better and prediction becomes more accurate.

Its important to note that transition of EKF prediction and its conversion is much smoother for datasets where more data points were available. To check accuracy of predictive model, absolute error in each prediction point was calculated for each molding compound. To calculate error, RUL (Remaining Useful Life) was calculated from each data point based on extrapolation. It was then compared with experimental RUL. Average error (in percent) for each molding compound is listed in Table 5.7. During calculation absolute error was used so that direction of error does not affect overall error percent. In Table 5.7 we can see that average error in prediction of RUL varies from 10% to 28%. In most of the cases, it is in the range on 15% to 20%. Average error of all prediction from all EMCs is 18.41%. Provided number of data samples in each case were very limited, these are accurate and acceptable results.

5.9 Summary and Conclusions

Degradation of Cu wirebonds at high temperature under biased testing was presented in this section. Degradation was captures in terms of change in resistance of wirebond pair which was correlated with change in shear strength of ball bond and evolution of shear failure modes. Experiment was performed on devices molded with six different molding compounds. They were subjected to wide temperature range from $150°K$ to $200°K$, either unbiased or with 2.5V bias. Effect of applied bias on the degradation rate of Cu wirebonds was established in the section. Combined effect of various operational parameters such as temperature and bias, along with material properties, such as ionic contamination, pH value etc. was studied. Dependence of acceleration factors on these parameters was also studied. ANN based fitting technique was used to develop model for prediction of remaining useful life. Bayesian regularization was used to optimize the weights of the neurons during the learning process. Feed-forward single layered structure was able to predict remaining useful life based on operational conditions as well as various material properties. Model was validated with the test dataset within acceptable error bound. Model was further validated with the experimental data for variation in selected variables. Predictive model was able to successfully capture various trends observed in the experimental data and was able to provide accurate predictions. Packages were also subjected to high temperature humidity environment. Their resistance and bond shear strength were monitored till failure. It was found that drop in resistance beyond initial 5% change is accompanied by significant drop in shear strength of the wirebond. This drop is because of micro cracking that takes place because of localized corrosion of Cu_9Al_4 phase. Typically for all EMCs at the time of failure, shear strength was reduced by 25%. Shear strength value initially goes up because of lateral growth of IMC, and then drops down because of degradation of wire bond. This trend remains the same irrespective of the type of molding compound used. The rate of degradation was found to be highly dependent of ionic contamination and pH value of molding compound. This is consistent with some of the earlier findings. EMC A with 10ppm Cl concentration failed after 648 hours, whereas EMC F which had 1 ppm Cl ion concentration failed

after 1850 hours of aging. This proves that molding compound selection process is very critical when packages are designed to sustain very harsh environments. The study has also shown successful implementation of exponential model based extended kalman filter in prediction of remaining useful life of the Cu wire bonded packages molded with different molding compounds. The model could predict remaining useful life of the molded packages with 18.41% error.

Chapter 6

High Temperature Storage life (HTSL) and Electromigration (EM) Reliability of Copper, Gold, Silver and PCC Wirebonds bonded onto Al pad

6.1 Overview

Typical diameter of the wirebonds for encapsulated packages varies between 0.8mil to 2mil. Since inception, Gold (Au) is a standard material used for wire bonding. Increase in the prices of Au within past decade has triggered search for an alternate materials candidate. Three of the leading candidates are Silver (Ag), Copper (Cu), and Palladium Coated Copper (PCC). The new materials are not only cheaper but also have better mechanical, electrical, and thermal properties, which is advantageous for fine pitch-high density electronics. The transition comes along with few trade-offs such as lack of knowledge base of the detailed responses of these systems when deployed in harsh environment applications. Current efforts in the wirebond reliability field are based on tracking number of failure occurred in a standard set of samples and performing failure analysis on the failed parts. Relationship between mechanical degradation of the wirebond and the change in electric response needs to be established for better understanding of the failure modes and their respective mechanisms. Understanding progression of damage in wirebonds from as-bonded state, until failure will help in development of more robust interconnects.

Small form factor of the latest electronics has significantly increased the current densities in the interconnects. Under high temperature operating conditions, these interconnects fail prematurely due to electromigration phenomenon as well as Joule heating. Electromigration (EM) is a mass transport of a material due to the momentum transfer between conducting electrons and atoms. High current densities in the wires can start mass transfer from one place

to another, depending on the direction of the current. Joule heating of the wirebonds can significantly increase EMC-wirebond contact temperature and cause localized degradation of the EMC; which results into rapid degradation of the bond wire. Mechanisms of electromigration behavior of PCC, Cu and Ag wirebonds are not widely reported in the literature. Relation between micro-structural changes due to electromigration with the change in electric response of these interconnects is not yet reported

In this section a detailed study of the degradation of wirebonds under high temperature exposure and very high current density $(8 * 10^4 A/cm^2)$is presented. The degradation was tracked using electric as well as mechanical responses of the wirebonds. Four wirebond candidates (Au, Ag, Cu and PCC) bonded onto Aluminum (Al) pad were subjected to high temperature storage life until failure to study the degradation of the bond-wire interface. Detailed analysis of intermetallic (IMC) phase evolution is presented along with quantification of the phases and their evolution over time. Few devices were decapsulated and ball shear tests were performed. Change in shear strength and different shear failure modes for different wirebond systems are further discussed and compared. Change in electric response was then correlated with change in IMC structure, change in shear strength and evolution of shear failure modes.

6.2 Test Vehicle

32 pin QFN devices were selected for this study as shown in Figure 6.1. Table 6.1 shows the package details. Au, Cu, and Ag wires were 1mil wires, bonded onto $0.9\,\mu\text{m}$ thick Al pad, and 0.8mil PCC wire was bonded onto the similar Al pad. Packages were molded with high temperature epoxy molding (rated for 200°C)compound with 5ppm Cl ion concentration, pH value of 6 and Tg of 170°C. Packages were post mold cured at 175°C for 4 hours. In each package, there were 32 wirebonds. Two wirebonds were connected to each other to form a pair. There were total 16 pairs of wirebonds in each package.

Table 6.1: 32 Pin QFN Dimensions

Parameter	**Dimensions (mm)**
Width	5.00
Length	5.00
Height	1.50
Pitch	0.5

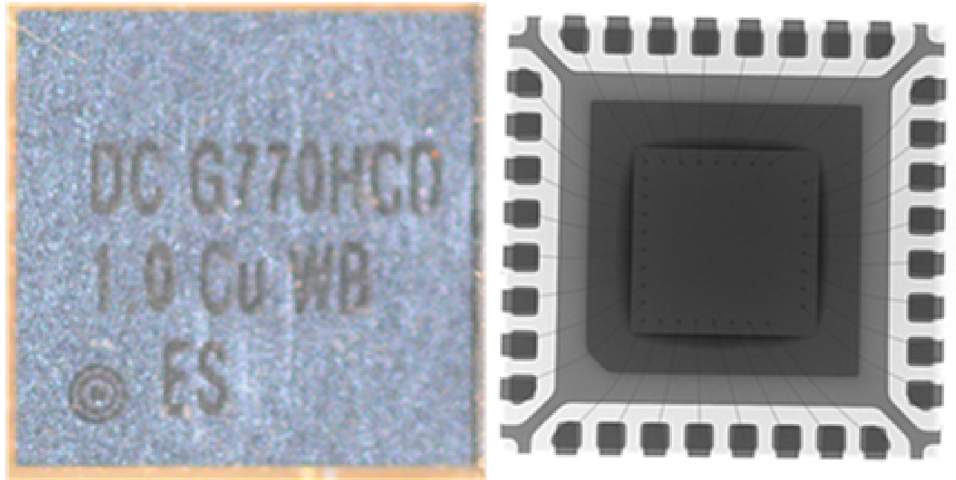

Figure 6.1: Optical and X-ray Images of the Package

6.3 Test Matrix and Protocol

To study high temperature storage life All packages were subjected to 200C isothermal aging condition. Packages were taken out at periodic time intervals and resistance of the wirebond pairs was measured using highly sensitive resistance spectroscopy technique till failure. Failure threshold for the parts was decided as 20% change in resistance. To study high current reliability of wirebonds, two layered, high Tg, FR4 PCB was designed so that all wirebonds were connected in series on each side of the package. Parts were mounted using SAC 305 solder paste. Fabricated part is shown in Figure 6.2. A, B, C, and D channels were then connected so that all 32 wirebonds were in series. Five such packages were connected in parallel with 30V, 5A DC power supply with constant voltage setting to avoid current surge in case of abnormal failure. All packages were held at the room temperature and very high current $8 * 10^4 A/cm^2$ was passed through each wirebond.

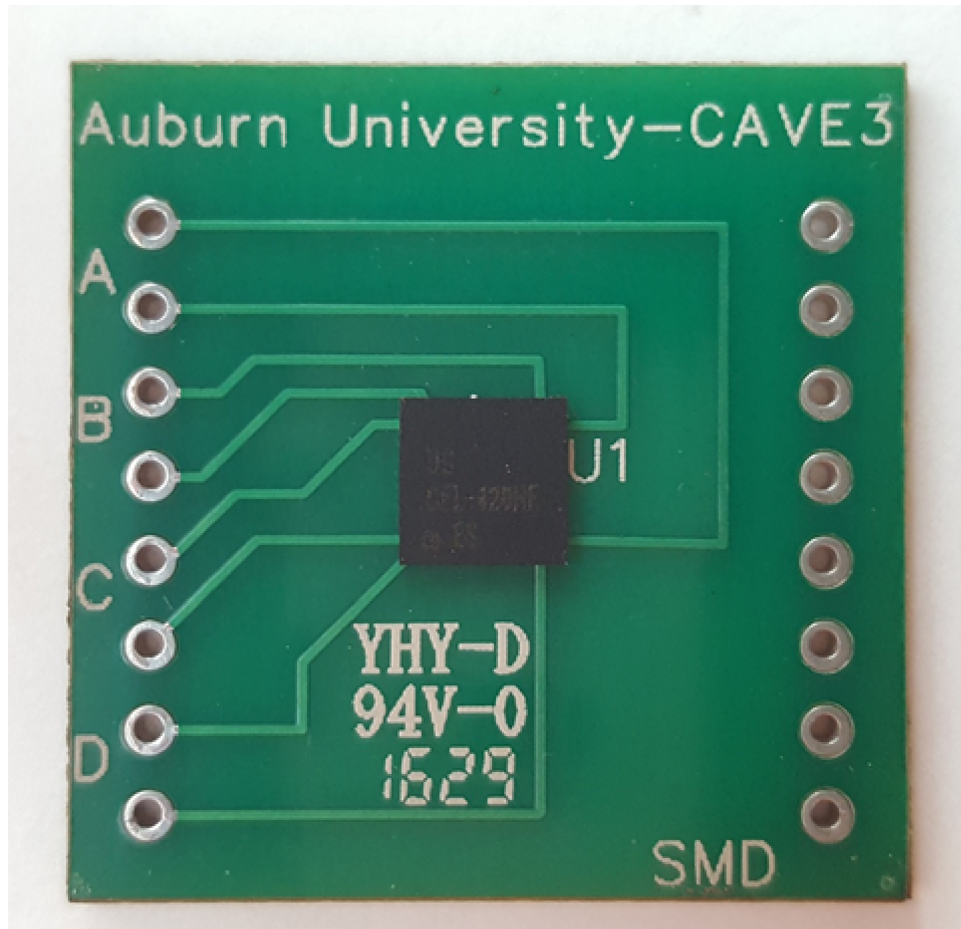

Figure 6.2: Optical Image of Fabricated Package

Very high current passing from wirebonds significantly increases temperature of the package. Quantification of the package temperature was performed using thermocouples placed on top of the package. Figure 6.3 shows temperature of the package when package was powered on and turned off. Under power off condition, package was at room temperature, i.e. 20°C, however as the current passed through package, temperature increases to 152°C. During the testing, power was never turned off, which exposed wirebonds to high temperature as well as high current simultaneously.

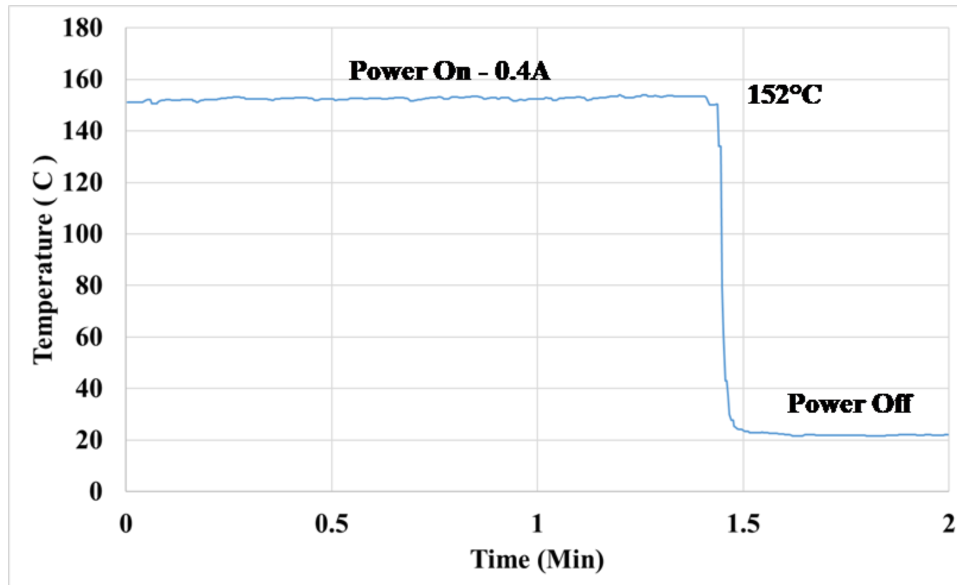

Figure 6.3: Temperature Change in The Package Due to Joule Heating

Packages were then cross-sectioned to analyze the change in morphology at the bond-pad interface. Multiple wirebonds were analyzed in each package to study the effect of current direction on the interface. Chemical etchants were used to enhance contrast between different IMC phases. Composition of IMC phases was confirmed using EDX analysis. To measure IMC thickness, first, number of pixels in the IMC area were calculated with the help of image processing software. Dividing the area by length of the IMC provides one thickness value of the IMC. Summarized process is shown in Figure 6.4. Change in the electric response of the package was then correlated with change in morphology of bond wire interface. Few packages were then decapsulated using fuming acids and ball shear test was performed to study change in shear strength of the wirebond interface. Ball shear test was performed using DAGE2400 ball shear tester. Shear tool height was set to be 2.5 µm above aluminum pad. Shear tool speed was 150 µm/s. Shear failure modes were then analyzed using scanning electron microscopy (SEM). Au Wirebonded packages were decapsulated using pure fuming nitric acid. Cu and PCC Wirebonded packages were decapsulated using chemistry suggested in Chapter 4. Change in electric response of the package was then correlated with the change in morphology of bond wire interface and with the change in shear change along with evolution of shear failure modes.

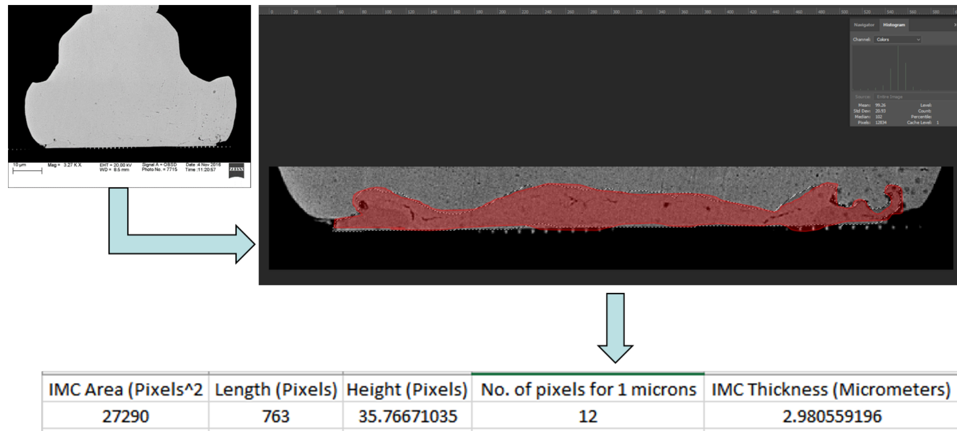

IMC Area (Pixels^2	Length (Pixels)	Height (Pixels)	No. of pixels for 1 microns	IMC Thickness (Micrometers)
27290	763	35.76671035	12	2.980559196

Figure 6.4: IMC Measurement Technique

6.4 Experimental Results

Results of the high temperature test are discussed first followed by high current test on four wirebond materials in this section. Result of the each wirebond is discussed separately followed by comparison section.

6.4.1 High Temperature Test

6.4.1.1 Cu Wirebond

Figure 6.5 shows change in resistance of Cu-Al wirebond system when subjected to 200°C of ambient temperature. Package failed after 720 hours of thermal aging. Red dashed line in the plot shows failure threshold. Initial rate of increase of resistance was constant. However, the rate changed after initial 5% change in resistance. Figure 6.6 shows the SEM images of the cross-section of bond pad interface. Significant growth in intermetallics was observed. IMC thickness was measured at each time interval as discussed in earlier section. Initially in as bonded state very thin layer of IMC was present. As the aging duration increased; IMC growth was observed. After failure, complete consumption of the Al pad was observed.

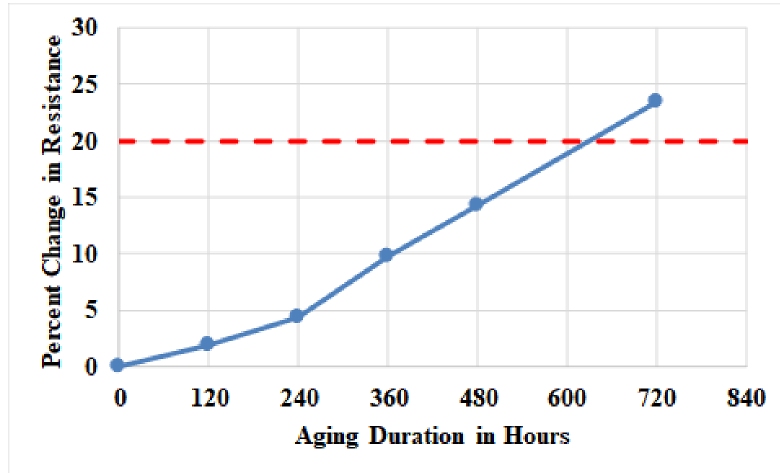

Figure 6.5: Increase in the resistance of Cu wirebonds at 200°C aging temperature

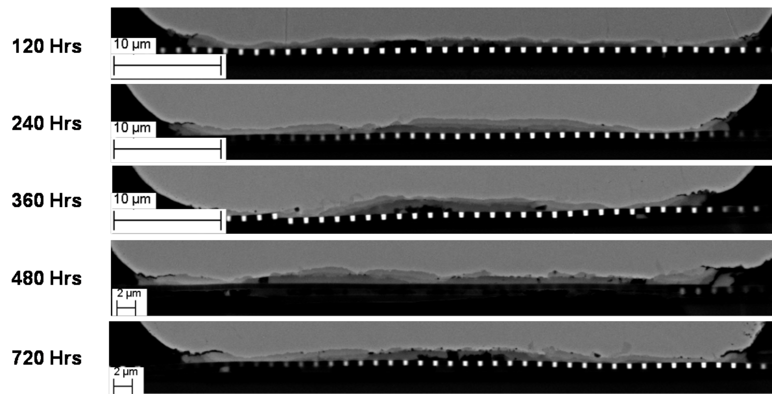

Figure 6.6: Growth of Cu-Al IMC at bond-pad interface

Figure 6.7 shows ln-ln plot of an IMC thickness against aging duration. After the fitting, exponent value of time was found to be 0.4764. Observed experimental value was close to the theoretical value of 0.5 for Fickian based diffusion. Initial growth rate of IMC was very high. The growth rate decreased as the aging duration increased. Different phases of the IMC which are present between copper and aluminum have different physical properties and affect the overall diffusion rate. Figure 6.8 shows that three distinct phases found at the Cu-Al interface. EDX point scans were performed at different locations to identify composition of the phases. Result of the point scan are shown in Table 6.2. IMC phase near copper (point A) was Cu_9Al_4, the phase present near Al pad (point C) was $CuAl_2$, and the phase in the middle (point B) was CuAl as shown in Table 6.2. The results are consistent with results published earlier [4], [97], [63].

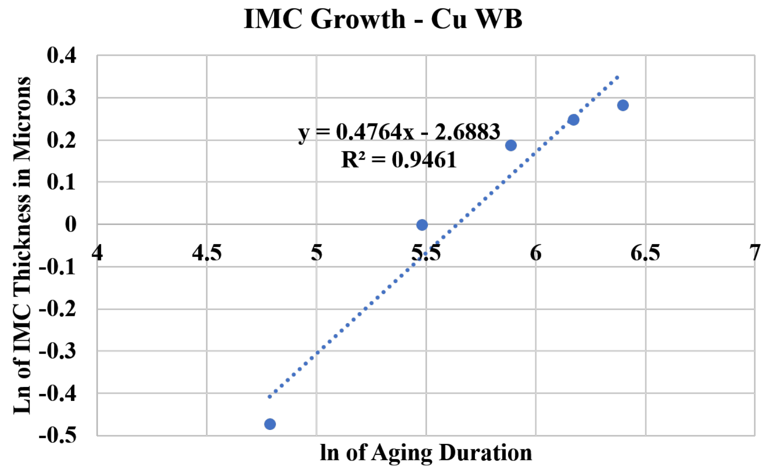

Figure 6.7: log-log plot of IMC thickness vs aging duration

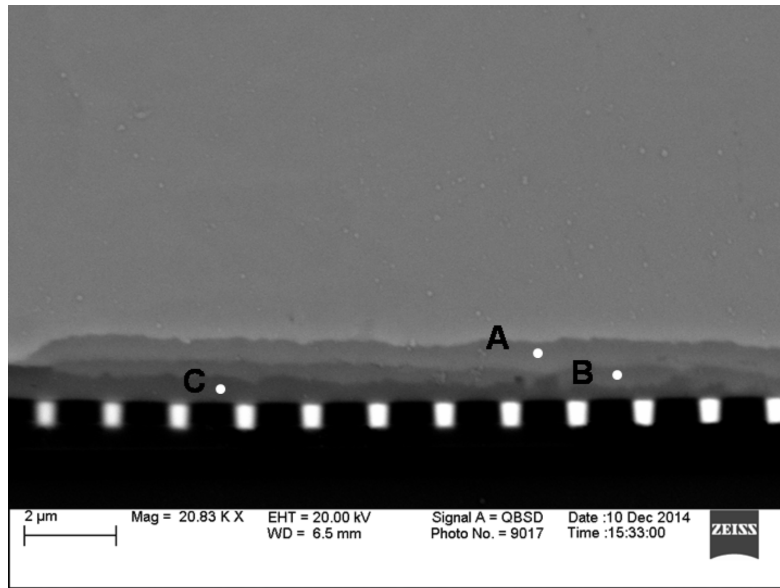

Figure 6.8: log-log plot of IMC thickness vs aging duration

Table 6.2: EDX analysis of IMC phases at point A, B and C

Element	Percent Atomic Content		
	Point A	Point B	Point C
Al	30.96	48.64	50.63
Cu	65.48	47.91	29.18
Au	3.56	3.45	1.79
Si	0.00	0.00	18.40

Figure 6.9 shows the evolution of various IMC phases during the testing. Only one phase $CuAl_2$ was present in as-bonded state. However, after 120 hours of aging, all three phases were observed. As the aging duration increases, Cu_9Al_4 phase was found to be dominating and started to consume other two phases. Increase in the thickness of IMC layer dropped significantly because the Al pad was completely consumed at this point (after 240 hours). However, due to abundant supply of the Cu form bond side, and lack of free Al, thickness of the Cu rich phase continued to increase. After 720 hours of aging, CuAl layer was barely visible. If the part is aged for more time, eventually Cu rich phase will consume rest two IMC phases and convert them into Cu_9Al_4 [4], [63].

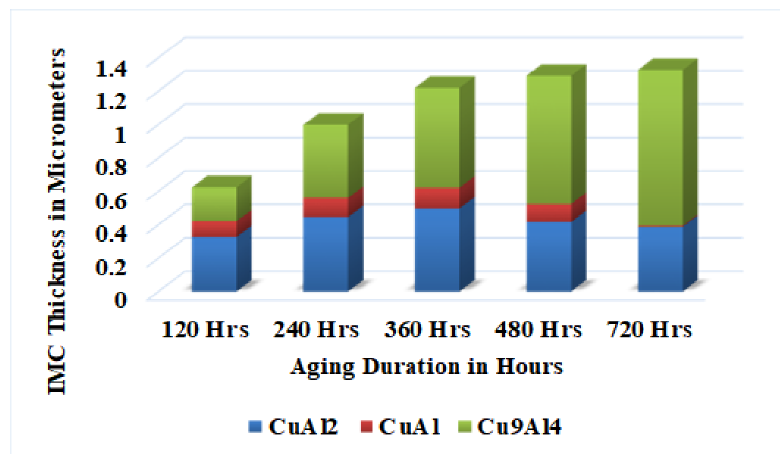

Figure 6.9: Evolution of different IMC phases due to high temperature exposure

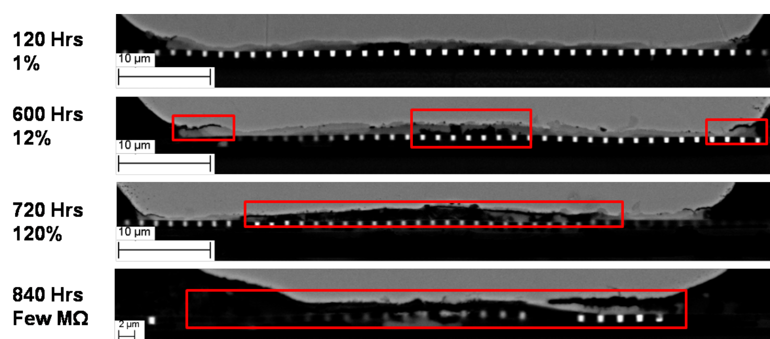

Figure 6.10: Crack initialization and propagation in Cu-Al wirebond system

Figure 6.10 shows the cracking observed at the wirebond interface. After 120 hours of aging, crack was found along the periphery of the ball bond at the interface of Cu rich IMC phase and Cu. This cracking is due to the corrosion of an IMC. Corrosion process takes place in

the presence of an ionic contamination, which is released by degraded molding compound and very high ambient temperature [34], [112]. The crack continued to grow towards the center of the wirebond as the part was subjected to more thermal stress. After 240 hours of aging, due to extremely high temperature and complete consumption of Al pad, silicon oxide which is present below the pad started to diffuse into the ball bond. This effect can be seen predominantly at the center of the ball bond as shown in Figure 6.10 (600 hours on wards). This defect starts from the center of the ball bond because IMC distribution at the center is more uniform and consistent as compared with the edges.

Figure 6.11 shows the change in the shear strength of the wirebonds due to accelerated aging. Each box plot consists of 32 data points. Initial shear strength was around 40grams, and it increased to 52gram force after 240 hours of thermal aging. Further aging caused drop in the shear strength and at the time of the failure recorded strength was 30grams. Drop in the shear strength indicates weaker connection at the bond pad interface due to degradation of the connection. Sheared surfaces were analyzed using SEM to identify different failure modes.

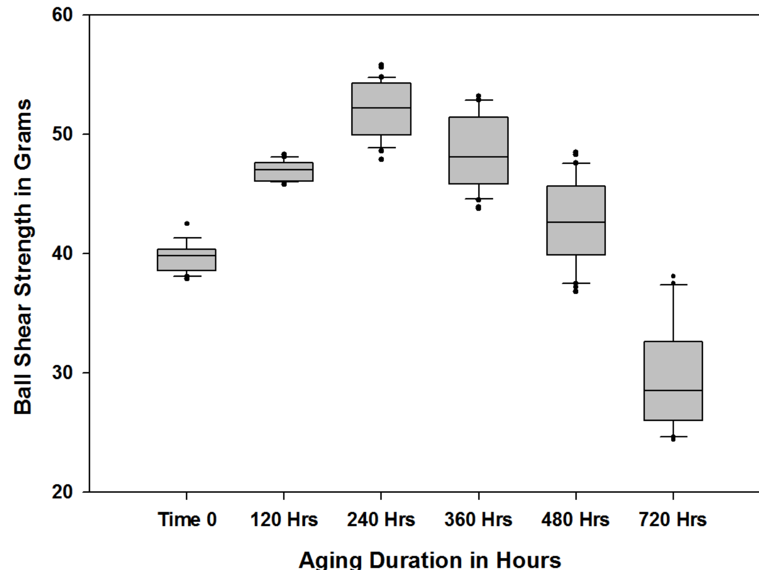

Figure 6.11: Change in shear strength of bond-pad interface as a function of time

Two modes were identified as shown in Figure 6.12. Mode I showed little or no residue of Cu or IMC on the sheared surface. Peeling of Al pad was observed. This failure mode ensures strong mechanical bond between Cu and IMC and is a desirable mode of failure. Mode II on the other hand showed residues of Cu or Cu-Al IMC on the sheared surface, as shown in (B).

The residues were concentrated along the periphery of the ball bond. This proves that the link between IMC and Cu ball bond along the periphery was the weakest. A clean cut was observed at the center of the ball bond, this proves that IMC-Cu interface was still strong, however IMC-silicon oxide interface was the weakest. Complete consumption of the Al pad caused localized detachment, which explains the clean cut observed in mode II type failure, at the center of the wirebond. The shear failure modes are consistent with the peripheral cracking, and complete consumption of Al pad that we found during the cross-sectioning (Figure 6.10). Figure 6.13 shows an evolution of the shear failure modes as the aging duration increases. During the initial part of aging, till 240 hours, mode I type is dominant. However, after that mode II became dominant and at the time of failure, only mode II was observed. The initial increase in resistance (Until 240 hours) takes place at slower rate compared with the later part. This increase in resistance can be contributed to growth different phases of IMC which have much higher resistivity than Cu and Al [113]. This void and defect free growth makes bond stronger, which increase the shear strength of the wire bonds as shown in Figure 6.11. Mode I type shear failure mode is dominant during this phase which reflects excellent health of the wirebond. As the aging duration increases furthermore, the rapid increase in the resistance was observed. This can be contributed to the reduction in area available for electron flow due to peripheral crack propagation and localized detachment of IMC and silicon dioxide (Figure 6.10). The physical detachments and degradation of interface yields into reduction of shear strength from 52 grams to 30 grams (Figure 6.11). Mode II type shear failure becomes dominant during the process, which confirms the findings.

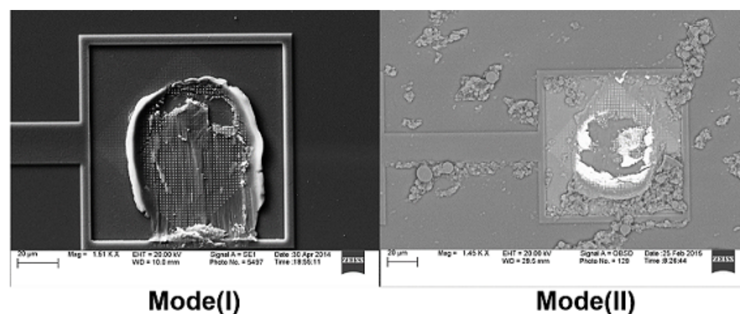

Figure 6.12: Shear failure modes (A) Mode I (B) Mode II

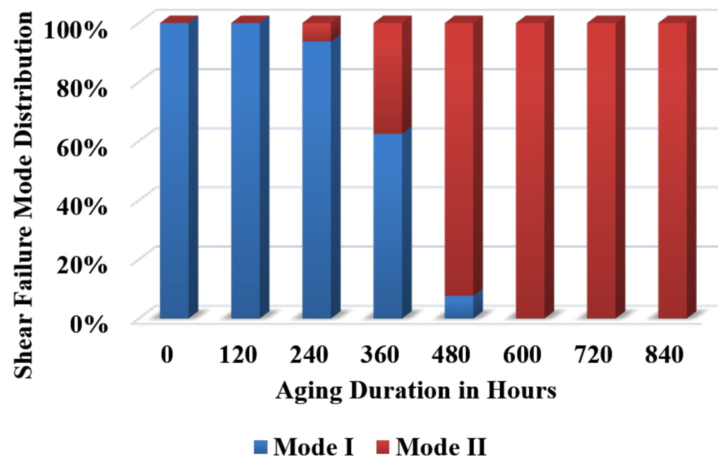

Figure 6.13: Evolution of shear failure modes

6.4.1.2 PCC Wirebond

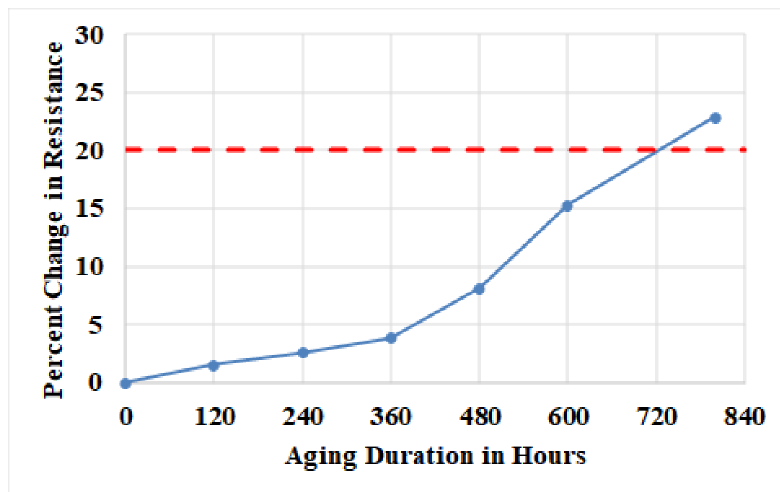

Figure 6.14: Increase in Resistance of PCC wirebonds

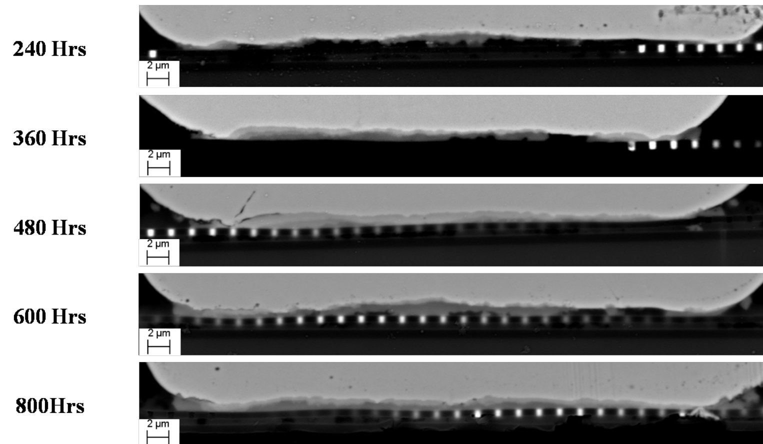

Figure 6.15: Growth of PCC-Al IMC at bond-pad interface

Figure 6.14 shows change in the resistance of the PCC wirebond due to aging at high temperature. Red dashed line in the plot shows failure threshold. After aging for 800 hours, change in resistance of the wirebonds was more than 20%. Rate of increase in resistance was slow during initial 5% change. After that, the rate increased and package failed at 800-hour interval. Figure 6.15 shows SEM images of bond-pad interface. Thicker IMC was observed for parts aged for longer duration. Thickness of the IMC was measured at each time interval and log plot of time versus thickness is shown in Figure 6.16.

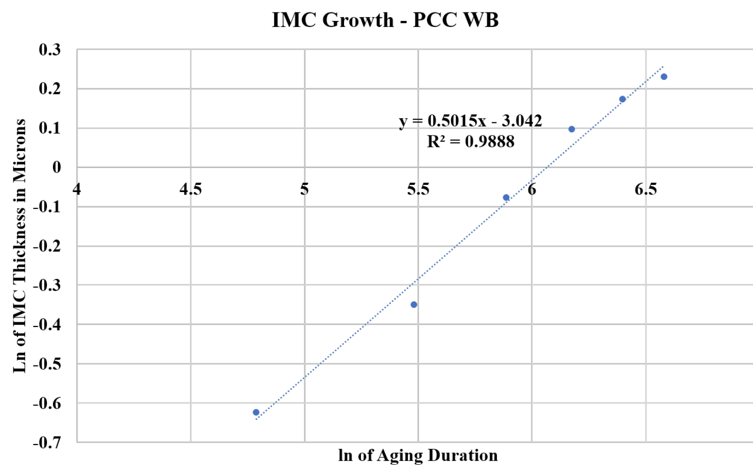

Figure 6.16: log-log plot of IMC thickness vs aging duration

Table 6.3: EDX analysis of IMC phases at point A, B, and C

Element	Percent Atomic Content		
	Point A	Point B	Point C
Al	31.58	48.04	62.80
Cu	62.01	46.57	30.49
Au	4.28	4.48	6.71
Pd	2.13	0.91	0.00

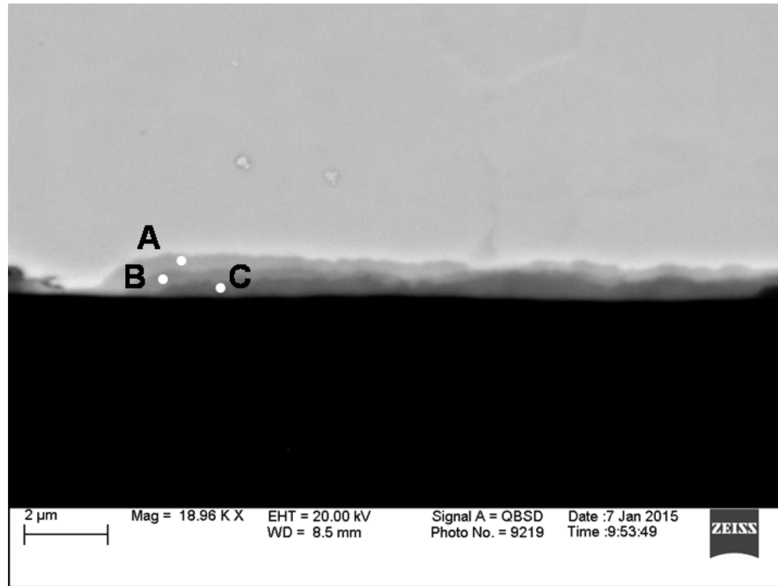

Figure 6.17: Phases in PCC-Al wirebond system due to exposure to high temperature

Maximum thickness of the IMC was 1.20 µm. This was lower than the maximum thickness of Cu-Al IMC, which was 1.33 µm. Exponent value of time was found to be 0.5018, which depicts that IMC growth was diffusion driven. Figure 6.17 shows close-up view of the three different phases found in the IMC layer. EDX point analysis was performed at A, B, and C point. Point A was Cu rich phase (Cu_9Al_4), and point C was Al rich phase ($CuAl_2$). Point B had equal content of both element (CuAl). Results of the EDX point scan are presented in Table 6.3. Very small amount of Pd was found in the phases near to Cu ball and it was absent in Al rich phase. Presence of Pd along the bond-pad interface acts as a diffusion barrier and slows down the growth of the IMC, making PCC wires slightly more reliable than bare Cu wires [114], [115].

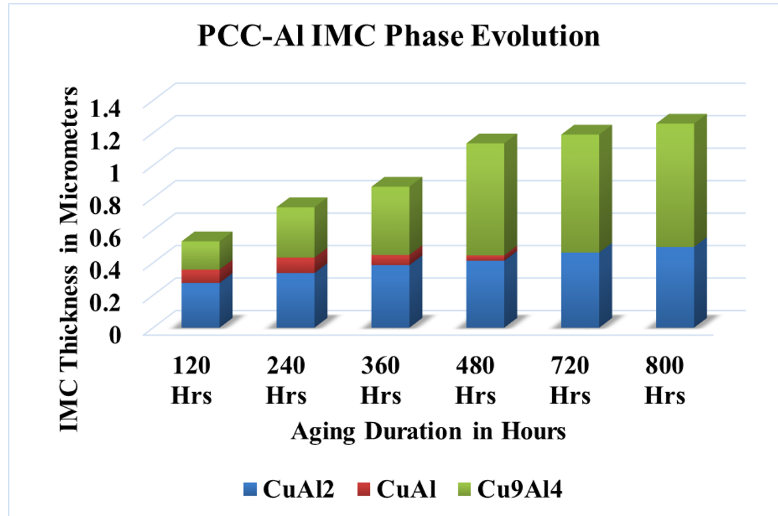

Figure 6.18: Evolution of different IMC phases due to high temperature exposure

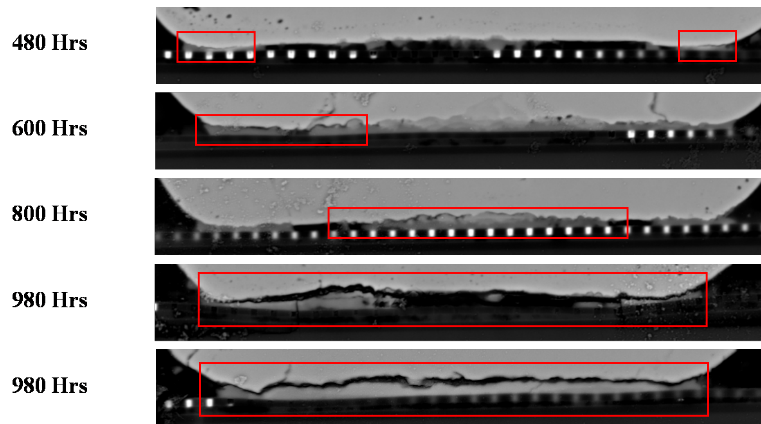

Figure 6.19: Crack initialization and propagation in PCC-Al wirebond system

Figure 6.18 shows evolution of IMC phases over time. After 120 hours of aging, three phases were found. However, as the aging time increases, after 480 hours of aging, CuAl IMC layer gets converted into copper rich phase. During the initial stages, $CuAl_2$ phase grows thicker. However, at the later stage, it also gets transformed into Cu rich phase. This behavior is due to abundance in Cu supply from the ball side and is consistent with behavior observed for bare Cu wires. Figure 6.19 shows crack initiation and propagation at the bond pad interface. Corrosion crack originates at the periphery of the ball bond during the initial stages. As the aging time increases, crack propagates towards the center of the ball bond. This type of cracking is observed in-between Cu rich phase and Cu ball bond. If the part is aged for prolonged

period (980 Hrs), complete cracking of the interface resulting into detachment of the interconnect was observed. Degradation of the PCC and bare Cu wirebond follow similar degradation mechanism. Presence of Pd in case of PCC wirebond seems to delay the degradation process by small amount. Figure 6.20 shows evolution of shear strength of the ball bond. At the start of the test, ball shear strength was found to be 30 grams. It increases till 360 hours of thermal aging. During further aging, the shear strength started to reduce and at the time of failure, it was around 12 grams. Sheared surfaces were then observed using SEM. Based on the morphology of the remaining area, shear failure modes were divided into two types. Failure modes for bare Cu and PCC were the same. Mode I type failure mode indicates strong bond between PCC and Al, and Mode II type indicates presence of cracking and degraded surface.

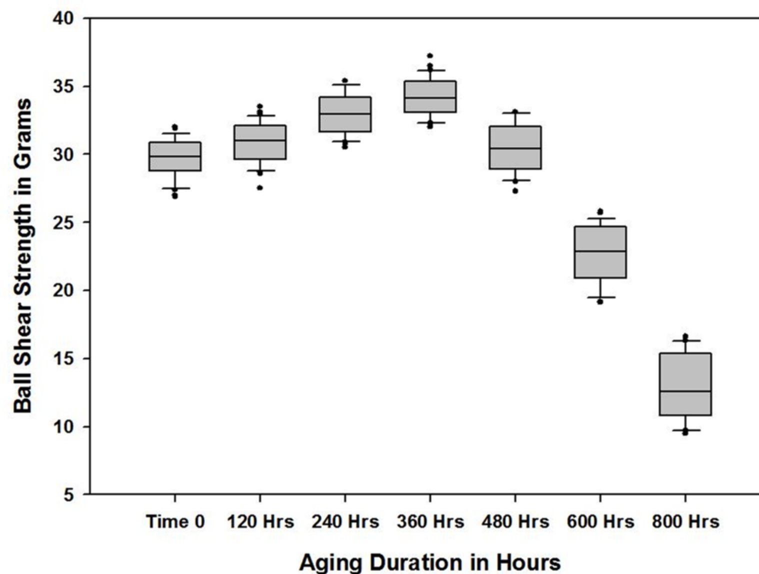

Figure 6.20: Change in shear strength of bond-pad interface as a function of time

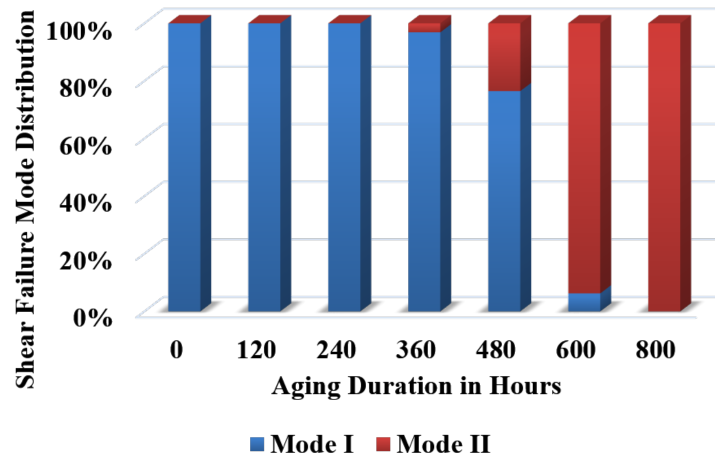

Figure 6.21: Evolution of shear failure modes

Figure 6.21 shows evolution of the shear failure modes. During first 360 hours of aging, Mode I type failure mode was dominant, accompanied by increase in shear strength. This is due to the initial growth of the IMC which makes bond stronger. After this point, the IMC starts to degrade and cracks initiates at the periphery of the bond as shown in Figure 6.19. This makes wirebond weaker and makes mode II type failure more dominant. After 800 hours of aging, only mode II type failure was observed at the sheared surface. The time-frame after which shear strength decreases with mode II type failure mode is dominant, rapid resistance increase was observed as shown in Figure 6.14. This rapid growth in resistance could be contributed to the thicker IMC, and the degradation of the IMC which reduces the contact area resulting into higher resistance. Overall failure mechanism for PCC wires was similar to the Cu wires. Presence of Pd at the bond pad delayed the degradation.

6.4.1.3 Ag Wirebond

Figure 6.22 shows increase in resistance of Ag wirebonds due to aging at high temperature. Red dashed line in the plot shows failure threshold. Package failed after 840 hours of thermal aging which is slightly higher than time to failure for the PCC wire. Unlike the Cu and PCC wires, Ag wires show approximately linear trend of change in resistance till 720 hours of aging. Figure 6.23 shows growth of IMC at Ag-Al interface due to high temperature exposure. Even after 120 hours of aging, significant IMC was present at the interface. Thickness increases

as parts were subjected for aging for longer duration. Ag wirebonds had overall thicker IMC formation and growth than Cu and PCC wires.

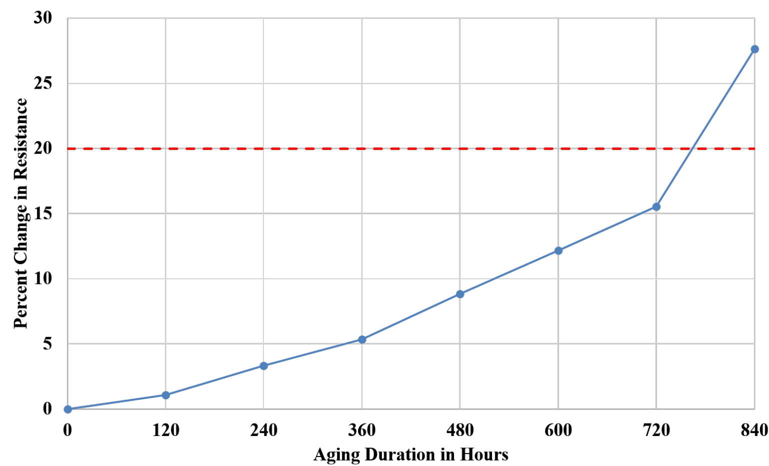

Figure 6.22: - Increase in Resistance of Ag wirebonds

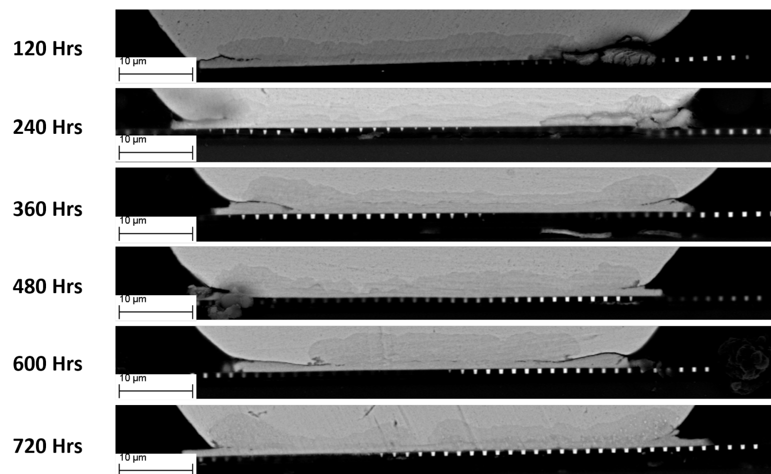

Figure 6.23: Growth of Ag-Al IMC at bond-pad interface

Log-log plot of IMC thickness and time is shown in Figure 6.24. Time exponent for the Ag wirebond was 0.4, which was far from ideal value of 0.5. Even through IMC growth is diffusion driven, it does not follow Fickian diffusion. This could be contributed to thicker IMC formation. IMC compounds often have different physical properties than the individual elements from which they are made off. Thicker IMC indicates that Ag or Al had to travel long distance via IMCs to form new compounds. Higher thickness of IMC could affect the rate at which Ag is diffusing in the Al pad and affect IMC growth rate.

Table 6.4: EDX analysis of IMC phases at point A, B

Element	Percent Atomic Content	
	Point A	Point B
Al	25.02	33.48
Ag	73.26	64.12
Au	1.72	2.40

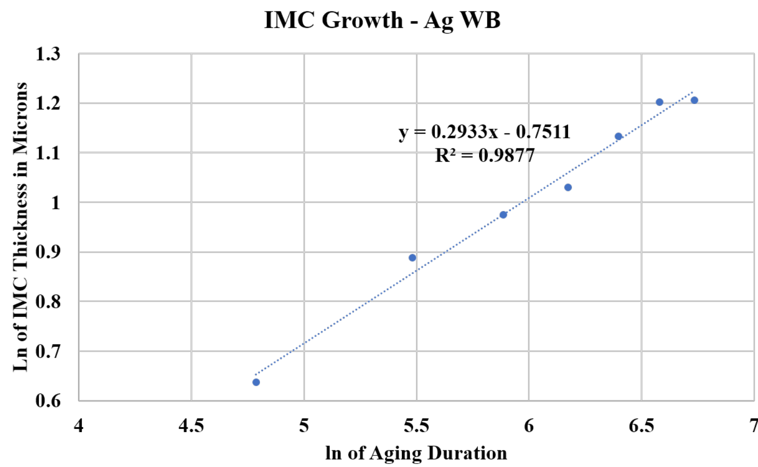

Figure 6.24: log-log plot of IMC thickness vs aging duration

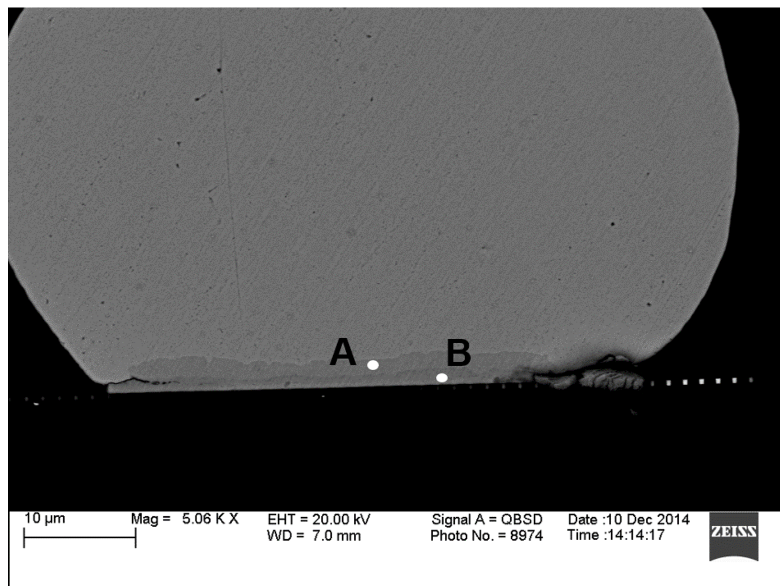

Figure 6.25: Phases in Ag-Al wirebond system due to exposure to high temperature

At the Ag-Al bond-pad interface, two different phases of IMC were observed. EDX point scans were performed at points A and B as shown in Figure 6.25. Results from Table 6.4 show that even though both layers were Ag tich layers, they had different formulation. Top

layer (near ball bond) consist of Ag_3Al compound, and bottom layer (near bond pad) consist of Ag_2Al. These measurements were in agreement with results reported in earlier articles [62], [60]. Figure 6.26 shows evolution of the IMC phases due to high temperature aging. During the initial stage of aging, both phases were thickening. After 480 hours of aging, Ag_3Al was found to be rapidly evolving than Ag_2Al. this can be contributed to limited supply of Al from the very thin pad and constant supply of Ag from the ball bond. After 840 hours of testing, both phases were present, but Ag3Al layer was found to be covering majority of the thickness.

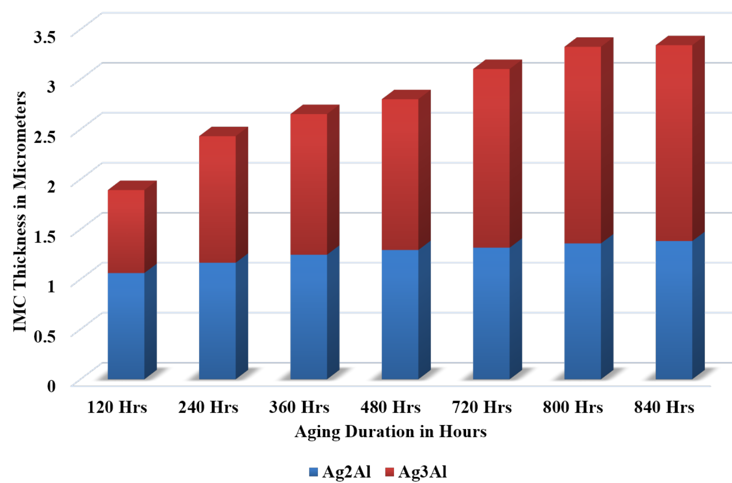

Figure 6.26: Evolution of different IMC phases due to high temperature exposure

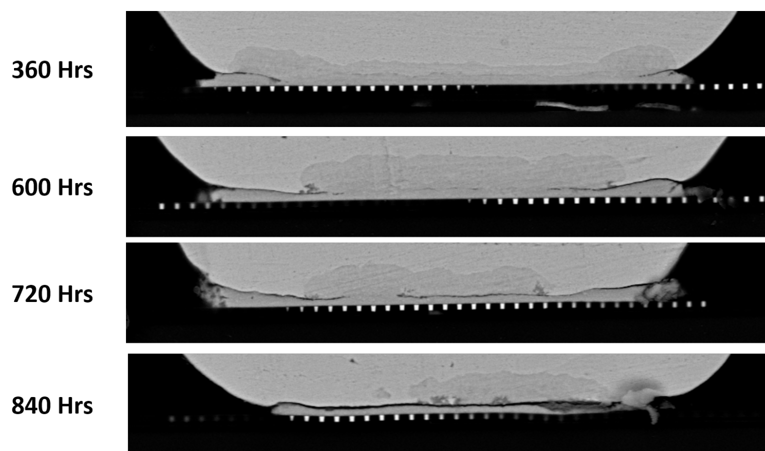

Figure 6.27: Crack initialization and propagation in Ag-Al wirebond system

Cracking at the wirebond interface was observed after 360 hours of aging as shown in Figure 6.27. The small peripheral crack was observed in between two phases of IMC. Unlike Cu and PCC wires, no cracking was observed at the interface of IMC-ball bond. The crack

grows rapidly towards the center as aging duration increases. After 840 hours of aging, majority of the interface was cracked. After 1200 hours of aging, full crack resulting into bond lift was observed. In Ag wirebonds, even though crack initiated at early stages, it did not cause major damage to the electric properties of the junction. Crack was slow to propagate when compared with the cracking in Cu and PCC wirebonds. After 720 hours of aging, crack had covered 40% of the cross-section, but resistance increase was still 15%. This could be contributed to higher electric conductivity of the Ag or very irregular growth of crack in out of plane direction.

6.4.1.4 Au Wirebond

Figure 6.28shows change in resistance of Au wirebonded packages at very high ambient temperatures. Red dashed line indicates failure threshold of 20% change in resistance.

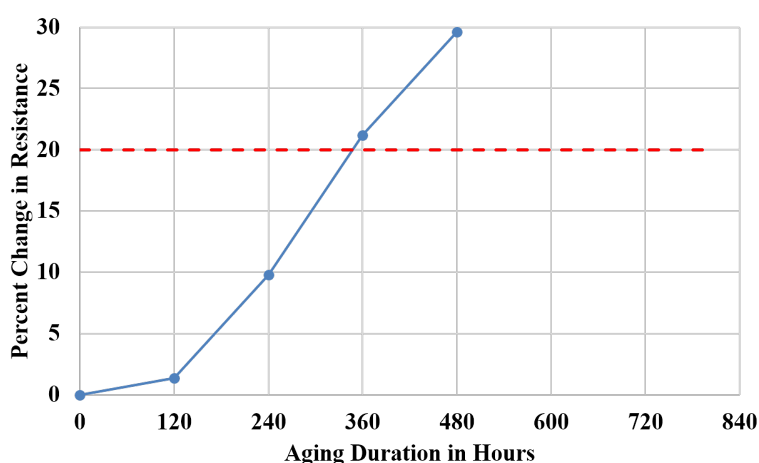

Figure 6.28: Increase in Resistance of Au wirebonds

Failure was observed only after 360 hours of aging. Au wirebonded packages failed fastest among all material candidates. Rate of change in resistance increased significantly after initial 120 hours of aging. Figure 6.29 shows change in the morphology of the bond-pad interface. Very thick layer of intermetallics was observed in as bonded state. Increase in thickness was observed as the aging duration increased. Au wirebonds were found to have the thickest IMC in as bonded state, compared with Cu, PCC, and Ag wirebonds. Voiding was observed in the IMC phases, along the periphery after 120 hours of aging. Extent of voiding increased with the aging time. After 360 hours of aging, very thick but voided layer of IMC was observed.

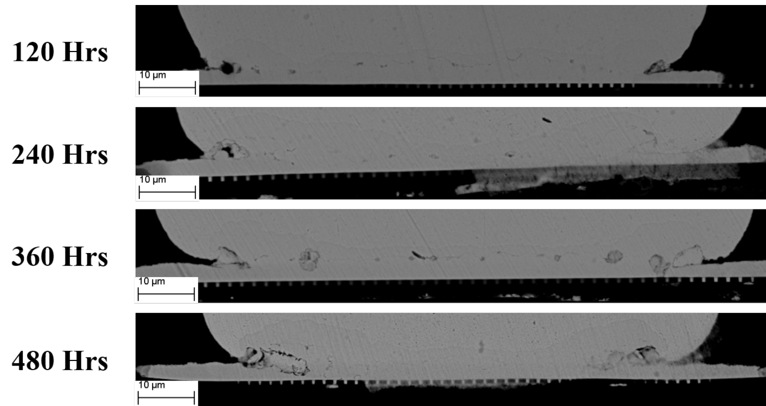

Figure 6.29: Growth of Au-Al IMC at bond-pad interface

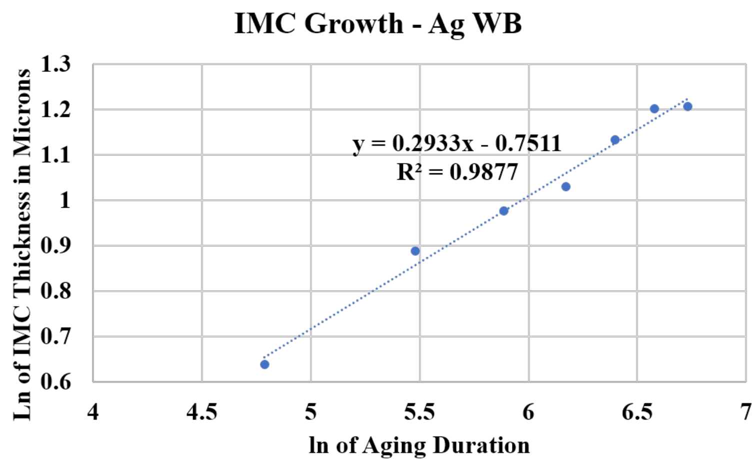

Figure 6.30: log-log plot of IMC thickness vs aging duration

Figure 6.30 shows log-log plot of increase of the IMC thickness due to thermal aging. Time exponent of the fit was found to be 0.28, which is least among all materials tested, and shows maximum deviation from Fickian diffusion. Ideally it is expected that the wirebond IMC will be due to Fickian diffusion, which was found to be true in case of Cu and PCC wires. In case of Au wires IMC which has different physical properties form very thick layer at interface, which affects the diffusion rate of the process. IMC phase transformation mechanisms add into this effect, making it more profound. EDX scan was performed on the cross-sections and is shown in Figure 6.31. Two phases were observed during the initial stages of aging (A), while only one phase was found after failure. Results of the EDX scan are shown in Table 6.5. Analysis revealed that in both figures (A and B), all observed phases were Au rich phases. The phase at point A in figure (A) was Au4Al and phase point B was Au_8 Al_3. After failure (figure

Table 6.5: EDX analysis of IMC phases at point A, B

Fig Number	Element	Percent Atomic Content	
		Point A	Point B
A	Au	80.38	69.40
	Al	19.62	30.60
B	Au	82.26	81.53
	Al	17.74	18.47

B), only Au_4Al phase was found which indicates that it is the terminal phase, and all other phases transform into Au_4Al. This is consistent with the results reported in [21][22].

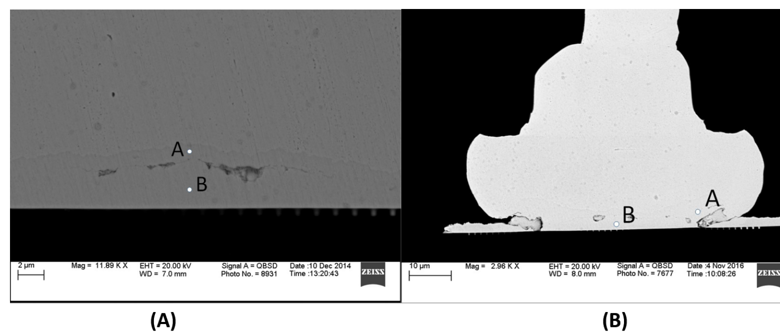

Figure 6.31: Phases in Au-Al wirebond system due to exposure

In Au wirebonds, rapid phase transformation is observed along with fast growing IMC. Due to very thick IMC, different phases of the IMC are supplied with Ag or Al atoms at different rates. The phase transformations at different rates along with higher diffusion rate of Au-Al system leads to Kirkendall voiding. Voiding becomes sever as aging period increases, as shown in Figure 6.32. During the initial phases of aging, only minor voiding was observed. Voiding was focused at the interface of the two phases of the wirebond. As the part is aged for prolonged time, voids grow and smaller voids merge together to form larger voids which could as big as few micrometers. Presence of such voids in between two phases of IMC confirms that different rates of the phase transformations was primary cause of the voiding. Au being chemically inert metal, does not show typical corrosion based degradation/cracking at the interface. In Au wires, voiding does not only reduce area available for current flow, but also weakens the Au-Al junction. Figure 6.33 shows change in shear strength of Au wirebonds over time. Initial observed strength of the bond was around 52 grams. Au wires had higher initial shear strength due to well developed and strong IMC that formed during the wirebonding process.

Shear strength increased to 54-gram force after 120 hours of aging, and then dropped rapidly. At the time of the failure, shear strength of the wirebond was around 39 grams. Higher data spread was observed when wirebond started to degrade (after 120 hours of aging).

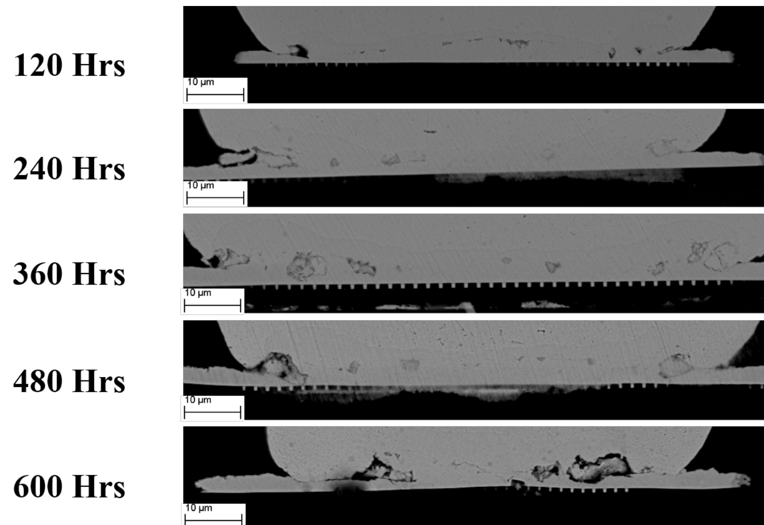

Figure 6.32: Voiding in Au-Al wirebonds

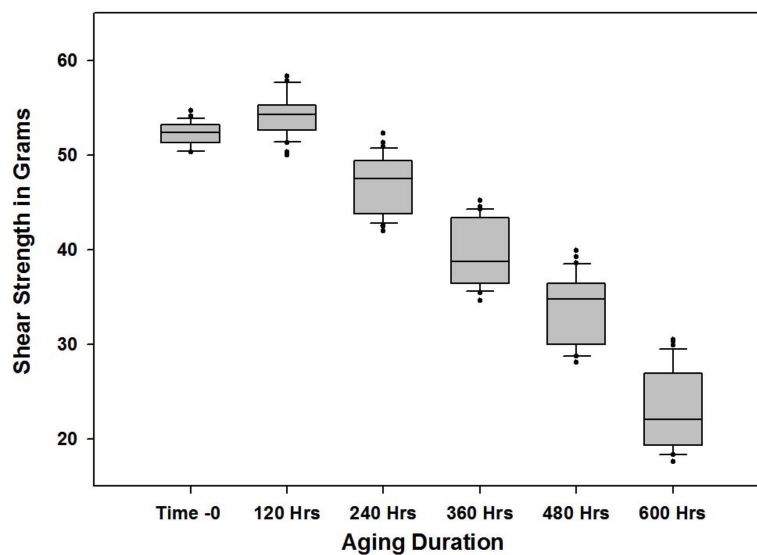

Figure 6.33: Change in shear strength of bond-pad interface as a function of time

Figure 6.34 shows shear failure modes for Au wirebonds. In mode I type failure, bulk Au wire shears and the residue was found at the sheared interface. This is a desired mode of failure showing strong bonding of Au wire and Al pad. In mode II type failure, peripheral ring of residual IMC, along with clean lift at the center of the ball bond was observed. The clean lift in the center was due to complete consumption of the Al pad. Along the periphery, even

though Al pad was consumed by Au, voided interface served as the weakest link and bond wire fractures along the voids, leaving a thick layer of IMC on the sheared surface. Similar type of failure was categorized as mode III when pad cracking was found beneath the ball bond. Figure 6.35 shows the distribution of the shear failure modes. In as bonded state, only mode I type failure was observed. However, after aging for only 120 hours, mode II type failure was found to be dominating, and at the time of failure, only mode II type was observed. Transition from mode I to more II is very drastic after 240 hours of aging. at this point, rapid drop in shear strength was observed along with major voiding at the periphery of the ball bond as shown in Figure 6.32. Decreasing shear strength with mode II type failure, presence of large amount of voiding could be correlated with the higher rate of increase in resistance, which ultimately leads to the failure.

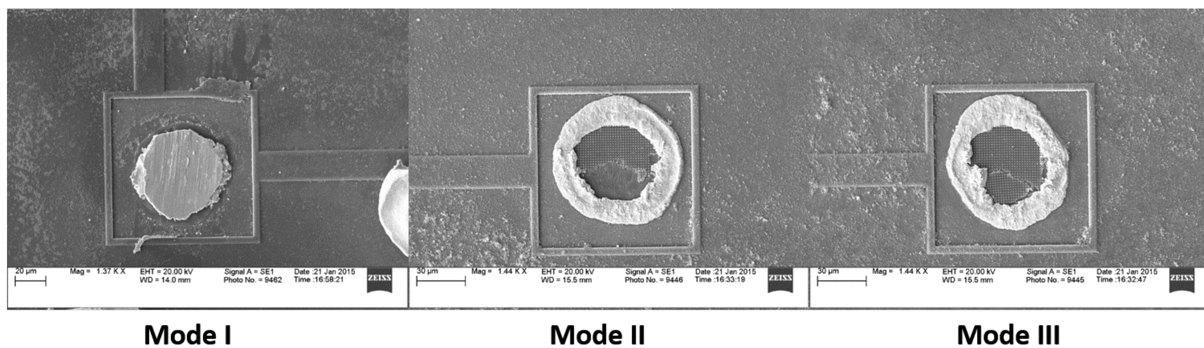

Figure 6.34: Change in shear strength of bond-pad interface as a function of time

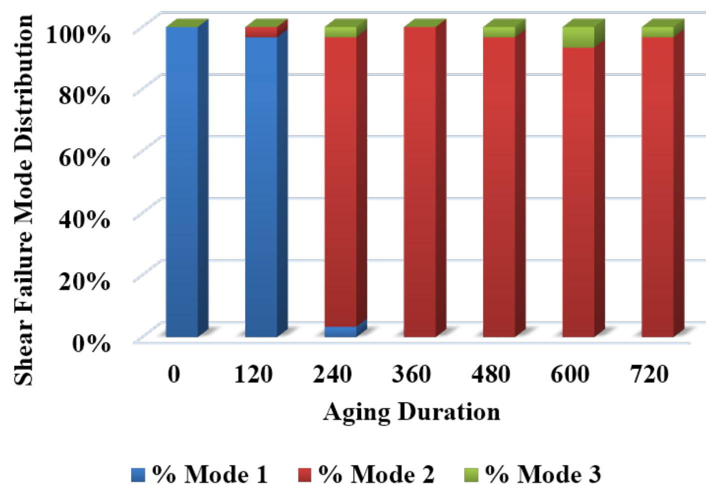

Figure 6.35: Change in shear strength of bond-pad interface as a function of time

6.4.1.5 Comparison of Wirebonds

Figure 6.36shows compiled resistance data for all four wirebond material candidates. Ag wirebonded samples were found to be most reliable, while the Au wirebonded packages were first one to fail. Cu, Ag, and PCC wirebonds had slower rate of increase in resistance at the initial stages. Change in resistance of the wirebonds pairs was contributed to growth of different IMCs at the bond-pad interface, followed by degradation.

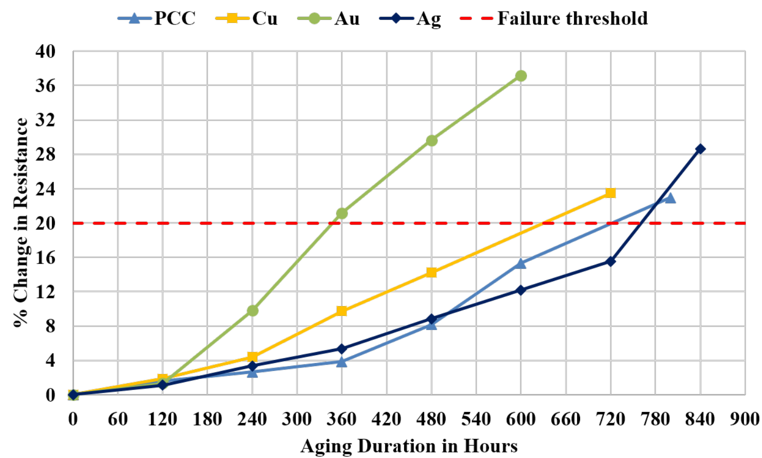

Figure 6.36: Change in resistance of wirebonds due to high temperature exposure

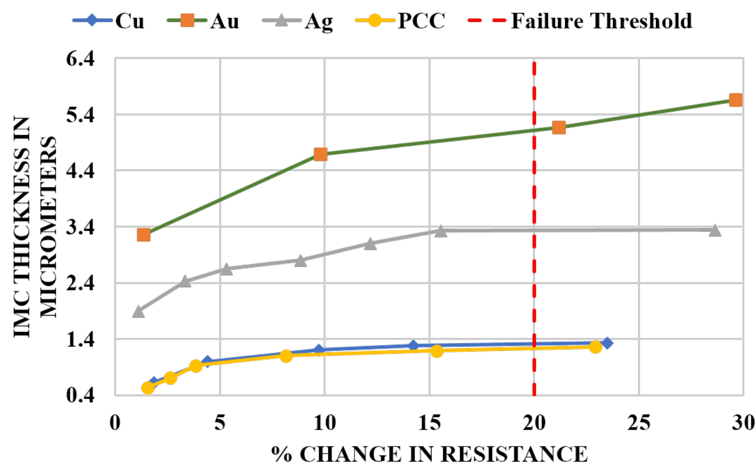

Figure 6.37: Change in resistance of the packages vs IMC growth

Figure 6.37 shows change in resistance for all wirebonds against IMC thickness. For Cu and PCC wires, IMC thickness increases rapidly for first few data points. After crossing 10% change in resistance, IMC continues to grow at very slower pace. For Ag wires, similar trend

was observed till 15% change in resistance. This proves that increase in the resistance at early stages is due to the IMC growth. Rapid resistance change that is usually observed before failure was due to the corrosion based degradation of the developed IMC. For Au wire, IMC continued to grow till the end and failure was observed not due to corrosion but due to very thick IMC along with Kirkendall voiding. Figure 6.38 shows log-log plot of IMC growth over time for all wirebond candidates. In as bonded state, Au had the highest IMC formation at the interface. As the parts were aged, it also showed maximum growth rate followed by Ag, Cu, and PCC wires. Presence of palladium at the bond pad interface has proven to lower the IMC growth rate when compared with bare Cu Similar behavior was observed in this study. Even though Ag had higher IMC thickness as well as growth rate than Cu, resistance increase for Ag wirebonds was slower than Cu wires. This can be contributed to higher resistivity of the Cu-Al IMC. IMC growth in Cu and PCC wirebonds took place because of Fickian diffusion. Au and Ag wires did not follow this trend because of the thicker, faster, and voided IMC formation. Thicker IMC affects the rate of the transportation of the atoms which leads to slower IMC growth at during the final stages of the testing, compared with the growth rate at the initial stages.

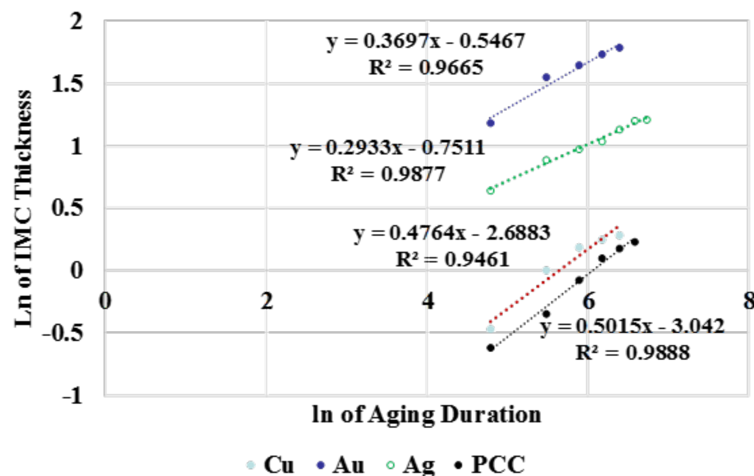

Figure 6.38: Change in resistance of the packages vs IMC growth

Cu and PCC wirebonds had different shear failure modes than Au wirebonds. Au wirebonds had local detachment at the center and brittle fracture along the periphery (due to Kirkendall voiding) at the time of the failure. Cu and PCC wires showed peripheral cracking (corrosion based cracking) with much thinner IMCs and partial cracking at the center. At the time

of the failure Au wirebonds, lots of voiding was observed. Cu and PCC wirebonds showed corrosion based cracking along the periphery of the ball bond in the later stages of the aging. Highly localized random detachment of the ball bond from silicone was observed for Cu wirebonds. This is due to complete consumption of Al pad as shown earlier. For Ag wirebonds, even though crack was observed during the early stages of the aging, crack propagated very slowly and at the time of failure, no complete cracking was observed.

6.4.2 High Current Test

Results of the high current testing (electromigration) are discussed in this section.

6.4.2.1 Cu Wirebond

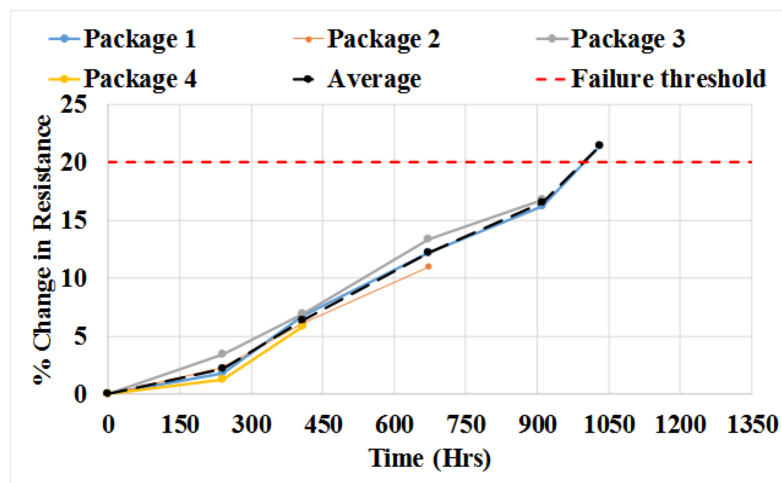

Figure 6.39: Increase in The Resistance of Cu-Al Wirebond

Figure 6.39 shows change in resistance of Cu-Al wire bonded packages. Black dashed line shows average value of change in resistance of all packages. After 1030 hours of aging, resistance change of around 22% was observed. Initial rate of change of resistance was lower (for 5% change) followed by faster rate which was constant till failure. Packages were cross-sectioned at the reading interval and micro-graph of the Cu-Al interface are shown in Figure 12. Black arrow indicates the direction of electron flow. Very thin IMC was observed at the start of the test. As the aging duration increased, IMC thickness also increased and thicker IMC with multiple phases was observed towards the end of the test. Three distinct phases of

the IMC were observed at the interface. Since part was not tested till open circuit failure, full crack at the bond-pad interface or bond lift was not observed.

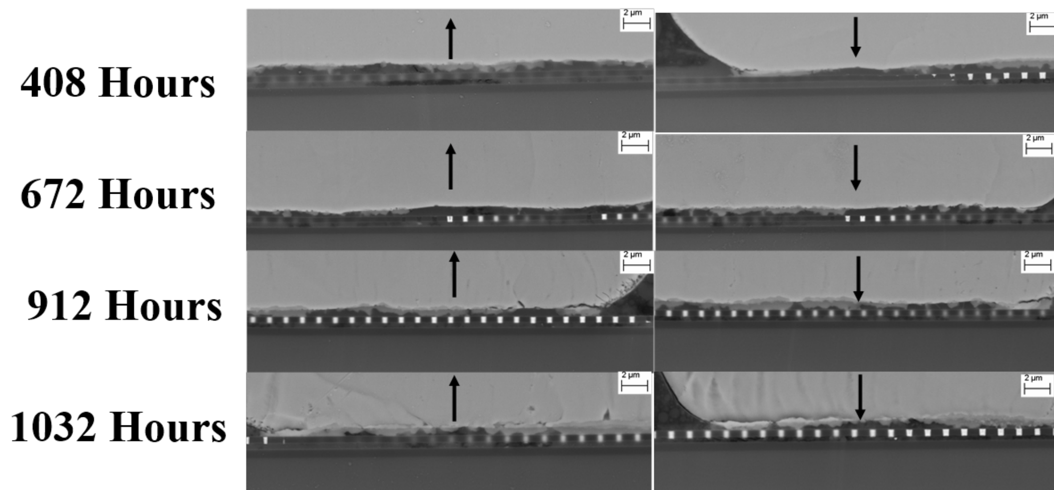

Figure 6.40: IMC Growth of Cu-Al Interconnect

These phases were identified as Cu_9Al_4, $CuAl_2$ and CuAl respectively. During the initial phase of aging, Al rich layer was more dominant, however as the aging duration increased, Copper rich phase started to become dominant. At the time of failure, all three phases were observed. Figure 6.41 shows morphology of Cu-Al interconnect at the time of failure. Interfacial crack was observed in between Cu rich phase and bulk copper wirebond, as highlighted using red box. This type of cracking indicates typical failure mode of Cu-Al wirebond system operating under high temperature environment. High current density can cause localized over heating of the Cu-Al junctions. This causes degradation of the molding compound near the overheated area. Degradation of an EMC can increase localized ionic contamination which intern yields into corrosion at the edge of the bond pad interface. Failure mode and IMC phases were consistent with prior literature focused on high temperature storage tests [4], [44]. The direction of current does not seem to cause any voiding or abnormal cracking at the interface.

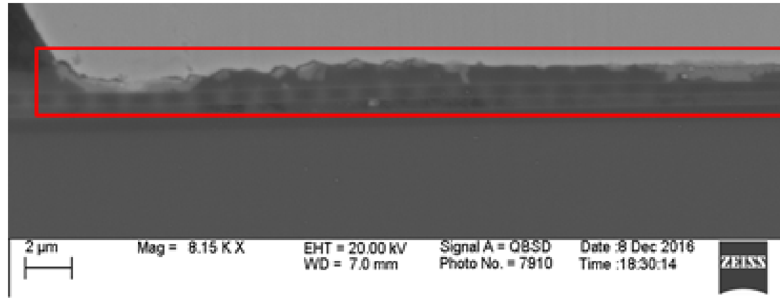

Figure 6.41: Interfacial Cracking in Cu Wirebonds

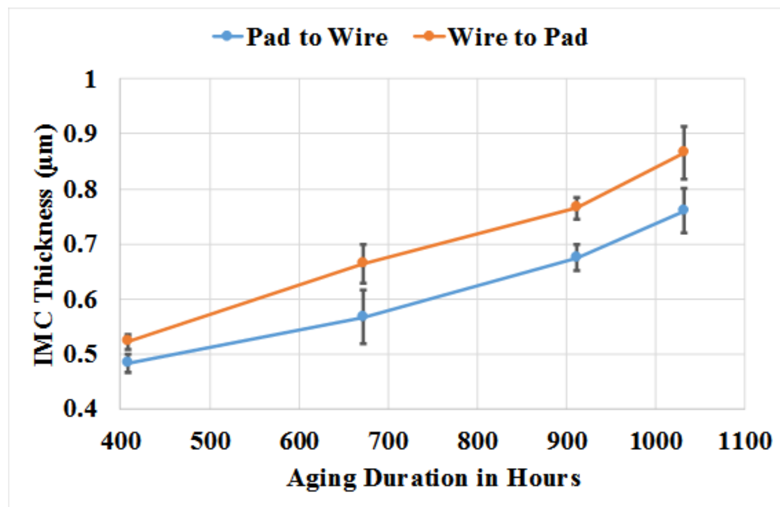

Figure 6.42: Evolution of Cu-Al IMCs

Figure 6.42 shows IMC thickness data of Cu-Al wirebond during the test period. Wider distribution of the observation points was due to wire to wire variation. After 400 hours of aging, IMC thicknesses were found to be $0.49\,\mu\text{m}$ (Pad to wire) and $0.52\,\mu\text{m}$ (Wire to Pad). The thickness increased continuously as the aging duration was increased. IMC thickness for the wirebonds with current flowing from wire to pad was consistently higher. At the time of failure, after 1030 hours of aging, IMC thicknesses were $0.87\,\mu\text{m}$ (Wire to pad) and $0.75\,\mu\text{m}$ (Pad to wire) respectively. When the electrons flow from wire to pad, even though the electromigration forces add into the diffusion process, no voiding or abnormal cracking was observed at the interface. This can be contributed to slower rate of diffusion in between Cu and Al. Figure 6.43 shows average difference in IMC thickness between the wirebond pairs, and its evolution over time. Initial difference between wirebond pair, after 400 hours of aging was $0.04\,\mu\text{m}$ (8% of maximum thickness). the difference increased continuously over time and at the time of

failure it was $0.105\,\mu m$ (12% of maximum thickness). It was found that direction of the current flow significantly affected the IMC growth rate at the wirebond interface, which reflected into abnormal resistance increase and accelerated the damage. However, this increase in resistance alone was not sufficient to cause failure. Failure mode observed here was peripheral cracking due to corrosion, which was independent of the current direction.

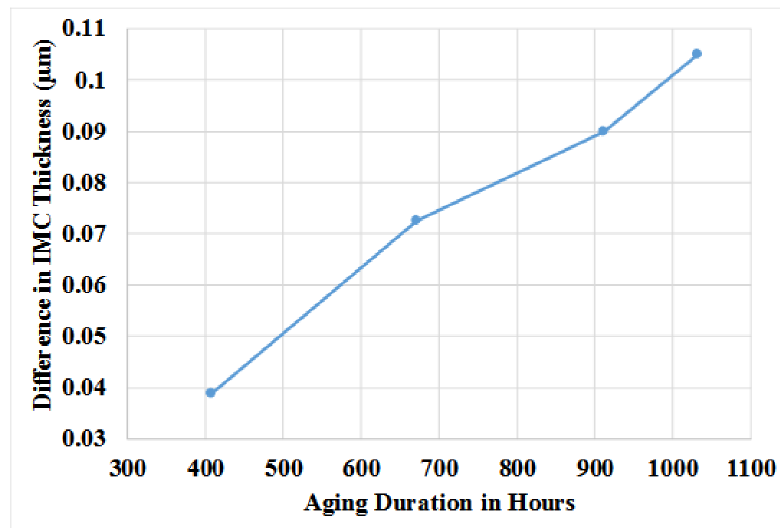

Figure 6.43: Effect of Current Direction on Cu-Al IMC Growth

6.4.2.2 PCC Wirebond

Figure 6.44 shows increase in resistance of the PCC-Al wirebond system subjected to high current at high temperature. Failure threshold of 20% change in resistance was crossed after aging for 1280 hours. PCC wirebond had the most robust performance among all wirebond material candidates. Rate of increase in the resistance was very low during initial stage. 5% increase in resistance was observed after approximately 370 hours of aging. Higher rate of increase was observed during the later phases of the testing. Figure 6.45 shows the change in the morphology of the bond-pad interface during the testing. Black arrow indicates the direction of the current flow. Very thin IMC layer was observed during the initial testing period. IMC formation and growth rate was lowest among all wirebond candidates.

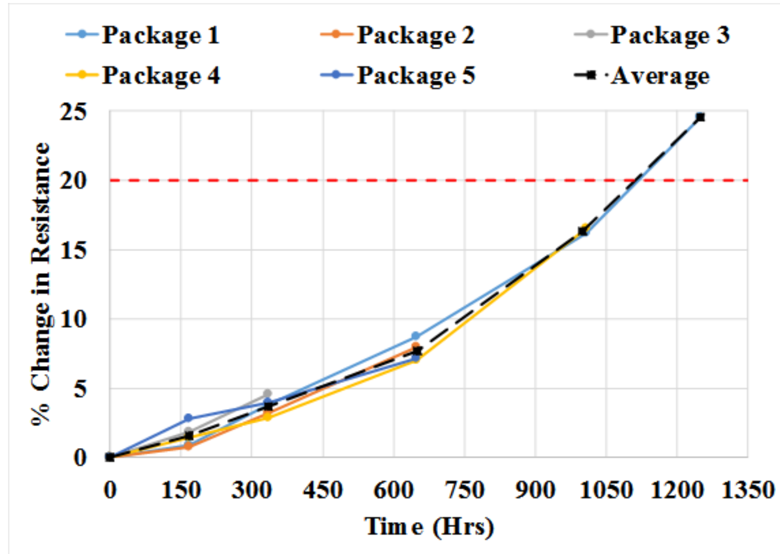

Figure 6.44: Increase in Resistance of PCC-Al Wirebond

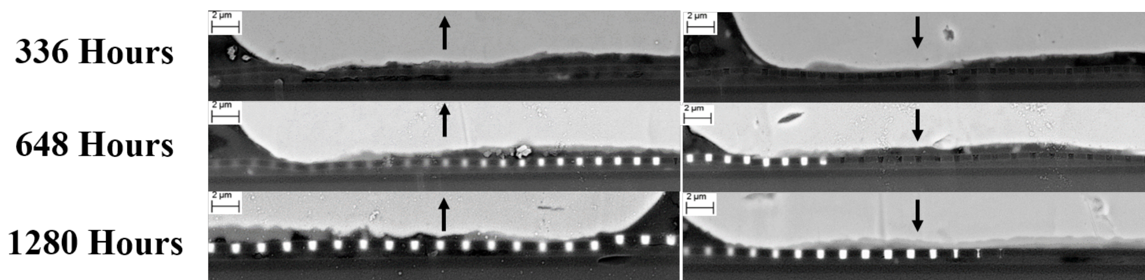

Figure 6.45: IMC Growth of PCC-Al Interconnect

Unlike Cu, upon cross-sectioning, only two distinct phases were observed. The topmost phase was found to be Cu rich phase Cu_9Al_4, which the darker bottom phase was Al rich phase $CuAl_2$. Al rich phase was observed at the bond pad interface from the as bonded state. The Cu rich phase appeared only after the testing had started. This shows that for PCC wires, $CuAl_2$ phase was the starting phase. This is consistent with the phase evolution observed for Cu wires.

IMC thicknesses were measured using image processing software, and the results are shown in Figure 6.46. No significant difference was found when IMC thicknesses of the wire-bond pairs were classified based on the electron flow direction. This proved that the direction of the current flow did not have any significant impact on the IMC growth rate. $0.63\,\mu m$ thick IMC was observed at the time of failure. IMC growth rate was the lowest for PCC wires. The slower IMC formation rate and absence of CuAl IMC phase was due to presence of palladium

along the periphery of the wirebond. researchers have shown that during the wirebonding process, palladium gets randomly distributed at the wire-pad interface. The scattered palladium acts as a barrier for the diffusion of Cu into Al when subjected to harsh environments. Vary slow diffusion results into slower IMC growth rate. This also affects the phase transformation process, and allows formation of very stable phases (Cu_9Al_4 and $CuAl_2$) only. Figure 6.47 shows the differences in the IMC thicknesses of the wirebonds due to opposite electron flow directions. During the initial stage of the testing, this difference was nearly zero. At the time of failure, difference in the IMC thickness was found to be less than $0.01\ \mu m$, which was 1.5% of the total IMC thickness.

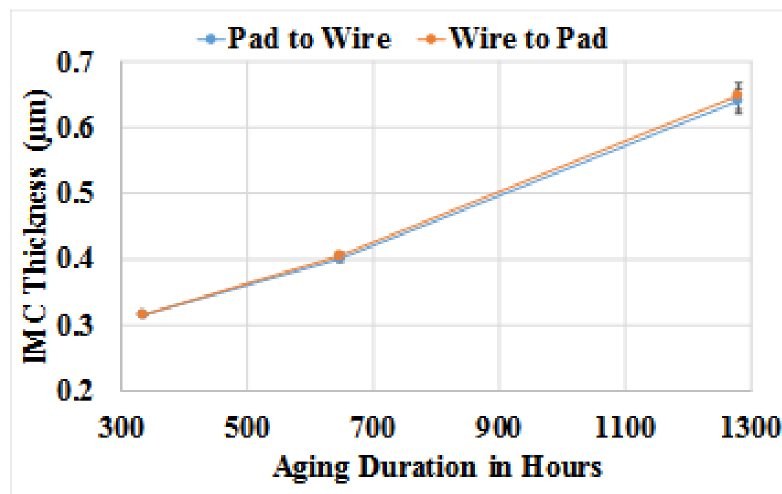

Figure 6.46: Evolution of PCC-Al IMCs

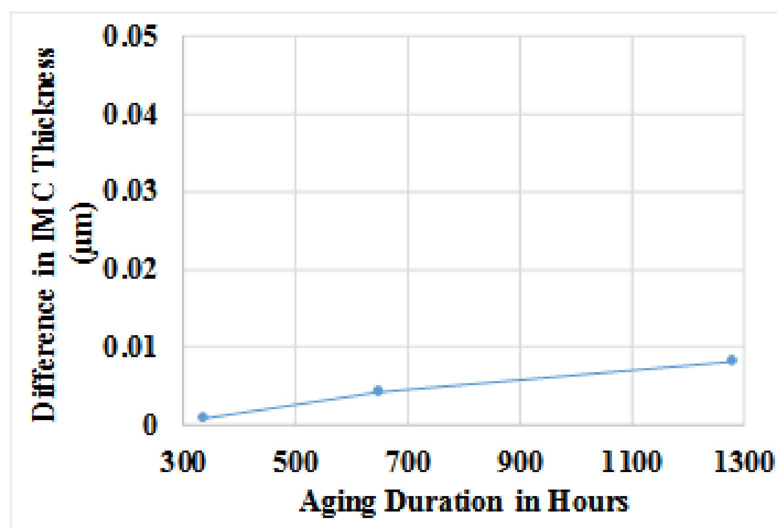

Figure 6.47: Effect of Current Direction on PCC-Al IMC Growth

Table 6.6: EDX Analysis at The Crack Front

Point	Percent Atomic Content						
	Au	**Al**	**Cu**	**W**	**Cl**	**Ti**	**O**
A	6.63	21.42	51.94	2.15	0.46	1.22	16.18

Figure 6.48 shows the crosses-section of the failed wirebond. No abnormal voiding was observed at the failed interface. Peripheral cracking was observed on the failed wirebonds. Crack was observed in between bulk Cu wire and Cu rich phase. EDX analysis was performed at the cracked interface to investigate the cause of the cracking. Result of the EDX point scan is shown in Table 6.6. Presence of Cl ions and oxygen confirms that the cracking was corrosion based. This is consistent with the failure mechanism observed for Cu wires. At elevated temperatures, molding compound degrades and releases the negatively charged ions (Cl, S). These ions get attracted towards positively charged wirebonds when the package was powered up. The ions accumulate at the interface and acts as a catalyst in the corrosion process. The crack-front typically originates at the periphery of the bond wire and propagates towards the center. Direction of the current flow did not affect the mechanism of the failure. The failure mechanism observed in this study was consistent with the failure mechanisms reported in the literature for high temperature storage tests [8], [4]. However, since the package was daisy chained, cracking was observed in the wirebonds experiencing positive bias.

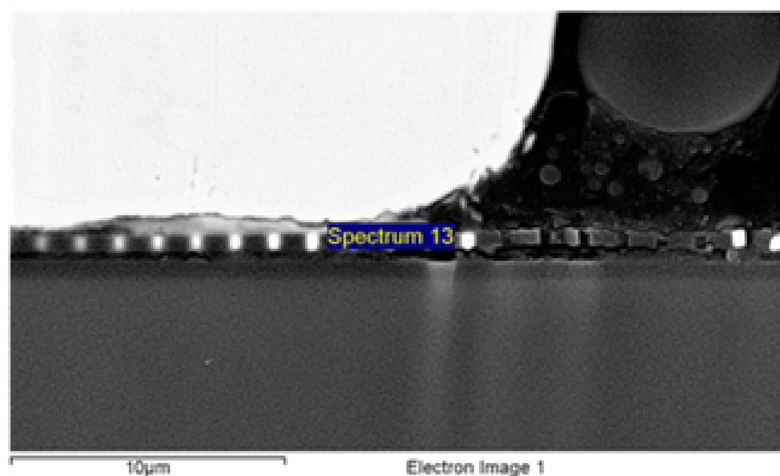

Figure 6.48: Interfacial Cracking Observed Upon Failure

6.4.2.3 Ag Wirebond

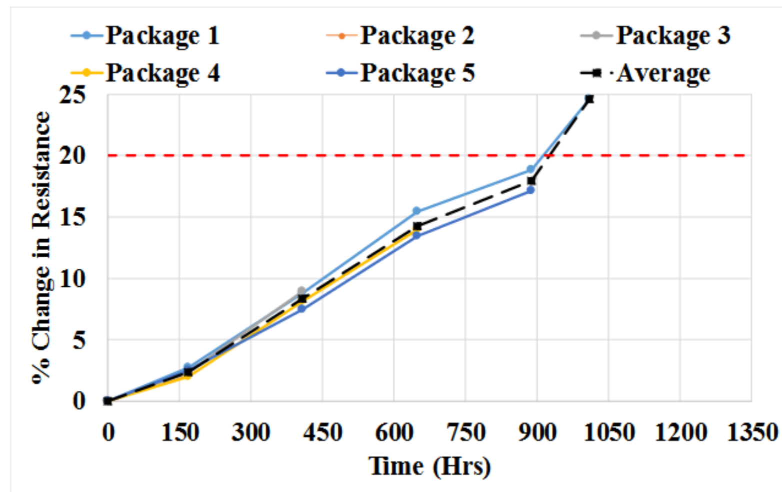

Figure 6.49: Increase in Resistance of Ag-Al Wirebond

Figure 6.49 shows increase in resistance of the Ag wirebonded packages due to exposure to high temperature and high current density. Black dashed line represents an average resistance increase. More than 20% change in resistance was observed after aging for 1010hours. Unlike Cu and Au wirebonds, resistance increase was observed at constant rate. Figure 6.50 shows interface morphology of Ag-Al interconnect. Black arrows indicate the electron flow direction. As the testing duration increased, continuous increase of the IMC layer was observed. After 648 hours of aging, lots of voiding along with peripheral cracking was observed at the interface. Initially only one darker IMC phase was observed. As the time evolved, second phase was also observed too. Both phases were found to be Ag rich phases. Dark phase was identified as Ag_2Al and bright one was Ag_3Al. As the aging time increases, due to abundant supply of Ag, Ag_3Al phase became dominant

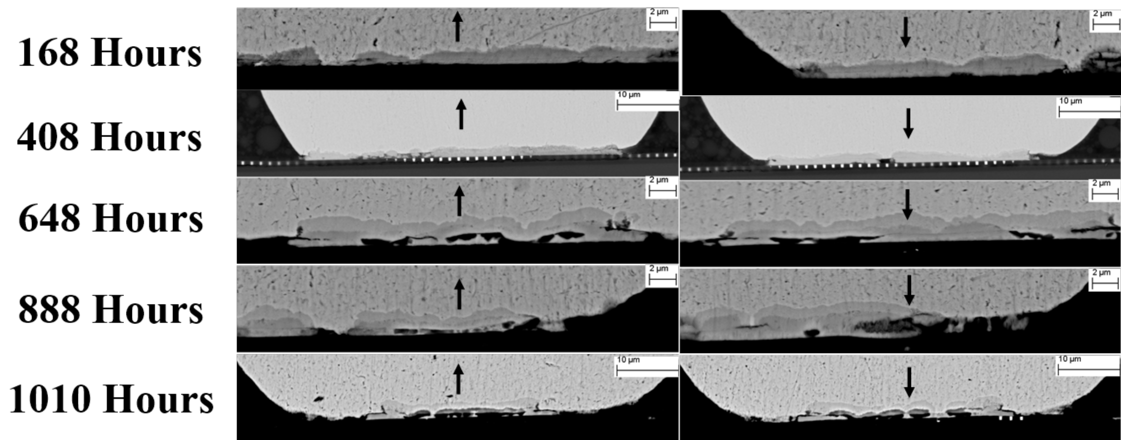

Figure 6.50: IMC Growth of Ag-Al Interconnect

Figure 6.51 shows the morphology of Ag-Al interface upon failure. Interfacial cracking was observed between two phases of the IMC and is highlighted in the red circles. The voiding found near the center of the wirebond is highlighted with black box. Peripheral cracking of the IMC which propagates towards the center of the wirebond is due to localized chemical changes of the EMC which are caused by electric overheating of the junction. Voiding observed at the center of the wirebond was a combined effect of high current density and corrosion cracking. When the electron flows from ball bond to the pad, larger voids distributed across wider areas were observed. When the electron flow was from pad to wire, voids were comparatively smaller and void free areas were still visible. Interfacial cracking was observed in both cases and was independent of the electron flow direction. Micro-cracks between two phases breaks the mechanical as well as electric contact. Due to the loss of mechanical adhesion, diffusion path gets reduced to smaller area. Electron density flowing from wirebond to pad increased the fracture surfaces. This promoted rapid phase transformations. Different diffusion and transformation rates of the IMC phases resulted into void formation. Void growth accelerated as more material flows from less area and eventually resulted into completely voided interface. For electrons flowing in the opposite direction, they tend to suppress this mechanism and limit the growth as well as size of the voiding.

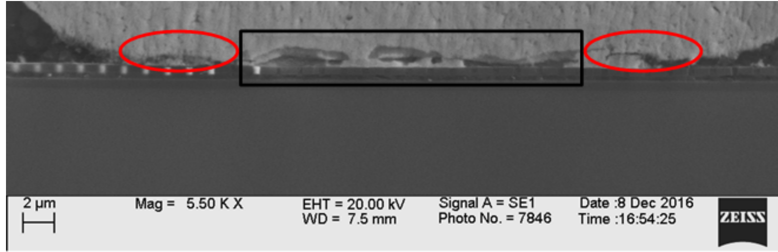

Figure 6.51: Interfacial Cracking Observed Upon Failure

Figure 6.52 shows growth of IMC as a function of aging duration. As discusses earlier, thicker IMC was observed when electrons flow from wirebond to Al pad. Electron flow in the opposite direction provides resistance to natural flow of Ag to diffuse into Al. IMC thickness after 148 hours of aging was 1.02 µm (Pad to Wire) and 1.13 µm (Wire to Pad). After failure, for the same flow directions, thicknesses were 1.90 µm and 2.11 µm respectively.

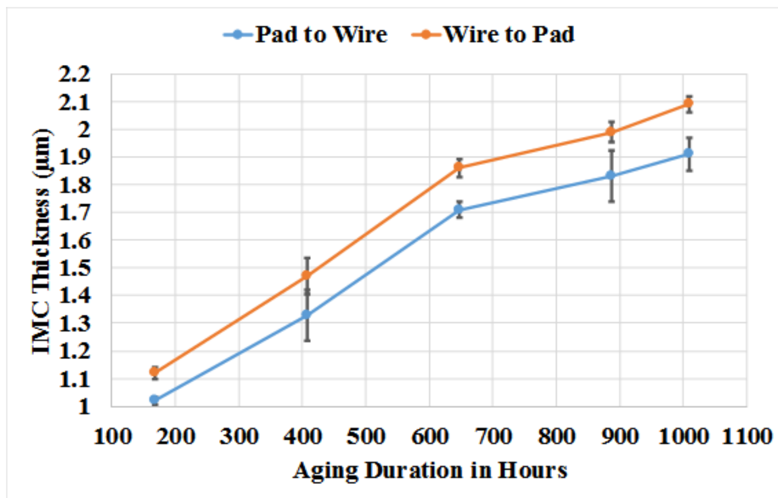

Figure 6.52: Evolution of Ag-Al IMCs

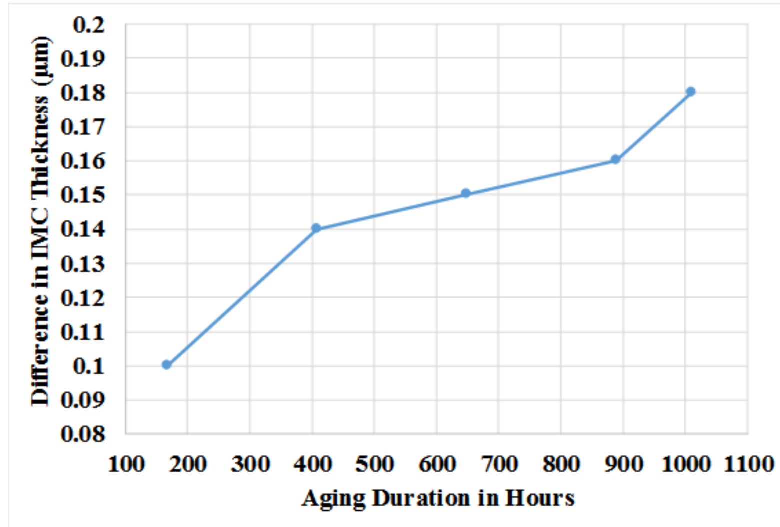

Figure 6.53: Effect of Current Direction on Ag-Al IMC Growth

Figure 6.53 shows the average IMC thickness difference between the wirebond pairs, and its evolution over time. Initial difference between wirebond pair, after 168 hours of aging was $0.1\,\mu m$ (8.8% of the maximum thickness). the difference increased continuously over time and at the time of failure it was $0.18\,\mu m$ (8.5% of the maximum thickness). It was found that direction of current flow significantly affected the IMC growth rate as well as large scale voiding at the Ag-Al interface. Excessive voiding (direction dependent) in conjuncture with the peripheral cracking (direction independent) of the interface caused failure of Ag-Al interconnects under high temperature-high current operating conditions.

6.4.2.4 Au Wirebond

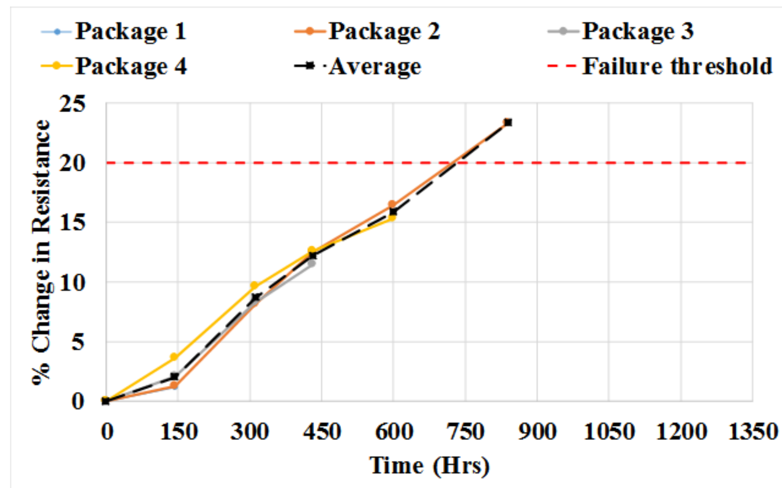

Figure 6.54: Increase in Resistance of Ag-Al Wirebond

Figure 6.54 shows the change in resistance of Au-Al wire bonded packages. Black dashed line shows the average value of the change in resistance of all packages. Since one package was taken out for cross sectioning at each time interval, for the last reading, only one data point was available. Package failed after 800 hours of thermal aging. 24% increase in resistance was observed at the time of the failure. After initial 3% change in resistance, rate of change of resistance increased and was constant till the failure. Cross-sectioned parts were inspected using SEM and EDX technique. In first few data points (Until 432 hours of aging) two phases of IMC were observed. Both phases were Au rich phases, however bottom phase had higher Al content than the top phase. Top phase was Au_4Al and bottom phase was Au_8 Al_3. As the aging duration increased, Au_8 Al_3 phase disappeared and was completely converted into Au4Al phase. Figure 6.55 shows growth of intermetallic phases in Au-Al system. Black arrow at the center of each image indicated the direction of the electron flow. IMC thickness increased significantly as the aging duration increased. Figure 6.56 shows voiding found in Au-Al wirebonds after 800 hours of aging. Higher voiding density was observed when the electron flow was from wire to pad as compared to the flow in an opposite direction.

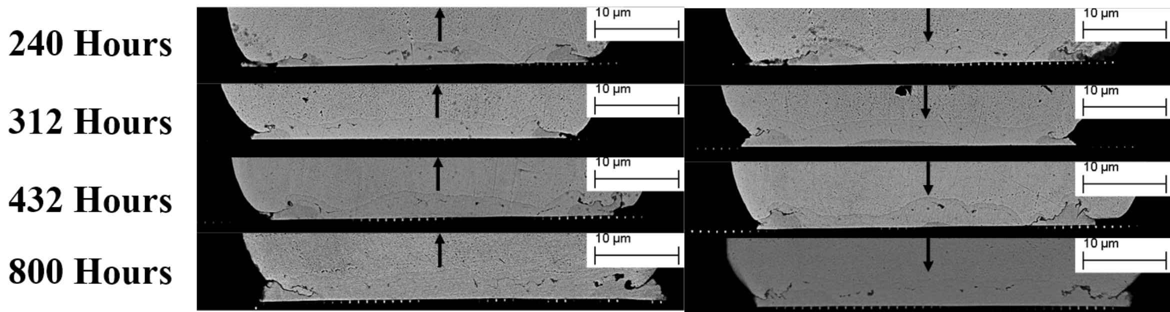

Figure 6.55: IMC Growth of Au-Al Interconnect

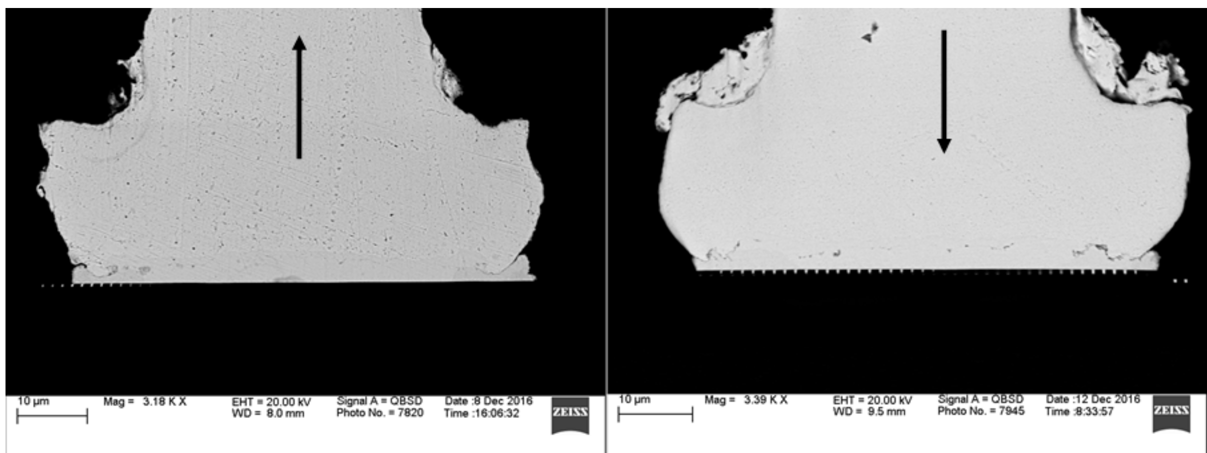

Figure 6.56: Interfacial Voiding Observed Upon Failure

Figure 6.57 shows IMC thickness data of the Au wirebonds. Plot shows that there was consistent different between wirebond pairs solely based on the current flow direction. Error bars at each point indicates the spread of the data for each measurement point. Irrespective of the aging duration, IMC thickness was different for wirebonds with different current directions. IMC thickness was consistently higher when electrons were flowing from Au wire to Al pad. Gold has natural tendency to diffuse into Al pad. Very high current density flowing from the wire to the pad provided additional momentum and accelerated the IMC growth. This also causes formation of Kirkendall voiding, as shown in Figure 6.56. However, when electrons flow was from Al pad to Au wire, the electromigration force opposes the natural diffusion flow and suppresses the IMC growth rate. The slower rate of IMC formation and phase transformations reduced the chances of void formation and much cleaner interface was observed as shown earlier.

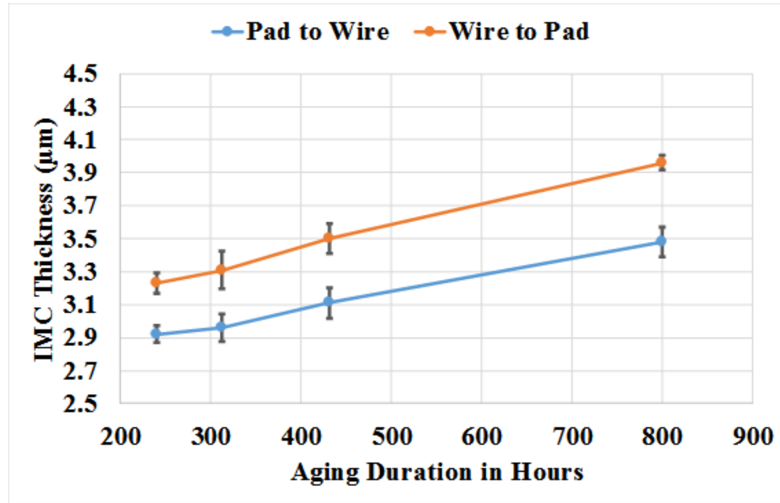

Figure 6.57: Evolution of Au-Al IMCs

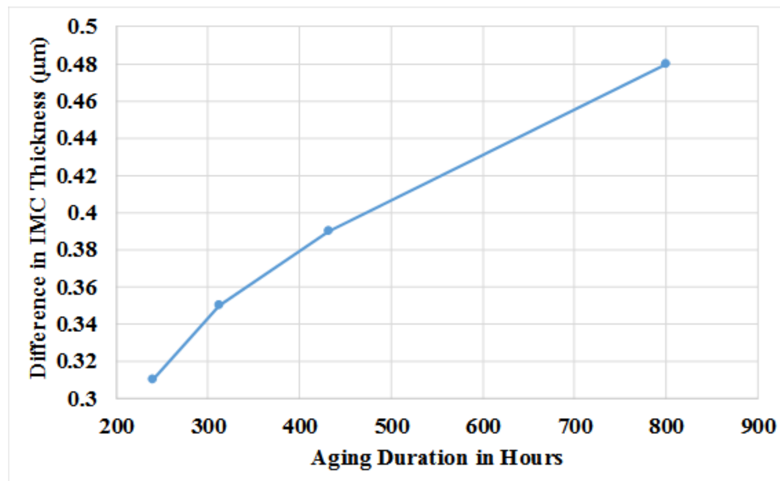

Figure 6.58: Effect of Current Direction on Au-Al IMC Growth

Difference in the average IMC thickness of wirebond pair over the testing duration is plotted in Figure 6.58. Initial difference between wirebond pair with opposite current flow directions was around $0.31\,\mu\mathrm{m}$. The difference continued to increase and at the time of the failure, the difference was around $0.48\,\mu\mathrm{m}$. It was evident that even though the high temperature environment accelerates IMC formation, direction of electron flow significantly affected the growth rate and the Kirkendall voiding. Both phenomenon combined affected the reliability of the Au wirebonds and caused premature failure for high electron density flowing from wirebond to pad.

6.4.2.5 Comparison of Wirebonds

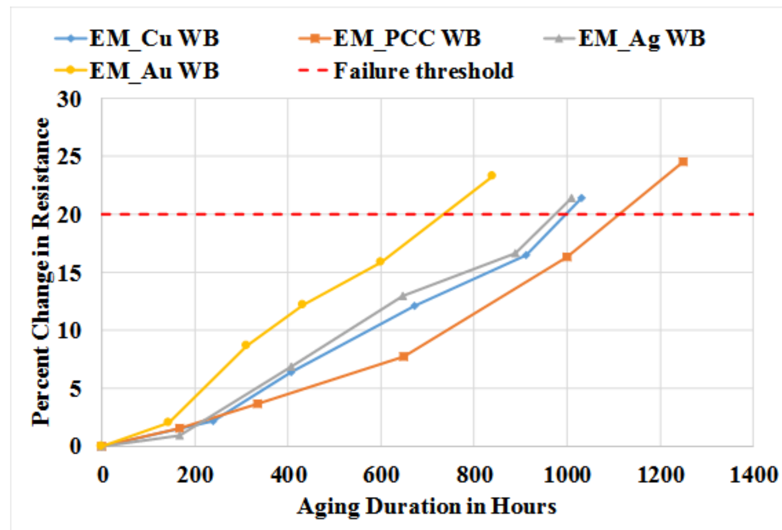

Figure 6.59: Compiled Resistance Data of All Wirebond Candidates

Figure 6.59 shows compiled resistance data of all four wire types. Au wirebond was found to be least reliable and failing first, followed by Ag, Cu and lastly PCC wires. Au wires failed after 888 hours of aging, while the PCC wires failed only after aging for 1350 hours. Au wirebonds had higher rate of resistance change. Ag and Cu wirebonds failed at around same time and had similar trend in the resistance change. IMCs have different properties than bulk materials and have higher resistivity than bulk material. Presence of thick IMC affects the phase transformation mechanisms as well as the overall resistance of the packages. This process also makes wirebond susceptible for voiding or corrosion based cracking.

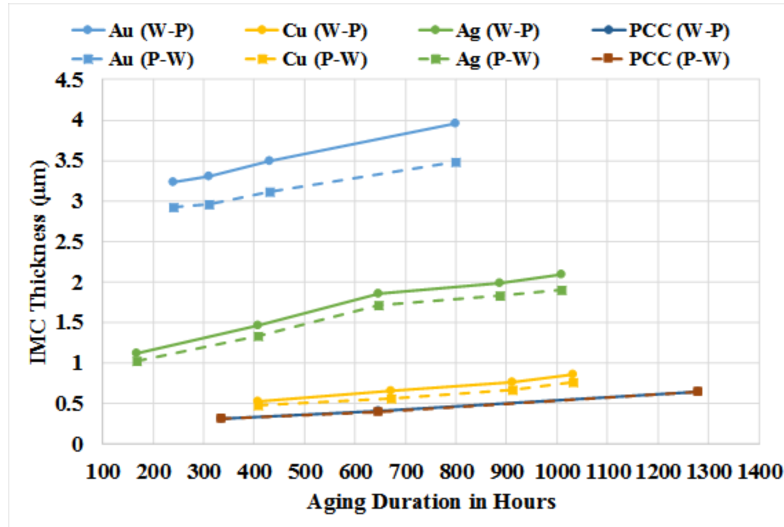

Figure 6.60: Compiled IMC Growth Data of All Wirebond Candidates

Figure 6.60 shows compiled data of IMC growth for Cu, Au, and Ag wirebonds. Except for PCC wirebond, all three wirebond candidates had electron flow directional dependent IMC growth rate. Electron flowing from wire to pad aids into the natural diffusion path and accelerated the IMC growth rate. When the electron flows from pad to wire, electron wind in the opposite direction slows down the IMC formation. Higher resistance of Au wirebonds was correlated with faster and thicker IMC growth. Au wirebonds had the thickest IMC, highest IMC growth rate. IMC growth was highly dependent on the direction of the electron flow. Difference between IMC thicknesses of the wirebond pair with different current direction was highest for Au wirebonds. PCC wires on the other hand had thinnest IMC between PCC-Al interface and exhibited slowest growth rate. This was contributed to presence of Pd at the wirebond interface. The current flow direction did not affect the IMC growth rate. but it was minimal and did not contribute into the failure of bond wire. In bare Cu wires, IMC growth rate was dependent on the electron flow direction. Cu wire had slightly higher IMC growth rate that PCC. Failure in Cu and PCC wirebonds was contributed to the corrosion based interfacial cracking between Cu rich IMC phase and bulk copper and was independent of the direction of the electron flow. Ag wirebonds had moderate IMC thickness at the start but high growth rate. Effect of the direction of the electron flow was very distinct and was magnified over time. Failure of the Ag-Al wirebond system was due to the combination of the interfacial cracking between two IMC phases and the voiding at the bond-pad interface, caused by rapid phase transformations and growth.

While the interfacial cracking was independent of the current flow direction, higher amount of voiding was observed when electron flow was from wirebond to pad, making it susceptible to premature failure.

6.5 Summary and Conclusions

Wirebonded and molded 32 pin QFN devices were subjected to HTSL and EM testing. Packages were molded with four different wirebond materials (1 mil Cu, Au, Ag and PCC) onto Al pad. Figure 6.61 shows comparison of electormigration test and high temperature no-current test for Cu, Au, PCC, and Ag wirebonds. For Au wirebonds, under high temperature test, parts failed after 480 hours of aging, whereas under EM test, parts survived 840 hours of aging. Under HTSL test, failure in wirebonds was contributed to excessive IMC growth followed by voiding at the Au-Al interface. Under EM testing, similar failure mechanisms was observed for the wires in which electron flow was from wire to pad. For all other wirebonds, IMC growth was slow and no significant voiding was observed.

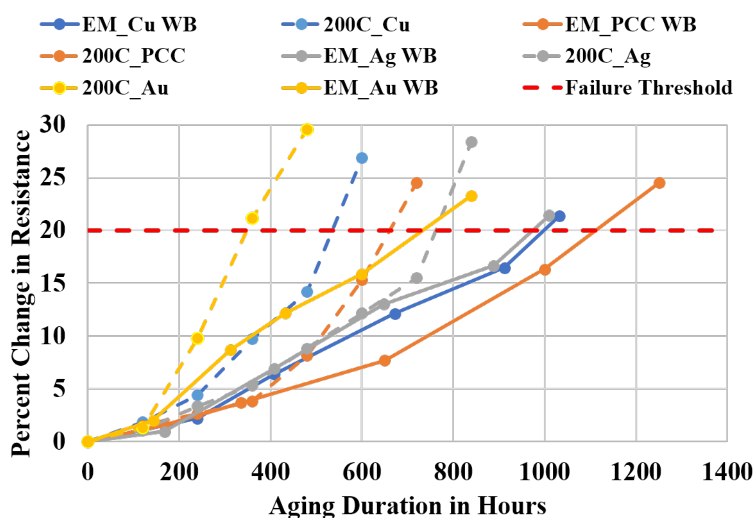

Figure 6.61: Compiled IMC Growth Data of All Wirebond Candidates

The copper wirebonded parts parts under EM survived for 1032 hours, while under HTSL they failed after 600 hours of aging. In both testing conditions, failure was contributed to corrosion based peripheral cracking. The degradation rate was very high under HTSL due to high ambient temperatures and uniform degradation of EMCs. Under electromigration test, IMC

thickness was found to be independent of current direction however failures were predominantly observed at positively charged terminals. Positively charged wirebonds attract negatively charged halied ions which resulted into accelerated failures. Similar observations were made for PCC wirebonds. Cu and PCC wirebonds shared the failure mechanisms under HTSL and EM. For PCC wires, presence of palladium at the wirebond interface delayed degradation which resulted into higher time to failure. For Silver wirebond presence of high density electron wind had adverse effect on the reliability. Under HTSL, they failed after 840 hours of aging which was best among all material candidates. Failure in HTSL condition was due to excessive IMC growth and corrosion based cracking at the bond pad interface. Under EM test, Ag wirebonded parts survived 1010 hours which was better than Au, but worst than Cu and PCC wires. IMC thickness in Ag wire-bonded part was highly dependent of direction of current flow. When electron flow was from wire to pad, IMC thickness was consistently higher. Failure at the wirebond interface was due to combination of corrosion based crack and EM driven voiding. This mixed degradation mechanism resulted into accelerated failure and severely affected reliability of Ag wirebonds under high current conditions.

Chapter 7

Effect of Green EMCs on Fatigue Reliability of Molded Wirebond Systems

7.1 Overview

Replacement of gold (Au) wires by copper (Cu) wires is being widely studied owing to the advantages of copper over gold. Researchers in the past have correlated reliability issues in the Cu wirebonds with higher ionic contamination in the epoxy molding compound (EMCs). New EMCs with 5ppm contamination or less are being developed to address this issue. Green EMCs often have very high filler content which reduces coefficient of thermal expansion (CTE) and increases the modulus (E) of EMC. Higher CTE mismatch between EMC and Cu wires can cause accelerated fatigue failures. Several attempts have been made to address this issue by performing finite element based 2D models of molded package by [80] and [48]. However, simplified 2D models cannot represent true geometry of the wirebonds and does not provide effect of wirebond location on the stresses experienced by wire. True geometry of the package must be represented and used for analysis purpose to achieve greater accuracy and to identify critical locations in the design. In this paper, a novel approach is presented to address this issue. Quad flat no leads (QFN) packages bonded with Cu wires were molded with variety of EMCs. The parts then were scanned using X-ray CT system and the scanned data was converted into FE platform. This 3D model includes all the details and represents true geometry of the package. Thermal cycling analysis was performed on the packages to study effect of different EMCs on the reliability of Cu wirebonds. Plastic equivalent strain (ϵ_p) was extracted in each case to assess the damage accumulated on the critical wire due to thermal loading. The new

Table 7.1: Package Dimensions

Parameter	Dimensions (mm)
Width	5.02
Length	5.02
Height	1.52
Pitch	0.5
Wire Diameter	25.4 μ
Pad Thickness	0.9 μ

methodology presented in the paper allows analysis on true geometries with the defects that might be present in an actual device.

7.2 Test Vehicle

32 pin molded QFN device was used for this study. The packages had 1 mil Cu wire bonded onto $0.9\,\mu m$ thick Al pad. Optical and X-ray image of the package is shown in Figure 7.1. There were 32 wirebonds in each package. Two wirebond were connected to each other on Si chip, forming one pair of wirebond. Detailed dimensions of package are listed in Table 7.1.

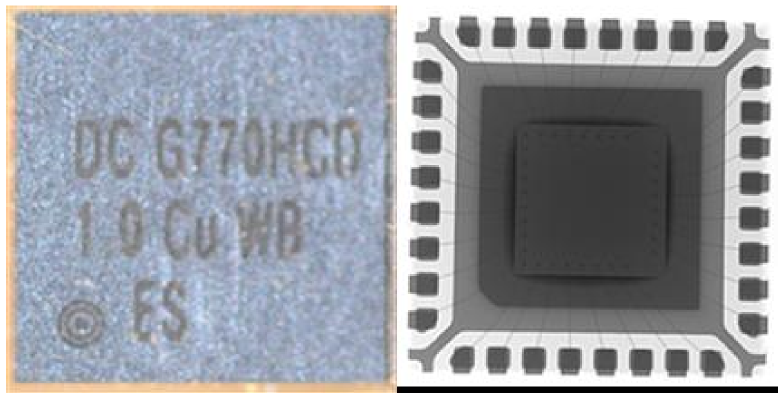

Figure 7.1: 32 Pin QFN

YXLON micro-computed system was used to scan the parts. Part was rotated continuously in the X-ray (100kV, 10μA) field by $360°$. Very low-density area such as Si chip, EMC were removed from the histogram selection to eliminate noise and get better edge detection. 2400 images were captured during the rotation. Images were combined using volume graphics 2.2

software. 3D model of the QFN assembly is represented in 7.2. Voxel size in the reconstructed volume was $2.06\,\mu m$.

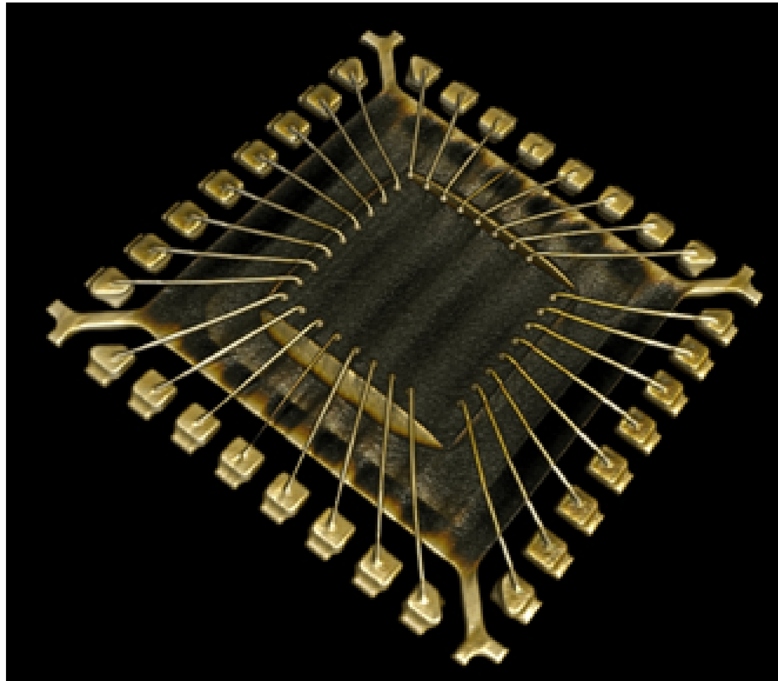

Figure 7.2: CT Reconstruction of 32 Pin QFN Package

7.3 Mesh Generation

Generation of mesh from CT scanned data involves different steps. These steps are explained in this section.

7.3.1 Image segmentation

In this step, boundaries of the model are identified based on the range of grey-scale value in the Digital Imaging and Communications in Medicine (DICOM) files. In semiconductor devices, different materials are often stacked on top of each other. Each layer has different gray-scale value owing to its material density, thickness, and atomic number of the constitutive elements. Difference in gray-scale value in a volume represents changing internal structure or material regime of the device. This is then used to identify clear material boundaries at multi-material interface such as bond-EMC-chip interface. Image thresholding was used to identify

different geometries and extract specific elements. Otsu method [116] which uses cluster-based image thresholding was used to process the images. This technique provides results in the bi-color format. The colored region represents the selected geometry and the black image represents the background noise. Algorithm assumes bi-modal distribution, i.e. image consist of pixel belonging to either the object or the background. The algorithm then calculates the optimum threshold that allows separation of two classes so that variance in each class is minimum and variance between two distributions is maximum. The within class variance is computed based on the weighted sum of the variance in the two classes and calculated as,

$$\sigma^2_{within} = w_0(t)\sigma^2_b(t) + w_1(t)\sigma^2_0(t) \tag{7.1}$$

Where, w is weight, o and b represents two classes of object and background, and σ_{within} is the within class variance for objected and background. The variance within the classes is minimized and variance between classes is maximized to formulate following functions,

$$\sigma^2_{between}(t) = \sigma^2_T(t) + \sigma^2_{within}(t) \tag{7.2}$$

$$\sigma^2_{within} = w_b(t)[\mu_b(t) - \mu_T]^2 + w_0(t)[\mu_0(t) - \mu_T]^2 \tag{7.3}$$

Where, σ^2_T is the combined variance, μ_T is the combined mean, w is weight of each class, and o and b represent class object and background respectively. The weights used for the calculation of the within class variance are based on the probability of gray scale values in the object and the background distribution.

$$w_b(t) = \sum_{i=0}^{t-1} p(i) \tag{7.4}$$

$$w_0(t) = \sum_{i=0}^{N-1} p(i) \tag{7.5}$$

Where, [0, N-1] represents grayscale levels in the image including object and background. Probability of each of the grayscale levels is represented by p(i). The combined mean of the

object distribution and the background distribution is calculated by,

$$\mu_T = w_b(t)\mu_b(t) + w_0(t)\mu_0(t) \tag{7.6}$$

The between class variance can be expressed in terms of the means of the distributions by substituting equation 7.6) into equation 7.3.

$$\sigma^2_{between}(t) = w_b(t)w_0(t)[\mu_b(t) - \mu_0(t)]^2 \tag{7.7}$$

Each of the threshold levels were then successively testes to maximize the between-class variance allowing for identification of grayscale levels. Marching cubes algorithm was used for extracting a polygon mesh of an iso-surface from three-dimensional discrete field based on identified greyscale values [117]. Figure 3 represents actual representation of different processes during image segmentation. Part (a) shows actual X-ray image consisting different materials represented by different grays-scale values. In (b) boundary of lead frame and individual leads was identified using Otsu method. Sub image (c) shows selected area (in green) for extraction purpose using matching cubes algorithm.

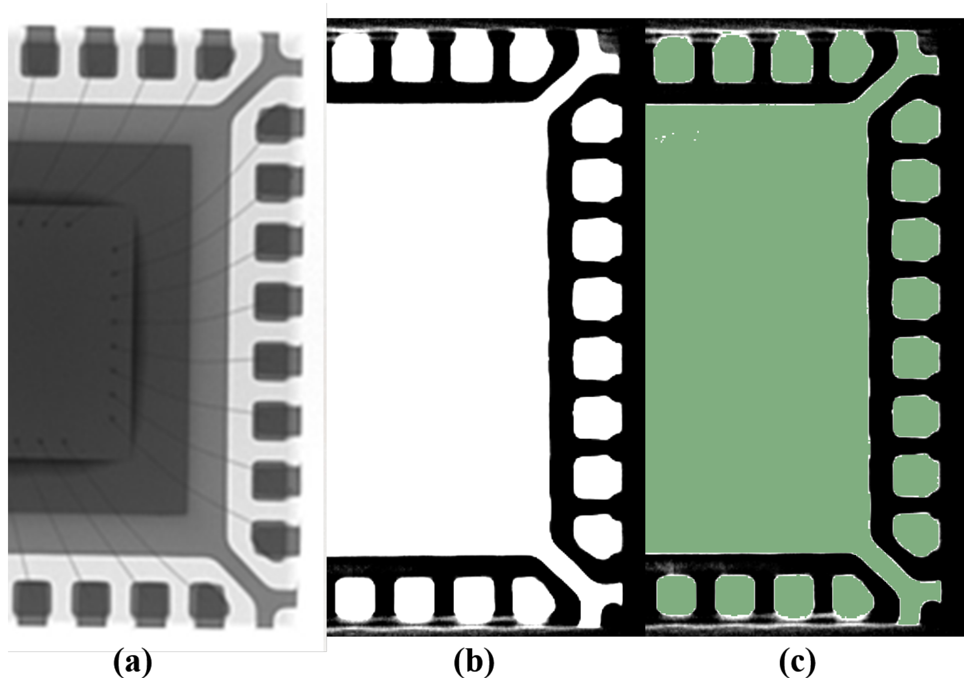

Figure 7.3: Image Segmentation using Otsu Method (a)X-ray projection, (b)Boundary identification (c)Area selection for conversion.

7.3.2 Surface Reconstruction

Surface definition at this point is often rough and has abnormal tetrahedron mesh. This can be fixed by fitting a new surface from the point cloud that represents current geometry. This technique is used to get rid of noisy data by creating new surfaces without over-fitting. In the Poisson surface reconstruction method, a 3D indicator function χ, is defined such that it has a value of 1 for points inside the model and a value of 0 for points outside the model. The gradient of the indicator function is a vector field of zeros everywhere apart from the points near the surface where it is equal to the inward pointed surface normal. Thus, the gradient of the indicator function are oriented point samples. The indicator function can thus be computed by inverting the gradient operator or finding the scalar function χ whose gradient best approximates the vector field, defined by the samples in a least squares sense.

$$min_{\chi} \parallel \bigtriangledown\chi - V \parallel \tag{7.8}$$

Application of the divergence operator allows for the problem to be transformed to a standard Poissons problem:

$$\triangledown \triangledown \chi = \Delta \chi = \triangledown V \tag{7.9}$$

Once solved, the surface is found via χ with a suitable surface. Figure 7.4 shows pre-and post-surface reconstruction lead from lead frame assembly. It can be seen clearly that surface irregularities and elements with extreme aspect ratio were removed for fixed using poisons surface reconstruction algorithm.

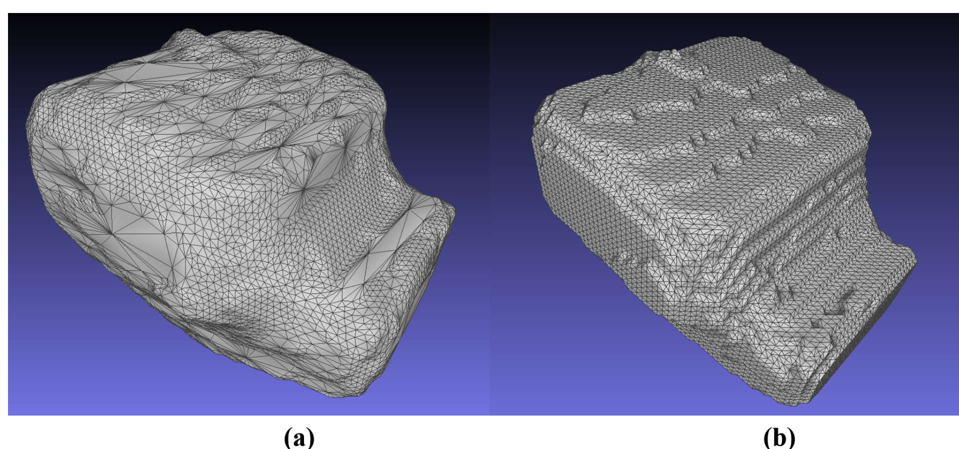

(a) **(b)**

Figure 7.4: Lead from lead-frame package (a) pre-surface reconstruction (b) post surface reconstruction

7.3.3 Mesh Decimation and Smoothing

The STL data contains point cloud and their unit normal vectors arranged in triangulated surfaces. A raw surface after surface fitting has a very dense mesh. Very small element size is computationally expensive and tedious for processing. The process of removing extra vertices and faces from mesh by simplifying the surface without losing the surface features is called mesh decimation. This step produces moderately coarse mesh which is essential for simplified computation. This reduction was performed based on quadratic error matrix [118]. The edge collapse algorithm reduces an edge into single vertex, i.e. two vertices are merged into one. The method is based on iterative contraction of vertex pairs (vi, vj) which needs to be replaced by a vertex v during the process of mesh simplification. Garland [118] associated a set of planes to each of the vertices. The decision and order of the edge collapse depends in the computed

error, which is based on the distance of the point to the plane. A vertex in 3D space may be represented as

$$v = [v_x, v_y, v_z, l]^T \tag{7.10}$$

A plane p, in Cartesian 3D space may be represented as,

$$ax + by + cz + d = 0 \tag{7.11}$$

The distance D of the vertex from the plane may be represented as,

$$D^2 = (p^T v)^2 = (p^T v)^T (p^T v) = v^T Kpv \tag{7.12}$$

The error of each vertex is defined as the sum of the squared distances to all the planes to which the vertex belongs and is represented as follows,

$$\Delta v = \sum_{P \in planes(v)} D^2 v = v^T (\sum_{P \in planes(v)} K_p) v \tag{7.13}$$

Where planes(v) represents all the triangles that meet at the vertex. The edge in the mesh is contracted when the resulting quadratic error is equal to the quadratic error of the two vertices,

$$\Delta v = \Delta v_i + \Delta v_j \tag{7.14}$$

In the current model, quadratic decimation has been used to reduce the number of edges by 75% for each component. Once the mesh decimation was performed, Laplacian smoothing was used to smoothen the mesh. In this process, vertices of the mesh are incrementally moved in the direction of Laplacian. The differential version of smoothing equation is,

$$\frac{\partial X}{\partial t} = \lambda L(X) \tag{7.15}$$

Where C is a vector of the vertices of the mesh, L is the Laplacian, and λ is a scalar that controls the diffusion speed. The continuous form of the Laplacian operator is,

$$\bigtriangledown^2 f = \sum_{i=1}^{n} \frac{\partial^2 f}{\partial x_i^2} \tag{7.16}$$

Where the subscript i corresponds to each of the independent variables. There are a few different approximations for the Laplacian operator. For a linear approximation of the operator, the smoothing equation can be written as

$$X(n+1) = (I + \lambda dt L)X(n) \tag{7.17}$$

The desirable property of diffusion smoothing is that it does not modify the connectivity of the mesh or add or delete any of the vertices. The process of smoothing instead focuses on modifying the position of the vertices. In addition, the discrete Laplacian smoothing can be implemented in a manner such that the smoothing operation requires information from its immediate neighbors. The size of the neighborhood is small and does not increase with the increase in the size of the mesh. The discrete approximations of the Laplacian Operator take the general form

$$L(x_i) = \sum_{j \in N_1 i} w_{ij}(x_j - x_i) \tag{7.18}$$

There are several options in calculations of the weights including (a) simple approximation also called the umbrella operator is one in which the Laplacian uses equal weights, such that $W_{ij} = 1/m$ where m is the number of nearest neighbors of X_i. Using the simple approximation defines the Laplacian as the vector from the vertex in question to the barycenter of the first ring neighbors. The advantage of the linear operator is that it does not change in the smoothing process and thus never needs to be recalculated. (b) scale-dependent Laplacian or the scale dependent umbrella operator uses Fujiwara weights proportional to the inverse distance between the vertices. The scale dependent Laplacian operator is represented by $w_{ij} = 1/eij$. The advantage of this method is that it preserves the distribution of triangle sizes. The scale dependent Laplacian needs to be recalculated as the vertices move. (c) Curvature normal approximation

Table 7.2: Sample Dimension Comparison

Parameter	Width (mm)	Height (mm)	Length (mm)
Meshed	0.3186	0.2651	0.4067
Original	0.3200	0.2500	0.4000

in which the tangential component of the Laplacian is eliminated using weights represented by,

$$W_{ij} = cot\alpha_j + cot\beta_j \tag{7.19}$$

Where, α_j and β_j are the angles opposite the edge in the two triangles that share the edge. In this paper, the umbrella operator has been used for mesh smoothing. Figure 7.5 (a) shows post surface reconstruction surface and (b) shows surface of leads after quadratic decimation and mesh smoothing.

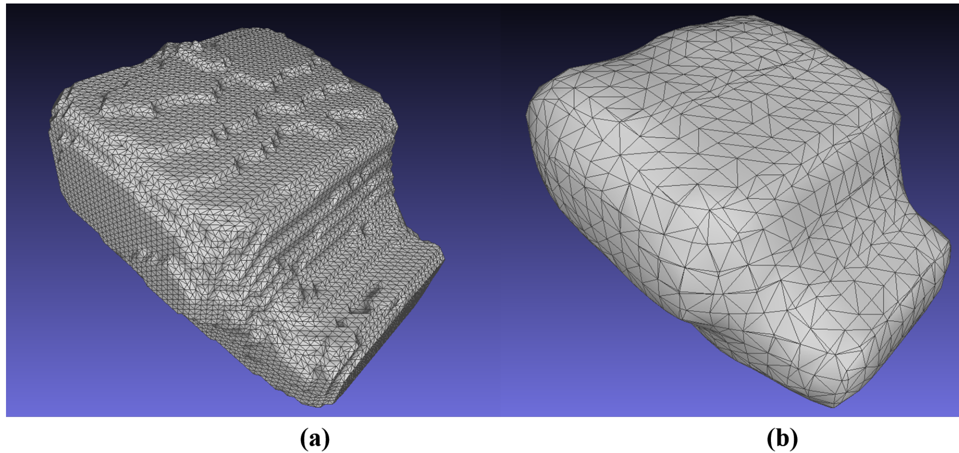

(a) **(b)**

Figure 7.5: Lead from lead-frame package (a) post-surface reconstruction (b) after quadratic decimation and smoothing

During the CT to mesh conversion, careful attention was provided towards achieving desired dimensional accuracy. Figure 7.6 Shows dimensions of a single lead. These dimensions were then compared with the real dimension of leads and are presented in Table 7.2. Once the dimensional accuracy was checked, all individual parts were then assembled to create complete model. Symmetry in the package was used and only quarter model was created. Once the full assembly was created, dimensional checks were performed on other aspects of the packages such as chip, wire, ball bond etc. The comparison of dimensions is shown in Table **??**.

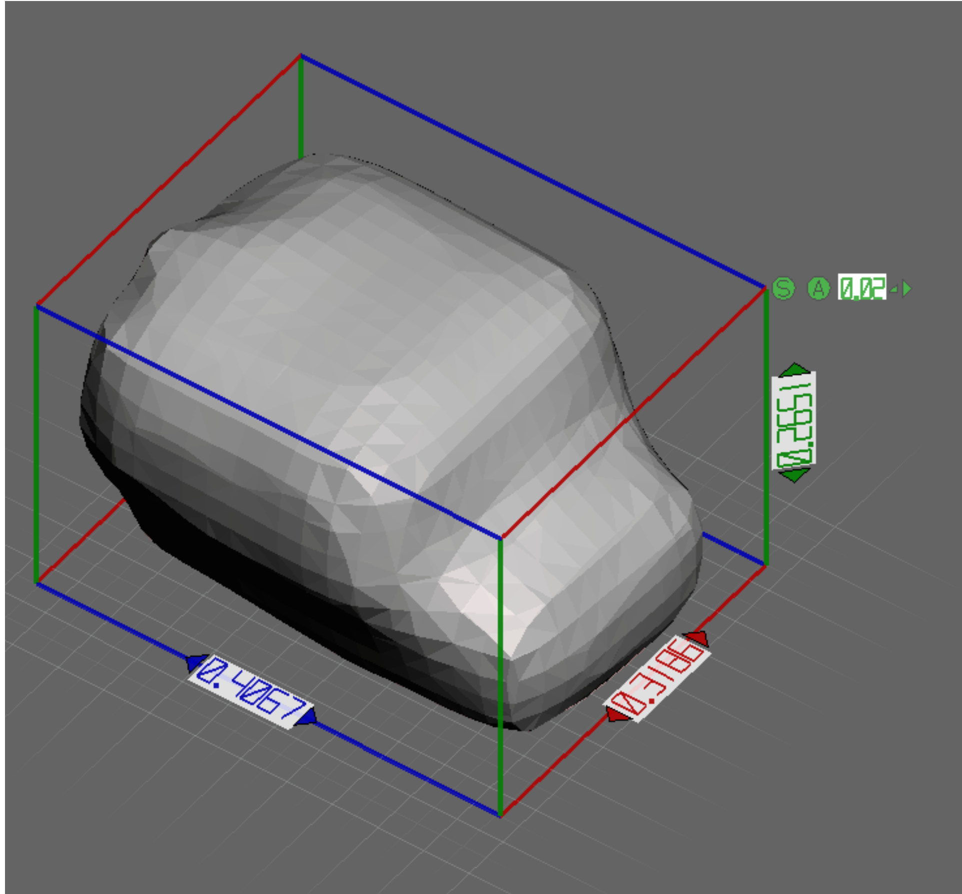

Figure 7.6: Dimension of single lead after CT to mesh conversion

Table 7.3: Dimensional Consistency

Components	Original	Meshed
Chip (mm)	2.00*2.00	2.03*2.03
Ball Bond (Microns)	69.85	70.95
Cu Wire (Microns)	25.40	26.97
Package (mm)	5.00*5.00	4.99*4.99

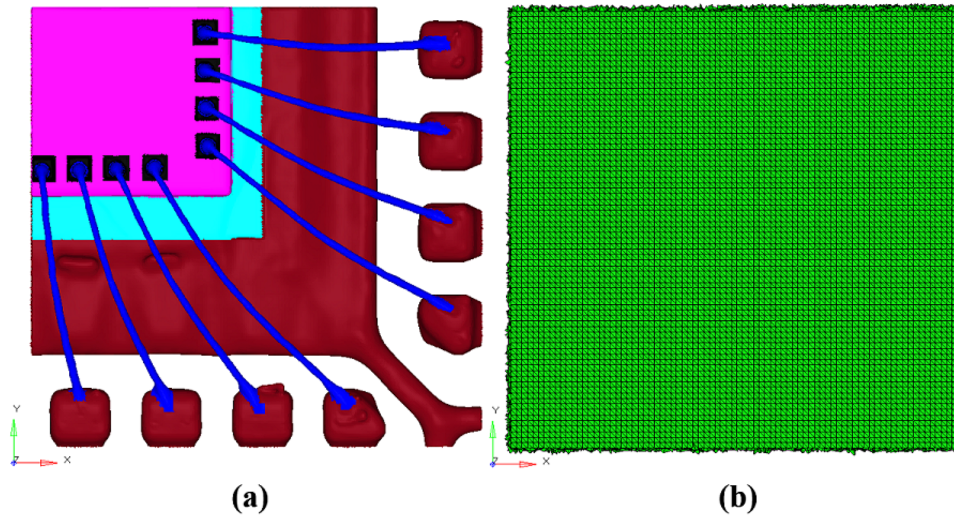

Figure 7.7: Dimension of single lead after CT to mesh conversion

7.4 FE Analysis

Similar procedure was used to extract leads, lead frame, wirebonds separately, and then they were assembled together. Si chip, EMC, die-attach, and Al pad were not detected in the CT reconstruction. These parts were modelled in CAD software and then imported into the assembly. Final overview of molded and un-molded assembly is shown in the Figure 7.7. Nodal compatibility was ensured at all interfaces. Total element count in the full assembly was slightly more than 6 million. Figure 7.8 shows sectional view of the package showing different layers of material sets such as lead frame, die-attach, chip, Al pad etc.

Linear elastic properties were assigned to all materials except for Copper wire. Material properties are tabulated in Table 7.4. Die-attach material was identified as CRM-1076NS. This is high CTE silver die-attach specifically designed for QFN applications. The lead frame material was C194 alloy. Six different EMCs were used for analysis and their properties are shown in Table 7.5 [80]. EMC A was green mold compound with very high filler content. This resulted into highest youngs modulus and lowest CTE. EMC F was traditional EMC with high CTE and lowest modulus. Rest of the EMCs were arranged in ascending order of the CTE.

Elastic-plastic material properties for Cu wire were obtained from [119]. Authors performed tensile test on 1.0 mil Cu wire and provided stress-strain curve. The stress-strain curve was used to provide non-linear material property for Cu wire. Young's modulus for Cu wire

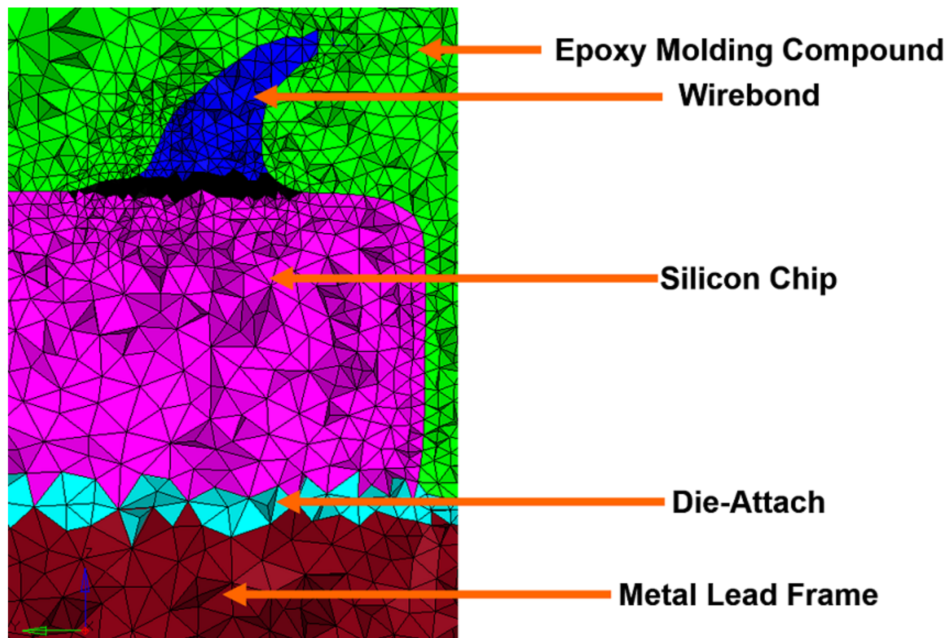

Figure 7.8: Dimension of single lead after CT to mesh conversion

Table 7.4: Table of material Properties

Components	E (MPa)	Poisson's Ratio	CTE (ppm)
Lead Frame C194	121000	0.34	16.7
Die Attach CRM1076NS	10000	0.35	45
Si Chip	163000	0.28	3.5
Aluminum Pad	68000	0.3	24

Table 7.5: Table of EMC Properties

EMC	E (MPa)	Poisson's Ratio	CTE (ppm)
A	30000	0.3	7
B	26500	0.3	8
C	24000	0.3	10
D	21000	0.3	12
E	18500	0.3	14
F	16000	0.3	16

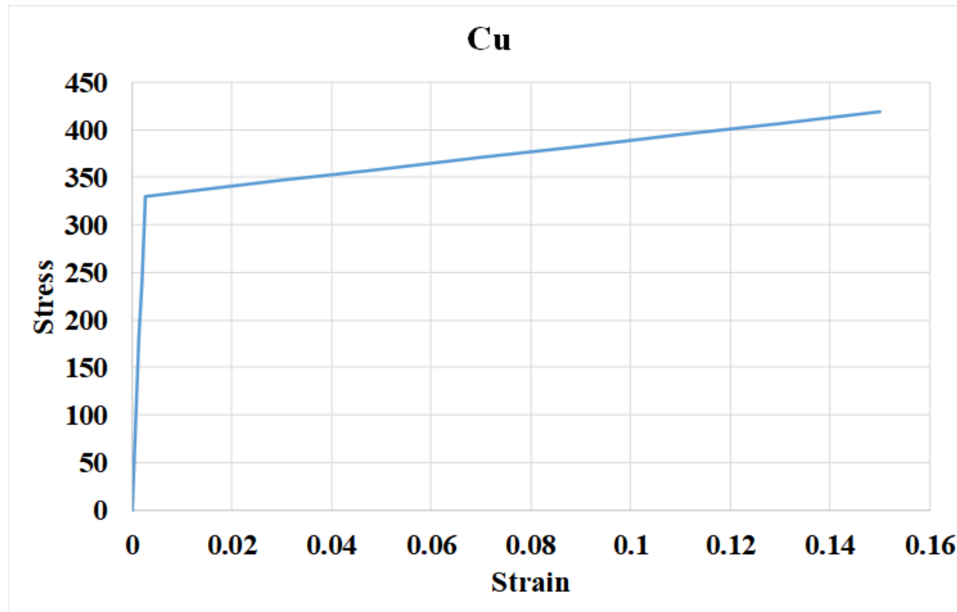

Figure 7.9: Stress-strain curve for 1mil Cu wire

was 129GPa and yield stress was 330MPa. Stress strain curve is as shown in Figure 9. Different sections in Cu wire can have different properties. Heat affected zone and ball bond often have different youngs modulus than bulk copper. In this analysis bulk property of copper was assigned to all sections of wire.

Once the material sets were identified and defined, boundary conditions were applied. Bottom central node of the package was constrained in all three directions. Symmetric boundary conditions were applied on the nodes representing cut plane of the model. The assembly was then subjected to thermal cyclic loading. Constant temperature was applied in step-wise manner to the assembly. Cycling profile was chosen as per AEC Q-100 standard for grade 0 packages. Peak temperatures were 150°C and −40°C respectively. Higher temperature was defined as reference or stress-free temperature, and one full cycle was analyzed. Dwell time at highest and lowest point was 10 min. and ramp time was 20 min. Representative single cycle is shown in Figure 10.

7.5 Finite Element Results

Analysis was performed using ABAQUS software. C3D4 elements (first order tetrahedron elements) were used. Since EMC A and EMC F have materials properties at the extreme ends

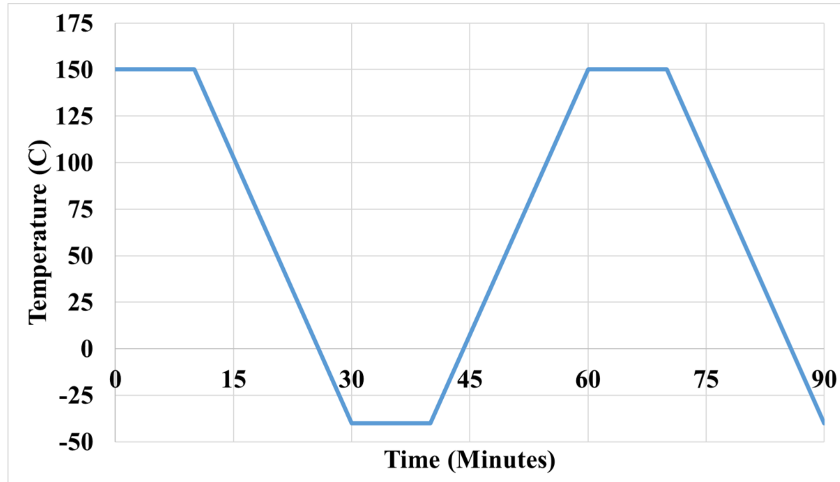

Figure 7.10: Thermal cycling profile

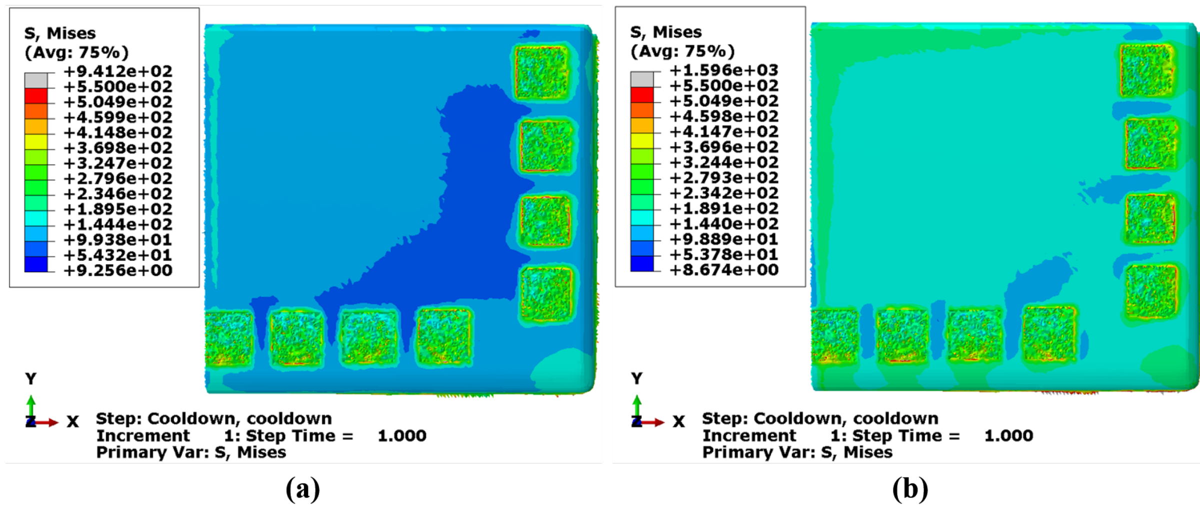

Figure 7.11: Von Mises stresses during cooling step on Si Chip for (a) EMC A (b) EMC F

of available spectrum, results for those materials are discussed in detail. Figure 7.11 shows von-mises stresses on the silicon chip for EMC A and F respectively during the cool-down phase. Since the mismatch between EMC and Si chip was very low, for EMC A, magnitude of imposed stresses on the chip was much lower than that of stresses observed in EMC F. This indicates that using low CTE mold compounds may reduce delamination related failures observed in the packages during assembly processes. Stresses around the Al pad region were higher in both cases owing to the high CTE mismatch between chip and pad.

Figure 7.12 shows von mises stresses experienced by the lead-frame during cooldown phase. When the EMC A was used, CTE mismatch was highest (9.7ppm). Difference was very small for packages molded with EMC F (1.7ppm). Higher CTE mismatch for EMC A resulted

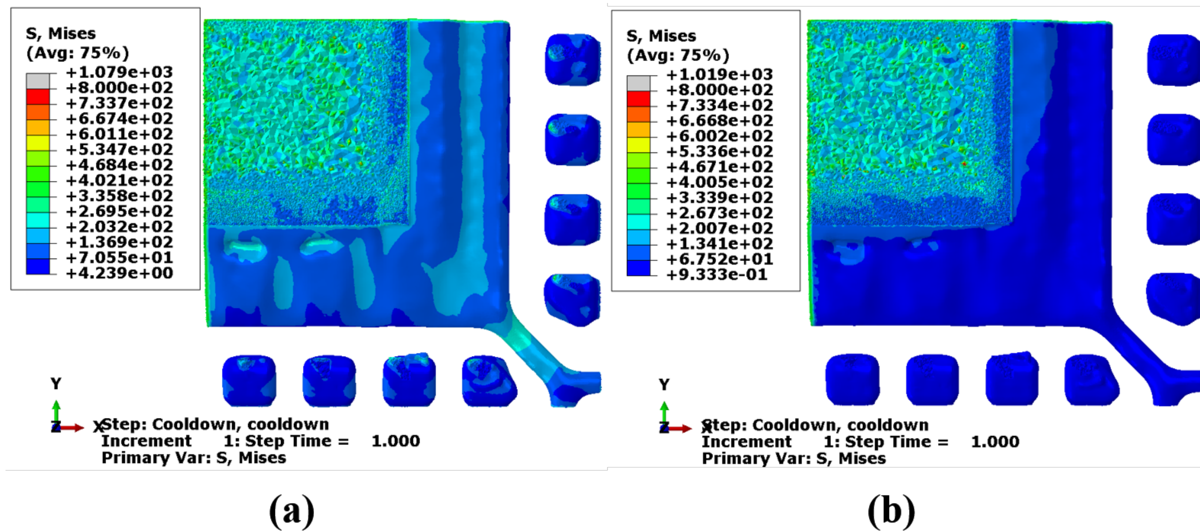

Figure 7.12: Von Mises stresses during cooling step on lead frame for (a) EMC A (b) EMC F

into more stresses on the metal lead-frame. Stresses at the die-attach and lead frame interface (CTE mismatch of 28.3ppm) were in the same range for both packages. In both cases, highest stresses were observed at this interface. Figure 7.13 shows von mises stresses in the molding compound during same step for both EMCs. Stresses at the leads-EMC interface was highest for EMC A (ΔCTE 9.7ppm) and were very small for EMC F (ΔCTE 1.7ppm). Higher stresses at leads-EMC interface indicates that special attention must be provided to analyze the bond strength between metal and epoxy interface. Poor adhesion may result into delamination related failures and accelerated corrosion related failures by providing easy path for moisture to diffuse into the package. Maximum stresses for both cases were at the corner of the die-attach-EMC interface due to very high CTE of die-attach material. Figure 7.14 shows von mises stresses at the Cu wires during the cooling phase for packages molded with both mold compounds. For EMC A, higher stresses were observed on all wires starting from wire neck region until the wedge bond. Stresses at the wedge bond were higher than yield criterion. However, for packages molded with EMC F, high stresses were observed in the half section of the wirebond, starting from ball bond. These stresses were result of the warpage of the package and were constant irrespective of the EMC used. It should be noted that for EMC F, no stresses were observed at the wedge bond region. It can be concluded that higher stresses in this region for

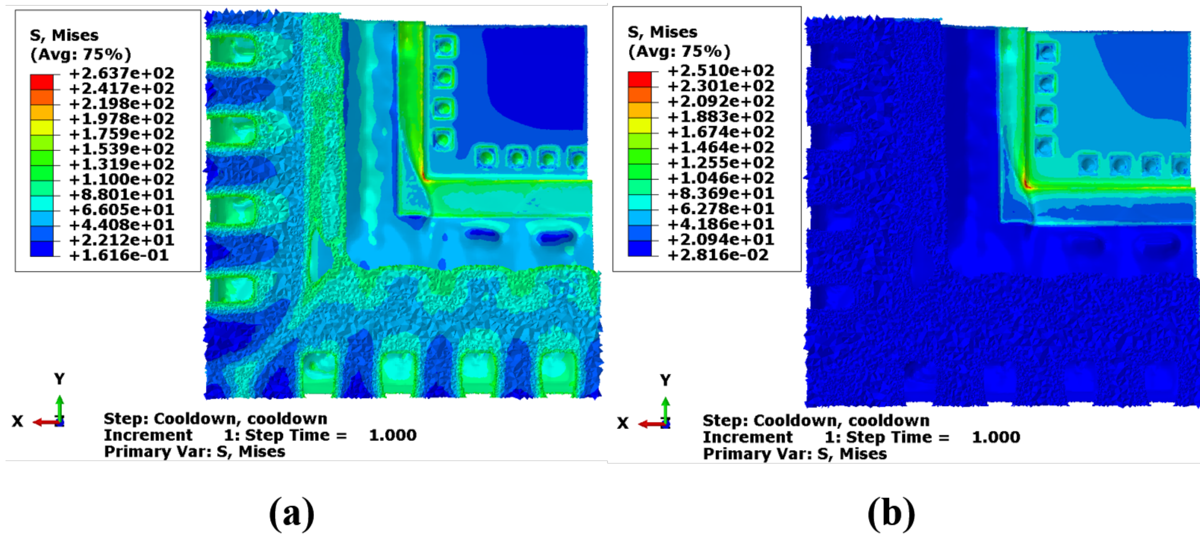

Figure 7.13: Von Mises stresses during cooling step on EMC for (a) EMC A (b) EMC F

EMC A were solely do to the higher CTE mismatch. After one complete cycle, plastic strain and stresses were observed only at the wire-chip interface and the wedge bond.

Figure 7.15 shows residual plastic strain in the Cu wedge bond after the completion of full cycle. Highest plastic strain was observed for the packages molded with EMC A. Figure 7.16 shows average and maximum plastic equivalent strain at the wedge bond for different EMCs. As the CTE of the EMC increases, plastic strain at the wedge bond reduced significantly. No plastic strain was observed for EMC D, E and F. Plastic strain will keep on accumulating as the cyclic loading is repeated. Wedge bond region of the Cu wirebond is known for its weak strength [4]. The damage accumulation can easily initiate the crack at the stitch joint and it can then propagate through the wire and result into complete cracking. The mode representation of the damage location and accumulation is consistent with the theoretical and experimental understanding of fatigue failures in wirebonds [4], [48].

Figure 7.17 shows (a) plastic equivalent strain and (b) residual Von Mises stresses in the wirebond after completion of 1 full cycle. Maximum plastic strain was extracted from each individual wire bond to study variation in the damage within package due to the physical location of wires. The plastic strain was then plotted against wire location as shown in Figure 7.18. Wire number 1 represents topmost wire in Figure 7.17, while wire number 8 represents right bottom most wire. Wire number 4 and 5 represents wires at the corner of the package.

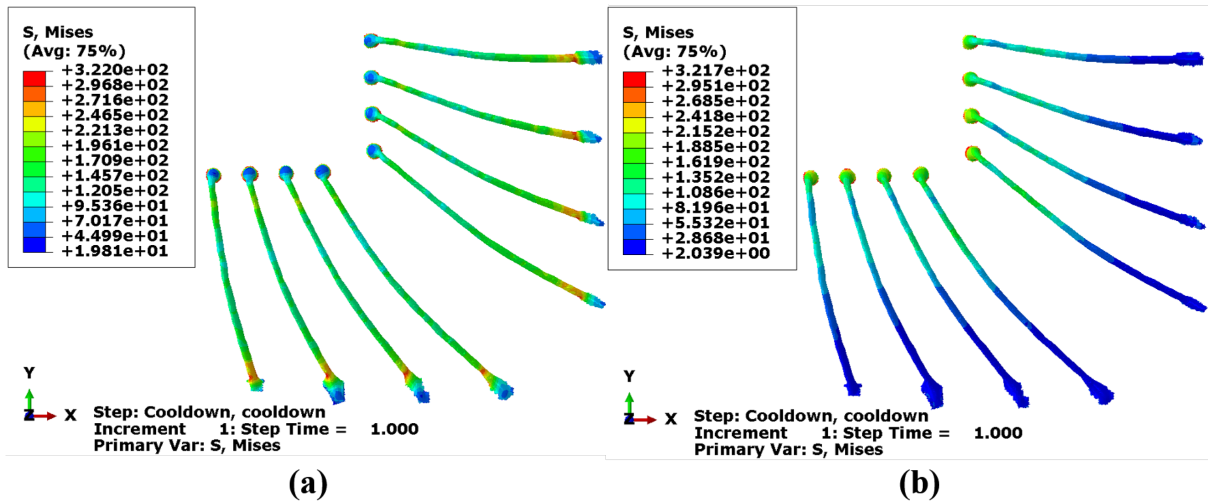

Figure 7.14: Von Mises stresses during cooling step on the Wirebond for (a) EMC A (b) EMC F

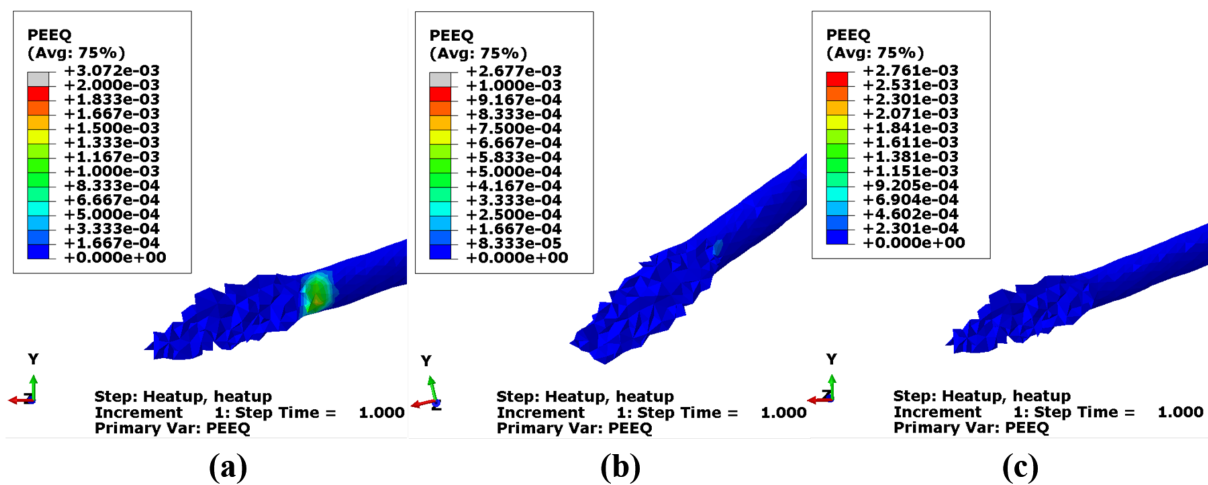

Figure 7.15: Plastic equivalent strain in the wedge bond at the end of one cycle for (a) EMC A (b) EMC C (c) EMC F

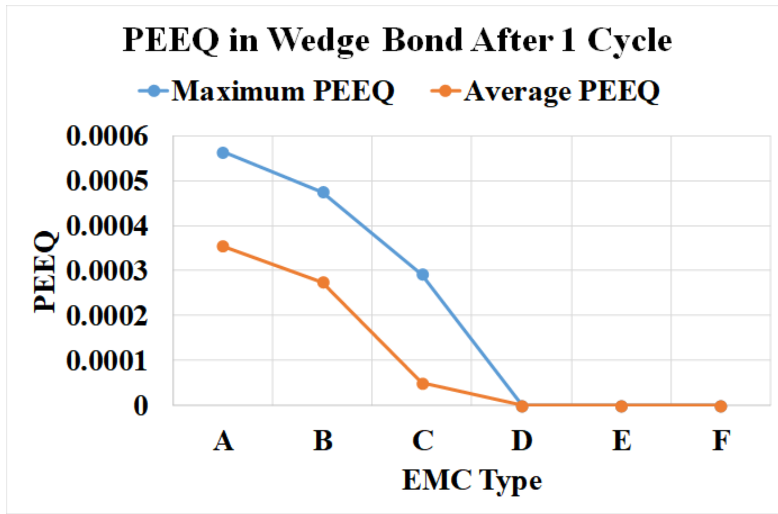

Figure 7.16: Plastic equivalent strain in Wedge bond after 1 cycle

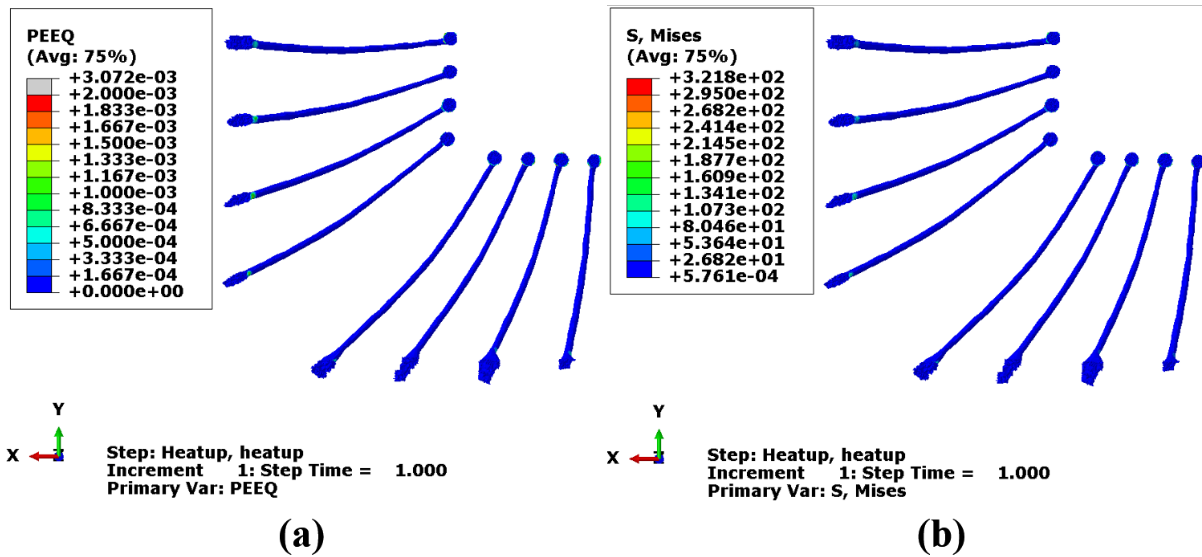

Figure 7.17: Wirebonds molded with EMC A after 1 cycle (a) Plastic Strain (b) Von Mises Stresses

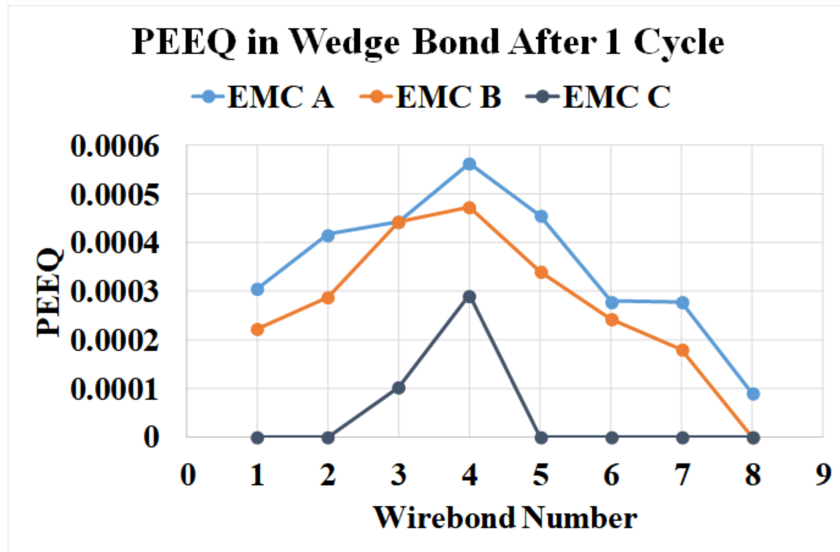

Figure 7.18: Plastic Strain in Wedge bond after 1 cycle

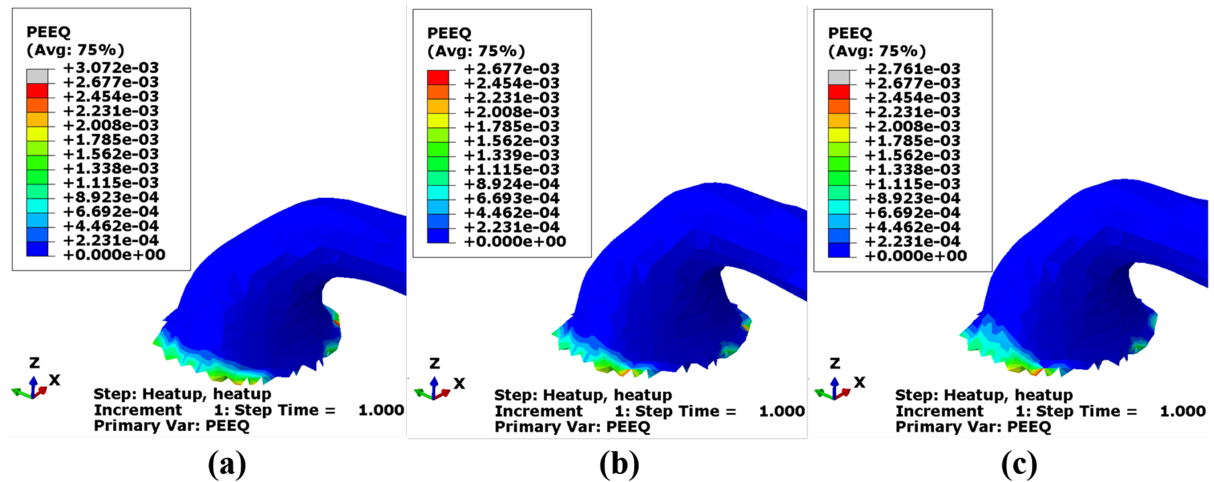

Figure 7.19: Plastic strain in the ball bond at the end of one cycle for (a) EMC A (b) EMC C (c) EMC F

Highest plastic strain was observed at wedge bonds located at the corner of the package. At this point, distance from neutral point is highest (DNP). High DNP in conjunction with high CTE mismatch results into maximum damage; making corner wire susceptible for premature failures. Magnitude of the p reduced for EMC B and EMC C. For EMC C, plastic strain was observed only at the near corner wedge bonds which confirms the mechanism described earlier.

Figure 7.19 shows residual plastic strain in the Cu ball bond after completing one complete cycle for EMC A, C and F. The plastic strain observed for all three cases was in the same range. This can be contributed to CTE mismatch between Si chip, Al pad and Cu wire in conjunction

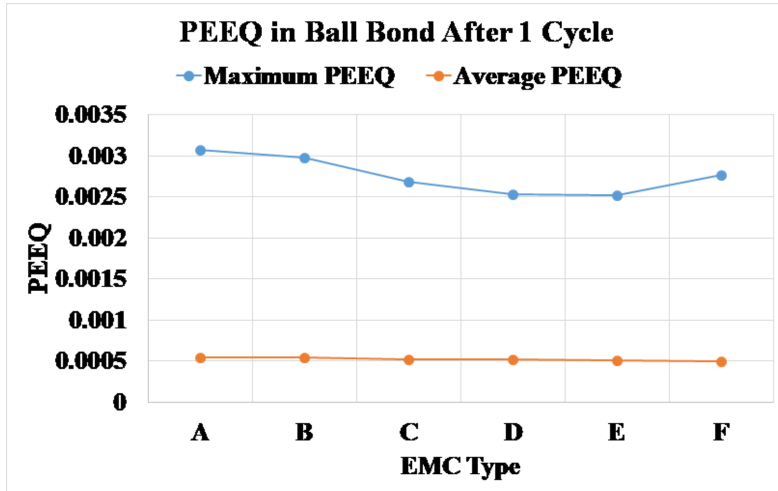

Figure 7.20: Maximum and Average Plastic Strain in Ball bond for various EMCs

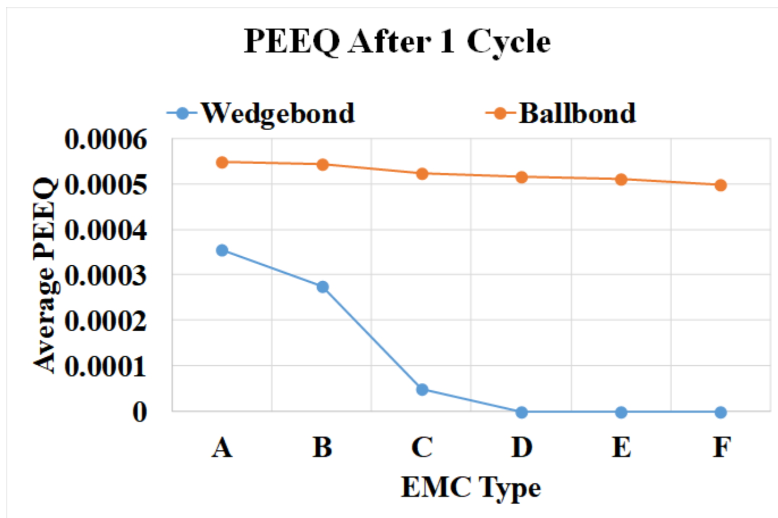

Figure 7.21: Comparison of plastic strain in wedge bond and ball bond after 1 cycle

with warpage due to thermal loading. The plastic strain values were extracted for each case. The maximum and average value was plotted for different EMCs as shown in Figure 7.20. A small drop was observed in the maximum and average plastic strain values from EMC A to EMC F. Average plastic strain was around 0.0005, and the maximum strain was 100 times bigger than average value. As observed in the earlier figures, the interfaces between wire and Al pad sets do not have smooth edges. This can cause abnormally high stresses in couple of elements which are protruding from the rest of the group. It can be hypothesized that by providing elastic-plastic properties of Al pad, accuracy at the ball bond end can be increased.

Figure 7.211 shows comparison between average plastic strain observed at the wedge and ball bonds at the end of 1 cycle. Average plastic strain at the ball bond was consistently higher

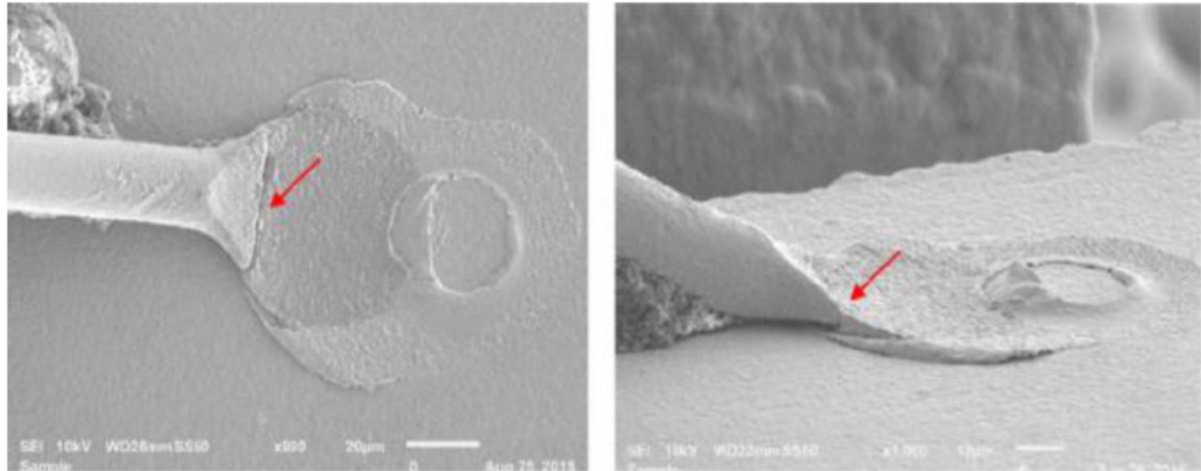

Figure 7.22: Fatigue crack in wedge bond after thermal cycling test

than the strain observed at the wedge bond irrespective of properties of molding compound. As discussed earlier, damage at the ball bond is due to CTE mismatch between Si chip and wire, and damage at wedge bond is due to mismatch between wire and EMC. Ball bond is significantly stronger than wedge bond due to presence of strong IMCs at the Cu-Al interface. Aluminum, which is softer material also absorbs the damage making ball bond region much safer. However, at the wedge bond, researchers have shown that adhesion between Cu wire and metal landing surface is often poor [4], [48]. The profile of the wire at the junction is highly non-uniform and has sharp edges. This makes wedge bond are more susceptible to cracking. Hence even though the plastic strain at the wedge bond is slightly less than that of ball bond, damage accumulation is faster at the wedge bond resulting into complete cracking. These results are consistent with experimental findings reported in [48]. Cracking in the wedge bond after thermal cycling test is shown in Figure 7.22 [48].

7.6 Summary and Conclusions

In this work, 32 pin QFN assembly was scanned using X-ray-CT system and the scanned data was used to build FE model. Different image processing techniques were used during the conversion. Dimensional and geometric accuracy of each component from the model was validated. Individual components were then assembled to create meshed quarter model. The model was free from contact elements or multi-point constrain. Six different EMCs were used

for this analysis ranging from low CTE green mold compounds to high CTE traditional EMCs. Thermal cyclic loading was applied on the package as per AEC-Q100 standard for grade 0 parts. Low CTE EMCs reduces residual stresses on the chip surface but resulted into higher stresses at the lead-frame-EMC interface and in the copper wires. Plastic strain was also observed at the ball bond which was contributed to the CTE mismatch between copper and Si chip. The residual stresses and plastic strains were concentrated along the wedge bond and were maximum for wires located at the corner of the package. As the CTE of EMC increased, damage at the wedge bond reduced and was non-existent for EMC D-F. It was concluded that wedge bonds are the critical area in the Cu wire and will fail first. The results reported in this work are consistent with experimental findings reported by prior researchers.

Chapter 8

Summary

8.1 Key Highlights

In this thesis, a methodical approach was presented to understand reliability related issues in wirebond systems under harsh environments. All four wire materials i.e. Cu, Au, Ag and PCC were studied with special emphasis on Cu wires. First study was conducted on molded packages to observe the morphological changes at bond-pad interface under high temperature and high humidity conditions. Detailed IMC formation, growth and corrosion mechanisms were presented in Chapter 3. Intermetallic growth was considered as leading indicator of failure and LM based prognostics matrix was developed to predict remaining useful life of wirebonds. The prognostics matrix was then validated with experimental findings. An extensive study was performed on daisy chained as well as commercial parts to develop acid based decapsulation technique. Acid mixing ratio of fuming sulfuric and fuming nitric acid was identified along with ideal process temperature. The specific process parameters reported in the paper can be used for decapsulation of packages with different architectures, mold compounds and wire geometries etc without damaging wire. Neural network based model was developed to study effect of process and geometric parameters of the packages on the decapsulation quality. Model was able to predict reduction in wire diameter and change in shear strength based on properties of EMC, acid ratio and process temperature. Change in electric response of the wirebond was correlated with increase in IMC growth and peripheral cracking at ball bond under HTSL and HTOL condition. For HTSL and HTOL conditions, significant IMC growth was observed and was correlated with increase in shear strength of the ball bond. Presence of corrosion based

peripheral cracking resulted in to approximately 15% increase in resistance, along with drop in shear strength and dominant mode II type shear failures. Under HAST conditions, IMC growth was non significant and failures were contributed to corrosion based cracking. Reliability of copper wirebonds is sensitive to material selection. Effect of different molding compounds properties such as pH value, ionic contamination, filler content was then studied and quantified. Low ionic contamination along with near neutral pH value usually results into reliable wirebonds. Neural network based model was developed to predict useful life of copper wirebonds molded with different EMCs, subjected to wide temperature range of 150°C to 200°C, with external bias in the range of 0V-2.5V. EKF based approach was presented for RUL prediction for parts subjected to high temperature-humidity conditions. Both Models were validated successfully with the experimental findings. Effect of high temperature and high current on different wirebond material was studied. Under HTSL condition, Au was least reliable wihle Ag wires outlasted all other candidates. Different IMC phases were identified for each wirebond system. Detailed changes in IMC phases, phase evolution in conjunction with change in shear strength and change in resistance was reported. Au wires failed due to excessive IMC growth and kirkindall voiding, while Cu, PCC and Au wires failed due to corrosion based cracking at the interface. Very high current was passed via wires under high ambient condition to study electromigration phenomenon in different wires. Au and Ag wires were most susceptible to the premature failures and were greatly affected by high current densities. Early failure were observed in wires where electron flow was moving from wire to pad; accelerating IMC formation rate. Cu and PCC wires were resilient to the high current test and did not fail prematurely. Failures in these wires were independent of current directions but dependent on polarity of external bias. A novel approach was presented to study fatigue related failures in wirebonded QFN packages molded with green EMCs. Instead of traditional CAD modeling approach, X-ray based CT scanned data was converted onto FE based platform. True geometries of different components of the package were successfully extracted, modeled and meshed. Under thermal cyclic loading for low CTE EMCs the residual stresses and the plastic strains were concentrated along the wedge bond and were maximum for wires located at the corner of the package. This

damage was non-existent for traditional high CTE EMCs. Model successfully predicted wedge bond region as the most critical region; which is consistent with current knowledge.

8.2 Recommendation for Future Work

This study can further be extended in different dimensions. Fe EMC suppliers are now introducing silicone based mold compounds which are green MCs, but have less filler content and high CTE. Understanding degradation mechanisms and wire-MC interaction of these next gen EMCs will be very significant. Palladium coated copper was found be slightly better than bare Cu wires in this study. This different was significant under HAST conditions. A similar multi-material and multi-condition study of PCC wires can help broaden current body of knowledge. A machine learning based model which can provide inputs on material selection by analyzing storage, operating, environmental conditions, manufacturing cost etc. will be very useful in industry. This will definitely aid in shortlisting existing pool of materials for new generation of products. CT to FE conversion approach can further be broadened by performing mesh sensitivity and convergence studies. This methodology can also be used for flip-chip based packages which are used in consumer electronic industry owing to their higher I/O densities. The process itself can be significantly improved if all operations can be consolidated onto single software platform.

References

[1] J. Suhling, "Lecture notes in mech6310 mechanics of electronics packaging," January 2017.

[2] Kulicke and S. Inc., "June quarter 2017 investor presentation," June 2017.

[3] G. P. B. Tools. (2017) Product catalogue. [Online]. Available: http://www.eurointech.ru/products/TPT/2016_Gaiser_Coorstek_-_Catalog.pdf

[4] P. S. Chauhan, A. Choubey, Z. Zhong, and M. G. Pecht, "Copper wire bonding," in Copper Wire Bonding. Springer, 2014, pp. 1–9.

[5] Y. Tian, C. Wang, I. Lum, M. Mayer, J. Jung, and Y. Zhou, "Investigation of ultrasonic copper wire wedge bonding on au/ni plated cu substrates at ambient temperature," Journal of materials processing technology, vol. 208, no. 1, pp. 179–186, 2008.

[6] G. Hu, "Comparison of copper, silver and gold wire bonding on interconnect metallization," in Electronic Packaging Technology and High Density Packaging (ICEPT-HDP), 2012 13th International Conference on. IEEE, 2012, pp. 529–533.

[7] Y. Xue, J. Lu, and A. Bhalla, "Method of making a copper wire bond package," Oct. 9 2012, uS Patent 8,283,212. [Online]. Available: https://www.google.com/patents/US8283212

[8] L.-J. Tang, H.-M. Ho, Y.-J. Zhang, Y.-M. Lee, and C.-W. Lee, "Investigation of palladium distribution on the free air ball of pd-coated cu wire," in Electronics Packaging Technology Conference (EPTC), 2010 12th. IEEE, 2010, pp. 777–782.

[9] N. Pascoe, Reliability Technology: Principles and Practice of Failure Prevention in Electronic Systems. John Wiley & Sons, 2011.

[10] S. Canumalla and P. Viswanadham, Portable Consumer Electronics: Packaging, Materials, and Reliability. PennWell Books, 2010.

[11] J. W. McPherson, Reliability physics and engineering. Springer, 2010.

[12] A. E. Council. (2014) Failure mechanism based stress test quantification for integrated circuits. [Online]. Available: http://www.aecouncil.com/Documents/AEC_Q100_Rev_H_Base_Document.pdf

[13] ——. (2016) Qualification requirements for components using cu wire interconnects. [Online]. Available: http://www.aecouncil.com/Documents/AEC_Q006_Rev_A.pdf

[14] ——. (2005) Wire bond shear test. [Online]. Available: http://www.aecouncil.com/Documents/AEC_Q101-003A.pdf

[15] E. Philofsky, "Intermetallic formation in gold-aluminum systems," Solid-State Electronics, vol. 13, no. 10, pp. 1391–1394, 1970.

[16] S. Murali, N. Srikanth, and C. J. Vath, "Effect of wire size on the formation of intermetallics and kirkendall voids on thermal aging of thermosonic wire bonds," Materials letters, vol. 58, no. 25, pp. 3096–3101, 2004.

[17] X. Zhang and T. Y. Tee, "Numerical and experimental correlation of high temperature reliability of gold wire bonding to intermetallics (au/al) uniformity," Thin solid films, vol. 504, no. 1, pp. 355–361, 2006.

[18] H. Xu, C. Liu, V. V. Silberschmidt, Z. Chen, and J. Wei, "The role of bonding duration in wire bond formation: a study of footprints of thermosonic gold wire on aluminium pad," Microelectronics International, vol. 27, no. 1, pp. 11–16, 2010.

[19] H. Xu, C. Liu, V. Silberschmidt, S. S. Pramana, T. White, Z. Chen, and V. Acoff, "New mechanisms of void growth in au–al wire bonds: Volumetric shrinkage and intermetallic oxidation," Scripta Materialia, vol. 65, no. 7, pp. 642–645, 2011.

[20] N. J. Noolu, N. M. Murdeshwar, K. J. Ely, J. C. Lippold, and W. A. Baeslack, "Degradation and failure mechanisms in thermally exposed au–al ball bonds," Journal of materials research, vol. 19, no. 5, pp. 1374–1386, 2004.

[21] E. Zin, N. Michael, S. Kang, K. Oh, U. Chul, J. Cho, J. Moon, and C.-U. Kim, "Mechanism of electromigration in au/al wirebond and its effects," in Electronic Components and Technology Conference, 2009. ECTC 2009. 59th. IEEE, 2009, pp. 943–947.

[22] B. Krabbenborg, "In-situ monitoring of bond degradation in power ics under high current stress," in Reliability Physics Symposium Proceedings, 1998. 36th Annual. 1998 IEEE International. IEEE, 1998, pp. 238–247.

[23] W.-B. Lee, K.-S. Bang, and S.-B. Jung, "Effects of intermetallic compound on the electrical and mechanical properties of friction welded cu/al bimetallic joints during annealing," Journal of Alloys and Compounds, vol. 390, no. 1, pp. 212–219, 2005.

[24] H. Xu, C. Liu, V. V. Silberschmidt, S. Pramana, T. J. White, and Z. Chen, "A re-examination of the mechanism of thermosonic copper ball bonding on aluminium metallization pads," Scripta Materialia, vol. 61, no. 2, pp. 165–168, 2009.

[25] C. Hang, C. Wang, M. Mayer, Y. Tian, Y. Zhou, and H. Wang, "Growth behavior of cu/al intermetallic compounds and cracks in copper ball bonds during isothermal aging," Microelectronics reliability, vol. 48, no. 3, pp. 416–424, 2008.

[26] H.-J. Kim, J. Y. Lee, K.-W. Paik, K.-W. Koh, J. Won, S. Choe, J. Lee, J.-T. Moon, and Y.-J. Park, "Effects of cu/al intermetallic compound (imc) on copper wire and aluminum pad bondability," IEEE Transactions on Components and Packaging Technologies, vol. 26, no. 2, pp. 367–374, 2003.

[27] C. Gan, E. Ng, B. Chan, F. Classe, T. Kwuanjai, and U. Hashim, “Wearout reliability and intermetallic compound diffusion kinetics of au and pdcu wires used in nanoscale device packaging,” Journal of Nanomaterials, vol. 2013, p. 4, 2013.

[28] M. Kouters, G. Gubbels, and O. D. S. Ferreira, “Characterization of intermetallic compounds in cu–al ball bonds: Mechanical properties, interface delamination and thermal conductivity,” Microelectronics Reliability, vol. 53, no. 8, pp. 1068–1075, 2013.

[29] H. Xu, C. Liu, V. Silberschmidt, S. S. Pramana, T. White, Z. Chen, and V. Acoff, “Behavior of aluminum oxide, intermetallics and voids in cu–al wire bonds,” Acta Materialia, vol. 59, no. 14, pp. 5661–5673, 2011.

[30] P. Ratchev, S. Stoukatch, and B. Swinnen, “Mechanical reliability of au and cu wire bonds to al, ni/au and ni/pd/au capped cu bond pads,” Microelectronics Reliability, vol. 46, no. 8, pp. 1315–1325, 2006.

[31] C. L. Gan, C. Francis, B. L. Chan, and U. Hashim, “Extended reliability of gold and copper ball bonds in microelectronic packaging,” gold Bulletin, vol. 46, no. 2, pp. 103–115, 2013.

[32] C. Breach and T. Lee, “Shear strength and failure modes of as-bonded gold and copper ball bonds on aluminum metallization,” Journal of electronic materials, vol. 41, no. 7, pp. 2018–2028, 2012.

[33] P. Su, H. Seki, C. Ping, S.-i. Zenbutsu, S. Itoh, L. Huang, N. Liao, B. Liu, C. Chen, W. Tai et al., “An evaluation of effects of molding compound properties on reliability of cu wire components,” in Electronic Components and Technology Conference (ECTC), 2011 IEEE 61st. IEEE, 2011, pp. 363–369.

[34] H. Seki, C. Ping, H. Nakatake, S.-i. Zenbutsu, and S. Itoh, “Study of emc for cu bonding wire application,” in CPMT Symposium Japan, 2010 IEEE. IEEE, 2010, pp. 1–3.

[35] V. Mathew, S. Chopin, L. Higgins, and Y. Zhang, “Copper wirebond compatibility with organic and inorganic ions present in mold compounds,” in International Symposium

on Microelectronics, vol. 2013, no. 1. International Microelectronics Assembly and Packaging Society, 2013, pp. 000 089–000 093.

[36] R. Rongen, G. O'Halloran, A. Mavinkurve, L. Goumans, and M.-L. Farrugia, "Lifetime prediction of cu-al wire bonded contacts for different mould compounds," in Electronic Components and Technology Conference (ECTC), 2014 IEEE 64th. IEEE, 2014, pp. 411–418.

[37] G. O'halloran, A. van IJzerloo, R. Rongen, and F. Zacharaisse, "Planar analysis of copper-aluminium intermetallics," in Proc. international symposium for testing and failure analysis (ISTFA), San Jose, CA, 2013, pp. 297–300.

[38] C. Gan, E. Ng, B. Chan, U. Hashim, and F. Classe, "Technical barriers and development of cu wirebonding in nanoelectronics device packaging," Journal of Nanomaterials, vol. 2012, p. 96, 2012.

[39] S. Kim, J. Park, S. Hong, and J. Moon, "The interface behavior of the cu-al bond system in high humidity conditions," in Electronics Packaging Technology Conference (EPTC), 2010 12th. IEEE, 2010, pp. 545–549.

[40] C. Tan, A. R. Daud, and M. A. Yarmo, "Corrosion study at cu–al interface in microelectronics packaging," Applied Surface Science, vol. 191, no. 1, pp. 67–73, 2002.

[41] J. Osenbach, B. Wang, S. Emerich, J. DeLucca, and D. Meng, "Corrosion of the cu/al interface in cu-wire-bonded integrated circuits," in Electronic Components and Technology Conference (ECTC), 2013 IEEE 63rd. IEEE, 2013, pp. 1574–1586.

[42] T. Boettcher, M. Rother, S. Liedtke, M. Ullrich, M. Bollmann, A. Pinkernelle, D. Gruber, H.-J. Funke, M. Kaiser, K. Lee et al., "On the intermetallic corrosion of cu-al wire bonds," in Electronics Packaging Technology Conference (EPTC), 2010 12th. IEEE, 2010, pp. 585–590.

[43] Y. Tian, C. Hang, C. Wang, G. Ouyang, D. Yang, and J. Zhao, "Reliability and failure analysis of fine copper wire bonds encapsulated with commercial epoxy molding compound," Microelectronics Reliability, vol. 51, no. 1, pp. 157–165, 2011.

[44] R. Rongen, A. van IJzerloo, A. Mavinkurve, and G. O'Halloran, "Degradation of cu-al wire bonded contacts under high current and high temperature conditions using in-situ resistance monitoring," in Electronic Components and Technology Conference (ECTC), 2015 IEEE 65th. IEEE, 2015, pp. 1396–1402.

[45] T.-H. Yang, Y.-M. Lin, and F.-Y. Ouyang, "Joule-heating-induced damage in cu-al wedge bonds under current stressing," Journal of Electronic Materials, vol. 43, no. 1, pp. 270–276, 2014.

[46] E. Arjmand, P. A. Agyakwa, M. R. Corfield, J. Li, B. Mouawad, and C. M. Johnson, "A thermal cycling reliability study of ultrasonically bonded copper wires," Microelectronics Reliability, vol. 59, pp. 126–133, 2016.

[47] A. Mazloum-Nejadari, G. Khatibi, B. Czerny, M. Lederer, J. Nicolics, and L. Weiss, "Reliability analysis of cu wire bonds in microelectronic packages," in Thermal, Mechanical and Multi-Physics Simulation and Experiments in Microelectronics and Microsystems (EuroSimE), 2016 17th International Conference on. IEEE, 2016, pp. 1–8.

[48] M. van Soestbergen, A. Mavinkurve, S. Shantaram, and J. Zaal, "Delamination-induced stitch crack of copper wires," in Thermal, Mechanical and Multi-Physics Simulation and Experiments in Microelectronics and Microsystems (EuroSimE), 2017 18th International Conference on. IEEE, 2017, pp. 1–4.

[49] M. Pecht and L. T. Nguyen, Plastic-encapsulated microelectronics: materials, processes, quality, reliability, and applications. Wiley-Interscience, 1995.

[50] J. Tang, A. Knobben, E. Reinders, C. T. A. Revenberg, J. Schelen, and C. Beenakker, "Microwave induced plasma decapsulation of thermally stressed multi-tier copper

wire bonded ic packages," in Electronic Packaging Technology (ICEPT), 2013 14th International Conference on. IEEE, 2013, pp. 981–986.

[51] S. Murali and N. Srikanth, "Acid decapsulation of epoxy molded ic packages with copper wire bonds," IEEE Transactions on Electronics Packaging Manufacturing, vol. 29, no. 3, pp. 179–183, 2006.

[52] X. Ma, D. Yang, and G. Zhang, "Decapsulation methods for cu interconnection packages," in Electronic Packaging Technology and High Density Packaging (ICEPT-HDP), 2012 13th International Conference on. IEEE, 2012, pp. 1387–1391.

[53] M. J. Lefevre, F. Beauquis, J. Yang, M. Obein, P. Gounet, and S. Barberan, "New method for decapsulation of copper wire devices using laser and sub-ambient temperature chemical etch." in Electronics Packaging Technology Conference (EPTC), 2011 IEEE 13th. IEEE, 2011, pp. 769–773.

[54] J. Tang, H. Ye, J. Schelen, and C. Beenakker, "Plasma decapsulation of plastic ic packages with copper wire bonds for failure analysis," in Electronic Packaging Technology and High Density Packaging (ICEPT-HDP), 2011 12th International Conference on. IEEE, 2011, pp. 1–5.

[55] Y. Tan, M. Ng, J. Khoo, C. Tan, C. De Silva, and K. Sim, "A microwave plasma dry etch technique for failure analysis of cu and pdcu wire bonds strength," in Physical and Failure Analysis of Integrated Circuits (IPFA), 2013 20th IEEE International Symposium on the. IEEE, 2013, pp. 153–157.

[56] E. J. N. De La Cruz, A. C. Sabate, and S. L. A. Estrera, "Comparative study of different copper wire decapsulation techniques for failure analysis," in Physical and Failure Analysis of Integrated Circuits (IPFA), 2013 20th IEEE International Symposium on the. IEEE, 2013, pp. 455–459.

[57] A. F. Cotton, G. Wilkinson, M. Bochmann, and C. A. Murillo, Advanced inorganic chemistry. Wiley, 1999.

[58] L. Instruments. (2012) Technical bulletin 4310 the preservation of copper during acid decapsulation. [Online]. Available: http://www.leftcoastinstruments.com/custInfo.php.

[59] S. W. Ng, H. B. Zhang, K. N. Liew, W. Lee, and R. De Lin, "Copper wirebond package decapsulation technique using mixed acid chemistry," in Physical and Failure Analysis of Integrated Circuits (IPFA), 2012 19th IEEE International Symposium on the. IEEE, 2012, pp. 1–5.

[60] Y. C. Jang, S. Y. Park, H. D. Kim, Y. C. Ko, K. W. Koo, M. R. Choi, H. G. Kim, N. K. Cho, I. T. Kang, J. H. Yee et al., "Study of intermetallic compound growth and failure mechanisms in long term reliability of silver bonding wire," in Electronics Packaging Technology Conference (EPTC), 2014 IEEE 16th. IEEE, 2014, pp. 704–708.

[61] L. J. Kai, L. Y. Hung, L. W. Wu, M. Y. Chiang, D. S. Jiang, C. Huang, and Y. P. Wang, "Silver alloy wire bonding," in Electronic Components and Technology Conference (ECTC), 2012 IEEE 62nd. IEEE, 2012, pp. 1163–1168.

[62] C. Cheng, H. Hsiao, S. Chu, Y. Shieh, C. Sun, and C. Peng, "Low cost silver alloy wire bonding with excellent reliability performance," in Electronic Components and Technology Conference (ECTC), 2013 IEEE 63rd. IEEE, 2013, pp. 1569–1573.

[63] J. Xi, N. Mendoza, K. Chen, T. Yang, E. Reyes, S. Bezuk, J. Lin, S. Ke, and E. Chen, "Evaluation of ag wire reliability on fine pitch wire bonding," in Electronic Components and Technology Conference (ECTC), 2015 IEEE 65th. IEEE, 2015, pp. 1392–1395.

[64] J. Tsai, A. Lan, D. Jiang, L. W. Wu, J. Huang, and J. Hong, "Ag alloy wire characteristic and benefits," in Electronic Components and Technology Conference (ECTC), 2014 IEEE 64th. IEEE, 2014, pp. 1533–1538.

[65] S.-W. Fu and C. C. Lee, "A corrosion study of ag–al intermetallic compounds in chlorine-containing epoxy molding compounds," Journal of Materials Science: Materials in Electronics, pp. 1–9, 2017.

[66] T.-Y. Hsu, J.-Y. Chang, F.-J. Leu, H.-M. Chang, and F.-Y. Ouyang, "Ag alloy wire bonding under electromigration test," in Electronic Packaging and iMAPS All Asia Conference (ICEP-IACC), 2015 International Conference on. IEEE, 2015, pp. 98–101.

[67] H.-W. Hsueh, F.-Y. Hung, and T.-S. Lui, "A study on electromigration-inducing intergranular fracture of fine silver alloy wires," Applied Physics Letters, vol. 110, no. 3, p. 031902, 2017.

[68] S. Wang, L. Gao, M. Li, D. Huang, K. Qian, and H. Chiu, "Electro-migration of silver alloy wire with its application on bonding," in Electronic Packaging Technology (ICEPT), 2013 14th International Conference on. IEEE, 2013, pp. 789–793.

[69] S. Kaimori, T. Nonaka, and A. Mizoguchi, "The development of cu bonding wire with oxidation-resistant metal coating," IEEE Transactions on Advanced Packaging, vol. 29, no. 2, pp. 227–231, 2006.

[70] A. B. Lim, A. C. Chang, C. X. Lee, O. Yauw, B. Chylak, and Z. Chen, "Palladium-coated and bare copper wire study for ultra-fine pitch wire bonding," ECS Transactions, vol. 52, no. 1, pp. 717–730, 2013.

[71] H. Abe, D. C. Kang, T. Yamamoto, T. Yagihashi, Y. Endo, H. Saito, T. Horie, H. Tamate, Y. Ejiri, N. Watanabe et al., "Cu wire and pd-cu wire package reliability and molding compounds," in Electronic Components and Technology Conference (ECTC), 2012 IEEE 62nd. IEEE, 2012, pp. 1117–1123.

[72] T. Uno and T. Yamada, "Improving humidity bond reliability of copper bonding wires," in Electronic Components and Technology Conference (ECTC), 2010 Proceedings 60th. IEEE, 2010, pp. 1725–1732.

[73] J. C. Krinke, D. Dragicevic, S. Leinert, E. Friess, and J. Glück, "High temperature degradation of palladium coated copper bond wires," Microelectronics Reliability, vol. 54, no. 9, pp. 1995–1999, 2014.

[74] C.-C. Lee, V. Mathew, T. Tran, R. Ibrahim, and P.-L. Eu, “Copper ball voids for pd-cu wires: Affecting factors and methods of controlling,” in Electronic Components and Technology Conference (ECTC), 2016 IEEE 66th. IEEE, 2016, pp. 606–613.

[75] K. Ravi and E. Philofsky, “Reliability improvement of wire bonds subjected to fatigue stresses,” in Reliability Physics Symposium, 1972. 10th Annual. IEEE, 1972, pp. 143–148.

[76] S. Ramminger, N. Seliger, and G. Wachutka, “Reliability model for al wire bonds subjected to heel crack failures,” Microelectronics Reliability, vol. 40, no. 8, pp. 1521–1525, 2000.

[77] A. Deyhim, B. Yost, M.-J. Lii, and C.-Y. Li, “Characterization of the fatigue properties of bonding wires,” in Electronic Components and Technology Conference, 1996. Proceedings., 46th. IEEE, 1996, pp. 836–841.

[78] G. C. Leong and H. Uda, “Correction: Comparative reliability studies and analysis of au, pd-coated cu and pd-doped cu wire in microelectronics packaging,” PloS one, vol. 9, no. 1, pp. 10–1371, 2014.

[79] H. Medjahed, P.-E. Vidal, and B. Nogarede, “Thermo-mechanical stress of bonded wires used in high power modules with alternating and direct current modes,” Microelectronics Reliability, vol. 52, no. 6, pp. 1099–1104, 2012.

[80] B. Vandevelde and G. Willems, “Early fatigue failures in copper wire bonds inside packages with low cte green mold compounds,” in Electronic System-Integration Technology Conference (ESTC), 2012 4th. IEEE, 2012, pp. 1–4.

[81] B. Czerny, A. Mazloum-Nejadari, G. Khatibi, L. Weiss, and M. Zehetbauer, “Fatigue testing method for fine bond wires in an lqfp package,” Microelectronics Reliability, vol. 64, pp. 270–275, 2016.

[82] R. Kothamasu, S. H. Huang, and W. H. VerDuin, "System health monitoring and prognosticsa review of current paradigms and practices," The International Journal of Advanced Manufacturing Technology, vol. 28, no. 9-10, pp. 1012–1024, 2006.

[83] R. Drees and N. Young, "Role of bit in support system maintenance and availability," IEEE Aerospace and Electronic Systems Magazine, vol. 19, no. 8, pp. 3–7, 2004.

[84] N. M. Vichare and M. G. Pecht, "Prognostics and health management of electronics," IEEE transactions on components and packaging technologies, vol. 29, no. 1, pp. 222–229, 2006.

[85] S. Mishra, M. Pecht, and D. L. Goodman, "In-situ sensors for product reliability monitoring," in Proceedings of SPIE, vol. 4755, 2002, pp. 10–19.

[86] N. Anderson and R. Wilcoxon, "Framework for prognostics of electronic systems," in Proceedings of International Military and Aerospace Avionics COTS Conference, Seattle, WA, 2004.

[87] M. Kanniche and M. Mamat-Ibrahim, "Wavelet based fuzzy algorithm for condition monitoring of voltage source inverters," Electronic Letters, vol. 40, no. 4, pp. 267–268, 2004.

[88] A. Saxena, J. Celaya, E. Balaban, K. Goebel, B. Saha, S. Saha, and M. Schwabacher, "Metrics for evaluating performance of prognostic techniques," in Prognostics and health management, 2008. phm 2008. international conference on. IEEE, 2008, pp. 1–17.

[89] P. Lall, N. Islam, and J. Suhling, "Prognostication and health monitoring of leaded and lead free electronic and mems packages in harsh environments," in Electronic Components and Technology Conference, 2005. Proceedings. 55th. IEEE, 2005, pp. 1305–1313.

[90] P. Lall, M. Hande, C. Bhat, and J. Lee, "Prognostics health monitoring (phm) for prior damage assessment in electronics equipment under thermo-mechanical loads," IEEE

Transactions on Components, Packaging and Manufacturing Technology, vol. 1, no. 11, pp. 1774–1789, 2011.

[91] P. Lall, R. Vaidya, V. More, and K. Goebel, "Assessment of accrued damage and remaining useful life in leadfree electronics subjected to multiple thermal environments of thermal aging and thermal cycling," IEEE Transactions on Components, Packaging and Manufacturing Technology, vol. 2, no. 4, pp. 634–649, 2012.

[92] D. Kwon, M. H. Azarian, and M. Pecht, "Remaining-life prediction of solder joints using rf impedance analysis and gaussian process regression," IEEE Transactions on Components, Packaging and Manufacturing Technology, vol. 5, no. 11, pp. 1602–1609, 2015.

[93] P. Lall, P. Gupta, and K. Goebel, "Decorrelated feature space and neural nets based framework for failure modes clustering in electronics subjected to mechanical-shock," in Prognostics and Health Management (PHM), 2011 IEEE Conference on. IEEE, 2011, pp. 1–16.

[94] P. Lall, R. Lowe, and K. Goebel, "Prognostics health management of electronic systems under mechanical shock and vibration using kalman filter models and metrics," IEEE Transactions on Industrial Electronics, vol. 59, no. 11, pp. 4301–4314, 2012.

[95] P. Lall, P. Sakalaukus, R. Lowe, and K. Goebel, "Leading indicators for prognostic health management of electrical connectors subjected to random vibration," in Thermal and Thermomechanical Phenomena in Electronic Systems (ITherm), 2012 13th IEEE Intersociety Conference on. IEEE, 2012, pp. 632–638.

[96] A. Laik, K. Bhanumurthy, and G. Kale, "Diffusion in cu (al) solid solution," in Defect and Diffusion Forum, vol. 279. Trans Tech Publ, 2008, pp. 63–69.

[97] P. Lall, S. Deshpande, Y. Luo, M. Bozack, L. Nguyen, and M. Murtuza, "Degradation mechanisms in electronic mold compounds subjected to high temperature in neighborhood of 200 c," in Electronic Components and Technology Conference (ECTC), 2014 IEEE 64th. IEEE, 2014, pp. 242–254.

[98] B. Beverskog and I. Puigdomenech, "Revised pourbaix diagrams for copper at 25 to 300 c," Journal of The Electrochemical Society, vol. 144, no. 10, pp. 3476–3483, 1997.

[99] E. McCafferty, Introduction to corrosion science. Springer Science & Business Media, 2010.

[100] A. Benedeti, P. Sumodjo, K. Nobe, P. Cabot, and W. Proud, "Electrochemical studies of copper, copper-aluminium and copper-aluminium-silver alloys: impedance results in 0.5 m nacl," Electrochimica Acta, vol. 40, no. 16, pp. 2657–2668, 1995.

[101] N. Birbilis and R. Buchheit, "Investigation and discussion of characteristics for intermetallic phases common to aluminum alloys as a function of solution ph," Journal of The Electrochemical Society, vol. 155, no. 3, pp. C117–C126, 2008.

[102] H. Liu, Z. Zhao, Q. Chen, J. Zhou, M. Du, S. Kim, J. Chae, and M. Chung, "Reliability of copper wire bonding in humidity environment," in Electronics Packaging Technology Conference (EPTC), 2011 IEEE 13th. IEEE, 2011, pp. 53–58.

[103] S. Na, T. Hwang, J. Park, J. Kim, H. Yoo, and C. Lee, "Characterization of intermetallic compound (imc) growth in cu wire ball bonding on al pad metallization," in Electronic Components and Technology Conference (ECTC), 2011 IEEE 61st. IEEE, 2011, pp. 1740–1745.

[104] C. S. Goh, W. L. E. Chong, T. K. Lee, and C. Breach, "Corrosion study and intermetallics formation in gold and copper wire bonding in microelectronics packaging," Crystals, vol. 3, no. 3, pp. 391–404, 2013.

[105] A. Saxena, J. Celaya, B. Saha, S. Saha, and K. Goebel, "On applying the prognostic performance metrics," 2009.

[106] M. Kayri, "Predictive abilities of bayesian regularization and levenberg–marquardt algorithms in artificial neural networks: A comparative empirical study on social data," Mathematical and Computational Applications, vol. 21, no. 2, p. 20, 2016.

[107] D. Titterington, "Bayesian methods for neural networks and related models," Statistical Science, pp. 128–139, 2004.

[108] D. Gianola, E. Manfredi, and H. Simianer, "On measures of association among genetic variables," Animal genetics, vol. 43, no. s1, pp. 19–35, 2012.

[109] F. D. Foresee and M. T. Hagan, "Gauss-newton approximation to bayesian learning," in Neural networks, 1997., international conference on, vol. 3. IEEE, 1997, pp. 1930–1935.

[110] R. E. Kalman, "A new approach to linear filtering and prediction problems," Journal of basic Engineering, vol. 82, no. 1, pp. 35–45, 1960.

[111] P. Zarchan, Progress in astronautics and aeronautics: fundamentals of Kalman filtering: a practical approach. Aiaa, 2005, vol. 208.

[112] I. Singh, J. On, and L. Levine, "Enhancing fine pitch, high i/o devices with copper ball bonding," in Electronic Components and Technology Conference, 2005. Proceedings. 55th. IEEE, 2005, pp. 843–847.

[113] F. W. Wulff, C. Breach, D. Stephan, K. Dittmer et al., "Characterisation of intermetallic growth in copper and gold ball bonds on aluminium metallization," in Electronics Packaging Technology Conference, 2004. EPTC 2004. Proceedings of 6th. IEEE, 2004, pp. 348–353.

[114] I. Qin, H. Xu, H. Clauberg, R. Cathcart, V. L. Acoff, B. Chylak, and C. Huynh, "Wire bonding of cu and pd coated cu wire: bondability, reliability, and imc formation," in Electronic Components and Technology Conference (ECTC), 2011 IEEE 61st. IEEE, 2011, pp. 1489–1495.

[115] H. Xu and E. Chew, "Effect of palladium on copper aluminide intermetallic growth in palladium copper bonding wire," in Electronic Packaging Technology and High Density Packaging (ICEPT-HDP), 2012 13th International Conference on. IEEE, 2012, pp. 346–351.

[116] N. Otsu, "A threshold selection method from gray-level histograms," IEEE transactions on systems, man, and cybernetics, vol. 9, no. 1, pp. 62–66, 1979.

[117] W. E. Lorensen and H. E. Cline, "Marching cubes: A high resolution 3d surface construction algorithm," in ACM siggraph computer graphics, vol. 21, no. 4. ACM, 1987, pp. 163–169.

[118] M. Garland, "Quadric-based polygonal surface simplification," CARNEGIE-MELLON UNIV PITTSBURGH PA SCHOOL OF COMPUTER SCIENCE, Tech. Rep., 1999.

[119] Y. Jiang, C. Tan, J. Gao, Y. Chen, X. Chen, Z. Yang, and Y. He, "Finite element analysis for the wire bonding process and impact force variation," in Electronic Packaging Technology (ICEPT), 2015 16th International Conference on. IEEE, 2015, pp. 1224–1229.

Appendices